CATHODIC ARC ZINC OXIDE FOR ACTIVE ELECTRONIC DEVICES

Dipl.-Ing. Salim Elzwawi

A thesis submitted in partial fulfilment of the requirements for the Degree of

Doctor of Philosophy in Electrical and Electronic Engineering

at the

University of Canterbury

February 2015

Special acknowledgement

to my loving parents,

and to my patient wife and children.

Abstract

The filtered cathodic vacuum arc (FCVA) technique is a well established deposition method for wear resistant mechanical coatings. More recently, this method has attracted attention for growing ZnO based transparent conducting films. However, the potential of FCVA deposition to prepare ZnO layers for electronic devices is largely unexplored. This thesis addresses the use of FCVA deposition for the fabrication of active ZnO based electronic devices. The structural, electrical and optical characteristics of unintentionally doped ZnO films grown on different sapphire substrates were systematically investigated. The potential of FCVA to grow both polar and non-polar ZnO films was demonstrated. The resulting films showed considerable promise for device applications with properties including high transparency($> 90\%$), moderate intrinsic carrier concentrations (10^{17} - 10^{19} cm^{-3}), electron mobilities up to 110 cm^2/Vs, low surface roughness (< 5 nm) and well-structured photoluminescence. Post-growth annealing in oxygen at temperatures up to 800 °C produced significant improvements in the electronic and optical properties of these films, due to the formation of larger grains with lower inter-grain potential barriers.

Silver oxide (AgO_X) and iridium oxide (IrO_X) Schottky diodes fabricated on annealed FCVA ZnO films showed ideality factors as low as 1.20, barrier heights up to 0.85 eV and high sensitivity to ultraviolet light (up to $\sim 10^5$ at -2V). Transparent and opaque MESFETs fabricated on these films showed well defined field effect characteristics, channel mobilities up to 70 cm^2/Vs and insensitivity to 1 mW/cm^2 visible light. These devices were further subjected to extensive bias and temperature stress tests. MESFET stability appeared to be strongly dependent on Schottky gate type, bias conditions and ZnO film morphology. Positive bias stress of AgO_X gated devices resulted in irreversible damage, that is thought to be due to Ag electromigration across the gate interface. Mapping of the surface potential of the ZnO channel material with Kelvin probe force microscopy suggested a strong relationship between the defect density at grain boundaries and both channel mobility and current stability. Interval growth techniques were found to reduce the density of defects at grain boundaries and

produced MESFETs with higher current stability. IrO_X gated devices showed superior bias stability and temperature resilience from 25 °C - 195 °C.

Acknowledgement

I would like to express my sincere thanks to my supervisor, associate Prof. Martin Allen for his valuable guidance and support throughout my research work and my stay in New Zealand, and for his continuous encouragement for publishing and presenting my work to peers. The excellent research and networking opportunities he offered, at the University of Canterbury and abroad, were academically enriching and had great impact on the outcome of this thesis. I want to thank my Co-supervisor as well, Prof. Roger Reeves, for his valuable recommendations and practical tips for optical spectroscopy.

I would also like to express my gratitude to Dr. Jim Partridge who introduced me to the world of the Filtered Cathodic Vacuum Arc deposition. I owe him the *kickstart* at the beginning of my research. The equipment training he provided, his continuous support and his efforts in growing the ZnO films at RMIT University, in Melbourne, were critical in shaping this work. Most of the XRD and the Raman spectroscopy measurements in this work were performed by him. I want to thank Prof. Dougal McCulloch as well, who hosted me for a couple of weeks in his research group at RMIT University.

Keeping the Nanofabrication Laboratory running despite all earthquakes, aftershocks, renovation works and displacements from one building to another is an almost impossible job. However, some exceptional people like Gary Turner and Helen Devereux can do it. Many thanks for their huge efforts and assistance. I am also grateful to Dr. Mikkel Schøler for his assistance in setting up the Kelvin probe force microscope, to David Kim and Dr. Giang Dang for their support and ideas in device characterization, to Adam Hyndman for performing some of the XRD measurements, and to Prof. Steve Durbin at Western Michigan University for conducting the ToF-SIMS measurements.

Away from the lab, I had the privilege to share the office with great people. During my years of research, I enjoyed drinking litres of my morning espresso shots with Robert Heinhold, Tom Cronje, Lynn Murray and Saurabh Saxena. The coffee conversations became an essential part of my daily life as a PhD student. I regret that I can't include

the findings of these conversations in my thesis. I am very thankful to Robert Heinhold, not only for being the most proficient office espresso maker, but also for spending many days in the dark, performing the PL measurements included in this work. Special thanks also to my helpful office mate, Alana Hyland, who spent lengthy days optimizing the sputtering conditions for the IrO_X and RuO_X Schottky contacts. Thanks also to the not so passionate coffee drinking office mates, Max Lynam and Matthew Whiteside, who contributed with their small talk to the inspiring office environment.

Finishing this work was somehow mentally exhausting. Few months into my PhD, the situation back home fell into violent turmoil. Worried about family and friends, distracted by the events and cut off from my original sponsor, I unthinkingly kept pushing my research up and down the list of my priorities. During these hard times, I have been offered *spontaneous* help by many parties. I am deeply grateful for the help of the student support team at the University of Canterbury, the college of engineering, the MacDiarmid Institute, and of course, my caring parents and my brother Zuher.

Publication List

[1] **Peer reviewed conference proceeding**: S. Elzwawi, H. S. Kim, R. Heinhold, M. Lynam, G. Turner, J. G. Partridge, D. G. McCulloch, R. J. Reeves, M. W. Allen. *Device quality ZnO grown using a Filtered Cathodic Vacuum Arc.* Physica B: Cond. Mat. **407**, 2903 (2012). DOI:10.1016/j.physb.2011.08.974.

[2] **Peer reviewed journal article**: S. Elzwawi, H-S. Kim, M. Lynam, E. L. H. Mayes, D. G. McCulloch, M. W. Allen, J. G. Partridge. *Stable n-channel metal-semiconductor field effect transistors on ZnO films deposited using a filtered cathodic vacuum arc.* Appl. Phys. Lett. **101**, 243508 (2012). DOI:10.1063/1.4769899.

[3] **Invited journal article**: S. Elzwawi, A. Hyland, M. Lynam, J. G. Partridge, D. G. McCulloch, M. W. Allen. *Effect of Schottky gate type and channel defects on the stability of transparent ZnO MESFETs.* Semicond. Sci. Technol. **30**, 024008 (2015). DOI:10.1088/0268-1242/30/2/024008.

Conference Contributions

[1] **Poster**: S. Elzwawi, H. S. Kim, R. Heinhold, M. Lynam, G. Turner, J. G. Partridge, D. G. McCulloch, R. J. Reeves, M. W. Allen. *Device quality ZnO grown using a Filtered Cathodic Vacuum Arc.* The 26th International Conference on Defects in Semiconductors (ICDS-26), July (2011).

[2] **Poster**: J. G. Partridge, S. Elzwawi, R. Heinhold, H-S. Kim, E. Mayes, M. R. Field, D. G. McCulloch, R. J. Reeves, M. W. Allen. *ZnO Oxide devices based on films deposited using a Filtered Cathodic Vacuum Arc.* Material Research Society (MRS), Fall Meeting (2011).

[3] **Poster**: S. Elzwawi, R. Heinhold, H. S. Kim, J. G. Partridge, E. Mayes, M. R. Field, D. G. McCulloch, R. J. Reeves, M. W. Allen. *ZnO thin film devices fabricated using a filtered cathodic vacuum arc.* The Sixth international Conference on Advanced Materials and Nanotechnology (AMN-6), February (2013).

Oral Presentations

[1] **Invited seminar**: S. Elzwawi, R. Heinhold, H. S. Kim, J. G. Partridge, E. Mayes, M. R. Field, D. G. McCulloch, R. J. Reeves, M. W. Allen. *High performance ZnO thin film devices fabricated using a filtered cathodic vacuum arc.* RMIT University, School of Applied Sciences, Melbourne, Australia, 4th July 2012.

Contents

List of Figures

List of Tables

Chapter 1

Introduction

1.1 Electronics beyond silicon

Mainstream semiconductor technology is largely based on silicon (Si) and will remain so in the foreseeable future. GaAs on the other hand has established itself as the main material for high speed and optoelectronic devices, due to its high carrier mobility and direct band gap. However, physical requirements for UV/blue photonics, transparent electronics and high-power/high temperature applications are intrinsically beyond the capabilities of silicon and GaAs, at least not without additional measures and sophisticated processes. The need for devices with these qualities has lead to the investigation of new compound semiconductors with ever increasing band gaps and has gradually brought wide band gap semiconductors to the forefront of research. The larger band gap of these materials is a prerequisite for the emission and detection of shorter wavelengths. Moreover, a wider band gap will inherently result in lower thermally generated leakage current and a higher dielectric strength. These properties are crucial for highly sensitive photo-detectors, high temperature and high power applications. Many wide band gap semiconductors have been successfully commercialized, with Gallium Nitride (GaN) and Silicon Carbide (SiC) being the most prominent examples.

In the last two decades, Zinc Oxide (ZnO) has become one of the most researched wide band gap semiconductors. Compared to its main competitors, it has many advantages. ZnO is non-toxic and abundant as a raw material (Fig. 1.1). Its direct band gap

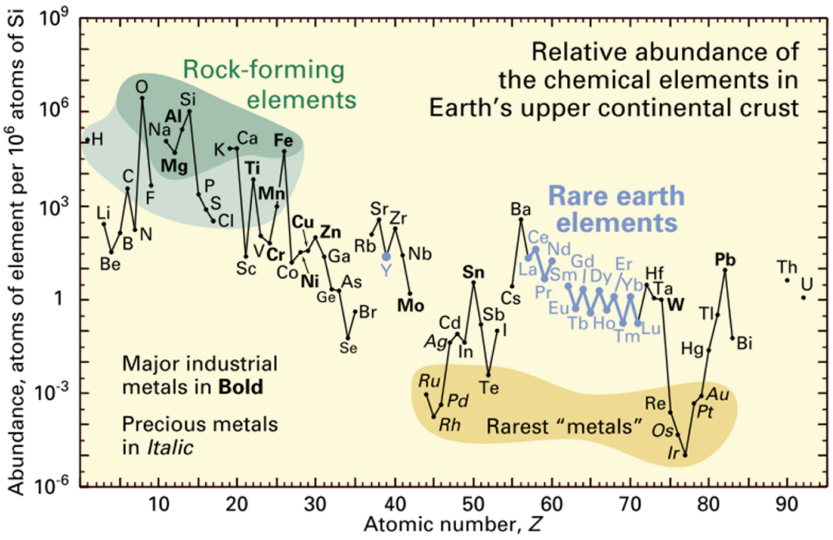

Figure 1.1: Relative abundance of the chemical elements in Earth's upper crust (Source: U.S. Geology survey [www.usgs.gov]).

matches the ultraviolet radiation energies which inherently qualifies it for applications such as UV photonics, transparent electronics and transparent conducting electrodes. In addition, it exhibits quite strong piezoelectric properties which are already being utilized for sensor applications [1, 17]. Among other advantages is the ease with which ZnO nanostructures, such as nanowires and nanorods, can be fabricated, enabling new applications in gas and bio-sensing [1]. In context of robustness, the radiation hardness of ZnO exceeds that of Si, GaAs and GaN [2], indicating a high potential for electronics capable of operating in harsh environments.

Despite the well known difficulties in achieving p-doped ZnO [3], its applications in uni-polar electronics are still numerous. Although, electronically, ZnO is not a match for crystalline Si, its electron mobility is still two orders of magnitude higher than that of amorphous silicon, which has been the standard material for thin film transistors in flat panel displays (FPD) since the early 1980s [4]. In an age where cathodic ray tubes are quickly disappearing in favor of FPDs, whose global market share has already exceeded 100 billion US dollars (Fig. 1.2), the prospects for transparent ZnO based transistors seem promising.

However, the chances for these applications being commercially realized will depend on the cost effective streamlining of ZnO fabrication technology. Zinc oxide can

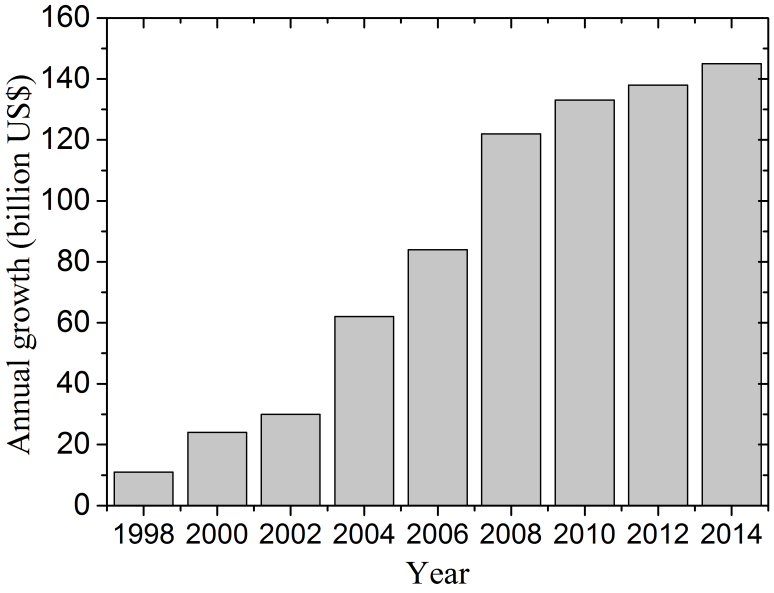

Figure 1.2: Annual market growth of flat panel displays since 1998 (Source: German flat panel display forum [www.displayforum.de]).

be readily processed with various wet chemicals and its thin films have been successfully deposited by a variety of techniques [5]. Growth methods such as molecular beam epitaxy (MBE), pulsed laser deposition (PLD) and atomic layer deposition (ALD) are typically employed to prepare n-type ZnO films of sufficient quality for device applications; however these methods incur high costs and offer limited throughput. Large area sputtering techniques on the other hand have the reputation of producing lower quality films [6]. In contrast, the filtered cathodic vacuum arc (FCVA) technique offers low system and operating costs combined with industrial scalability. Degenerately Al-doped ZnO layers have been already grown via FCVA deposition for applications such as transparent conducting coatings [7]. However, the potential of this technique to deliver high quality, moderately doped semiconductor films for use in electronic devices is largely unexplored.

ZnO is known to have a complicated defect chemistry. Different ZnO growth and deposition techniques often produce uniquely different electronic and optical properties. This thesis is intended to contribute to ZnO research through a systematic investigation

of films grown by the FCVA technique. Two primary goals are pursued in this work. The first is to investigate the structural and electronic properties of FCVA deposited ZnO films and how they relate to substrate type, growth temperature and post-growth thermal treatment. In this first step, the focus lies on examining the controllability of film morphology and identifying the defects that dominate the carrier concentration and carrier transport in the films. Secondly, after establishing the conditions for device grade film growth, the focus switches to the fabrication and characterisation of Schottky diodes and metal-semiconductor field-effect transistors. Although ZnO is known to be a robust material, the reliability of these devices depends on the interaction of the device contacts with the ZnO film. Hence, investigating device reliability by studying the effect of channel and interface defects will be addressed in detail.

1.2 Basic electronic and optical properties of zinc oxide

ZnO is a II-VI compound semiconductor. Like most compound semiconductors, individual atoms bond in a tetrahedral coordination where each anion is surrounded by four cations and vice versa. In most conditions, ZnO occurs almost exclusively in the hexagonal wurtzite crystal structure as depicted in Fig. 1.3, although zincblende and rocksalt structures are possible by growing on cubic substrates and at relatively high pressures [1]. Due to the high electronegativity of oxygen, the Zn-O bond has a considerable degree of polarity that places ZnO at the borderline between covalent and ionic bonding. The ionic character of the bond results in a larger band gap ($\approx$ 3.35 eV at room temperature) than typical in covalent semiconductors, while the extraordinarily high cohesive energy per bond (7.52 eV) leads to a very high thermal stability [8]. These properties are an essential physical requirement for building devices for high-temperature and high-power operation, with low thermally generated noise and a high breakdown voltage.

The room temperature electron Hall mobility in single crystal ZnO is approximately

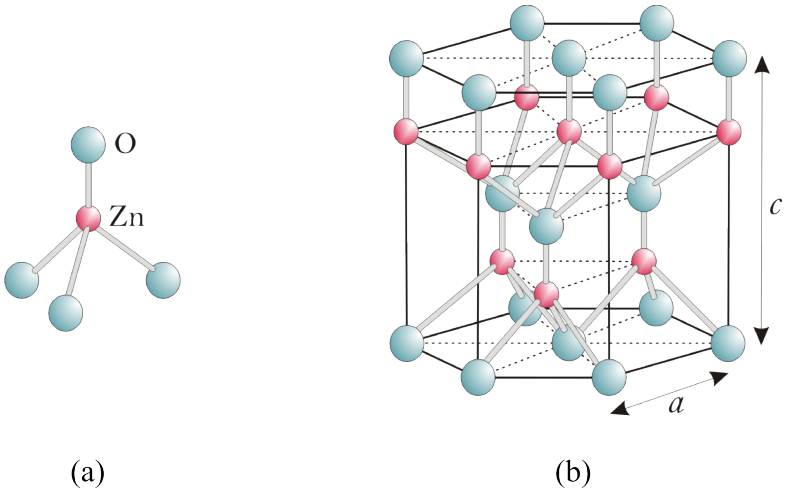

Figure 1.3: (a) A Zn-O tetrahedron and (b) the hexagonal wurtzite crystal structure of ZnO.

200 cm^2/Vs. Although this value is much lower than that achieved in mainstream semiconductors such as Si and GaAs, it is still sufficient for many applications. Moreover, for short channel hot electron devices, where electric fields are very high, it is the maximum saturation drift velocity v_{sat} that is crucial. Theoretical calculations predict a v_{sat} of about 3.2×10^7 cm/s in ZnO [9], even larger than that of Si, GaAs and GaN. In addition to high optical transparency and UV responsivity, as a consequence of its direct wide band gap, research interest in ZnO is strongly motivated by its high free exciton binding energy of 60 meV. Since this binding energy is much higher than the maximum energy of thermal phonons at room temperature ($k_B T \approx 25\ meV$), free excitons in ZnO are theoretically stable up to about 400 °C, which consequently allows UV lasing at higher temperatures and lower threshold voltages [8]. Table 1.1 compares the main electronic properties of ZnO with Si and with GaN, its main competitor for UV optoelectronics.

ZnO is natively an n-type semiconductor which at room temperature exhibits defect- or impurity-dominated n-type conductivity. This is as a consequence of its large band gap combined with the unavoidable presence of electrically active shallow defects with low ionization energies, typically 10-100 meV, at moderate concentrations [2, 10]. Intentional n-type doping is readily achieved through the use of column-III elements such as Al, Ga, or In, or column-VII elements such Cl, F, I and electron

Table 1.1: Comparison of semiconductor properties of ZnO with those of Si and GaN [8, 13, 14, 15].

Semiconductor	**Unit**	**Silicon**	**GaN**	**ZnO**
electron mobility	cm^2/Vs	2000	1000	200
band gap (300 K)	eV	1.1 (indirect)	3.39 (direct)	3.35 (direct)
crystal structure		diamond	wurtzite	wurtzite
lattice constants	nm	a=0.543	a=0.3189	a=0.3250
			c=0.5185	c=0.5205
exciton binding energy	meV	10	25	60
breakdown field strength	V/cm	3.0×10^5	3.3×10^6	5.0×10^6
saturation electron drift velocity	cm/s	1.1×10^7	3.0×10^7	3.2×10^7

concentrations as high as 10^{21} cm^{-3} are achievable [11]. However, adequate and stable p-type doping remains challenging. The reason for this doping asymmetry is complicated and is still the subject of debate. Self-compensation due to intrinsic n-type defects, solubility limitations and activation energy limitations are among the many factors that have limited the availability of p-type material to date [3].

1.3 Thesis outline

This thesis describes an investigation of the suitability of the filtered cathodic vacuum arc technique (FCVA) to deliver device grade ZnO thin films. A range of polycrystalline FCVA ZnO films were grown and their structural, optical and electrical properties were characterized to determine optimal growth and post-treatment conditions. Active semiconductor devices utilizing Schottky junctions were fabricated on these optimized films and then analysed in detail. Accordingly, the thesis is structured following this bottom-up approach. Relevant literature, experimental methods and background theory are reviewed and presented where necessary in the relevant individual chapters:

Chapter 2 contains a brief literature review of ZnO film growth technologies. These methods are evaluated in terms of the characteristic figures of merit of film quality as applied to electronic devices and also in terms of industrial scalability. The advantages and disadvantages of the FCVA growth technique are compared to other technologies.

Chapter 3 describes the morphological and structural properties of films grown by the FCVA technique. After introducing the experimental setup used, the effect of substrate type, growth temperature and post-growth annealing on crystal structure and surface morphology is investigated.

Chapter 4 is devoted to the analysis of the electronic and optical properties of FCVA ZnO films. Here again, the physical principles of the analytical techniques used, such as photoluminescence spectroscopy (PL) and Hall-effect measurements, are explained first. The relationship between film properties and growth/post-treatment conditions is established in this chapter. It concludes with the identification of the major extrinsic and intrinsic film defects and their effect on film quality.

Chapter 5 reviews the current status of ZnO based field effect devices with a focus on thin film transistors. Subsequently, a detailed theoretical treatment of Schottky contact formation and the operation of metal-semiconductor field-effect transistors (MESFETs) is presented. Based on the current-voltage measurements, the important performance metrics of these devices are derived and their electrical characteristics are presented accordingly. The electrical characteristics of the MESFETs are correlated with the results obtained in chapter 3 and 4. The limiting factors on device performance resulting from film quality and contact types are then explored.

Chapter 6 is dedicated to the reliability of Schottky diodes and MESFET devices. The influences of continuous bias stress, temperature and light illumination stress on MESFET devices are also reported in this chapter. The principle degradation mechanisms occurring in ZnO based MESFETs under bias stress are identified.

Chapter 7 concludes with a review of the main findings of this work and an outlook for recommended future work to further explore the potential of the FCVA ZnO deposition and its applications.

Chapter 2

The Filtered Cathodic Vacuum Arc in context

Zinc oxide films have been grown by many deposition methods and on a variety of substrate types [6]. These techniques can be divided into two different categories; either chemical deposition or physical deposition. As the name implies, chemical deposition methods such as metalorganic chemical vapor deposition (MOCVD) and atomic layer deposition (ALD) involve growth in a reaction chamber using chemical precursors. Physical deposition on the other hand involves physical processes, such as high-temperature vacuum evaporation as in molecular beam epitaxy (MBE), or plasma sputter bombardment as in sputter deposition methods. The filtered cathodic vacuum arc (FCVA) technique belongs to the latter class. Though cathodic arcs were first demonstrated several decades ago [12], the method has only been recently applied for the deposition of ZnO films. This chapter presents a review of ZnO thin film deposition techniques that are commonly used to deposit device grade films. The chapter concludes with a discussion of the main features of FCVA and a description of the system

used in this thesis.

2.1 A Synopsis of ZnO Growth Techniques

2.1.1 Physical processes

The main physical processes used to form thin crystalline ZnO films are sputtering techniques and pulsed laser deposition. RF and DC sputtering, as described in more detail in chapter 5, utilize plasma bombardment of a target to generate particles which are deposited onto a growth substrate. Sputtering techniques have the advantage of a high deposition rate and a low substrate temperature (200 °C - 300 °C). Reports on sputtered ZnO date back to the early 1980s. In a highly cited paper, *T. Minami et al.* [16] reported on highly conductive RF sputtered ZnO as an alternative for expensive indium tin oxide (ITO) films in display and photovoltaic devices. The undoped and Al-doped ZnO films, grown on glass, were polycrystalline with weak c-axis orientation. Mobilities ranging from 7.2 - 14 cm^2/Vs and resistivities as low as 2×10^{-4} Ω.cm were achieved for Al doped ZnO (AZO). Interestingly, AZO showed a much higher thermal stability than unintentionally doped ZnO which was explained by the chemisorption of oxygen at that time. These properties together with a reported optical transparency of 85%, in the visible range, triggered significant subsequent research interest. Initially, RF sputtering of ZnO was aimed at growing transparent conductive oxides (TCO) or films for acoustoelectric and acoustooptic devices, such as surface acoustic wave (SAW) filters and sensors [17, 18] as ZnO thin films with a c-axis orientation exhibit strong piezoelectric and piezooptic effects. Sputtering processes are cost effective, industrially scalable and capable of covering large substrates. Accordingly, some of the first ZnO thin film transistors (TFTs) were deposited by RF sputtering [19, 20]. However, due to the mobility limitations of the resulting polycrystalline ZnO films, research on sputtered ZnO based TFTs slowed in favour of transparent amorphous oxides such as gallium-indium-zinc-oxide (GIZO) and zinc-tin-oxide (ZTO).

In pulsed laser deposition (PLD), a high power pulsed laser beam is used to ablate the target material. The vaporized targeted material forms a plasma plume which

subsequently condensates as a thin film on a growth substrate. Since the laser source is located outside the growth chamber, the use of ultrahigh vacuum (UHV) and reactive ambient gases is possible. Overall, this technique is versatile and allows a great deal of flexibility in controlling growth conditions. One of its major advantages is the (almost) stoichiometric transfer of multi-element compound targets to the deposited films. Hence, PLD is a widely used technique to grow ZnO films [21, 22]. Multistep epitaxial ZnO films with Hall mobilities around 150 cm^2/V on c-plane sapphire as well as high quality heterostructure ZnO/ZnMgO interfaces, confining a two dimensional electron gas (2DEG) with an electron mobility of 1000 cm^2/V, have been demonstrated [23, 24]. Using this technique, high performance ZnO TFTs operating at microwave frequencies have been reported [25]. Most importantly in the context of this thesis, the first high-quality n-channel ZnO MESFETs, which have the potential to drive flat panel displays were grown via PLD [26]. However, despite the advantages of PLD as a prototyping tool in research, it suffers from a number of drawbacks [22]. Upscaling to larger substrate areas is limited to a diameter of about 5 inches due to the highly directional nature of the plasma plume. Moreover, droplets ($\sim$1 μm in size) are often found on PLD deposited ZnO films. Techniques used to reduce droplet occurrence, such as blocking the direct path between the target and sample using a small shadow mask (eclipse PLD) [213], come at the cost of a significant reduction in growth rate and hence drastically reduce throughput. In addition, reproducibility requires tedious fine tuning procedures in order to eliminate effects such as target ageing and changes in laser intensity due to window contamination. All these factors limit the scalability of PLD.

A less frequently used physical technique to grow ZnO is molecular beam epitaxy (MBE) [27]. In this process, the solid source elements are usually heated in effusion cells such that the evaporated beams of atoms or molecules are condensed on a heated substrate in an ultra-high vacuum environment. The technique has the capability of growing device-quality layers of semiconductors with atomic resolution of the growth thickness and abrupt heterostructure interfaces. Hence, in the case of ZnO, MBE was

mainly used in research to attempt growing epitaxial films for high value optoelectronic and heterostructure field effect devices. Originally, the first reported MBE ZnO [28] was grown to serve as a buffer layer to achieve epitaxial GaN with low dislocation densities. In this seminal paper, an electron mobility of 34 cm^2/Vs was achieved in a ZnO film grown on c-plane sapphire substrate at a growth temperature over 400 °C and at a growth rate of 1.16 μm/h. The much higher electron mobility of 260 cm^2/Vs reported in the same paper can not be considered for critical comparison here, as it involved a ZnO film grown on a conducting SiC substrate. *Y. Chen et al.* [29, 30] reported on the structural and optical properties, including room temperature excitonic stimulated emission, of MBE ZnO films grown on c-plane sapphire. Thin films with very sharp XRD rocking curve (0002) peaks were demonstrated. However, 2D growth was shown to be strongly dependent on film thickness and could not be maintained in films thicker than 15 nm at growth temperatures of 450 °C - 700 °C. The electrical properties of the films were not reported. Later, *P. Fons et al.* [47] reported epitaxial ZnO films on *a*-plane sapphire with a Hall mobility of 120 cm^2/Vs, without using any buffer layer. To overcome the effect of lattice mismatch on *c*-plane sapphire, low temperature ZnO or MgO buffer layers were often used and Hall mobilities as high as 169 cm^2/Vs were achieved using plasma assisted MBE [31, 48]. High quality ZnO/ZnMgO interfaces confining a 2DEG and resulting in high frequency (2.45 GHz) heterostructure field effect transistors (HFET) have been successfully grown by MBE [32]. Though industrially applicable, ultra high vacuum MBE systems are relatively costly. Furthermore, achieving film uniformity at large areas is limited by the width of the evaporated particle beams and system configuration [33]. Due to its limited scalability, MBE is traditionally restricted to growing high quality films for optoelectronic and high frequency devices.

2.1.2 Chemical processes

The most common chemical techniques used to grow thin film ZnO involve solution based processing. These techniques do not require a high vacuum environment and

thus provide a simple and low-cost way to grow ZnO films [34]. To date, in order to achieve a moderate channel mobility of about 5 cm^2/Vs in ZnO TFTs, most solution processed thin films have required high temperature annealing (300 °C - 500 °C) of either the ZnO channel layer [35] or the gate dielectric layer [36]. Very recently, an impressive high Hall mobility of 169 cm^2/Vs was reported by *N. Jayah et al.* [49] in ZnO films grown at 70 °C using hydrothermal deposition. However, the growth was carried out homoepitaxially on a thick CVD-grown ZnO seed layer deposited on *a*-plane sapphire substrate.

In recent years atomic layer deposition (ALD), a gas phase chemical process, has attracted considerable attention. ALD offers many advantages including large area capability and low temperature growth with good control over the composition and homogeneity of the resulting film [37]. This technique is attractive for applications involving low cost and flexible substrates and the integration of ZnO thin film devices with mainstream complementary metal-oxide-semiconductor (CMOS) technology where energetic deposition of ZnO could damage existing devices/epilayers. Another critical advantage of ALD is its ability to deposit all the metal, dielectric and semiconductor materials required for a complete device [38]. The capability of ALD has been demonstrated in many prototyped high mobility TFTs and circuits on flexible substrates [39] and in AM-OLED displays [40]. However, it involves layer-by-layer growth, and consequently it is an extremely slow process compared to sputtering methods with typical growth rates of 10-20 nm/min [41].

Comparing all these ZnO growth techniques is not straight forward, since film quality depends on many factors such as substrate type, film thickness and growth conditions. For electronic devices, carrier mobility is normally crucial. Since the vast majority of the reported films in the literature are polycrystalline in nature, carrier mobility is only weakly dependent on carrier concentration and rather strongly dependent on crystal structure, in particular grain size. Fig. 2.1 depicts representative Hall mobility measurements achieved for ZnO films using different growth methods at different growth and post-growth treatment temperatures. Mobility values over 100

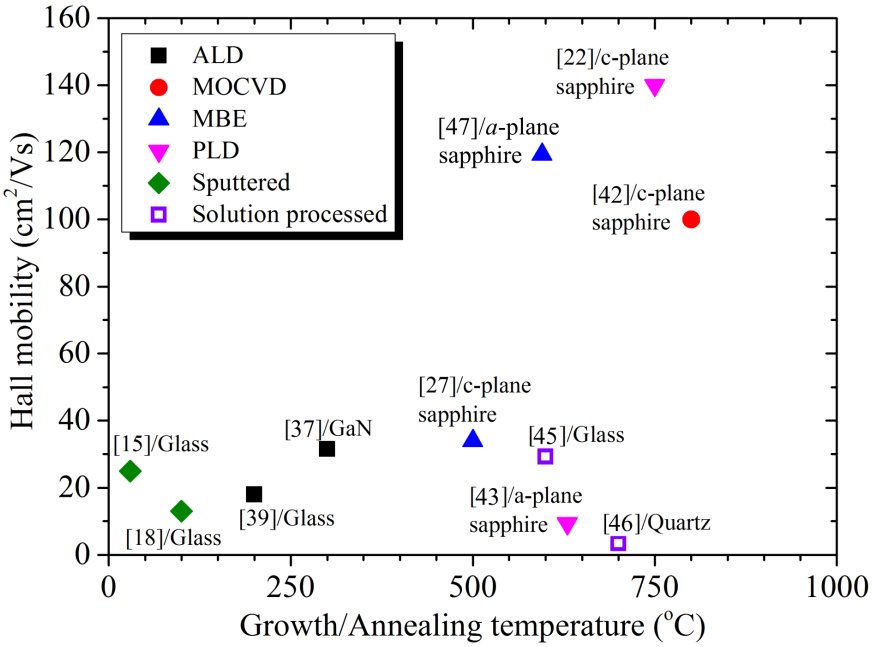

Figure 2.1: Representative values of electron Hall mobilities of ZnO films grown and annealed at different temperatures with different deposition techniques (annotations in figure refer to reference number and substrate type).

cm^2/Vs have only been achieved in thick films (resulting in higher crystallinity), at high temperatures and have often required low temperature ZnO buffer layers. Usually, the best reported ZnO thin films exhibit typical electron carrier mobilities close to 30 cm^2/Vs.

2.2 The Filtered Cathodic Vacuum Arc

2.2.1 A general overview

Like PLD and magnetron sputtering, the cathodic arc (CA) deposition technique falls into the category of physical plasma deposition. However, ablation from the cathode (target) is achieved using an electric discharge. The vaporized material then condenses on a substrate, forming a thin film. The system is fairly simple to implement. The first patent describing a cathodic arc plating system was filed by *Thomas Edison* under the title "Art of Plating One Material with Another" as early as 1894 [12]. However, broad commercialization of vacuum cathodic arc systems only took place in the 1970s-

80s in the former Soviet Union, where up to 4000 systems were industrially deployed to deposit wear resistant coatings on tools and machine components. The interest in these systems was driven not only by their industrial scalability but also by the attractive mechanical properties of the deposited films, which are believed to be a consequence of the highly energetic deposition and the complete ionization of the deposited species [50]. In contrast to sputtering techniques, ion induced damage caused by high energy (around 100 eV) negative oxygen ions is inherently avoided in cathodic arc deposition [55].

Ions of cathodic arc plasmas are produced at cathode spots, which are locations of extremely high current density ($\sim 10^{12}$ A/cm^2), plasma density ($\sim 10^{26}$ cm^{-3}) and pressure gradient ($\sim 10^{12}$ Pa/m) [51]. As a result, a significant fraction of the particles arrive at the substrate surface with a kinetic energy greater than the bulk displacement energy of the substrate, hence, penetrating the substrate and displacing near-surface atoms. According to *A. Anders* [51], the general expression for the total energy of an ion arriving at the substrate surface is

$$E(Q) = E_{kin,0} + QeV_{sheath} + E_{ic} + E_{exc} + E_C + \sum_{Q'=0}^{Q-1} E_{Q'}, \tag{2.1}$$

where the first three terms are the kinetic ion energy in the plasma, the kinetic energy gained in the space-charge sheath between the plasma and substrate surface, and the kinetic energy gained by image charge acceleration, respectively. The remaining terms account for the different forms of potential energy stored in the ion. E_{exc} is the excitation energy available in ions having electrons in an excited state, E_C is the cohesive energy, and the last term is the cumulative ionization energy. The ionization energy E_Q is defined as the energy needed to remove a bound electron from an ion of charge state Q, forming an ion of charge state $Q + 1$. The ionization energy can be very significant, especially for multiply charged ions, since the ionization energies add up for each ionization level. While the kinetic energy of a Zn ion in a cathodic arc plasma is estimated to be 36 eV, the ionization energy for triply ionized ion can be as high

as 67 eV [51]. Therefore, both kinetic and potential energy are expected to have a significant effect on the film growth and the resulting film properties. It is believed that the total energy released upon the impact of the ions on the substrate surface causes atomic scale heating that can be significant in improving the surface diffusivity of the deposited species, and consequently alleviating the need for high substrate growth temperatures. Moreover, since the cathodic arc plasma plume is highly ionized, the energy of the depositing flux can be controlled using an applied substrate bias. The high level of ionization also enables effective filtering of macro-particles in the plasma plume by a magnetic filter [52]. Systems involving a magnetic filter are classified as a filtered cathodic vacuum arc (FCVA).

Recently, the FCVA technique has attracted considerable attention as a method for depositing metal oxides for many applications such as optical filters, transparent conductive electrodes, and even corrosion-resistant electrodes for alkaline-electrolyte batteries [56, 57]. The first ZnO deposition using an FCVA system was reported by *X.L. Xu et al.* in 2000 [53]. Due to the industrial scalability of this technique, the research was mainly focused on ZnO for transparent conductive coatings. *R. Mendelsberg et al.* [7] used a compact FCVA system with a short plasma path to deposit AZO at a very high rate (250 nm/min). The reported AZO films had a resistivity as low as 3.9 $\times$ 10^{-4} Ω.cm and an electron mobility as high as 60 cm^2/Vs, achieved at a reasonably low temperature of 200 °C. The high quality of the film was attributed to the high kinetic and potential energy of the plasma flux as a result of the short plasma path. Up to 2011, only one publication reported the fabrication of active ZnO based devices using FCVA. The devices involved n-type Al:ZnO deposition on a p-SiC(4H) substrate to form heterojunction light emitting diodes [54]. Otherwise, the application of FCVA to the fabrication of electronic ZnO devices is largely unexplored.

2.2.2 FCVA: System description

The FCVA system used to deposit the ZnO films in this thesis is shown in Fig. 2.2(a) and illustrated schematically in Fig. 2.2(b). A cylindrical 99.99% purity zinc cathode

Table 2.1: Typical ZnO growth conditions of the FCVA system used in this work.

Sub. temp.	**Arc current**	**Filter current**	**O_2 flow**	**Ar flow**	**Proc. pressure**
100, 200, 300 °C	45 A	10 A	40 ml/min	2-5 ml/min	1.3 mTorr

is located in a water-cooled stainless steel block at one end of a double bend magnetic filter. An arc current between the cathode (target) and a neighbouring anode is established using a mechanical conductive striker. Once the discharge is initiated, the ablated cathode material forms a plasma plume composed of mainly ionized Zn atoms. An anode coil current (typically 1 A) produces a magnetic field that helps to confine the ablated plasma into the opening of the double bend filter. While macro-particles are deposited on the wall of the double-bend filter, the ionized zinc plasma is steered by the magnetic field of the filtering coil towards the growth chamber, as depicted in Fig. 2.2(b) and 2.2(c). Oxygen fed into the chamber provides the reactive environment for the growth of ZnO on a given substrate. A sample heater is used to maintain the desired substrate temperature during growth. The substrate temperature was monitored using a thermocouple fixed to the substrate holder. Growth can be controlled by manipulating a variety of conditions including arc current, filter coil current, chamber vacuum pressure, substrate temperature and substrate bias. However, technical and stoichiometric considerations impose some constraints on these parameters.

Table 2.1 lists the standard growth conditions used in this work. In general, the growth parameters were selected based on the previous work and expertise of the research group running the FCVA system at RMIT university in Melbourne, Australia. Prior to this work, a series of trial depositions with different O_2 flow rates were conducted and the resulting ZnO films were analyzed using X-ray photoelectron spectroscopy (XPS), Hall-effect and optical measurements. A fixed oxygen flow rate of 40 ml/min was found to be just sufficient to produce quasi-stoichiometric ZnO films over the desired growth temperatures. Lower flow rates resulted in degenerate non-stoichiometric ZnO films. In contrast, excessive O_2 flow rates/pressures can lead to oxidization of the Zn cathode (known as cathode poisoning). The flow rate of Ar into

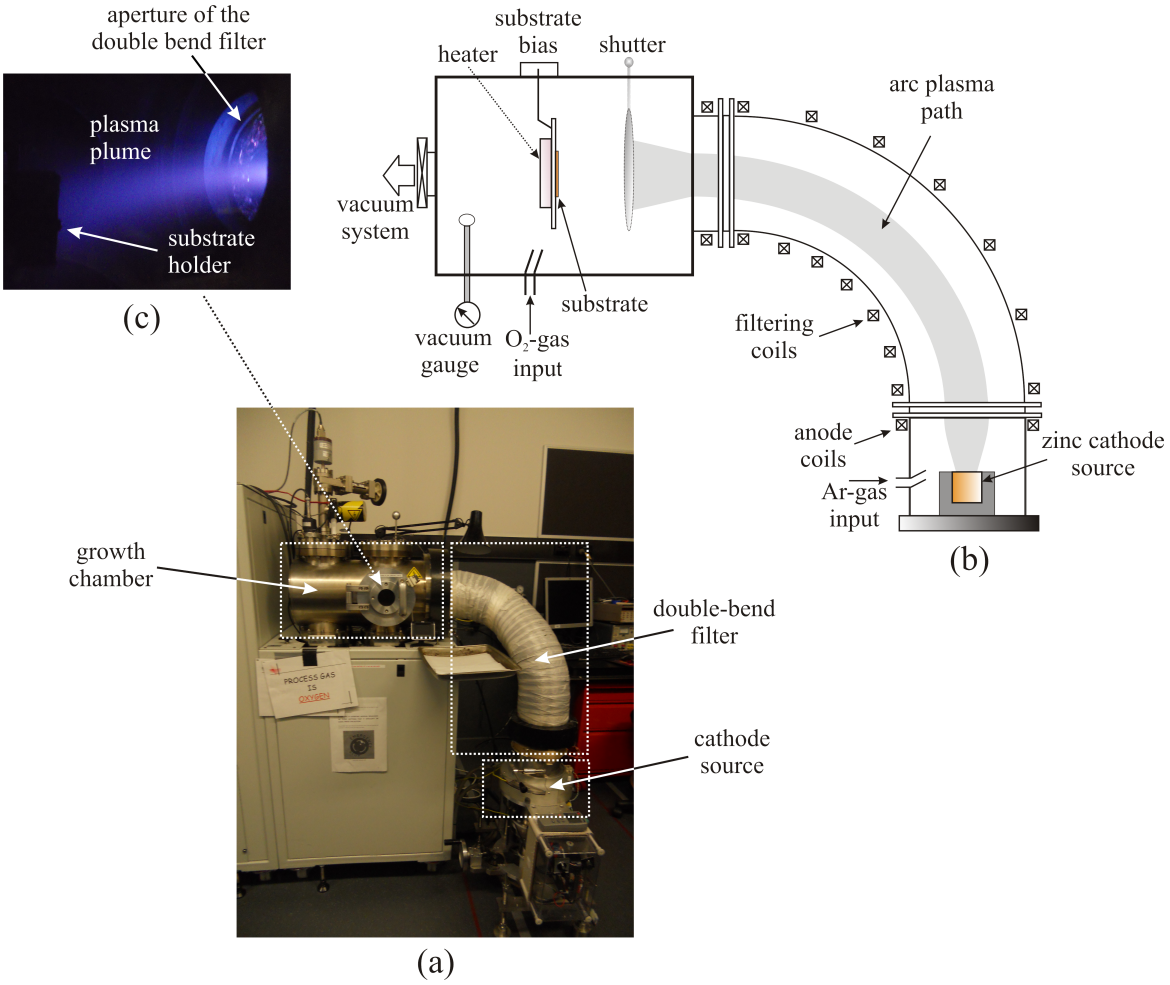

Figure 2.2: (a) A picture of the FCVA system used to grow films in this thesis, (b) a schematic depicting the components of the systems, and (c) a picture of the plasma plume inside the growth chamber during ZnO deposition.

the cathode chamber was optimized to maintain a stable plasma. However, before every deposition, the chamber was pumped down to a typical base pressure of 2×10^{-6} Torr. On the other hand, the Zn plasma flow rate is highly dependent on the arc current. A higher arc current increases the Zn plasma flow rate, and consequently leads to Zn rich films. An arc current of 45 A, which was also found to produce quasi stoichiometric films for the given O_2 flow rate, was used for all depositions. The substrate potential was always allowed to float. Although the number of process variables is large, the only growth condition that was changed in the experiments here was the substrate temperature, since this has been previously identified as one of the most critical parameters [55]. Depending on the substrate temperature, the film growth rate varied from 1–5

nm/min. Substrate temperatures higher than 300 °C were found to cause very slow growth, due to the partial re-evaporation of Zn [55].

2.3 Summary

ZnO has been deposited by many chemical and physical deposition methods. In general, device quality ZnO films have mostly been achieved at high growth temperatures and/or using sophisticated growth techniques. On the other hand, energetic deposition using cathodic arcs has long been recognized as a powerful method for the growth of dense films with tailored mechanical, tribological and optical properties. The FCVA technique has been developed extensively in the last decade, yielding practical deposition systems with efficient magnetic filters. Recent advancements have shown that the synthesis of high quality metal oxide thin films for optoelectronic applications, such as optical filters, and highly conductive AZO is technologically viable. The unique properties of films deposited by FCVA is attributed to the nature of the cathodic arc ablation process which produces an almost exclusively ionized plasma plume. The high kinetic energy and the high level of ionization of the ejected ions constitute a high total energy which leads to atomic scale heating, thus promoting adhesion while also enhancing the diffusivity of the deposited species. Moreover, the high level of ionization allows for efficient magnetic filtering of macro-particles from the plasma plume. However, many aspects of ZnO growth by FCVA are yet to be fully investigated, particularly with respect to its potential for electronic applications. In the next chapter, the effect of substrate type and growth temperature on structural and morphological properties of ZnO films deposited by FCVA is discussed.

Chapter 3

The different faces of FCVA ZnO films

The properties of semiconductor thin films are largely dictated by their microstructure, morphology and surface properties. The existence of lattice defects significantly impacts the optical and electronic properties of ZnO films and hence the performance of the fabricated devices. Moreover, the surface morphology is very important for the interface quality of metal-semiconductor junctions which form the base for active devices such as Schottky diodes and MESFETs. The preferred crystal orientation of ZnO growth is known to be dependent on the structure of the underlying substrates [29, 72]. Growth in different crystal orientations results in different morphologies which could be more or less desirable depending on the application. Another important aspect is the existing anisotropic polarization in ZnO. Non-polar growth is often desired for optoelectronic devices where polarization induced electric fields can degrade the quantum efficiency of optoelectronic devices [63]. On the other hand, for the implementation of ZnO based SAW devices, it has been shown that optimum surface wave propagation occurs along the [0001] direction, with the c-axis parallel to the surface [64]. Hence, the ability of a deposition technique to promote growth in different crystal directions is highly desirable. There are a considerable number of reports on the effect of substrate type on ZnO grown by other growth techniques [6, 22, 65, 21, 66]. However, no com-

prehensive study has been performed on the effect of underlying substrate structure on the growth of cathodic arc ZnO films. The highly energetic deposition of Zn ions on the substrate is expected to lead to displacement of bulk atoms and sub-surface implantation where film growth potentially starting from under the substrate surface rather than on the surface itself [45]. These physical phenomena suggest that ZnO films grown by a cathodic arc may involve a unique growth behaviour. In this chapter, the influence of substrate type and substrate temperature on the structural and morphological properties of ZnO films are investigated. Since it is often necessary to expose the deposited films to thermal treatment after deposition, the chapter concludes with the effect of thermal annealing on the properties of ZnO thin films deposited on different sapphire substrates.

3.1 Microstructural characterization techniques

Three experimental tools were used for the microstructural investigation of ZnO films; Scanning electron microscopy (SEM), atomic force microscopy (AFM) and X-ray diffraction (XRD). SEM and AFM are microscopic techniques which deliver high resolution images of the scanned surfaces. Important properties such as grain size and shape can be determined with these tools. XRD is a diffractometric technique and is the standard method for identifying the crystal structure and determining the lattice parameters of semiconductor films.

3.1.1 Scanning Electron Microscopy (SEM)

SEM uses an electron beam to construct a magnified image of the sample surface. The image is produced by scanning the sample with a focused electron beam and detecting the low energy secondary electrons emitted from the surface [58]. The secondary electron intensity is measured as a function of the position of the scanning primary electron beam which results in an image of the sample surface as shown schematically in Fig. 3.1. The short wavelength of electrons, compared to photons, enables a much larger magnification and spatial resolution. Moreover, the very high depth of field pro-

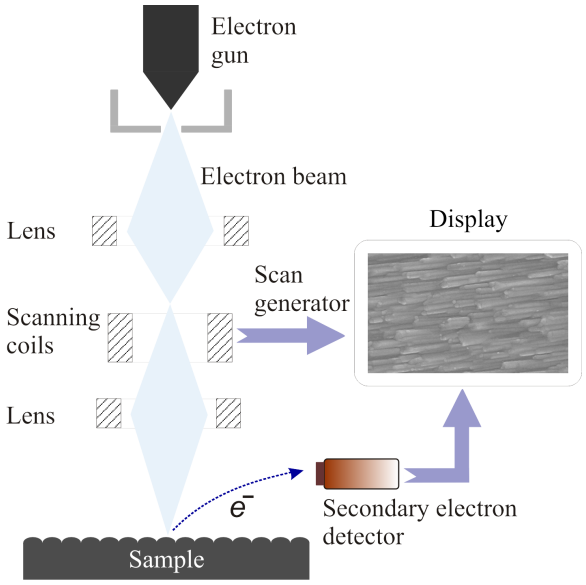

Figure 3.1: A schematic illustrating the working principle of the scanning electron microscope. The sample surface is imaged by measuring the emitted secondary electron intensity as a function of the position.

vides for sharp images that closely approximate the physical features of the surface. In this work, a Raith 150 instrument was used to generate SEM images of the FCVA ZnO films. All images were taken using an electron accelerating voltage of 10 kV. According to De Broglies's wave-particle duality equation ($h/\lambda_e = mv$), such an accelerating voltage produces an electron wavelength of $\lambda_e = 0.012$ nm which corresponds to a theoretical resolution limit of $\lambda_e/2 = 0.006$ nm. However, noise issues can limit the maximum achievable magnification. In the context of this dissertation, the SEM images were taken routinely as a complement to AFM imaging and in conjunction with data obtained by XRD.

3.1.2 Atomic Force Microscopy (AFM)

Atomic force microscopy (AFM) operates by measuring the repulsive or attractive force between a scanning probe and the sample surface [58, 59]. Practically, the topography of any surface, whether it is an insulator, conductor or organic can be imaged. AFM instruments can be operated in several modes. The most common is contact mode and tapping mode. In contact mode, a cantilever with tip is placed in intimate contact

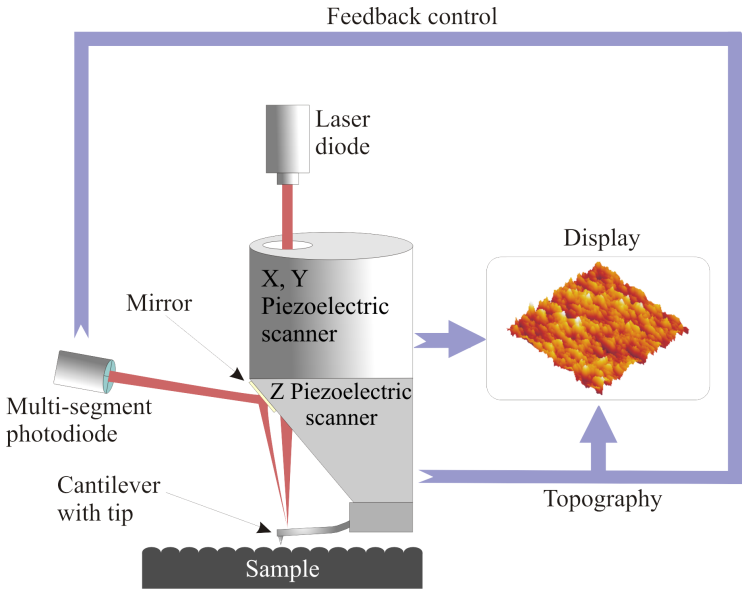

Figure 3.2: A schematic illustrating the working principle of the atomic force microscope. The piezoelectric tube scanner ensures precision nanoscale x and y raster-scan, and z position. The deflection of the cantilever is measured using a laser spot reflected from the top surface of the cantilever onto an array of photodiodes.

with the sample surface. As it is dragged across the surface, the contours of the surface are measured. However, the measurement of a static signal is prone to noise and drift. Therefore, during this work, tapping mode has been commonly used. In tapping mode, a stiff cantilever with a sharp tip is brought within close proximity of the sample surface, as shown schematically in Fig. 3.2. During the raster scan, the force between the tip and the sample causes changes in the frequency and amplitude of the cantilever oscillation. The amplitude and frequency changes, with respect to the reference amplitude and frequency, are used as feedback signals to obtain the topography of the sample surface. To avoid damaging the tip due to collisions with the surface, a feedback mechanism is employed to maintain a constant tip-sample distance. Typically, the deflection of the cantilever is measured using a laser spot reflected from the top surface of the cantilever into a photodiode array.

For this thesis, the AFM (Nanoscope III from Digital Instruments, USA) has been primarily used to measure the surface roughness of the grown films, estimate the grain size of the polycrystalline films, and in general to analyse the effect of substrate type and growth temperature on surface morphology. The resolution of the AFM depends

greatly on the tip shape. Monolithic silicon probes with cantilever resonant frequencies between 200-400 kHz and a tip radius of less than 10 nm were typically used. These probes were found to be adequate to image the polycrystalline films deposited in this work.

3.1.3 X-ray Diffractometry (XRD)

X-ray diffractometry is the most widely used method for determining the crystal structure of solids. In XRD, an incident beam of monochromatic X-rays is used to examine the target material. According to Bragg's Law, constructive interference occurs when the path difference between the incident and diffracted beams is an integer multiple n of the X-ray source wavelength λ

$$2d \cdot sin\,\theta = n \cdot \lambda, \tag{3.1}$$

as illustrated in Fig. 3.3. Based on this law, a spectrum of diffraction intensity versus the angle between the incident and diffraction beams can be obtained by continuously changing the angle between the incident X-ray beam and the sample. However, for the characterization of thin films, the incident X-ray beam angle is kept constant at a shallow level while a detector moves along an arc to capture the diffracted rays [59]. The resulting intensity peaks occur at angles corresponding to the constructive interference of the beams diffracted by the first few atomic planes of the sample. The locations (angles) of these peaks reveal the underlying crystal structure. The crystal quality, on the other hand, can be inferred from the full-width half-maximum (FWHM) of the peaks, where the peak width is inversely related to the crystal grain size. For polycrystalline materials, the average grain size D can be estimated from the FWHMs of the diffraction peaks using Scherrer's formula

$$D = \frac{\beta \cdot \lambda}{FWHM \cdot cos\theta} \tag{3.2}$$

where λ is the wavelength of the X-ray, θ is Bragg's angle in radians and β is a

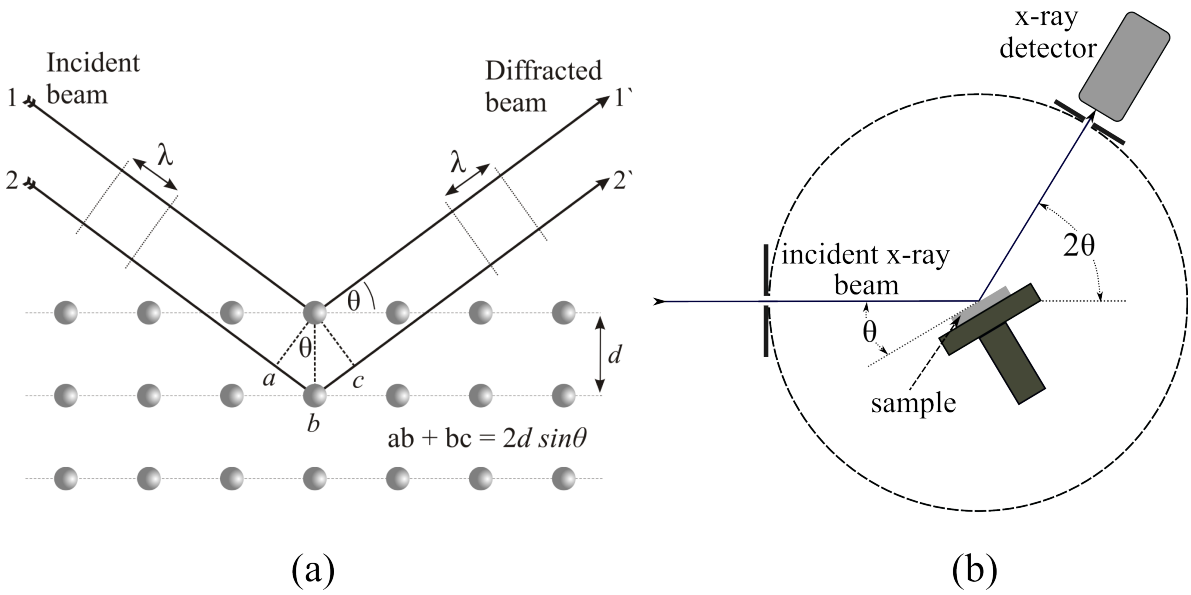

Figure 3.3: (a) Bragg's diffraction law. Two beams of identical wavelength and phase are scattered off two different atomic planes. The lower beam traverses an extra length of $2dsin\theta$. Constructive interference occurs when this length is equal to an integer multiple of the wavelength. (b) Schematic setup of the XRD measurement system.

correction factor close to unity [60]. Unless otherwise stated in this work, a Bruker D4 Endeavor diffractometer was used. This instrument was fitted with a Cu Kα radiation source providing X-rays of wavelength 0.1541 nm. The crystal orientation of the grown films were identified by matching their diffractograms with standard diffractograms published in the literature and in the powder diffraction files of ZnO.

3.2 Effect of substrate on FCVA ZnO film growth

3.2.1 Sapphire and ZnO lattice vectors and planes

Sapphire has traditionally been the substrate of choice for ZnO growth. This is mainly due to its reasonable cost, temperature stability, transparency, availability in large area wafers and its hexagonal structure which provides a reasonable match to the structure of ZnO. In addition to sapphire, corning glass and quartz were also used as low cost alternatives. The ZnO films in this thesis were grown on a-plane, c-plane, r-plane and m-plane sapphire as well as quartz substrates. Lattice points (space planes) of hexagonal crystals such as sapphire and ZnO are usually indexed with four indices, u

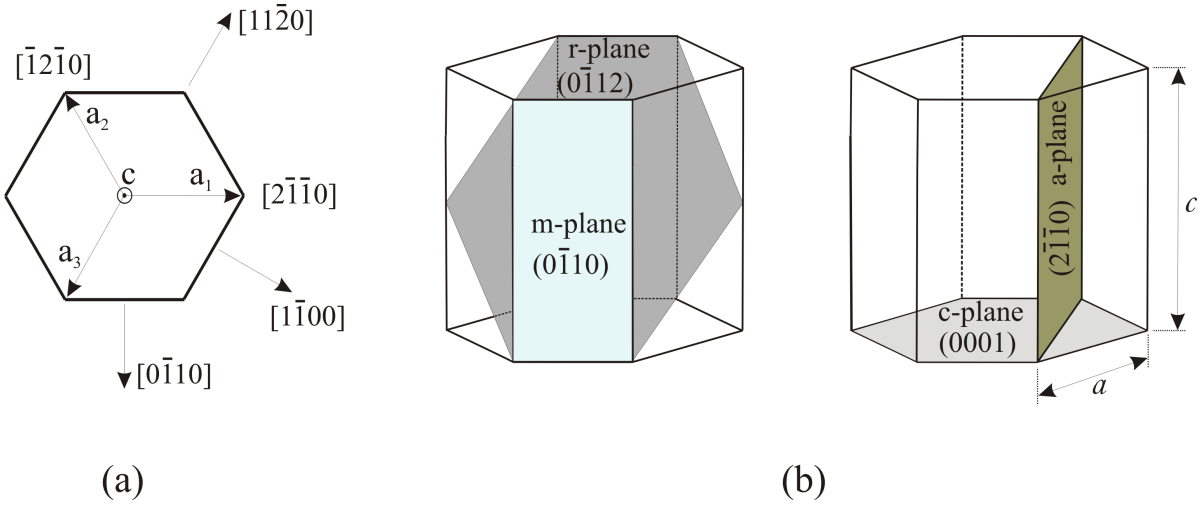

Figure 3.4: Fundamental lattice vectors (a) and indices (b) of typical planes in a hexagonal structure.

v s w (*h k i l*), using three basic vectors $\mathbf{a}_1$, $\mathbf{a}_2$, $\mathbf{a}_3$ in one plane and a fourth basic lattice vector **c** perpendicular to that plane. The third index is simply the sum of the first two indices $s = -u - v$ ($i = -h - k$). For a hexagonal structure, the lattice constants a and c can be given by

$$\frac{1}{d_{hkl}^2} = \frac{4}{3}\left(\frac{h^2 + hk + k^2}{a^2}\right) + \frac{l^2}{c^2}, \tag{3.3}$$

where h, k and l are the Miller indices and d_{hkl} is the inter-planar spacing of the planes which can be readily extracted from XRD 2-θ diffraction patterns [60]. The Miller indices of the different crystal directions and the four typical crystal planes used as growth substrates in this work are illustrated in Fig. 3.4. The corresponding lattice spacings are listed in Table 3.1. In this work, the out-of-plane lattice constants

Table 3.1: Common crystallographic planes in ZnO.

Plane designation	**Miller index**	**d-spacing**
a	(11$\bar{2}$0)	1.62475 Å
c	(0001)	2.60394 Å
m	(10$\bar{1}$0)	2.81512 Å
r	(1$\bar{1}$02)	1.91134 Å

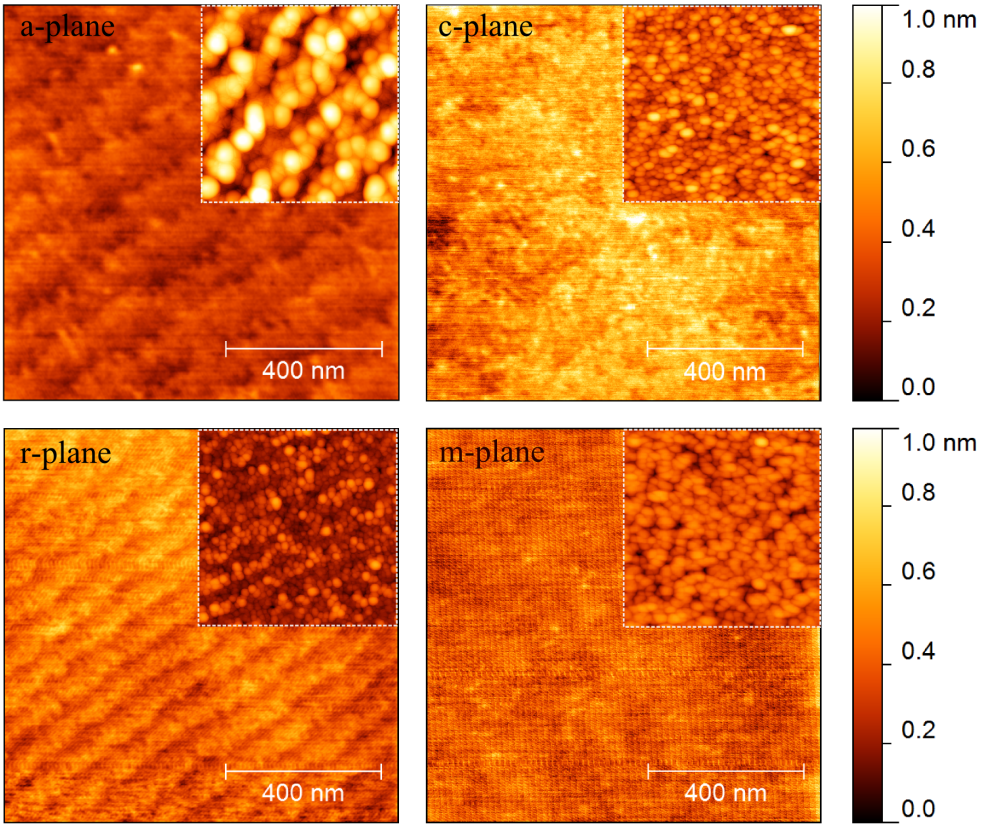

Figure 3.5: 1x1 μm^2 AFM images of a-plane, c-plane, r-plane and m-plane sapphire surfaces. The insets show sample AFM images of FCVA ZnO films deposited on the corresponding substrates [vertical scale of the inset is 20 nm].

(c for c-plane ZnO and a for r- and m-plane ZnO films) were always determined from the XRD-diffractogramms using Eq. 3.1. The in-plane lattice constants, however, were calculated from the experimentally determined out-of-plane lattice constant using Eq. 3.3 and a reference d-spacing value of 2.47642 $\AA$ corresponding to the $(10\bar{1}1)$ plane [61, 62].

In addition to the crystallographic orientation, the surface morphology of the substrate is very important in thin film growth. AFM images of as-received a-plane, c-plane, r-plane and m-plane sapphire substrates are shown in Fig. 3.5. For all substrates, the root mean square (RMS) roughness was in the range of 0.1 - 0.2 nm. The c-plane sapphire surface was the roughest, displaying coarse terracing. On the other hand, a-plane and r-plane sapphire surfaces show periodic terraces with mean widths of 100 nm and 80 nm, respectively. The m-plane surface appears homogeneously smooth with

no visible surface features. Surface images of 40 nm thick FCVA ZnO films deposited at 200 °C on each substrate are shown in the insets of Fig. 3.5. The films deposited on a-plane and r-plane sapphire exhibit periodic stripes containing polycrystalline grains that appear to match the substrate morphology. The step edges of substrates are thought to influence the diffusion of deposited species on the surface and consequently have considerable impact on the film growth and the resulting morphology [67, 65].

3.2.2 Growth of c-plane ZnO

X-ray diffractogramms and AFM images of FCVA ZnO films deposited on a-plane and c-plane sapphire at a substrate temperature of 300 °C are shown in Fig. 3.6. In general, all depositions resulted in dense, macro-particle free polycrystalline films, confirming the effective magnetic filtering of the plasma plume. The sharp peaks centred at 34.51° in Fig. 3.6(a) and at 34.65° in Fig. 3.6(c) confirm that FCVA ZnO films grow with a preferred c-axis orientation on a- and c-plane sapphire. Fig. 3.6(b) and (d) show that the films contain well rounded grains with mean grain sizes of 90 nm and 100 nm on a-plane and c-plane sapphire, respectively. However, the ZnO film on c-plane sapphire shows a different surface morphology with substantially rougher surface that resembles typical columnar grain growth [23].

A-plane sapphire, $(11\bar{2}0)$, has an in-plane c lattice parameter of 1.299 nm which is approximately 4 times the lattice parameter of ZnO ($a = 0.3250$ nm). As a result, ZnO usually grows with a preferred (0001)-orientation with a lattice mismatch as low as 0.08% on a-plane sapphire [68]. On the other hand, growing a c-axis oriented ZnO film on c-plane sapphire leads typically to a lattice mismatch of about 18%. The larger lattice mismatch results in a different surface morphology with larger grains, yet similar XRD diffractogramms. *Y. Chen et al.* suggested that a thin mismatched and defect-rich layer is created at the interface of a ZnO film on c-plane sapphire [29]. Such a layer would act as a defect absorbing buffer layer above which lattice-matched layers of higher quality are grown [29]. Using Bragg's law (Eq.3.1) the c and a lattice

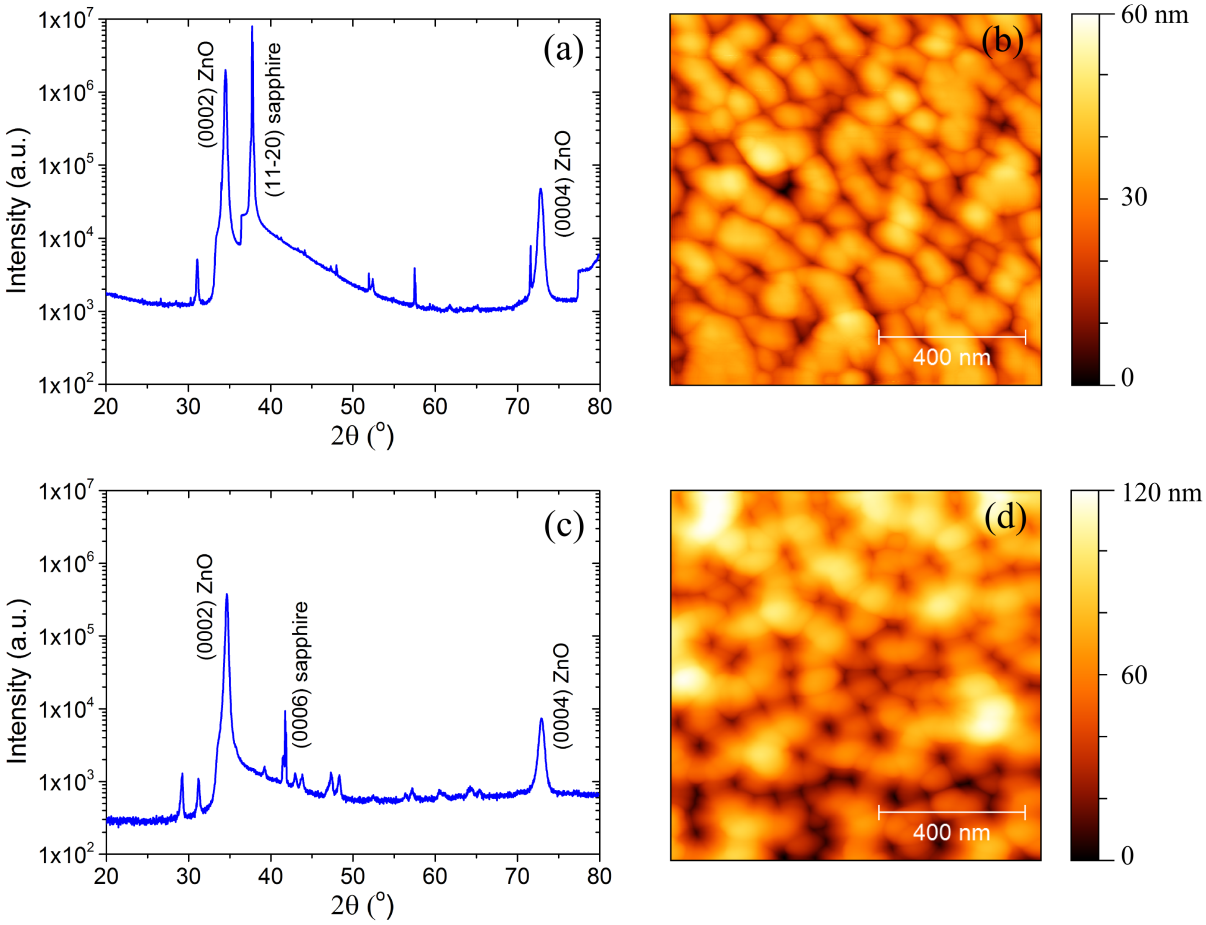

Figure 3.6: XRD diffractogramms and 1x1 μm^2 AFM images of 300 nm thick FCVA ZnO films deposited at a substrate temperature of 300 °C on (a-b) a-plane sapphire, (c-d) c-plane sapphire. Both films show a preferred c-axis orientation.

constants evaluated from the XRD diffractogramms are listed in Table 3.2. For both c-axis oriented films, the measured lattice constants are in good agreement with standard reference values [70].

3.2.3 Growth of nonpolar a-plane and m-plane ZnO

FCVA ZnO films grown on r-plane and m-plane sapphire substrates at a substrate temperature of 300 °C are shown in Fig. 3.7(a)-(d). The XRD from the film deposited on r-plane sapphire (Fig. 3.7(a)) has its dominant ZnO-related peak at $\sim$ 66.75°[using a 0.17905 nm X-ray source], indicating that the film is predominantly a-plane polycrystalline ZnO. However, a weaker reflection corresponding to (0002) ZnO was also

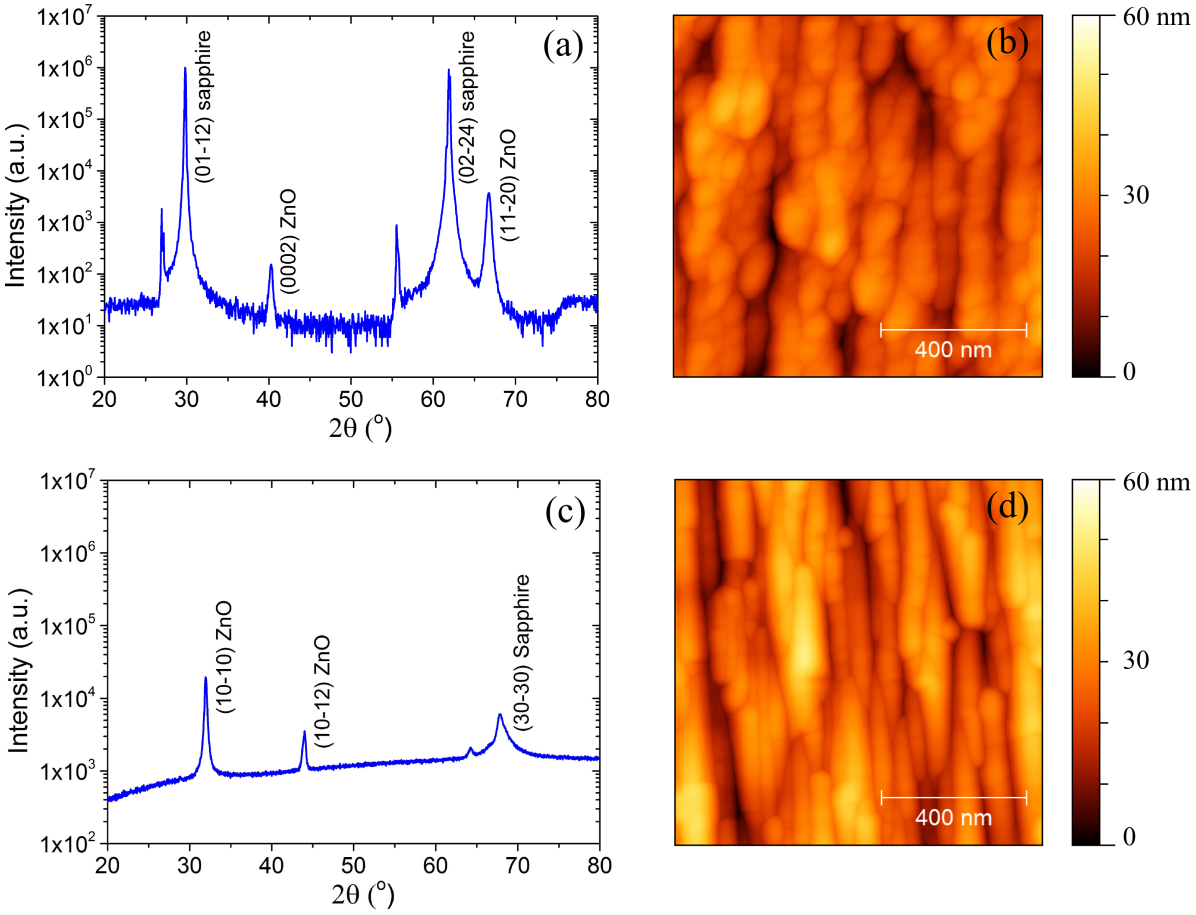

Figure 3.7: XRD diffractogramms and 1x1 μm^2 AFM images of a 300 nm thick FCVA ZnO film deposited at a substrate temperature of 300 °C on (a-b) r-plane sapphire, (c-d) m-plane sapphire. Depositions on r-plane and m-plane sapphire yielded predominantly non-polar a-plane and m-plane ZnO films, respectively.

detected. The ZnO film deposited on m-plane sapphire has its predominant ZnO-related peak centred at 31.96°(Fig. 3.7(c)), which is attributed to m-plane ZnO. The surface morphology of these a-plane and m-plane ZnO films, shown in Fig. 3.7(b) and (d), consists of well aligned 40-80 nm wide stripes. A similar surface morphology has frequently been observed in ZnO films grown on r-plane sapphire [66, 71, 72] and m-plane sapphire [72, 75, 76] using MBE, PLD and MOVPE. According to this literature, these stripes are aligned in the c-axis direction.

The exact epitaxial relationships between the deposited ZnO films and the underlying sapphire substrates cannot be solely determined by 2θ-ω XRD scans. However, in this work, the stripes observed on the a-plane and m-plane ZnO films were always aligned in one direction, along one of the sides of the r-plane and m-plane square

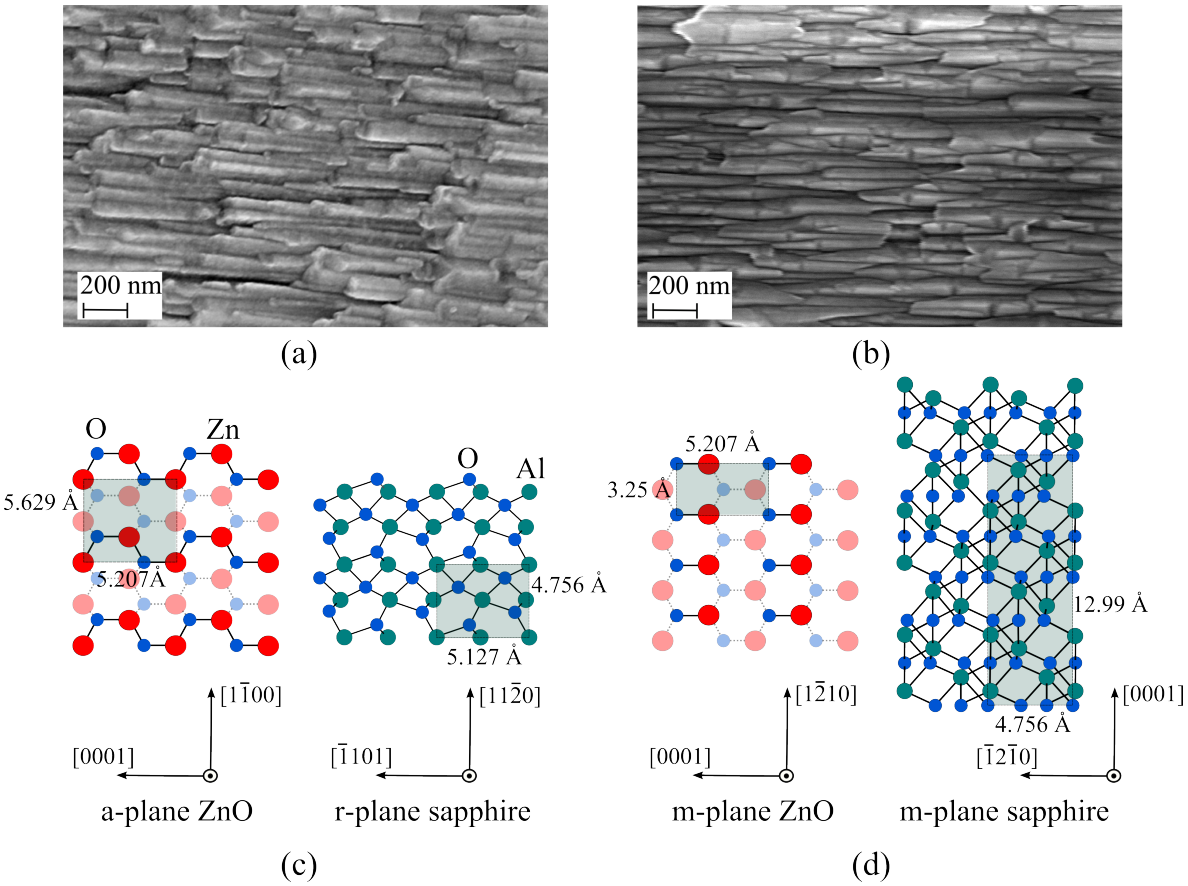

Figure 3.8: (a) and (b) SEM images of 300 nm a-plane and m-plane ZnO films deposited on r-plane and m-plane sapphire, respectively, at a substrate temperature of 300 °C. (c) and (d) Schematics of the corresponding ZnO and underlying sapphire surfaces and the epitaxial relationships usually reported in the literature [78].

sapphire substrates. This suggests that FCVA ZnO growth on r-plane and m-plane sapphire follows a specific epitaxial relationship, similar to ZnO films deposited by other growth techniques. The anisotropic morphology and stripe formation is usually attributed to a faster surface diffusion along [0001] direction and to the large anisotropy of the lattice mismatch [66]. Fig. 3.8(a) and (b) show SEM images of the deposited a-plane and m-plane ZnO films scanned along one of the substrate sides. Fig. 3.8(c) and (d) show the corresponding structures of the ZnO film and sapphire surfaces and their epitaxial relationships as determined by *J. Chauveau* et al. [78] and *S.K Han* et al. [66] using MBE grown films. The unit cells indicated in these figures illustrate the anisotropic lattice mismatch between both surfaces. While a small lattice mismatch of 1.55% exists between the [0001]ZnO and [$\bar{1}$101]Al_2O_3 direction in the a-plane ZnO film

Table 3.2: Results of XRD and morphology analysis of 300 nm FCVA films deposited on a-plane, c-plane, r-plane, and m-plane sapphire at a substrate temperature of 300 °C. The the c-lattice constants of the c-plane films and a-lattice constants of the r-plane and m-plane films are inferred directly from XRD diffractogramms using Eq. 3.1. The rest of the lattice constants was calculated using Eq. 3.3 and a nominal d-spacing value of 2.47642 $\AA$ for the $(10\bar{1}1)$ plane.

Parameter	**a-Sapphire**	**c-Sapphire**	**r-Sapphire**	**m-Sapphire**
cryst. orientation	c-plane	c-plane	a-plane	m-plane
rms roughness (nm)	11	19	8	10
FWHM (deg)	0.22	0.25	0.43	0.24
lattice constants (Å)	a = 3.2524	a=3.2559	a=3.2547	a=3.2312
	c = 5.1938	c = 5.1748	c=5.1810	c=5.2337
grain size (nm)	90	100	-	-

(Fig. 3.8(c)), the mismatch along the $[1\bar{1}00]$ZnO and $[11\bar{2}0]Al_2O_3$ direction is 18.3%. For the m-plane ZnO film in Fig. 3.8(d), a compressive lattice mismatch of 9.4% is expected to exist along the [0001]ZnO direction. Considering four unit cells of m-plane ZnO along the $[\bar{1}2\bar{1}0]$ZnO direction and one unit cell of sapphire along $[0001]Al_2O_3$, the lattice mismatch is 0.06%. Among the four FCVA ZnO films deposited simultaneously on a-plane, c-plane, r-plane and m-plane sapphire, the film deposited on r-plane sapphire produced the broadest XRD peak with a FWHM= 0.43°. Although, it was proposed in the literature that the smaller lattice mismatch along [0001]ZnO enhances the migration of Zn atoms, resulting in the elongated grains that form the observed stripes [66], it is important to note that the same anisotropic surface morphology has also been observed in ZnO films grown homoepitaxially on lattice matched substrates [73, 74]. This suggests that the striped surface morphology is mainly due to the faster surface diffusion along the c-axis direction. For other deposition methods, the striped surface morphology was only observed at much higher growth temperatures (> 500 °C) that provide sufficient surface diffusivity [66, 69, 75].

Table 3.2 lists the characteristics of the four ZnO films (shown in Fig. 3.6 and 3.7) that were deposited simultaneously on the four different substrate types. The lattice constants of the films deposited on a-plane, c-plane and r-plane sapphire are very close in value and are in very good agreement with values reported in the literature

[8]. However, the noticeably larger deviation of the m-plane ZnO lattice constants from nominal values indicates the presence of a high in-plane tensile (c-axis) and out-of-plane compressive strains in the film. This is inconsistent with the epitaxial relationship otherwise reported in the literature (shown in Fig. 3.8(d)). An in-plane tensile and an out-of-plane compressive strains would rather result when $[\bar{1}2\bar{1}0]$ZnO is aligned along $[\bar{1}2\bar{1}0]Al_2O_3$. In this case, a significantly higher lattice mismatch, ∼31.6% along $[\bar{1}2\bar{1}0]$ZnO and ∼19.8% along [0001]ZnO, is likely to exist.

3.3 Effect of substrate temperature and annealing

3.3.1 The impact of substrate temperature on the microstructural properties of FCVA ZnO thin films

As is usually the case in thin film growth, the crystal quality and grain size of the FCVA ZnO films are dependent on film thickness. As the film grows thicker it relaxes, reducing strain and consequently improving crystal quality [79]. Thicker films of higher crystal quality, such as those shown in Fig. 3.6 and 3.7, are very useful in context of material characterization. However, they are not practical for active electronic devices, particularly low operating voltage MESFETs, for which smooth (1-5 nm roughness) and thin (30-80 nm) films are usually desirable.

A comparison of the morphology of 40-50 nm thick ZnO films deposited on a-plane, c-plane, r-plane and m-plane sapphire at 100 °C, 200 °C and 300 °C is shown in Fig. 3.9. All films at each specific temperature were deposited simultaneously. The influence of sapphire substrate morphology, discussed in section 3.2.1, is clearly visible in the periodic diagonal arrangement of the grains in Fig. 3.9(b,g,h,i). In general, all depositions at these temperatures resulted in smooth (1.5 - 3 nm RMS roughness) and macro-particle free surfaces. In terms of surface morphology, ZnO films on a-plane and c-plane sapphire show uniformly distributed grains, 40-55 nm in size. On the ZnO films deposited on r-plane sapphire, the striped structure of the elongated grains was not visible despite the a-plane orientation confirmed by XRD in Fig. 3.10. Apparently,

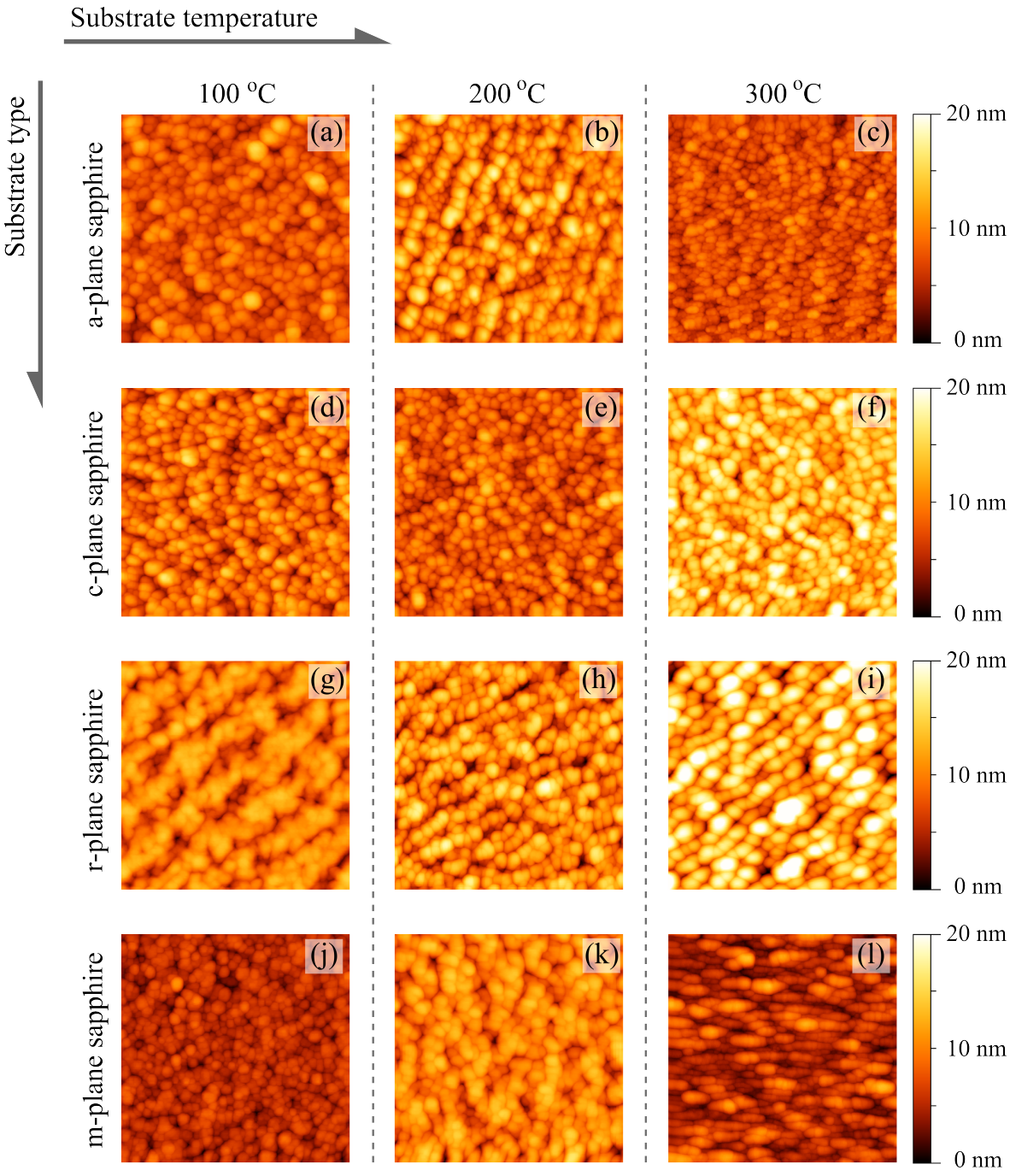

Figure 3.9: 1x1 μm^2 AFM images of 40-50 nm thick polycrystalline ZnO films deposited at a substrate temperatures of 100 °C, 200 °C and 300 °C on a-plane (a, b, c), c-plane (d, e, f), r-plane (g, h, i), and m-plane (j, k, l) sapphire. All films showed an RMS surface roughness of 1.5 - 3 nm.

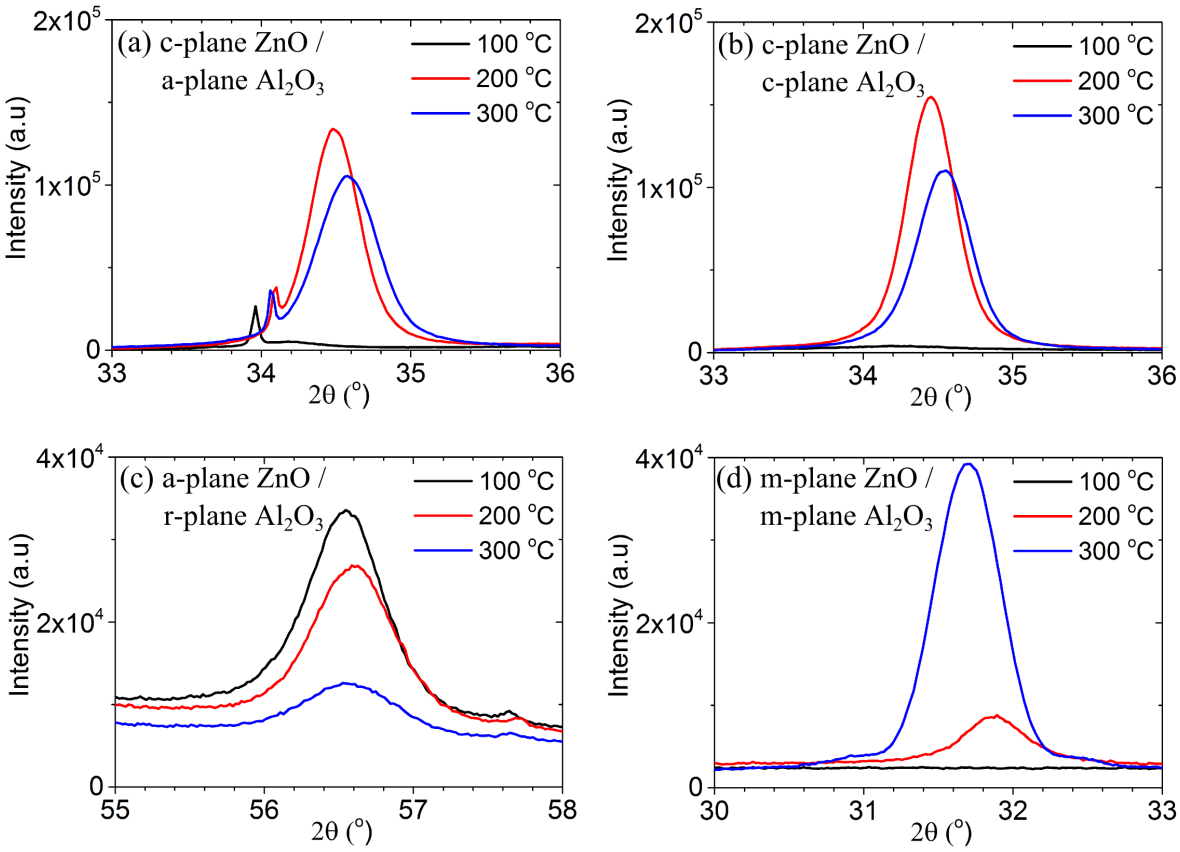

Figure 3.10: Dependence of crystal quality on growth temperature of 40-50 nm thick ZnO films on (a) a-plane sapphire, (b) c-plane sapphire and (c) r-plane sapphire and (d) m-plane sapphire.

the shorter growth time does not allow the grains to evolve into stripes such as those shown in Fig. 3.7(b). Interestingly, the ZnO film deposited on r-plane sapphire at the lowest temperature of 100 °C (Fig. 3.9(g)) was the smoothest among the a-plane ZnO films and it appears that the grains are well coalesced along the diagonal substrate induced stripes. On m-plane sapphire, anisotropic grain shape formation is only visible at a substrate temperature of 300 °C as shown in Fig. 3.9(l). At lower temperatures, well-rounded grains uniformly cover the thin m-plane ZnO films.

Fig. 3.10 shows the effect of growth temperature on the XRD diffractogramms of the 40-50 nm thick ZnO films shown in Fig. 3.9. Apparently, the growth temperature affects the diverse ZnO films in different ways. Films deposited on a-plane and c-plane sapphire are rather amorphous when deposited at a growth temperature of 100 °C. Growth on these substrates at 200 °C yielded the best crystallinity. The crystal quality of films

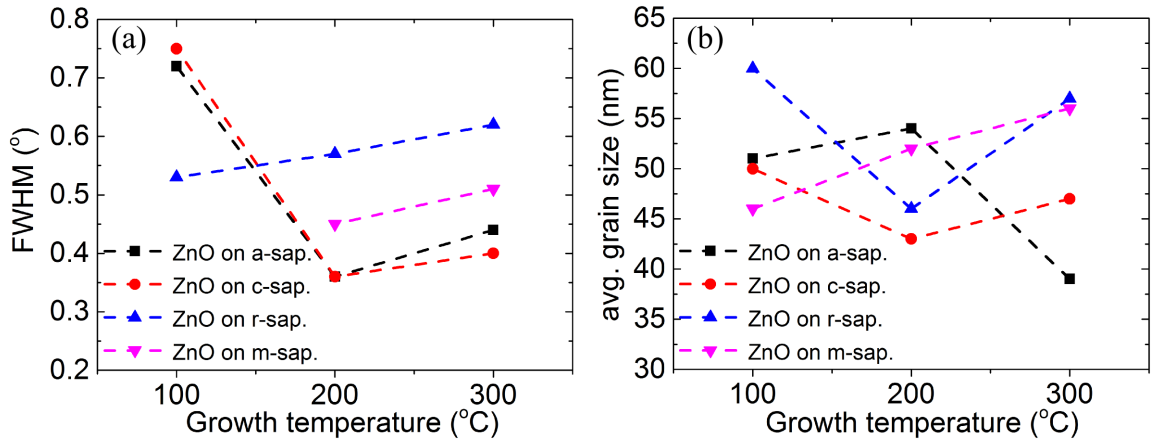

Figure 3.11: Effect of deposition temperature on the (a) FWHM of the XRD peaks and (b) grain size of 40-50 nm thick ZnO films deposited simultaneously on a-plane, c-plane, r-plane and m-plane sapphire at 100 °C, 200 °C and 300 °C.

deposited on r-plane sapphire deteriorated with increasing substrate temperature as shown in Fig. 3.10(c). This trend has also been observed in a-plane ZnO deposited on r-plane sapphire by other methods [71]. A monotonic improvement in crystal quality with deposition temperature was only observed in ZnO films deposited on m-plane sapphire (Fig. 3.10(d)). However, it is important to note that for XRD diffractogramms of anisotropic films, the FWHM of the XRD peaks was found to be dependent on the azimuth angle of the XRD beam [71]. Hence, two XRD scans, one along and one perpendicular to the c-axis are necessary for more precise characterization.

Fig. 3.11 shows a compilation of the FWHM values, as a metric of crystal quality, and the grain sizes of four 40-50 nm thick ZnO films deposited simultaneously on the four different faces of sapphire at different growth temperatures. The best combination of FWHM (0.36 °) and grain size (54 nm) was achieved with the deposition of ZnO on a-plane sapphire at 200 °C. Although the intensity and FHWM of XRD peaks of ZnO films on a-plane and on c-plane sapphire are almost identical, the different sapphire-ZnO interfaces apparently lead to different evolutions of grain size with temperature.

3.3.2 Post-deposition annealing

Fig. 3.12 shows the XRD (0002) peaks and lattice constants of FCVA ZnO deposited on a-plane sapphire as a function of annealing temperature in oxygen gas at 1 atmosphere.

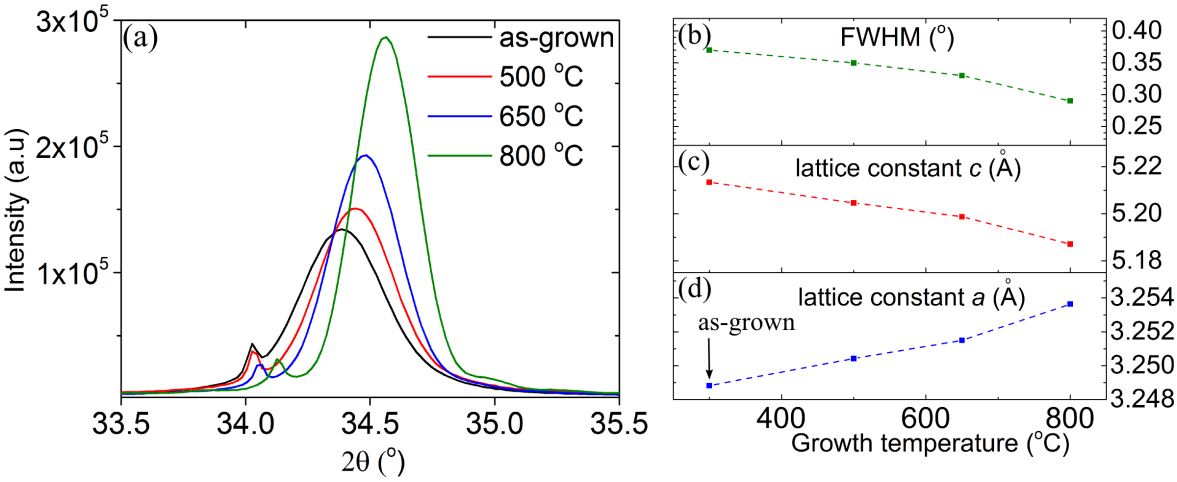

Figure 3.12: Effect of annealing temperature on the crystalline properties of a 50 nm thick ZnO film deposited on a-plane sapphire at 300 °C. Evolution of (a) (0002) XRD peak, (b) FWHM of the XRD peak, (c) lattice constant c, and (d) lattice constant a, after annealing at 500 °C, 650 °C and 800 °C.

As a result of post-deposition annealing, a considerable improvement in crystal quality takes place as shown in Fig. 3.12(a) and (b), where the XRD FWHM falls from 0.37 ° to 0.28 °. As the annealing temperature increases, the diffraction peak shifts to higher 2θ. This shift is usually associated with the relaxation of lattice strain [80]. Concurrently, the out-of-plane tensile and the in-plane compressive strains are relaxed as indicated by changes in the lattice constants shown in Fig. 3.12(c) and (d) [77]. The reduction in FWHM and the right-shift of the peak position also imply an increase in grain size (Eq.3.2). However, up to an annealing temperature of 800 °C, no significant change in the type of surface morphology of the ZnO films on a-plane sapphire was observed.

All films, deposited on a-, c-, r- and m-plane sapphire, were found to preserve their initial crystal orientation after annealing at 800 °C in oxygen gas. However, the improvement in crystal quality varies considerably with the type of substrate, as shown in Fig. 3.13. In general, the FWHM of the XRD peaks is related to crystal size and lattice defects [83, 29], where the FWHM of a Bragg peak in a θ-2θ scan is related to two effects described by the equation

$$\delta\theta = \frac{\lambda}{2D} cos\theta + \varepsilon_{in} tan\theta, \tag{3.4}$$

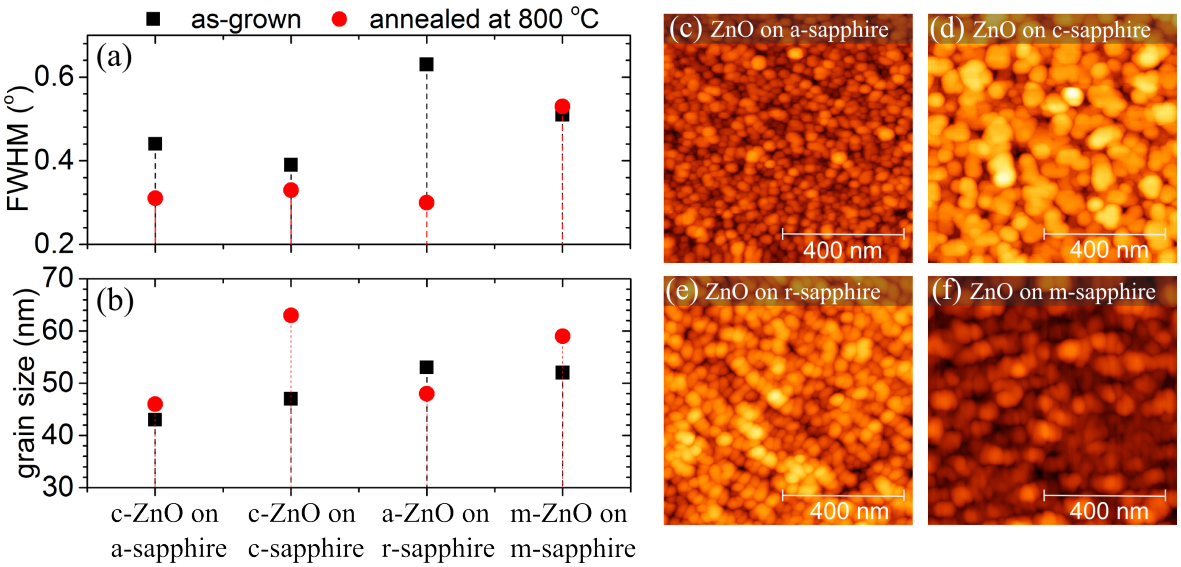

Figure 3.13: (a-b) Effect of annealing at a temperature of 800 °C in flowing oxygen (1 hour) on the FWHM of the XRD peaks and RMS grain size of 50 nm thick films deposited on a-plane, c-plane, r-plane and m-plane sapphire. (c-f) The surface morphology of the corresponding ZnO films after annealing. All films were grown at 300 °C.

where D is the domain or grain size, θ is the peak location and ε_{in} is the RMS strain averaged over the effective domain size. Accordingly, by comparing the FWHM values in Fig. 3.13(a) with the measured RMS grain size in Fig. 3.13(b), conclusions can be drawn about the effect of high temperature annealing on crystal quality. After annealing at 800 °C, ZnO films on a-plane and r-plane sapphire yield the best crystal quality (Fig. 3.13(a)) while preserving their surface morphology, as shown Fig. 3.13(c) and (e). Although the grain size increased only slightly for ZnO films on a-plane sapphire and actually decreased for ZnO films on r-plane sapphire, the XRD FWHM of the two films improved considerably. This implies that the improvement is predominantly caused by the relaxation of the existing strain and healing of lattice defects. For ZnO on c-plane and m-plane sapphire the grain size increased considerably but with almost no improvement in the corresponding FWHM. This suggests that annealing at 800 °C has little effect on the density of lattice defects in ZnO on c-plane and m-plane sapphire films. The induced lattice strain upon annealing is usually determined by the combination of lattice and thermal mismatch between ZnO and sapphire [84]. The mismatch in the thermal expansion coefficient in a-plane and m-plane ZnO is strongly anisotropic; it is

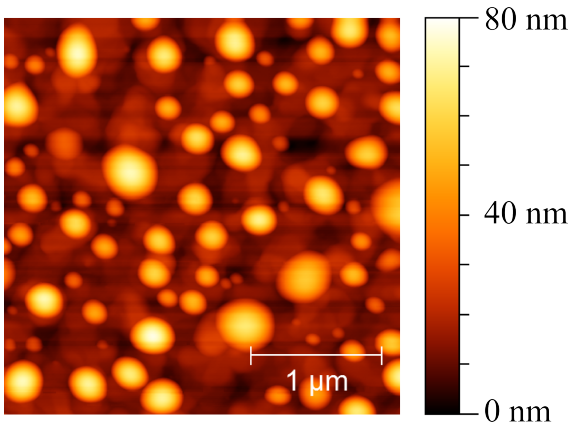

Figure 3.14: A FCVA ZnO film deposited on a-plane sapphire after annealing in O_2 at 950 °C.

almost twice as high perpendicular to the c-axis than parallel to the c-axis [85]. An understanding of the changes in crystal quality would require deeper investigation using other complementary characterization techniques that enable a study of the interface structure.

Fig. 3.14 shows the effect of annealing at 950 °C in oxygen gas on the morphology of ZnO deposited on a-plane sapphire. Annealing at this very high temperature resulted in a discontinuous surface morphology and electrically insulating films, probably due to the mismatch of thermal expansion coefficients between sapphire and ZnO.

3.4 Summary

ZnO films were deposited via a filtered cathodic vacuum arc (FCVA) on a-plane, c-plane, r-plane and m-plane sapphire substrates. In general, all depositions resulted in dense polycrystalline films free of voids and macroparticles, confirming the capability of FCVA in delivering ZnO material of high structural quality. Furthermore, ZnO films of different crystal orientations were produced on different sapphire substrates. Deposition on a-plane and c-plane sapphire substrates resulted in polar ZnO films with a preferred c-axis orientation. On the other hand, FCVA ZnO deposition on r-plane and m-plane sapphire yielded predominantly non-polar a-plane and m-plane films, respectively. The resulting anisotropic surface morphologies of the a-plane and m-plane films

are consistent with published results obtained by high-quality epitaxial techniques such as MBE, PLD and MOVPE. The anisotropic diffusion of the deposited species along preferred crystal directions indicates that FCVA ZnO deposition on sapphire adheres to specific epitaxial relationships. In general, the morphological properties of FCVA ZnO films were found to be dependent on their thickness, growth temperature, and in particular post-deposition annealing in oxygen gas. Overall, the ZnO films deposited on a-plane sapphire exhibited the highest crystallinity with FWHM values as low as 0.24 ° and RMS surface roughness in the range 1.5 - 3 nm.

Chapter 4

FCVA ZnO: Defect analysis

The control of defects is essential for the successful use of semiconductors in electronic and optoelectronic applications. In addition, native defects and impurities may also play a critical role in the stability of the fabricated devices. Despite the simple chemical nature of ZnO, it has a very rich and complicated defect chemistry which is strongly dependent on the growth environment and post-growth treatments. In addition to bulk intrinsic and extrinsic defects inside polycrystalline grains, imperfections at the grain boundaries of polycrystalline films are known to act as carrier traps and scattering centres that play a critical role in electron transport. This chapter explores the electronic and optical properties of FCVA ZnO films. In order to establish a relationship between film defects and electronic properties, several experimental techniques were used, including electrical Hall effect measurements, Kelvin probe force microscopy, optical transmission measurements, photoluminescence spectroscopy (PL) and time of flight secondary ion mass spectroscopy (TOF-SIMS).

4.1 Essential background: Defects in ZnO

As-grown unintentionally doped ZnO has commonly an n-type character, with a background electron concentration ranging from 10^{15} to 10^{18} cm^{-3}. Previous research using photoluminescence spectroscopy and temperature-dependent Hall-effect measurements (T-Hall) has revealed the existence of shallow donors with binding energies $E_d \sim$ 30-75 meV [8, 86, 87]. However, a definitive assignment for the source of these shallow donors

has not been fully established and this question continues to be actively studied and debated. The background charge carriers have been attributed to a variety of native defects and ever-present impurities. Some of the most common and most relevant to this thesis are briefly discussed below.

4.1.1 Intrinsic donor and acceptor states

Possible native point defects in ZnO are: Oxygen and zinc vacancies (V_O and V_{Zn}), interstitials (O_i and Zn_i) and antisites (O_{Zn} and Zn_O) [88]. The bonding chemistry of ZnO suggests that point defects such as oxygen vacancies and zinc interstitials are donors. Theoretical investigations and experimental T-Hall studies provide substantial evidence that Zn interstitials are shallow donors [2, 89, 90]. However, theoretical calculations using first-principles methods, conducted by *A. Janotti et al.* [89], suggest that Zn_i has a high formation energy in n-type ZnO. Further experimental investigations by *F.A. Selim et al.* [92] using positron annihilation spectroscopy on as-grown bulk ZnO and on ZnO annealed in Zn vapour showed that Zn_i is not the source of shallow donors in as-grown ZnO. However, there exists some experimental evidence that complexes involving Zn_i and acceptors such as N (on O site) may exist as shallow donors with low formation energies that can be produced in significant concentrations [93]. On the other hand, in n-type ZnO, oxygen vacancies are rather deep donors with high formation energies [89, 91]. In addition to Zn_i and V_O, recent theoretical analysis has shown that Zn_O (Zn on O site) is a shallow donor with a high formation energy [10]. Due to their high formation energy and/or deep states, concentrations of isolated point defects such as Zn_i, V_O and Zn_O are unlikely to account for the high electron concentrations present in native n-type ZnO. In contrast to n-type material, the Fermi level in p-type ZnO should be close to the valence band maximum. Consequently, these native defects possess lower formation energies for p-type material and tend to limit p-type doping through self-compensation [91].

Theoretical calculations predict that V_{Zn}, O_i and O_{Zn} (O on Zn site) are acceptors [10, 91, 94]. For n-type ZnO, both theoretical predictions and experimental evidence

Table 4.1: A summary of native point defects and extrinsic dopants in n-type ZnO. Defects are considered shallow if their energy level is less than 100 meV from the conduction or valence band. Native point defects are unlikely to contribute significantly to the high electron concentration in as-grown films [10, 89, 92, 91, 95, 96, 97, 98, 87, 100].

	Defect	**Energy level**	**Formation enegry**	**Type**
native	Zn_i	shallow	high	donor
	V_O	deep	high	donor
	Zn_O	shallow	high	donor
	V_{Zn}	shallow	low	acceptor
	O_{Zn}	shallow	high	acceptor
extrinsic	H	$\sim$ 35 meV	low	donor
	Al	$\sim$ 52 meV	low	donor
	Ga	$\sim$ 55 meV	low	donor
	In	$\sim$ 63 meV	low	donor
	Ag	$\sim$ 400 meV	low	acceptor
	Au	$\sim$ 500 meV	low	acceptor
	Cu	$\sim$ 700 meV	low	acceptor

suggest that V_{Zn} defects are deep acceptors with low formation energies, acting rather as compensating centres in n-type material [10, 95]. In p-type material, the high formation energy of V_{Zn} prevents its generation in significant concentrations [10]. O_i are believed to form O_2 molecule-like defects in the ZnO lattice which are electrically neutral [10]. Finally, O_{Zn} is predicted to have the highest formation energy among native acceptors and, therefore, should be present in negligible concentrations. These intrinsic defects can exist in neutral as well as in single or double ionized states and can give rise to various mid-gap states in ZnO.

4.1.2 Extrinsic donor and acceptor impurities

As the assumption of n-type background conductivity due to native donors in ZnO has been challenged by many theoretical and experimental studies, there is a growing tendency to attribute the conductivity to hydrogen impurities. Theoretical calculations based on density functional theory conducted by *C. G. Van de Walle* and *A. Janotti* [96, 97] have identified hydrogen as a shallow donor. These predictions have been backed by experimental evidence showing that one of the two frequently observed

shallow donors, with an activation energy of 35 ± 5 meV, is related to hydrogen [98]. Hydrogen is always present as a background impurity and is known to be very difficult to remove from growth environments. In contrary to other semiconductors where hydrogen acts as an amphoteric impurity, it always acts as a donor in ZnO [96].

Intentional n-type doping is readily achievable with group III elements such as Al, Ga and In, substituting the Zn sublattice. One or more of these elements often appear in photoluminescence spectra of undoped ZnO, with donor binding energies of 52 (Al), 55 (Ga) and 63 meV (In) [87]. Hence, residual concentrations of these elements are likely to contribute to the background electron concentration present in ZnO. Both Al and Ga doping has been used to achieve electron concentrations in the order of 1×10^{-20} cm^{-3} in ZnO for transparent conductive oxide applications [7, 99].

To date, intentional p-type doping has been problematic. This is a result of (but not limited to) high residual n-type carrier concentration, solubility issues and the deep level of the proposed acceptor states [3, 91]. However, some acceptor elements which are frequently used in semiconductor processing may be unintentionally introduced during film growth and device fabrication. For example, first principle calculations performed by *Y. Yan et al.* [100] revealed that substitutional (at Zn site) group IB elements such as Ag, Cu and Au are deep level acceptors (0.4 - 0.7 eV above valence band) with low formation energies. Experimental evidence for the behaviour of Ag^{+} as a stable acceptor on Zn sites already exists [101, 102]. These elements could be potentially incorporated via diffusion during ohmic or Schottky contact formation, hence, compensating some of the existing electron concentration in ZnO. To summarize, a compilation of the native defects in ZnO and some of the relevant extrinsic donors and acceptors is shown Table 1 (page 47).

4.1.3 Understanding the role of grain boundary defects

Charge carrier transport in polycrystalline ZnO films cannot be fully understood without considering electron trapping at grain boundaries (GB). In a polycrystalline semiconductor, the crystalline grains (crystallites) are isolated from each other by grain

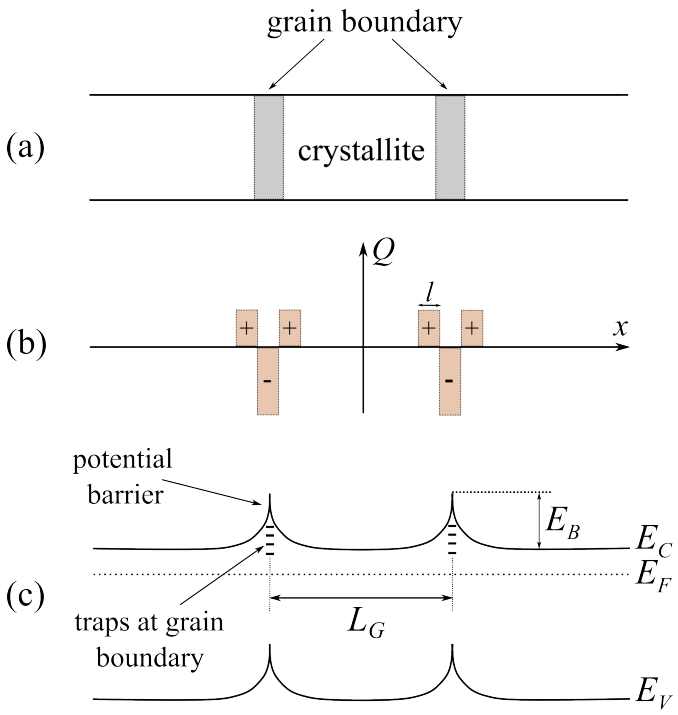

Figure 4.1: Grain boundary trapping model. (a) Idealized grain structure, (b) charge distribution, and (c) band diagram.

boundary regions. Inside each crystallite, the atoms are arranged in a periodic manner such that they can be considered as single crystals. However, the grain boundary adjoining the grains consists of few atomic layers of disordered atoms that contain a higher density of defects due to incomplete bonding. This results in the formation of trapping states. These states are capable of trapping carriers and thereby charging the GB regions. As a result of mobile charge (electrons in n-ZnO) trapping, depletion regions are created at the GB. These depletion regions give rise to potential energy barriers which impede the motion of carriers from one crystallite to another, thereby reducing their mobility.

A grain-boundary model describing the conduction mechanism in polycrystalline semiconductors was first proposed by *J. Seto* [104] and further refined by *G. Baccarani et al.* [105] and *J. Levinson et al.* [106]. According to this model, the film can be pictured as a periodic arrangement of equally sized single crystal grains and thin GB regions, as shown in Fig. 4.1(a). The resulting GB potential barrier heights (Fig. 4.1(c)) can be derived by applying Poisson's equation across the depletion region (Fig. 4.1(b))

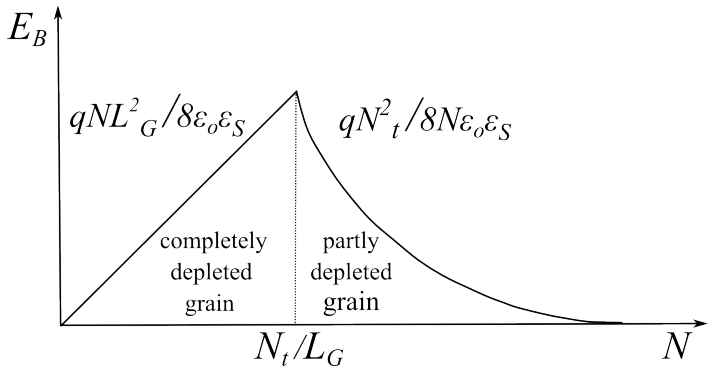

Figure 4.2: Functional dependence of the potential barrier height E_B on the carrier concentration N.

[104, 106],

$$\frac{d^2V}{dx^2} = \frac{qN}{\epsilon_o\epsilon_S}, \qquad l < |x| < \frac{1}{2}L_G, \tag{4.1}$$

where N is the carrier concentration, q the elementary charge, ϵ_S the relative semiconductor permittivity, L_G the grain size and l is the width of the depletion region. Eq. 4.1 is solved under the assumption that the grain boundary is of negligible thickness and contains a trap density of N_t [cm^{-2}]. Furthermore, for a given crystallite size, there exist two possible conditions depending on the carrier concentration: (a) $L_G \cdot N < N_t$, and (b) $L_G \cdot N > N_t$, for which Eq. 4.1 yields the following possible solutions [104]:

$$E_B = \frac{qN{L_G}^2}{8\,\epsilon_o\epsilon_S} \qquad NL_G \leq N_t, \tag{4.2}$$

$$E_B = \frac{q{N_t}^2}{8\,N\,\epsilon_o\epsilon_S} \qquad NL_G \geq N_t. \tag{4.3}$$

For a high density of GB traps such that ($NL_G \leq N_t$), the grains are fully depleted and the traps are partially filled. Under this condition, the material would be very resistive. Increasing the carrier concentration would fill the remaining traps and increase the potential barrier height until a maximum barrier is reached at ($NL_G \approx N_t$), where the trap charge balances with the carrier charge in the grain. Yet, for ($NL_G \geq N_t$)

the grain is only partly depleted and the GB traps are filled. An increasing carrier concentration in this case would reduce the width of the depletion region and hence the potential barrier height at the GB. This behaviour is illustrated in Fig. 4.2. For the latter case of partial grain depletion, the GB can be modelled electrically as back-to-back Schottky contacts whereby the current density J over the potential barrier is determined by thermionic emission [106, 107],

$$J = q^2 N \left(\frac{v_c}{kT}\right) V_d \, exp\left(-E_B/kT\right). \tag{4.4}$$

This yields an effective GB conductivity of [105]

$$\sigma = q^2 L_G N \left(\frac{v_c}{kT}\right) \, exp\left(-E_B/kT\right), \tag{4.5}$$

where V_d=V_D/N_G is the voltage drop across the GB, V_D voltage drop across the sample, and N_G the number of grain boundaries. v_c =$(kT/2\,\pi\ m^*)$ is the thermal collection velocity with m^* being the effective electron mass. From Eq. 4.5, the mobility in the GB region can be considered as $\mu_{GB} = \mu_0 \exp(\text{-}E_B/kT)$, with μ_0= $(q\, v_c\, L_G/8kT)$. Accordingly, for a polycrystalline semiconductor, an effective mobility model that accounts for the contributions of the grain (μ_G) and grain boundary regions (μ_{GB}) can be expressed as

$$\frac{1}{\mu} = \frac{1}{\mu_G} + \frac{1}{\mu_0\, exp(-E_B/kT)} \quad , \tag{4.6}$$

where the mobility in the grain is assumed to approach the mobility of a single crystal. This indicates that in a polycrystalline film, the effective mobility is critically dependent on the GB potential barrier E_B. Consequently, according to Eq.4.3, good electron conduction necessitates a large grain size L_G, high carrier concentration N and low trap densities at grain boundaries N_t.

4.2 Electrical and spectral characterization techniques

4.2.1 Hall effect measurements

The Hall effect is one of the fundamental techniques used to characterize the electrical properties of semiconductor materials. In conjunction with the Van der Pauw technique, it is routinely used to measure the carrier concentration, carrier type, carrier mobility and resistivity of materials [58]. The underlying principle of a Hall effect measurement is illustrated in Fig. 4.3(a). Given an appropriate constant current (I) flowing through the sample and by applying a known constant magnetic field (B) perpendicular to the current flow, the charge carriers (q) drifting with a velocity (v) will be subjected to a Lorentz force ($F_L = q \cdot v \times B$) perpendicular to both the current flow and magnetic field direction. As a result, charge carriers are deflected in the y-direction based on their type. The electric field (E_y) produced by the resulting charge separation generates an electrostatic force ($F_E = q \cdot E_y$) which balances the Lorentz force. For an n-type semiconductor, such as intrinsic ZnO, it can be shown using the force balance equation and basic carrier transport physics (J = -nqv, where J and n are the current and electron densities) that the carrier concentration is [58]

$$n = \frac{-I\,B}{q\,d\,V_H}, \tag{4.7}$$

where the Hall voltage V_H is the potential difference associated with the lateral electric field (V_H=$E_y\,w$). The factor

$$R_H = -\frac{1}{nq} = \frac{d\,V_H}{I\,B} \tag{4.8}$$

is known as the Hall coefficient. Typically, the semiconductor sample is contacted in a squared Van der Pauw geometry, as shown in Fig. 4.3(b). Using this configuration, the resistivity of the material is evaluated by a 4 point measurement using the Van der

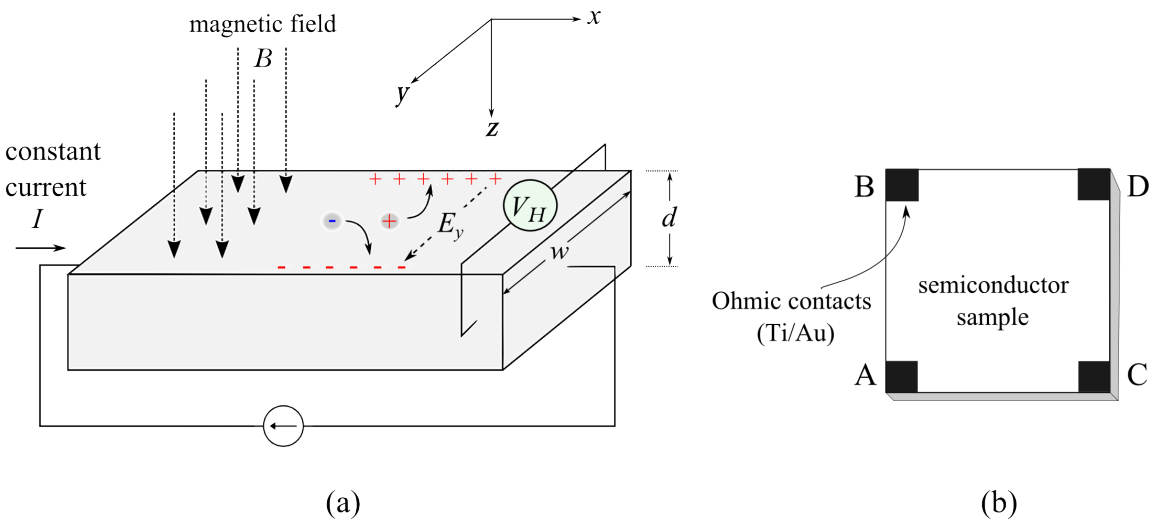

Figure 4.3: (a) Schematic illustrating the Hall effect. (b) Van der Pauw contact layout for Hall effect measurements.

Pauw equation:

$$exp\left(\frac{-\pi\, R_{horiz}}{R_s}\right) + exp\left(\frac{-\pi\, R_{vert}}{R_s}\right) = 1, \tag{4.9}$$

where R_S is the sheet resistance (Ω), and R_{horiz} and R_{horiz} are the resistances measured between the different edge points on the sample (Fig. 4.3(b)). If the sample thickness d is known, the resistivity (ρ) of the sample and its carrier mobility (μ_H) is calculated from

$$\rho = R_S d, \tag{4.10}$$

and

$$\mu_H = \frac{1}{qn\rho}. \tag{4.11}$$

However, these derivations only apply under the condition of sample homogeneity and single charge carrier transport. In reality, in particular for ZnO films, this condition is often not fulfilled. The deviation of homogeneity results from parallel conduction paths with different carrier concentrations and/or carrier mobilities. In ZnO, surface

layers with different electronic properties are known to occur due to polarity related near-surface band-bending and adsorption of ambient gases [108, 109]. Moreover, for high growth or annealing temperatures, degenerate thin layers can form at the interface between the film and the substrate [110, 111]. Usually, for the investigation of mixed conduction effects, temperature dependent Hall measurements are fitted with a two-layer model to determine the different mobilities of each carrier [112]. In this thesis, only single-field room temperature Hall effect measurements were used. This measurement yields the effective mobility of the film.

4.2.2 Kelvin probe force microscopy

Kelvin probe force microscopy (KPFM) is a versatile tool for studying the electronic properties of semiconductor surfaces and interfaces. This technique was first developed and introduced by *M. Nonnenmacher et al.* [113], as an extension to atomic force microscopy, described in section 3.1.2. Using the same AFM setup as illustrated in Fig. 3.2, this method allows the measurement of surface potentials and the contact potential difference between two materials. When using KPFM for surface potential measurements, quantitative voltage measurements can be inferred from the relative voltages across the same sample, e.g. when measuring the potential difference between the grain boundary and grain centre. Consequently, a surface potential image can be made, showing the potential barriers present in polycrystalline materials [114].

The surface potential image is obtained by two interleaved measurements. In the first pass, a topographic image is obtained using standard tapping-mode AFM. In the second pass, the cantilever follows the stored surface topography from the first pass at a constant lift height above the sample surface to obtain the surface potential image, as shown in Fig. 4.4(a). During the second pass, the tapping drive piezo is turned off and an oscillating voltage $V_{AC}\ sin\omega t$ is applied directly to the probe tip, at a frequency ω matching the resonant frequency of the cantilever. The principle of operation and its governing equations can be derived by considering the cantilever tip and the sample surface as a parallel plate capacitor. For a voltage difference of ΔV between the tip

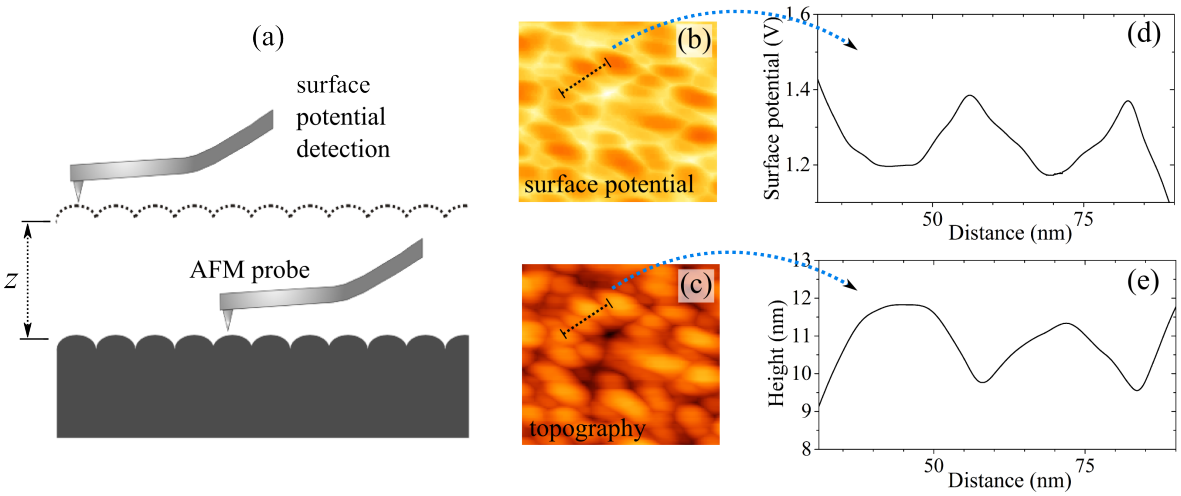

Figure 4.4: Kelvin probe force microscopy: (a) The surface topography is detected using tapping-mode AFM in the first pass. In the second pass the surface potential is measured in lift-mode; (b) and (c) show $0.25 \times 0.25\ \mu m^2$ images of the surface potential and the corresponding topography of a polycrystalline ZnO film. (d) and (e) show the surface potential and topography profiles from selected cross-sections.

and the sample, the energy stored in the system is $U = (1/2)\ C\ \Delta V^2$, where C is the local capacitance between the tip and the sample. The electrostatic force between the tip and the sample is equal to the rate of change of the stored energy (U) with the separation distance z:

$$F(z) = -\frac{\partial U}{\partial z} = -\frac{1}{2}\Delta V^2 \frac{\partial C}{\partial z}. \tag{4.12}$$

However, due to the work function difference between the sample surface and the tip as well as surface charge effects, a DC voltage component is superimposed on the applied AC voltage such that the tip-sample voltage difference is:

$$\Delta V = \Delta V_{DC} + V_{AC} sin\omega t. \tag{4.13}$$

As a result, the electrostatic force in Eq.4.12 can be broken down to three components:

$$F(z) = \frac{\partial C}{\partial z}\left(-\frac{1}{2}(\Delta V_{DC}^2 + \frac{1}{2}V_{AC}^2) - \Delta V_{DC} V_{AC}\, sin(\omega t) + \frac{1}{4}V_{AC}^2\, cos(2\omega t)\right). \tag{4.14}$$

The cantilever responds only to forces at or very near its resonant frequency. Therefore, the DC and the 2ω terms in Eq. 4.14 do not cause any significant oscillation of the cantilever. Consequently, the amplitude of the oscillating electric force acting on the cantilever (at a frequency ω) is:

$$|F(z)| = \frac{\partial C}{\partial z}\Delta V_{DC} V_{AC}. \tag{4.15}$$

The local surface potential is determined by adjusting the DC voltage on the tip until it equals the voltage of the sample ($\Delta \mathrm{V}_{DC}$ = V_{tip} - V_{sample} = 0), at which point the cantilever amplitude should be zero. The tip potential is then used to generate a voltage map of the surface. Fig. 4.4 shows a schematic illustrating the principle of operation and typical AFM and surface potential images of a polycrystalline ZnO film deposited by FCVA on a-plane sapphire.

4.2.3 Photoluminescence spectroscopy

The radiative recombination of electrons and holes in a semiconductor is referred to as luminescence. In addition, if the electron-hole pairs are generated by means of photons, the emitted light is called photoluminescence. The wavelengths of these photoemissions are characteristic of the material and the particular radiative process involved. This forms the basis of photoluminescence spectroscopy (PL), which is routinely used to probe the electronic structure of semiconductors [58]. In the case of wide band gap semiconductors such as ZnO, a UV laser with photon energy larger than the bandgap (E_G) is usually used for photoexcitation. Furthermore, if the photoluminescence is stimulated at very low temperatures, i.e. at liquid helium temperatures of $\sim$ 4 K, the collected PL spectrum can give an excellent picture of the overall crystal quality, purity and the defect complexes present in the semiconductor.

After excitation, the photo-generated electrons (holes) rapidly thermalize to the bottom (top) of the conduction (valence) band by emitting phonons. For this reason there is typically no observable luminescence above the bandgap energy. Once the

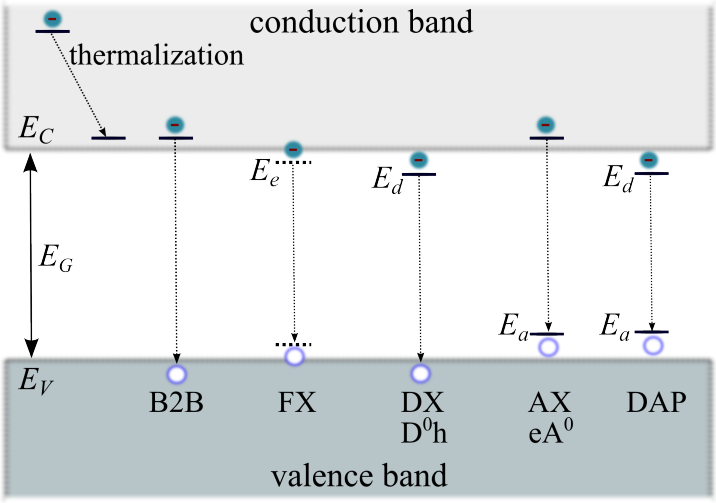

Figure 4.5: Overview of basic radiative recombinations in a semiconductor [(B2B) Band to band recombination, (FX) free exciton, (DX) donor bound exciton, (AX) acceptor bound exciton, (eA) electron to acceptor-hole, (Dh) hole to donor-electron, and (DAP) donor-electron to acceptor-hole recombination].

photogenerated carriers have relaxed at the band edge, many recombination mechanisms contribute to the PL spectrum. At low temperatures and in sufficiently pure semiconductors, an electron (in the conduction band) and a hole (in the valence band) can correlate their motion and bind together via the Coulomb interaction to form a hydrogen-like quasi-particle called an exciton. This exciton eventually recombines radiating an energy slightly less than the bandgap, i.e. reduced by the binding energy of the exciton electron-hole pair. Due to the high dielectric constant (ϵ_S) of semiconductors such as ZnO, the Coulomb force is very weak and the Bohr radius (r_B) of the bond is very large (potential energy: $P_E \propto 1/\epsilon_r\, r_B$). These weakly bound excitons with Bohr radii larger than lattice spacing are generally known as Wannier-Mott excitons [115]. The free exciton binding energy in ZnO is around 59 meV ($r_B = 1.4$ nm) which is about 2.4 times more than room-temperature thermal energy. This is one of the key advantages of ZnO, since it is a prerequisite for stable lasing at room temperature.

Fig. 4.5 shows an overview of radiative recombinations that can occur in a semiconductor. Band-to-band (B2B) transitions take place when a free electron in the conduction band recombines with a hole in the valence band. B2B emissions domi-

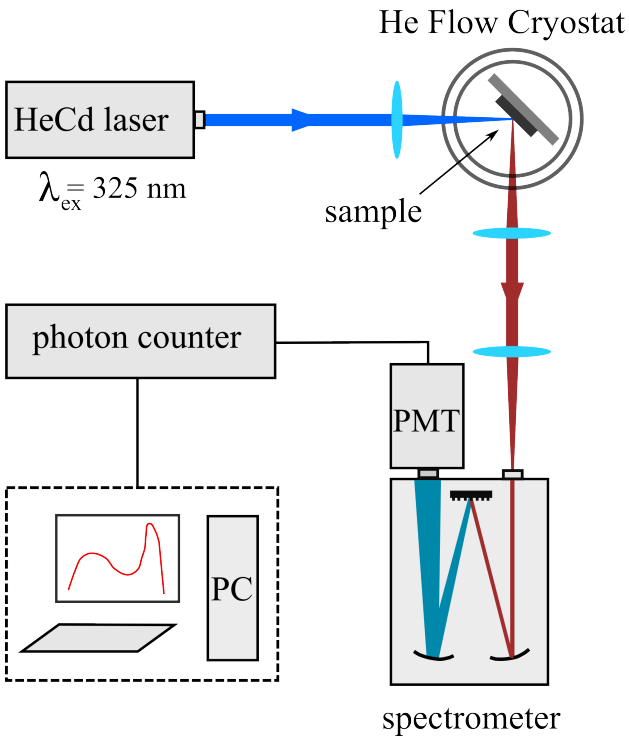

Figure 4.6: Experimental setup for photoluminescence measurements at the University of Canterbury.

nate at room temperature. They give rise to a broad peak with a sharp edge at the bandgap and a long tail towards lower energies. Other possible, non-excitonic radiative recombinations are a free electron with a neutral acceptor (eA^0), a free hole with a neutral donor (D^0h), and donor-acceptor pair transition (DAP). The latter occurs when an electron from a neutral donor and a hole from a neutral acceptor radiatively recombine. At cryogenic temperatures, the probability of forming excitons increases and it becomes possible to observe many types of excitonic emissions. In addition to free exciton emissions (FX), discussed above, excitons can also bind to native defects, impurities and crystal imperfections. They become localized around these defects and trapped until they recombine. As a result of losing some of their energy due to these bonds, radiative recombination of localized excitons produce photons that are red-shifted from those produced by free excitons. Detecting the wavelength of these red-shifted recombinations is extremely useful in identifying the type of the associated defect and the energy level of the impurities involved. Since ZnO is intrinsically n-type, neutral donors are present in considerable concentrations at low temperatures. Exci-

tons bound to neutral donors, forming a complex called a neutral-donor-bound exciton are commonly notated as DX. Neutral acceptors can also bind excitons, forming AX complexes. However, due to the low concentration of acceptors in n-type ZnO, these emissions are less likely to occur. Finally, excitons are also found to bind to extended structural defects such as dislocations and stacking faults [136, 137].

In this work, a continuous wave HeCd laser, emitting at 325 nm (3.815 eV), was employed, resulting in above bandgap excitation ($E_G{}^{ZnO}$(3K)=3.44 eV) with an excitation power of 10.5 mW after focusing optics. Samples were mounted using silver paste in an Oxford OptistatCF2 helium flow cryostat. A stable base temperature between 3 K and 4 K was used for the low temperature PL measurements. Although it is possible to submerge the sample completely in liquid helium, inevitable He gas bubble formation dramatically reduces the luminescence intensity leading to reduced resolution. The luminescence emitted from the sample was then focused via lenses with a UV transmittance of $> 92\%$ into a 1m Spex1400 monochromator equipped with a 1200 lines/mm holographic grating. A Hamamatsu R943-02 GaAs photomultiplier tube (PMT) operating at an integration time of 1s was used for detection. A schematic of the setup used is shown in Fig. 4.6.

4.2.4 Raman spectroscopy

When light is scattered from the surface of a sample, the scattered light is found to contain mostly wavelengths that are incident on the sample (Raleigh scattering) but also different wavelengths at very low intensities due to the interaction of the incident light with the material. Frequency of the re-emitted photons is shifted up or down in comparison with the original monochromatic frequency. This frequency shift is referred to as the Raman effect, after its discoverer *C. C. Raman* [116].

The frequency shift in the scattered light is caused by the interaction with the lattice optical and acoustic phonons. Since the intensity of Raman scattered light is very weak, Raman spectroscopy is only practical when an intense monochromatic light source such as a laser is used. In the Raman microprobe, a laser illuminates

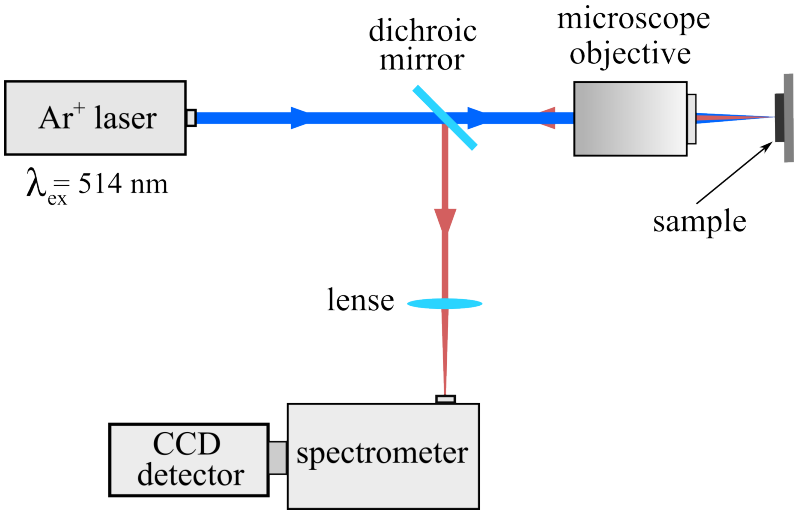

Figure 4.7: A schematic illustrating the working principle of the Raman spectrometer used in this thesis.

the sample through a microscope. Laser power is usually held below 5 mW to reduce sample heating and specimen decomposition. The weak scattered light or signal is passed through a double monochromator to reject the Rayleigh scattered light and the Raman-shifted wavelengths are detected by a photodetector. The technique is non-destructive and requires no contacts to the sample. Most semiconductors can be characterized by Raman spectroscopy. The wavelengths of the scattered light are analysed and matched to known wavelengths for identification. Various properties of the sample can be characterized such as its composition, i.e. the presence of impurities as well as the crystal orientation. Raman spectra in this thesis were obtained using a Renishaw InVia system operating with an excitation wavelength of 514 nm and a grating of 2400 lines/mm. The measurements were conducted by Dr. Jim Partridge at Industrial Research Institute Swinburne (IRIS), Australia. A schematic of the used Raman microscope is shown in Fig. 4.7.

4.2.5 Time-of-Flight Secondary Ion Mass Spectroscopy

Time-of-flight secondary ion mass spectroscopy (ToF-SIMS) is a surface-sensitive analytical method that uses a pulsed ion beam to sputter surface layers, displacing surface atoms into the vacuum. The sputtered atoms (in the form of secondary ions) are then

accelerated into a flight tube and their mass is determined by measuring the exact time at which they reach the detector (time of flight). Under typical operating conditions, ToF-SIMS produces an atomic mass spectrum that surveys the constituents of the sputtered sample. Moreover, by recording the mass spectrum and sputtering time, it is possible to generate a depth profile of the elemental composition of the material. ToF-SIMS measurements can be a valuable tool to investigate doping effects and assist in interpreting PL spectra and Hall effect measurements. In this thesis, SIMS was performed at the University of Buffalo, USA using an ION-TOF GmbH SIMS 5-100 instrument. Liquid bismuth (Bi^+) and carbon-60 ($C60^+$) were used as ion sources for mass spectroscopy and depth profiling.

4.3 Electrical and optical characterization of FCVA ZnO films

4.3.1 Effect of annealing on electrical characteristics

Annealing is an effective method for improving the quality of thin films by relaxing intrinsic stress and lattice mismatch [80]. At sufficiently high temperatures, annealing in specific ambients can be used to intentionally (or unintentionally) introduce impurity dopants, expel impurities from the film and passivate (or generate) intrinsic defects [117, 118, 119]. Most importantly, in terms of defect analysis, observing the evolution of electrical characteristics and PL spectra as a function of annealing temperature is useful in identifying the defects that contribute to the material's charge carrier concentration. The properties of annealed ZnO films are also known to be dependant on the ambient/gas used during annealing. Annealing in oxygen gas is often found to have a profound effect on ZnO film quality [118, 120, 121] and consequently the FCVA ZnO films in this work were post-annealed in oxygen flow in 1 atm for 1 hour, at 500 °C, 650 °C and 800 °C.

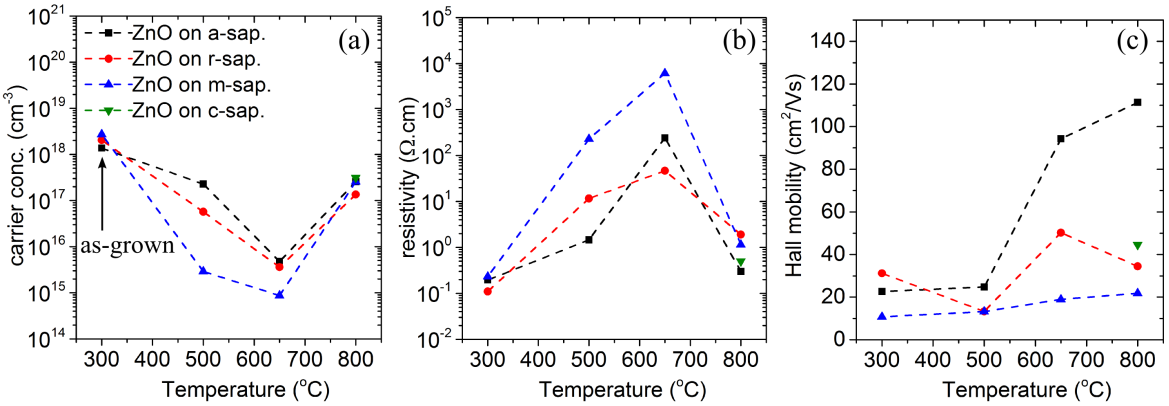

Figure 4.8: Electron concentration, resistivity and Hall mobility as a function of annealing temperature. The 300 nm thick ZnO films were deposited simultaneously on a-plane, c-plane, r-plane and m-plane sapphire at 300 °C and subsequently annealed at 500 °C, 650 °C and 800 °C. Only one measurement was performed on ZnO/c-plane sapphire, after annealing at 800 °C.

Overview

Fig. 4.8 shows the electron concentration, resistivity and Hall mobility of four 300 nm thick ZnO films as a function of annealing temperature. The films were deposited simultaneously on a-plane, r-plane and m-plane sapphire at 300 °C and subsequently annealed at 500 °C, 650 °C and 800 °C. All of the as-deposited films were n-type with an electron concentration of approximately 1×10^{18} cm^{-3} (Fig. 4.8(a)). From Fig. 4.8, it can be seen that the electron concentration initially decreases with increasing annealing temperature. The carrier concentration reaches a minimum after annealing at 650 °C, ranging from 9×10^{14} cm^{-3} for ZnO on m-plane sapphire to 7×10^{15} cm^{-3} for the ZnO film on a-plane sapphire. After annealing at 800 °C, the carrier concentration increases to approximately 2×10^{17} cm^{-3}. As expected, the resistivity in Fig. 4.8(b) follows a trend which is inversely proportional to the carrier concentration. This trend was found to exist for all films regardless of the initial growth temperature and film thickness. On the other hand, the mobility increases with annealing temperature for the ZnO films on a-plane and m-plane sapphire, exceeding 110 cm^2/Vs for ZnO on a-plane sapphire. This high mobility compares very favourably with high quality films deposited epitaxially via PLD and MBE [23, 122]. The improvement in mobility is consistent with the improvement in crystal quality and grain size shown in Figs. 3.12

and 3.13. However, for the film deposited on r-plane sapphire no clear trend was observed. In addition to ingrain scattering, mobility is determined by grain size and grain boundary barrier heights. For the film deposited on r-plane sapphire, the grain size of the films decreased slightly upon annealing (Fig. 3.13). The lack of a specific trend may be a result of competing carrier scattering mechanisms in the film. The ZnO film deposited on c-plane sapphire, represented by only one measurement point at 800 °C, showed a significantly lower Hall mobility compared to the film deposited on a-plane sapphire, consistent with the lower structural quality discussed in section 3.3.2.

Origin of carrier concentration

The behaviour of carrier concentration as a function of annealing temperature is known to vary with the initial growth temperature, substrate type, growth method and annealing ambient [118, 120, 123, 124]. In agreement with the results presented here, both *K. Ogata et al.* and *W.C.T. Lee et al.* [118, 120] reported an initial decline in carrier concentration, reaching a point of maximum resistivity, followed by an increase in carrier concentration, after annealing in an oxygen ambient at temperatures from 500 °C - 1000 °C. The reported as-deposited films, which were grown by MBE on sapphire substrates, had comparable carrier concentrations of 10^{18}-10^{19} cm^{-3}. *Otaga et al.* analysed this trend based on the assumption that Zn_i and V_O were the dominant donors. It was suggested that at intermediate annealing temperatures (500 °C - 700 °C) the O_2 atmosphere passivates Zn_i and V_O causing the carrier concentration to decrease, while at higher temperatures the carrier concentration increases as a result of oxygen re-evaporation, generating Zn_i and V_O. However, as already discussed in section 4.1, V_O are rather believed to be deep donors [89, 91]. The assumption of Zn_i being a dominant donor is also being challenged by theoretical predictions and experimental evidence suggesting that hydrogen is the main contributor to native carrier concentration [96, 97, 92, 98]. Other possible contributors are shallow effective-mass-like Group III impurities in particular Al, Ga and In which could be present in the

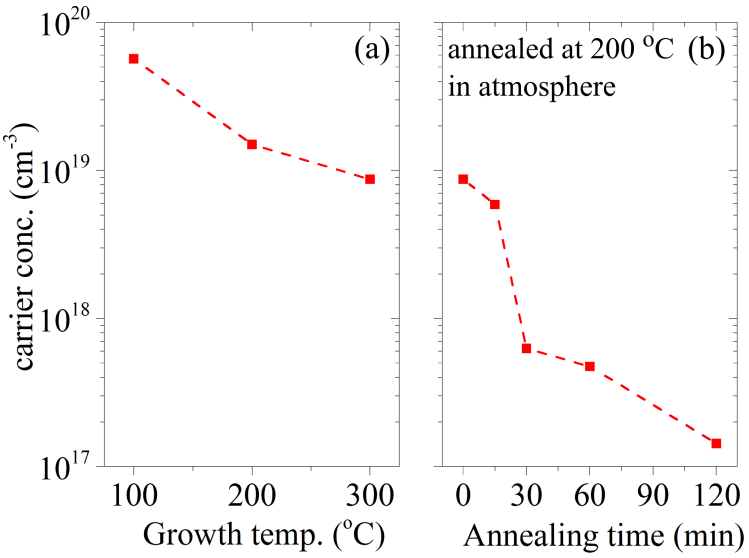

Figure 4.9: (a) Electron concentration as a function of growth temperature for a c-axis oriented FCVA ZnO films deposited on quartz substrates. (b) Evolution of carrier concentration with annealing time of a film deposited at 300 °C and annealed on a hotplate at 200 °C in air. Annealing for 4 hours resulted in completely insulating films.

growth material or the substrate.

As demonstrated by *M.G. Wardle et al.* [125] using first principles calculations, hydrogen in ZnO is already mobile at temperatures as low as 200 K. Experiments on bulk ZnO doped with hydrogen showed that an annealing step of just 150 °C for 30 min decreases the introduced carriers by an order of magnitude [126]. Fig. 4.9(a) shows the carrier concentration of c-axis oriented FCVA ZnO films deposited on quartz substrates. With increasing growth temperature, a decrease in carrier concentration was observed. Films deposited on sapphire showed similar trend. To investigate the thermal stability of the native carriers, samples of the film deposited at 300 °C were annealed at 200 °C in air for 15 - 120 minutes as shown in Fig. 4.9(b). In agreement with the results of *G.A. Shi et al.* [126], the carrier concentration decreased by approximately an order of magnitude after just 30 minutes. Long-term annealing for 4 hours, at a temperature of 200 °C, of FCVA films deposited on quartz and sapphire in air, nitrogen, oxygen or forming gas resulted in the films becoming permanently insulating. Consequently, ambient-surface interactions are unlikely to be responsible. A similar increase in resistivity on annealing at low temperatures has also been observed by *T.*

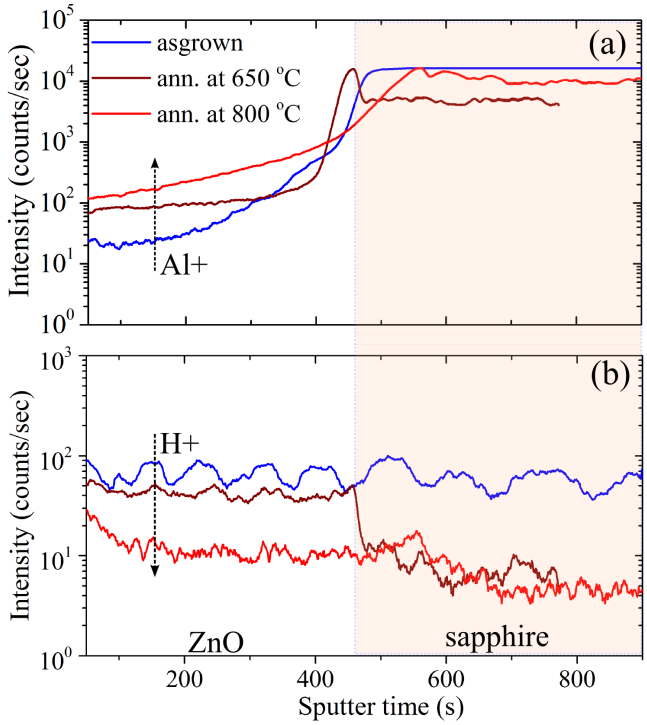

Figure 4.10: ToF-SIMS of a 50 nm thick ZnO film deposited on sapphire at 200 °C. (a) Al diffusion from sapphire substrate and (b) Hydrogen content reduction after annealing at 650 °C and 800 °C in oxygen flow.

Minami et al. [16] for sputtered ZnO films where it was linked to the chemisorption of oxygen. However, in view of recent evidence [125, 126, 92] it is more likely that the low-temperature, thermally unstable carrier concentration is dominated by hydrogen donors.

However, for ZnO films deposited on sapphire substrates the carrier concentration increases again after annealing at temperatures higher than 650 °C, indicating a substrate-related effect. Fig. 4.10 shows time-of-flight secondary ion mass spectroscopy (ToF-SIMS) obtained from a 50 nm thick ZnO film deposited on a sapphire substrate at 200 °C and two other samples of the same film annealed at 650 °C and 800 °C. The results in Fig. 4.10(a) indicate a gradual diffusion of Al from the sapphire (Al_2O_3) into the film after annealing. Al is a well known shallow donor in ZnO and is often used to produce degenerately doped ZnO films for transparent conducting layers [7, 99]. The increase in Al content due to diffusion would explain the increase in n-type carrier concentration in FCVA ZnO films on sapphire substrate after annealing at higher

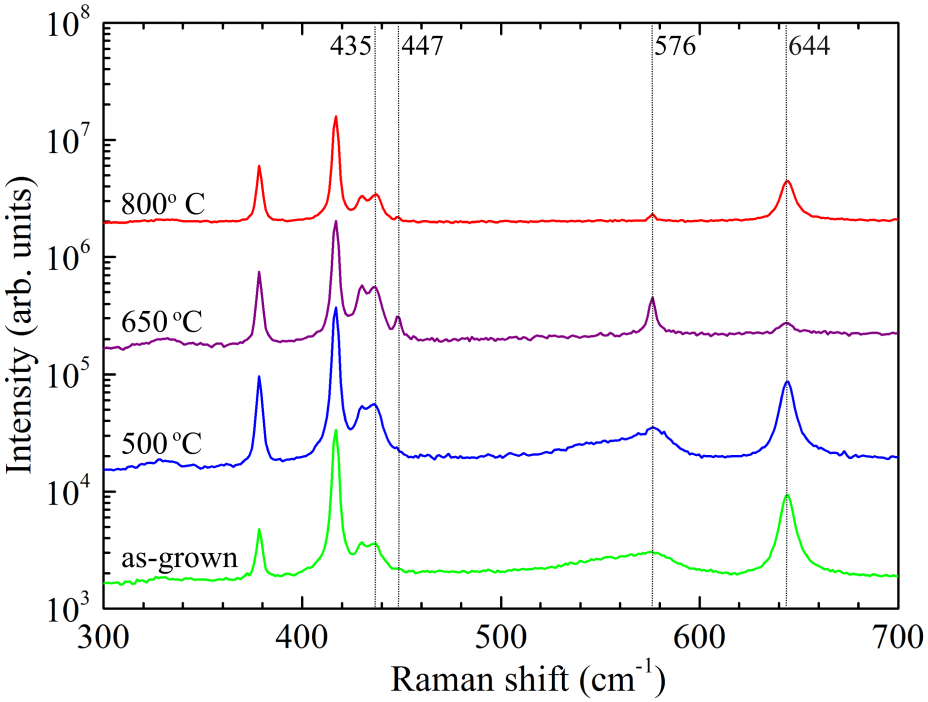

Figure 4.11: Raman spectra of a ZnO film, as-deposited and after annealing at 500 °C, 650 °C and 800 °C. The plots are offset for clarity.

temperatures. Along with the increase in Al, Fig. 4.10(b) shows a concurrent decrease in hydrogen in the sample after annealing at 650 °C and 800 °C which indicates that hydrogen is unlikely to be the source of carrier concentration after annealing at higher temperatures in oxygen.

To gain further insight into the influence of annealing on the defects nature of FCVA ZnO films, Raman spectroscopy was performed on the film deposited at 300 °C on a-plane sapphire. Of special interest here are the phonon mode frequencies at 576 and 644 cm^{-1} shown Fig. 4.11. The phonon mode around 576 cm^{-1} is initially weak and broad in the as-grown film. However, this mode reached a maximum strength after annealing at 650 °C and almost vanished after annealing at 800 °C. The same applies to the mode at 447 cm^{-1}. The asymmetric band centred around 576 cm^{-1} falls within A1(LO) (574-576 cm^{-1}) and quite close to the E1(LO) (581-588 cm^{-1}) longitudinal optical phonon modes [127]. Both modes are commonly associated with local vibration modes of intrinsic defects such as oxygen vacancies and interstitial zinc cations [128, 129, 130, 131]. The weak Raman signal at 576 cm^{-1} observed in the as-

deposited film is consistent with the previous assumption that hydrogen is the dominant donor. Based on first-principles investigations, *C. Van de Wall* [96] suggested that a complex consisting of an oxygen vacancy and a hydrogen atom is feasible and behaves as a shallow donor. Moreover, Raman experiments conducted by *C.F. Windisch et al.* [131] on ZnO powders and thin films showed that this phonon mode (576 cm^{-1}) can be fully suppressed by exposure to hydrogen in gaseous form (7% in N_2 and 2.9% in Ar). Hence, due to the presence of hydrogen in the as-deposited film, the A1(LO) and E1(LO) modes are likely to be suppressed. On annealing, hydrogen would diffuse out of the oxygen vacancies, causing an increase in the phonon modes associated with oxygen deficiencies (576 cm^{-1}) as shown in Fig. 4.11. However, further annealing in oxygen gas at 800 °C would suppress this mode due to the in-diffusion of oxygen as shown elsewhere [128].

On the other hand, the mode centred at 644 cm^{-1} follows an opposite trend. *C. Bundesmann et al.* [132] observed that this mode only appears in films doped with Fe, Sb, Al and Ga while it was not observed in pure ZnO. Consequently, they associated this mode with intrinsic host lattice defects, which either become activated as vibrating complexes or their concentration increases upon dopant incorporation. This reinforces previous assumptions that extrinsic impurities, in particular H and Al, are significant contributors to conduction since this mode is correlated with states of high conduction in the FCVA ZnO film.

Carrier mobility

Due to the polycrystalline nature of the films, the effective carrier mobility in FCVA ZnO is set by an interplay of carrier concentration, grain size and grain boundary defects, as illustrated earlier in Fig. 4.2. Consequently, the change in mobility due to annealing can vary considerably depending on the grain size of the sample. The effect of annealing on the electrical properties and morphology of a 40 nm thick ZnO film, deposited at 200 °C is shown in Fig. 4.12. Despite the increase in grain size shown in Fig.4. 12(b), no improvement was observed in the Hall mobility (Fig. 4.12(c)) of

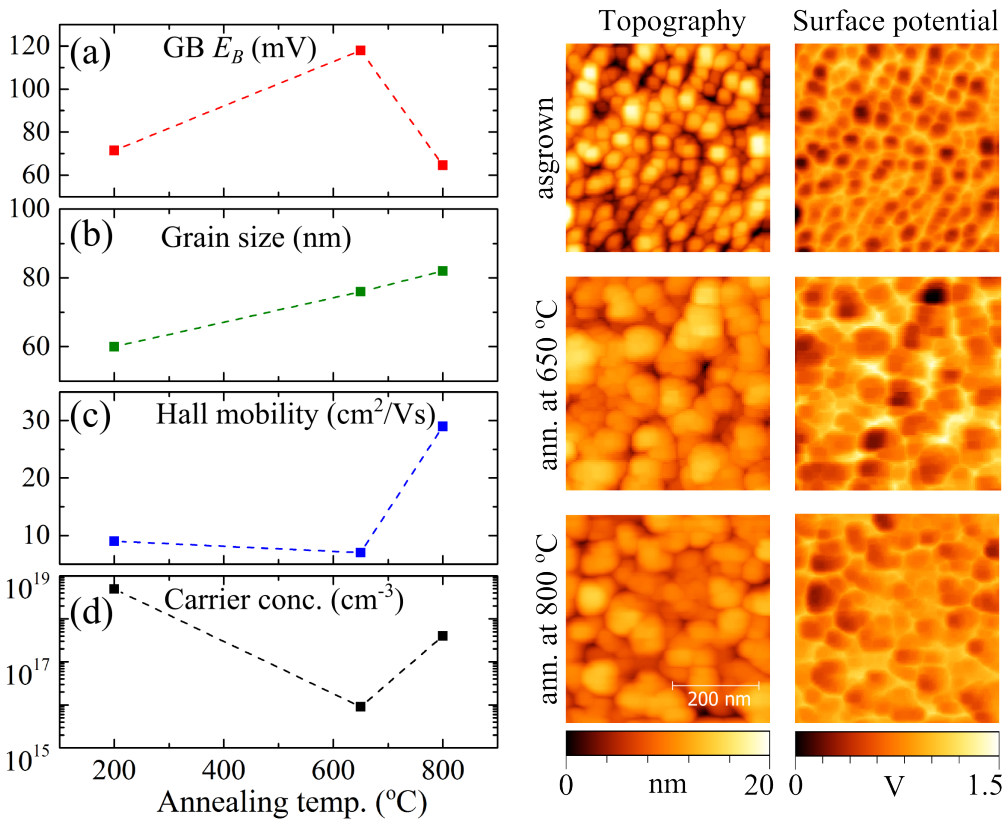

Figure 4.12: Right: AFM and surface potential images of a 40 nm thick ZnO film as-deposited at 200 °C, annealed at 650 °C and at 800 °C. Left: (a) Average grain boundary potential barrier height (E_B), (b) average grain size, (c) Hall mobility, and (d) carrier concentration of the film as a function of annealing.

the film after annealing at 650 °C. This can be attributed to the decrease in carrier concentration which subsequently increases the grain boundary potential barrier height as predicted by the GB model for a partly depleted grains (Fig. 4.2). After annealing at 800 °C, the Hall mobility rises significantly due to the increased carrier concentration resulting from Al diffusion from the sapphire substrate and consequent lowering of the GB barrier heights. In agreement with the GB model, the average GB potential barrier heights measured from KPFM surface potential maps has a maximum (120 mV) for films annealed at 650 °C (Fig. 4.12(a)). This suggests that grain boundary scattering is the dominant factor restricting carrier mobility. Nevertheless, for sufficiently thick films with larger grains as shown in Fig. 4.8, the grain boundary scattering would have less impact on carrier transport due to a significantly lower density of grain boundaries and an increase in mobility can be observed (Fig. 4.8), after annealing at 650 °C.

4.3.2 Photoluminescence of ZnO films

ZnO on a-plane sapphire

Fig. 4.13 shows the 3 K near-band-edge (NBE) PL spectrum corresponding to the 300 nm thick ZnO film deposited on a-plane sapphire shown in Fig. 4.8. The figure shows the PL of the as-deposited film and after annealing at 500 °C, 650 °C and 800 °C in 1 atmosphere O_2. The most prominent emissions have been identified using the line positions published by *Meyer et al.* [87]. With increasing annealing temperature, the I_6 emission, attributed to excitons bound to neutral Al donors, becomes sharper and more pronounced, indicating a significant improvement in the near-surface material quality. The appearance of the I_6 line is consistent with Al diffusion from the substrate. The first-order longitudinal phonon (LO) replica of the free exciton transition F_X*-1LO* and phonon replicas of the I_6 (I_6*-1LO,* I_6*-2LO,* I_6*-3LO*) can also be seen at a spacing (and multiple spacing) of 71-73 meV from their coupled excitons. The observation of the free exciton and its associated LO phonon replicas indicates a significant improvement in film quality since these emission lines can only be observed under the condition of long-range Coulomb coupling.

A broad emission peak around 3.33 meV is clearly visible in the PL spectra of the as-grown film and the films annealed at 500 °C and 650 °C. The broad peak was significantly suppressed and reduced to a smaller narrow peak after annealing at 800 °C. This emission line, commonly referred to as the Y-line has been reported in a number of different ZnO samples, such as bulk ZnO, homoepitaxial films, and heteroepitaxial films [133, 134, 135]. Several different interpretations for the emission centered around 3.333 eV (Y) are discussed in the literature. Most recently, a comprehensive investigation conducted by *Wagner et al.* [136], using a multitude of luminescence techniques and uniaxial pressure measurements, concluded that the Y emission lines are radiative recombinations of excitons bound to extended structural complexes. Monochromatic cathodoluminescence (CL) images presented by *Wagner et al.* showed a direct association between the origin of the Y lines and localized structural defects. The narrowing of the Y emission line upon annealing, observed here in Fig. 4.13, may indicate a re-

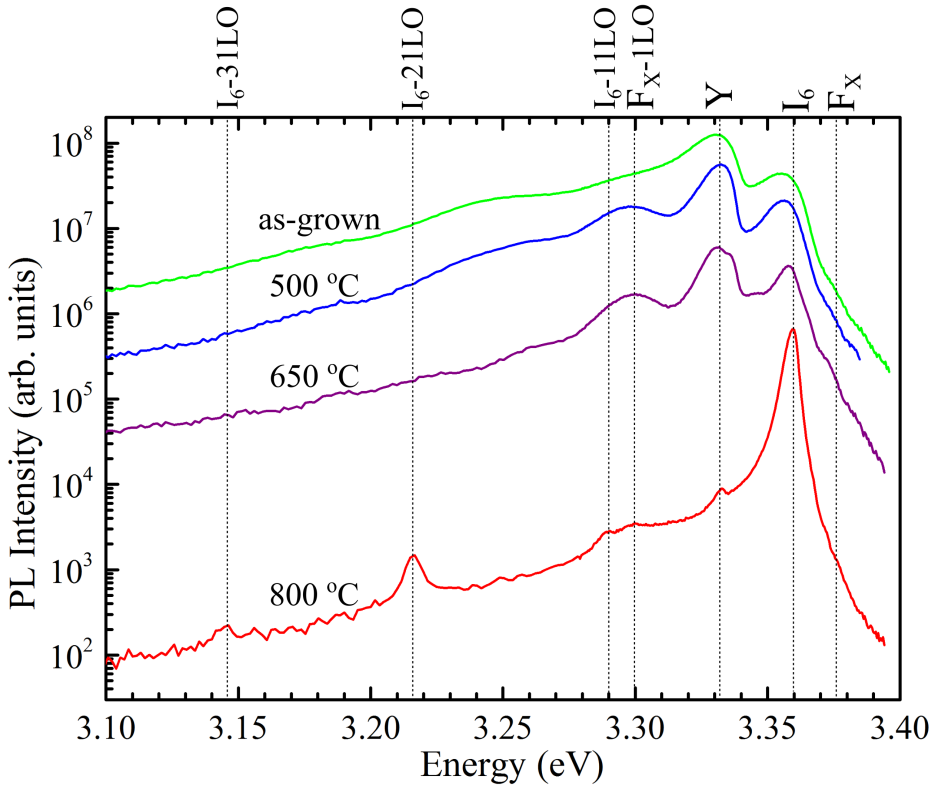

Figure 4.13: PL spectra at 3K of a 300 nm thick ZnO film deposited on a-plane sapphire at 300 °C and annealed at 500 °C, 650 °C and 800 °C in 1 atmosphere O_2 (for 1 hour). The plots as offset for clarity.

duction of structural defect density, in line with the improvement in crystal quality reported in Chapter 3.

The defect-band (DB) 3K PL emission of the same ZnO sample is shown in Fig. 4.14, as-grown and after annealing in oxygen gas for 1 hour. The deep level emission of the as-deposited film is very broad, with no detectable features. After annealing at 800 °C, a structured DB emission centered around 2.4 eV (green defect band) with a number of longitudinal optical (LO) phonon replicas spaced 71-73 meV apart, becomes visible. Moreover, the ratio of the NBE to DB PL intensity increased to $\approx 10^4$, again indicating an improvement in near-surface material quality. Green luminescence, which is frequently observed in ZnO crystals and thin films, is commonly attributed either to transitions involving native defects or Cu impurities [8, 10, 138]. *Y. Heo et al.* [139] observed a strong correlation between Zn partial pressure and the green luminescence from MBE grown ZnO films, and suggested that the green emission was related to

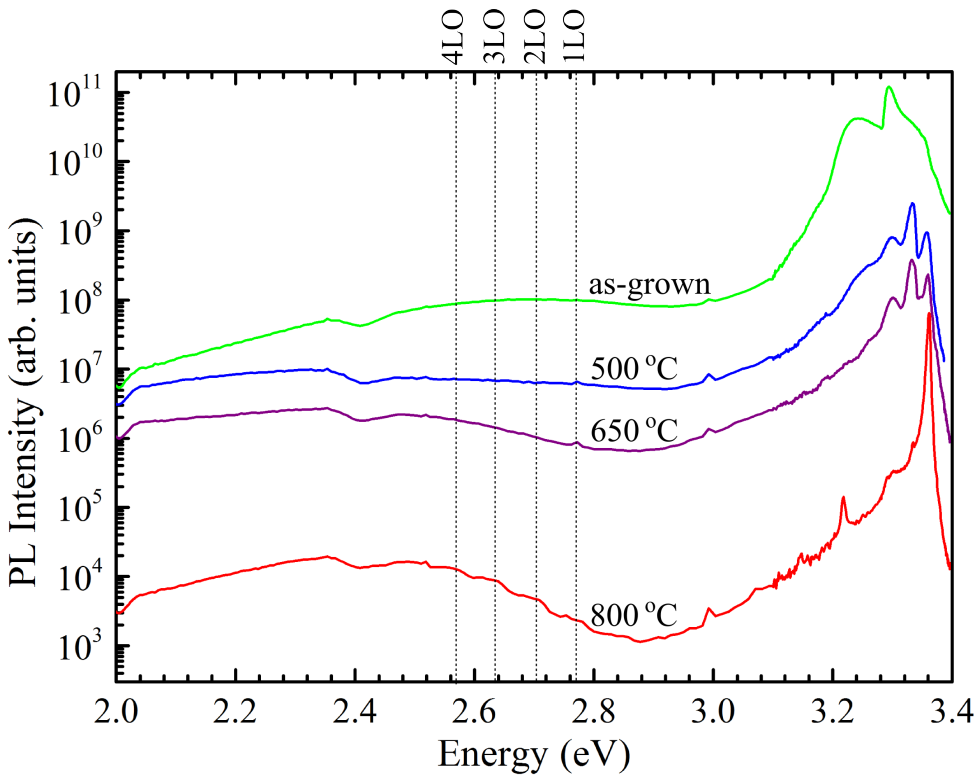

Figure 4.14: PL spectra at 3K of a 300 nm thick ZnO film deposited on a-plane sapphire and annealed at 500 °C, 650 °C and 800 °C. The plots are offset for clarity. The dip just above 2.4 eV is due to the grating used for the measurement.

donor-deep acceptor (DAP) transitions. First principles calculations conducted by *A. Janotti et al.* [10] showed that a shallow donor to Zn vacancy (V_{Zn}) acceptor level is likely to give rise to a transition around 2.5 eV. Generation of V_{Zn} at high annealing temperatures is likely possible due to Zn re-evaporation. On the other hand, there exists strong evidence associating the well structured green emission around 2.45 eV in bulk and annealed ZnO films with deep Cu acceptors. The Cu-related band is usually attributed to transitions of photogenerated holes trapped at the excited state of Cu_{Zn} located at $\sim$ 0.4 V above the valence band to the ground state of this centre located at 0.2 eV below the conduction band [8, 141]. This transition gives rise to a zero-phonon line (ZPL) at 2.859 eV and a well structured multi-phonon side band due to the strong electron-phonon coupling [142], as can be seen more clearly in Fig. 15. Although Cu atoms are believed to be adsorbed from the annealing environment [141], the concentration of Cu impurities in the FCVA ZnO films was below the detection

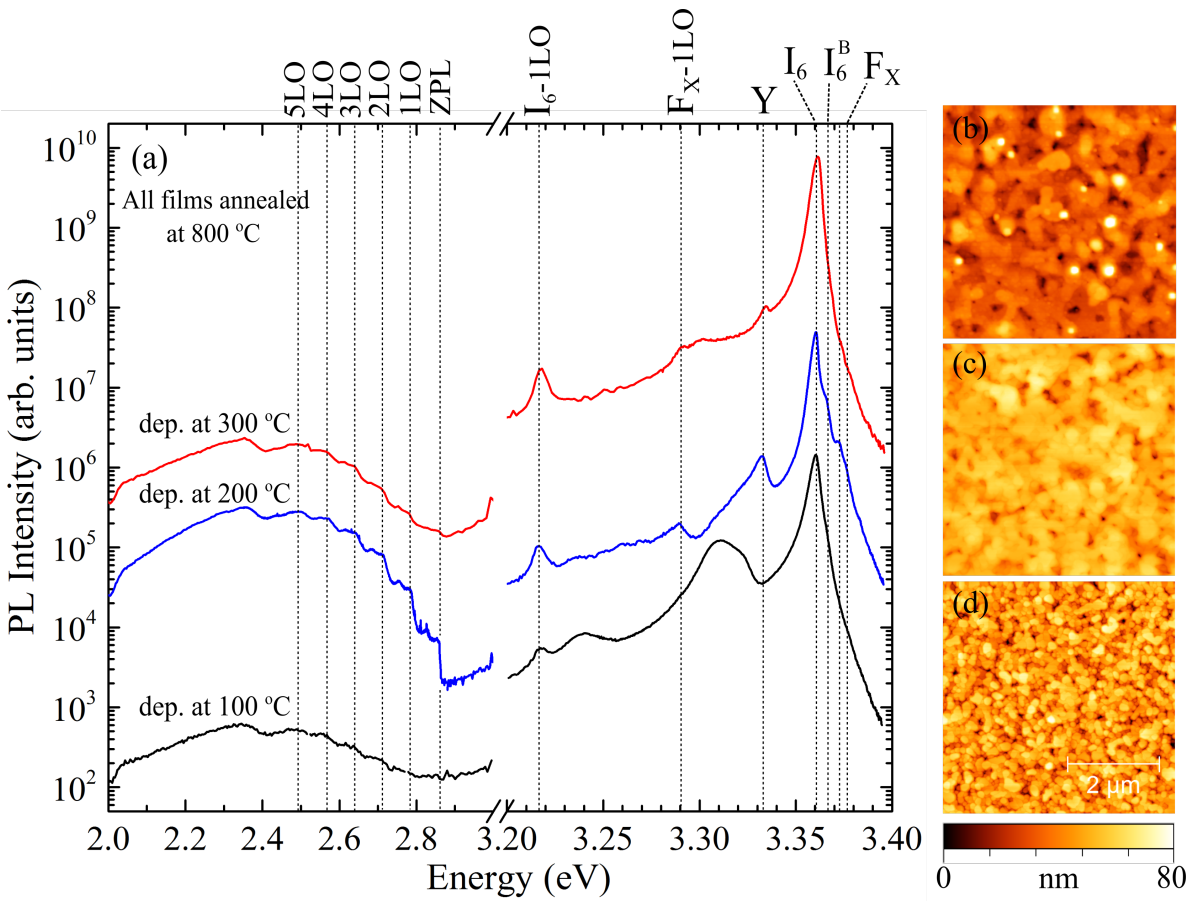

Figure 4.15: (a) PL spectra at 3K of three 300 nm thick ZnO films deposited on a-plane sapphire at 100 °C, 200 °C and 300 °C and then subsequently annealed at 800 °C in oxygen gas. (b) AFM image of the film deposited at 300 °C and annealed at 800 °C. (c) AFM image of the film deposited at 200 °C and annealed at 800 °C. (d) AFM image of the film deposited at 100 °C and annealed at 800 °C. The plots are offset for clarity. The dip at $\sim$ 2.4 eV is an artifact caused by the grating used for the PL measurements.

limit of SIMS, and so transitions from shallow donors to deep V_{Zn} defects are perhaps likely to be involved as well.

Fig. 4.15(a) shows the effect of growth temperature (100 °C, 200 °C and 300 °C) on the photoluminescence properties of ZnO films after annealing at 800 °C in oxygen gas for 1 hour. All as-deposited films showed a similar polycrystalline morphology (see Fig. 3.6(b)). However, after annealing at 800 °C the crystal structure of these films evolved differently as shown in Figs. 4.15(b), (c) and (d). Interestingly, the film deposited at 200 °C shows the most structured NBE and DB photoluminescence spectra along with a well coalesced surface morphology (Fig. 4.15 (c)). In comparison, the film

initially deposited at 300 °C, although coalesced, shows signs of surface decomposition (voids) and its PL spectrum is slightly less well structured. In contrast, the film deposited at the lowest temperature (100 °C) preserved its granular morphology and was only slightly coalesced with the least structured PL. This is consistent with the findings in chapter 3 where it was shown that the films deposited at 200 °C have the highest crystal quality (Fig. 3.11). Achieving the highest crystal quality at a temperature of 200 °C is rather unique and indicates that the growth mechanisms involved in FCVA are distinctly different from other epitaxial growth techniques such as PLD and MBE where high substrate temperatures are required for optimum crystal quality [81, 143]. In agreement with the results presented here, *X. Xu et al.* [144] observed that c-plane ZnO films deposited by FCVA at 230 °C on silicon substrate produced the best PL, which was attributed to reduced oxygen vacancies inferred from Raman spectroscopy. On the other hand, *A. Anders et al.* [55] reported substantial decrease in FCVA ZnO growth rates at temperatures of 300 °C or higher due to the re-evaporation of the arriving Zn ions, leading potentially to Zn deficient films. In this thesis, a notable decrease in growth rate was also observed after increasing the substrate temperature from 200 °C to 300 °C.

The PL spectra shown in Fig. 4.15 also raise some interesting questions regarding the relationship between structural quality and photoluminescence. From the film deposited at 100 °C, no Y emission line that has been associated with structural defects was observed. Instead, its PL spectrum shows a broad emission band from 3.30 to 3.33 eV that is usually associated with two-electron-satellites (TES). *Wagner et al.* observed an anti-correlation between the green luminescence and the Y emission lines in bulk ZnO and speculated (in the absence of copper) that Y lines constitute an alternative recombination channel for mobile native defects such as Zn vacancies [136]. No such anti-correlation was observed here. Both types of emission are more pronounced in the film deposited at 200 °C (see Fig. 4.14(c)), which had the best surface morphology in terms of grain size and coalescence.

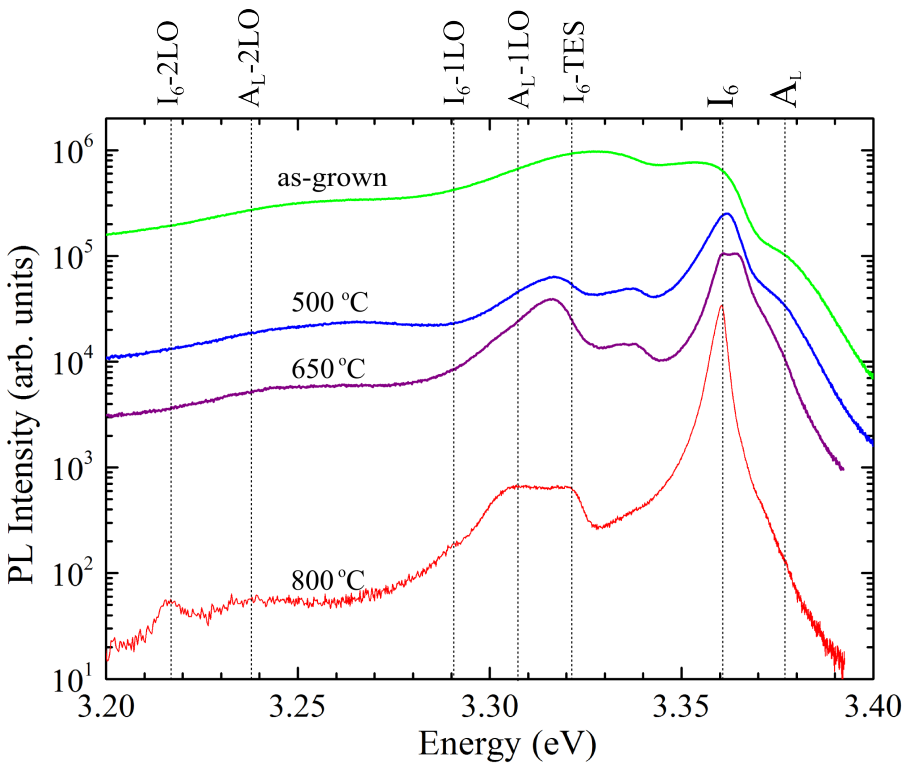

Figure 4.16: PL spectra at 3K of a 300 nm thick ZnO film deposited on r-plane sapphire at 300 °C and annealed at 500 °C, 650 °C and 800 °C in O_2 gas. The plots are offset for clarity.

PL of A-plane and m-plane FCVA ZnO

Fig. 4.16 shows the low temperature (3 K) NBE PL spectra from a 300 nm a-plane ZnO film deposited on r-plane sapphire at 300 °C and subsequently annealed at 500 °C, 650 °C and 800 °C in oxygen gas. The PL spectrum from the as-grown film is very broad and does not show any specific features. As expected, the PL spectra significantly improve upon annealing. After annealing at 800 °C, the NBE PL spectrum becomes well structured with a dominant peak at approximately 3.3608 eV (I_6). Its phonon replicas (I_6-*1LO* and I_6-*2LO*) can also be identified. The emission at 3.377 eV is usually attributed to the longitudinal free A-exciton state (A_L). The PL of the a-plane film showed a broad emission band from 3.30 - 3.325 eV. *J.M. Chauveau et al.* [145] investigated similar ZnO films grown by MBE and showed that this emission band persists even when using an excitation wavelength lower than the NBE excitonic emission. Accordingly, it was assumed that emissions involving structural defects are

partly responsible for this feature. This was further confirmed using transmission electron microscopy (TEM) which showed considerable presence of basal stacking faults [145]. Other investigations using temperature dependent PL, spatially resolved CL and TEM assigned emissions in the same band to free electron-acceptor transitions (eA^0) related to basal plane stacking faults (BSF) [147]. However, the A_L first order LO phonon replica (A_L-*1LO*) and the two-electron-satellite (*I6 TES*) also fall in the same spectral region, which may explain the large width of the band. Despite being mostly deposited by MBE and PLD, PL studies on non-polar a-plane ZnO thin films are relatively limited, and mostly show low to moderate PL quality [66, 148, 149, 150]. The relatively high quality of the PL presented in Fig. 4.16 suggests that achieving high quality non-polar ZnO films for optoelectronic applications using FCVA is possible. However, defect related emissions are more prominent in the PL spectra from m-plane FCVA ZnO films deposited on m-plane sapphire. As shown in Fig. 4.17, the PL from the m-plane ZnO is fairly weak and broad with no distinctive features. An emission band, appearing as a composite of two broad peaks at 3.315 eV (BSF related eA^0) and 3.3 eV (Y-line), is the most pronounced feature in the very broad spectrum.

Stacking faults occur when a single plane of atoms within the crystalline lattice is misoriented or out of order. Basal stacking faults (BSF) seem to be always present in the microstructure of non-polar hetero-epitaxially deposited wurtzite films such as ZnO and GaN, regardless of growth method and conditions [145, 151, 152, 153, 154]. BSF defects are traditionally attributed to lattice mismatch relaxation, growth errors or the condensation of vacancies [155]. Growth errors occur when the adatoms are deposited in a wrong position due to insufficient surface diffusion. However, since the ZnO films deposited on a-plane, r-plane and m-plane sapphire were deposited simultaneously, these mechanisms are unlikely to be predominant. *P. Vennégues et al.* [154] conducted a thorough investigation into the origin of basal stacking faults in nonpolar ZnO and GaN films grown epitaxially on sapphire substrates. Based on theoretical considerations and using high resolution transmission electron microscopy (HRTEM) it was concluded that BSF's arise at the early stage of growth to compensate translations

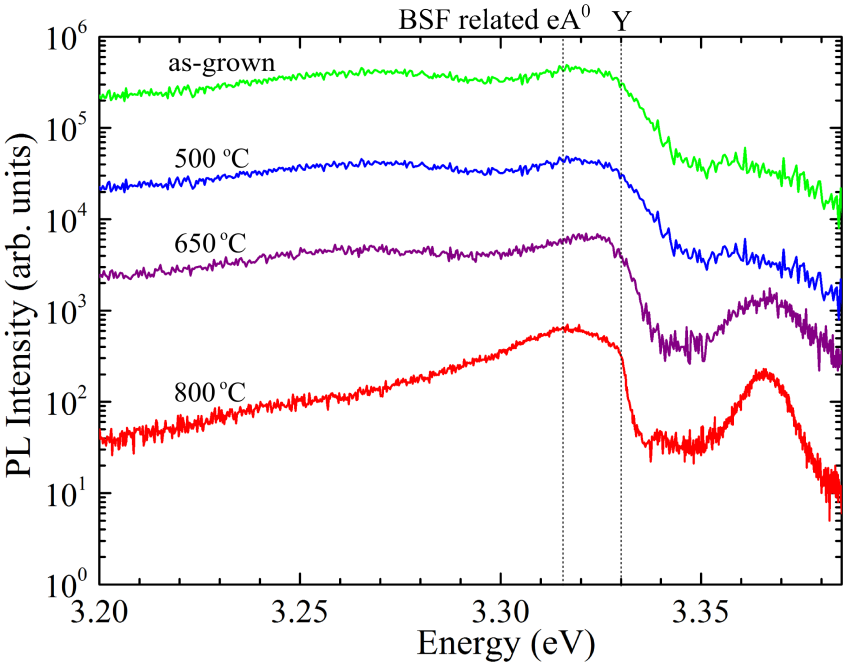

Figure 4.17: PL spectra at 3K of a 300 nm thick ZnO film deposited on m-plane sapphire at 300 °C and annealed at 500 °C, 650 °C and 800 °C in O_2 gas. The plots are offset for clarity.

of lattice planes during the coalescence of neighbouring 3D nuclei [154]. However, for polar orientations, the compensation of lattice plane translations occur more favourably with perfect dislocations. Consequently, the BSF defect density is expected to be significantly higher in nonpolar films. Overall, the formation of BSF's seem to be intrinsic to heteroepitaxial growth of wurtzite materials along nonpolar orientations on highly dissimilar substrates. However, since the density of BSF's depends on the density of nuclei at the start of growth, reducing these defects should be feasible by optimizing growth conditions [154].

4.3.3 Optical transmittance

Optical transmittance spectra of 45 nm thick ZnO films deposited on a-plane, c-plane, r-plane and m-plane sapphire are compared in Fig. 4.18, in the wavelength range of 200 - 800 nm. All films exhibited a transmittance higher than 85% within the visible region, with a sharp fundamental absorption edge at around 380 nm. In general, the transmittance increased with growth temperature. Typically, the bandgap (E_g) of a

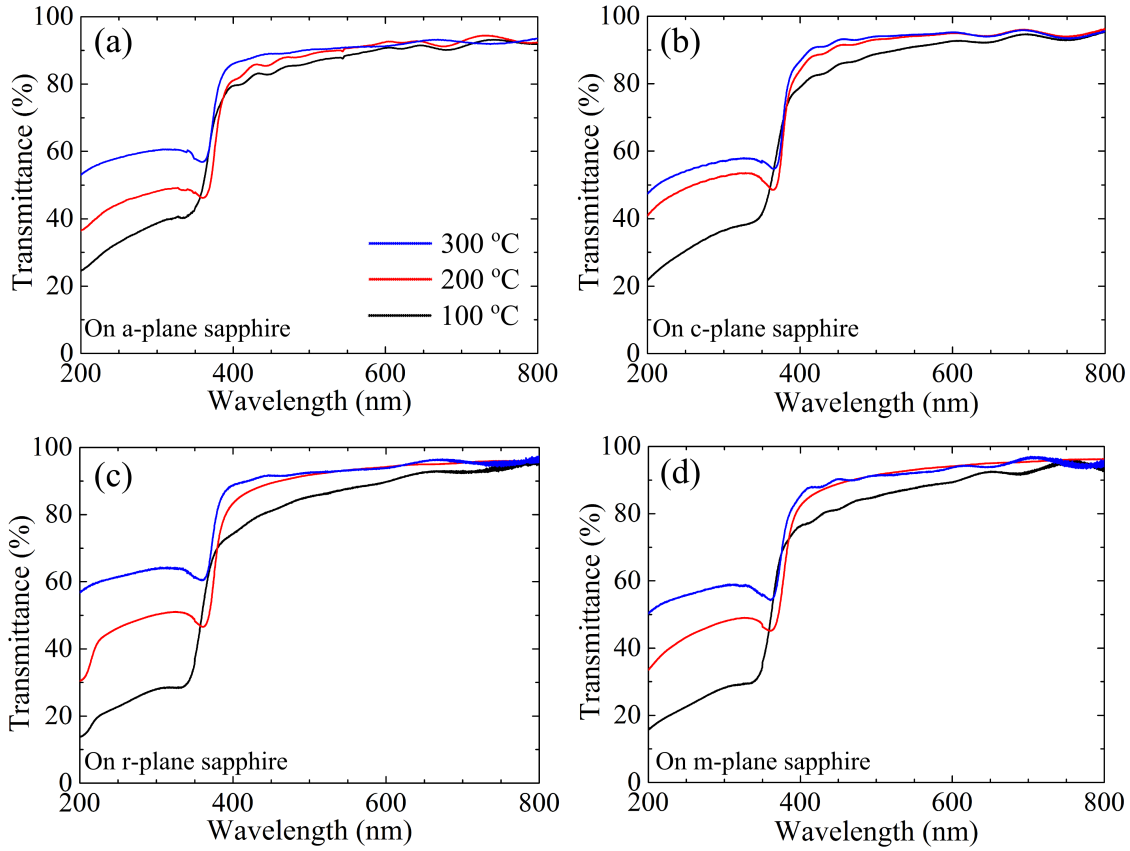

Figure 4.18: Optical transmittance of 45 nm thick FCVA ZnO films deposited on (a) a-plane, (b) c-plane, (c) r-plane and (d) m-plane sapphire at 100 °C, 200 °C and 300 °C. Due to the low thickness of the films, the UV spectrum range is not completely absorbed.

direct gap semiconductor is determined from the measured optical absorption spectra by making a linear extrapolation of the square of the absorption coefficient (or this value multiplied by the square of the photon energy) to the energy axis [156]:

$$(\alpha h\nu)^2 = A(h\nu - E_G), \tag{4.16}$$

where h is Planck's constant, ν is the frequency, and A is a constant. The absorption coefficient α is derived from the transmittance (T) using

$$\alpha = \frac{1}{d} ln \left(\frac{1}{T} \right), \tag{4.17}$$

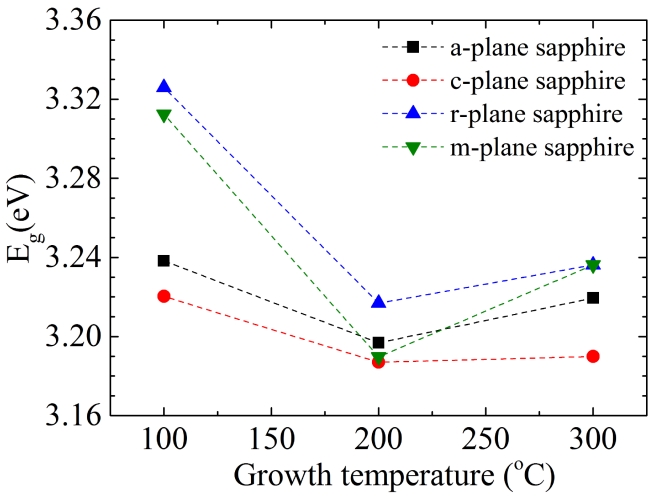

Figure 4.19: The optical band gap of 45 nm thick ZnO films as a function of growth temperature and substrate type.

where d is the thickness of the film. The values of the resulting optical bandgaps are given in Fig. 4.19. The bandgap values are within the range reported for ZnO films and single crystals [157, 8]. The position of the band-edge is generally sensitive to various factors, such as: (1) the microstructure of the film, (2) stress induced elastic deformations, (3) crystal orientation, (4) carrier concentration and (5) native defects and impurities [80, 79, 157, 158]. Interestingly, the ZnO films deposited at 200 °C have the narrowest bandgap and were found to generally have the sharpest absorption edges, regardless of substrate type. Structural related factors are unlikely to be responsible for this effect, since the evolution of structural properties with temperature was found to vary with the substrate type, as shown in Fig. 3.11 (section 3.3.1). Carrier concentration effects can be also excluded, since the carrier concentration decreases monotonically with temperature (Fig. 4.9). The bandgap of FCVA deposited ZnO films at room temperature has been reported to be very sensitive to oxygen pressure, narrowing with increasing oxygen content [159]. Hence, it is suggested that the bandgap narrowing observed here occurs due to stoichiometric changes, since the degree of oxygen incorporation and Zn re-evaporation [55] is likely to be strongly temperature dependent.

4.4 Summary

The electrical and optical properties of polar and nonpolar ZnO films deposited by FCVA on different sapphire substrates were studied. Electrical Hall effect measurements, Kelvin probe force microscopy, low temperature (4 K) photoluminescence and Raman spectroscopy were combined to investigate the intrinsic and extrinsic defects that determine the overall electronic and optical quality of the films. The key findings were:

- As-deposited ZnO films exhibit a carrier concentration in the range 10^{17}-10^{19} cm^{-3}. The carrier concentration decreases with growth temperature and with annealing up to 650 °C in the case of films deposited on sapphire. Long-term low temperature annealing at 200 °C yielded significant loss in carrier concentration, leading eventually to insulating films. The instability of the carrier concentration at this low temperature is consistent with reports suggesting hydrogen as a dominant donor in as-grown films. This suggestion was further supported in this thesis by observing the behaviour of phonon modes at 574 cm^{-1} and 644 cm^{-1} in the Raman spectra of the as-deposited and annealed films. After annealing at 800 °C in O_2, a significant increase in carrier concentration was observed due to Al diffusion from the sapphire substrates, as confirmed by ToF-SIMS and PL measurements.

- Surface potential imaging using Kelvin probe force microscopy and electrical Hall measurements showed that the carrier mobility in the polycrystalline FCVA ZnO films was predominantly limited by the grain boundary potential barriers. Achieving a high mobility required films with a high carrier concentration and sufficiently large grains. For example, in 300 nm thick ZnO films on a-plane sapphire, with an average grain size more than 100 nm and carrier concentration of $\sim 10^{18}$, a carrier mobility as high as 110 cm^2/Vs was achieved. This compares favourably with carrier mobilities achieved using epitaxial growth techniques such as MBE and PLD.

- Low temperature PL spectroscopy indicated a significant improvement in the electronic structure of the films after annealing in O_2. ZnO films deposited on a-plane sapphire at 200 °C and 300 °C and annealed at 800 °C showed well structured photoluminescence with pronounced Al donor-bound exciton (I_6), free exciton (F_X) and multiple phonon replica emission. A-plane ZnO films deposited on r-plane sapphire, also showed well structured luminescence after annealing at 800 °C, but also exhibited a wide emission band at 3.300 -3.325 eV, commonly associated with structural defects such as basal stacking faults. The PL spectra of as-deposited and annealed m-plane ZnO films showed only broad features, indicating a rather low structural quality. Generally, the quality of the measured PL spectra was related to the density of structural defects induced by lattice mismatch, in agreement with XRD data presented in chapter 3 (Fig. 3.13).

- Optically, all ZnO films deposited at 200 °C and 300 °C on sapphire showed a transmittance over 85%, with sharp absorption edges. The measured optical bandgaps ranged from 3.19 - 3.32 eV, within the range of typical values for ZnO thin films and bulk crystals. All ZnO films regardless of substrate type exhibited the narrowest bandgap and sharpest absorption edge at an intermediate growth temperature of 200 °C, suggesting a dependence on film stoichiometry rather than on structural quality and carrier concentration.

Chapter 5

MESFET devices: Theory and fabrication

Despite the lack of stable p-type ZnO, unintentionally and deliberately n-doped ZnO films can be used to fabricate a range of unipolar electronic devices such as Schottky diodes, UV photodetectors, metal-semiconductor field effect transistors (MESFET) and metal-insulator-semiconductor field effect transistors (MISFET). For the past decade, a considerable proportion of ZnO related research has focused on the development of transparent thin film transistors (TFTs), based mainly on MISFET structures [160]. Following recent advances in the fabrication of high quality Schottky contacts on ZnO, MESFET devices have been increasingly investigated [26]. The realization of ZnO devices, mainly MESFETs on cathodic arc grown ZnO thin films, will be the focus of this chapter. The first part is devoted to the physical principles of MESFETs, following which the fabrication and electrical characterisation of devices fabricated on FCVA ZnO are presented and then discussed.

5.1 ZnO thin film transistors: State of the art

Thin film transistors based on MISFET and MESFET structures can be traced back to the work of *Lilienfield* in the 1930s [161]. However, their fabrication and development was only effectively considered three decades later during the emergence of large area

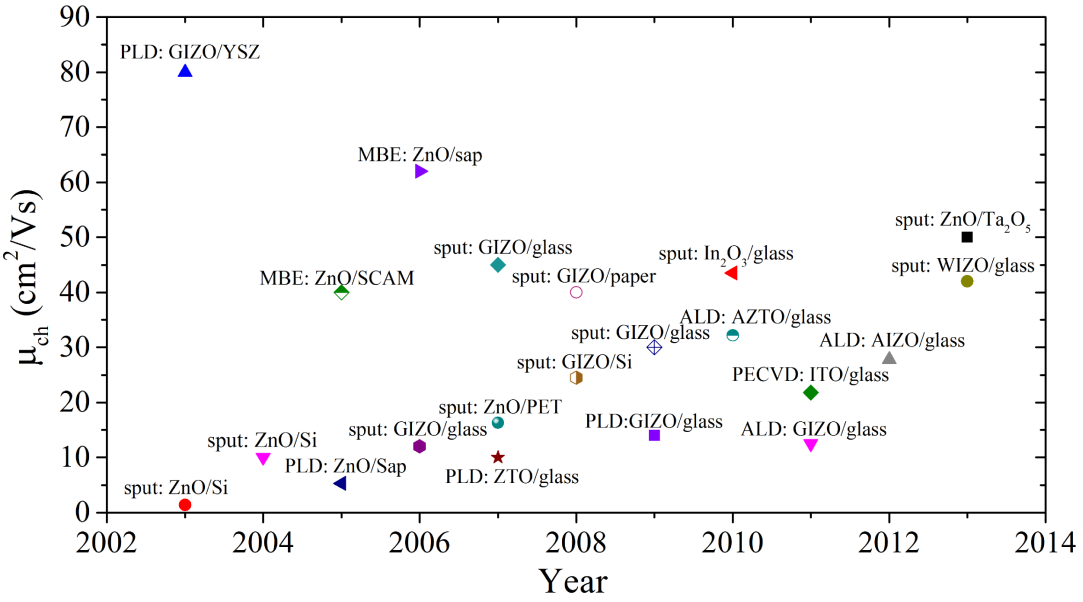

Figure 5.1: Channel mobilities of some of the best published results of ZnO and amorphous metal oxide based MISFET TFTs. Deposition methods (Sput: sputtering, PLD: pulsed laser deposition, MBE: molecular beam epitaxy, ALD: atomic layer deposition, PECVD: plasma enhanced chemical vapour deposition). Channel materials (ZnO: zinc oxide, GIZO: gallium indium zinc oxide, ZTO: zinc tin oxide, AZTO: aluminium zinc tin oxide, ITO: indium tin oxide, AIZO: aluminium indium zinc oxide, WIZO: tungsten indium zinc oxide). Substrates (Si: silicon, sap: sapphire, YSZ: Yttria-stabilized zirconia, SCAM: ScAlMgO4, PET: Polyethylene terephthalate).

electronics. One of the first applications of thin film transistors was demonstrated by *P.K. Weimer et al.* [162] using integrated cadmium sulfide (CdS) based TFTs as a scan generator in a solid state imaging panel. With the emergence of flat panel displays, *T.P. Brody* demonstrated a 6×6 inch liquid crystal display using cadmium selenide (CdSe) TFTs as the switching elements to drive the display pixels [163]. Cadmium is a highly toxic element that was soon replaced by the cheap and scalable amorphous silicon (a-Si) technology in the early 1980s [4]. To date, active matrix displays still rely mainly on a-Si TFTs. Although these devices have been in existence for more than 30 years, their channel mobilities rarely exceed 1 cm^2/Vs due to the inherent physical limits of a-Si [164].

In order to overcome the physical limits of a-Si, the focus has gradually moved towards TFTs based on metal-oxide semiconductors such as polycrystalline ZnO and amorphous metal oxides such as InGaZnO (IGZO) and ZnSnO (ZTO) [19, 166, 167,

169]. These materials offer a higher carrier mobility (> 30 cm^2/Vs), improved optical transparency and lower sensitivity to visible light [181, 182]. Nevertheless, the MISFET architecture traditionally implemented in TFTs suffers from inherent drawbacks caused by a high density of traps at the gate insulator-semiconductor interface. These traps are partly responsible for channel mobility degradation, bias and light instability [183, 184, 185]. Therefore the growth of a high quality gate insulator with very low interface defect states has been the most critical process step, which is usually achieved using sophisticated growth methods such as ALD, PLD or PECVD. The requirement for a high on-current and, consequently, a low operating voltage requires a gate insulator with a high capacitance per unit area. To achieve this, either a decrease in insulator thickness and/or an insulator material with a high dielectric constant is desired. However, thickness reduction is limited by leakage current considerations. As a result of these design constraints and the physics of MISFETs, it has been very challenging to produce TFTs with low operating voltages, which is essential for mobile applications and for integration with silicon CMOS technology. *H. Frenzel et al.* [160] noted in a recent review that only 10% of published transparent TFTs operate at a gate voltage lower than 5 V. Very recently, *C. Brox-Nilsen et al.* [186] reported the fabrication of sputtered ZnO TFTs with a channel mobility of over 50 cm^2/Vs and operating voltage of 4 V. This exceptional result was achieved on a Si substrate using a high-k Ta_2O_5 gate insulator in a back-gate configuration.

Fig. 5.1 shows an overview of some of the best TFTs based on ZnO and other metal oxides, published in the literature over the last decade. A more comprehensive chronological list, including the main performance metrics of a featured number of TFTs is shown in Table 5.1. This shows, in recent years, an increasing focus on amorphous metal oxides. This was mainly driven by the difficulties in realizing new high performance ZnO TFTs using economically scalable deposition techniques. Amorphous oxide semiconductors are readily deposited with scalable methods, at lower temperatures on low cost substrates. However, the amorphous state is more defect-rich, and consequently sensitive to light and prone to bias stress instabilities [183]. For an overview

Table 5.1: A chronological list of featured publications representing the advancements in TFT technology, including the corresponding figures of merit of each device. [*: on Si, ⋄: indium zinc oxide, ‡: HFET, §: aluminum indium zinc oxide, ⋆: tungsten oxide, $: MESFET., ⊗ aluminum zinc tin oxide.]

Year/Ref.	**method**	**channel**	$\mathbf{I}_{on}/\mathbf{I}_{off}$	$\Delta\mathbf{V}_{GS}$ (V)	$\Delta\mathbf{V}_{DS}$ (V)	μ_{ch} (cm^2/V)	***SS*** (mV/dec)
1964/[162]	evaporation	CdS	-	2	5	50-100	-
1973/[163]	evaporation	CdSe	-	-	20	20	-
1980/[4]	sputtering	a-Si	10^7	30	30	0.4	-
2002/[165]	PLD	ZnO*	10^5	10	5	0.03	-
2003/[19]	sputtering	ZnO*	10^6	50	20	1.2	3000
2003/[166]	spin coating	ZnO	10^7	40	40	0.2	-
2004/[167]	PLD	a-IGZO	10^2	5	10	10	-
2004/[168]	sputtering	ZnO*	10^6	75	30	10	-
2005/[169]	sputtering	ZTO	10^7	35	40	50	-
2006/[170]	MBE	ZnO	10^3	5	5	62	-
2006/[171]	PLD	ZTO	10^5	8	5	11	-
2007/[172]	sputtering	IZO⋄	10^6	20	20	108	800
2008/[43]$	PLD	ZnO	10^8	2.5	2	11	120
2009/[173]$	sputtering	a-IGZO	10^8	1	1	28	110
2009/[174]	sputtering	a-IGZO	10^8	10	10	30	190
2010/[175]	PLD	a-IGZO	10^7	10	10	5	150
2010/[176]	sputtering	In_2O_3	10^8	5	12	43	280
2010/[177]	sputtering	AZTO⊗	10^8	10	10	32	450
2011/[32]‡	MBE	ZnO	-	6 6	165	23	
2012/[178]	sputtering	AIZO§	10^9	20	20	28	510
2013/[186]	sputtering	ZnO	10^5	4	4	100	330
2013/[179]	sputtering	IGZO	10^7	15	10 1.2	13	330
2013/[180]	sputtering	WIZO⋆	10^6	1.2	1.2	43	108

of the 'state of the art' of polycrystalline metal-oxide and amorphous compound oxide TFTs, some excellent reviews are referenced here [181, 182, 160]. In general, meeting the requirements of scalable low temperature deposition, low material cost (e.g. low or zero indium content), and high switching performance is still a challenge.

Charge trapping problems associated with insulator-semiconductor interfaces can be avoided using a MESFET structure instead of a conventional MISFET TFT. Consequently, higher channel mobility and improved bias stability can be potentially achieved by using MESFETs. This is made possible by the presence of the depletion layer that acts to isolate the channel from the gate interface. Furthermore, the operating volt-

age range can be drastically reduced by adjusting the film thickness. The first proof of concept device was demonstrated by *Frenzel et al.* [43] using ZnO films grown by PLD (on a-plane sapphire) and reactively sputtered Ag Schottky contacts as the gate material. The resulting MESFETs had a mobility of 11.3 cm^2/Vs, a current on-to-off ratio of about 10^8 and operated using a gate voltage range of less than 3 V. Subsequent publications by the same group showed that the stability of these devices under bias and illumination stress compared favourably with ZnO MISFETs [26, 160].

5.2 Thin film MESFETs

MESFETs were first demonstrated by *C. A. Mead* in 1965 under the name "Schottky Barrier Gate Field-Effect-Transistor" [210]. Since then, MESFETs based on GaAs epitaxial layers have found widespread use in high speed electronics due to the high electron mobility of GaAs [107]. As well as avoiding reliability and stability problems related to oxide-semiconductor interfaces, a high quality metal Schottky gate requires only low temperature processing. However, compared to MISFETs, the MESFET has a less robust gate contact as a result of the lower breakdown voltage of the Schottky junction. The following sections describe the working principle and *I-V* relationships of Schottky contacts and MESFETs, as relevant to the devices fabricated in this thesis.

5.2.1 The Schottky contact

The switching operation of a MESFET transistor is made possible by forming a rectifying metal-semiconductor contact on the semiconductor material, in the form of a channel. The conductance of the channel is then controlled by depleting its charge carriers via a reverse bias voltage applied to the Schottky contact. Rectification as a phenomena was first reported in 1874 by *F. Braun* [188] who investigated the electric conductivity through metal-sulphide contacts. The theoretical foundations for describing the current transport through rectifying metal-semiconductor contacts was initially developed by *W. Schottky* and *N.F. Mott* [189, 190].

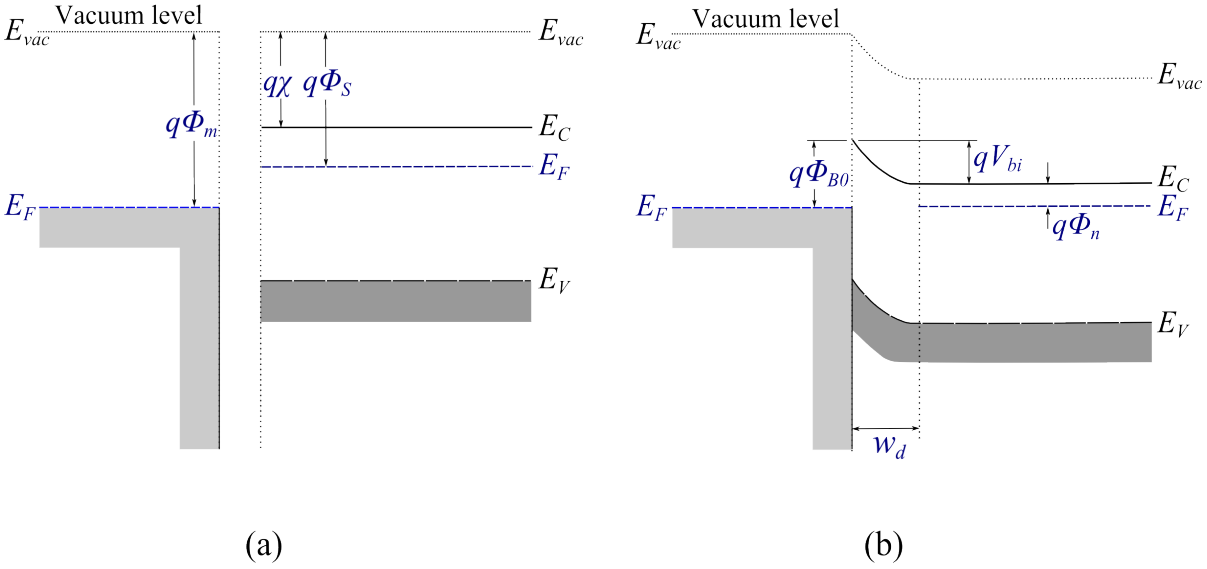

Figure 5.2: (a) Energy diagram of a metal and an n-type semiconductor before contact formation; (b) ideal energy band diagram of a metal-n-semiconductor contact for $\phi_m > \phi_S$. Due to the resulting band bending, a potential barrier ϕ_{B0} is formed at the interface.

Band diagram

The ideal energy-band diagram for a metal and n-type semiconductor prior to contact formation is shown in Fig. 5.2. The vacuum level is used as a reference. The parameter ϕ_m is the metal work function (in eV), ϕ_S is the semiconductor work function, χ is known as the electron affinity, and $\phi_n = E_C$ - E_F is the energy difference between the conduction band edge E_C and the Fermi level E_C. According to the Schottky-Mott model, a Schottky contact is obtained when $\phi_m > \chi + \phi_n$. Before contact formation (Fig. 5.2(a)), the Fermi level in the semiconductor is higher than that in the metal. As shown in Fig. 5.2(b), when both materials are brought into ideal contact, and neglecting any surface states, electrons from the semiconductor will move to the lower energy states in the metal. Consequently, a temporary current flows until the Fermi level becomes constant through out the entire system. Positively charged donor atoms remain in the semiconductor, creating a space charge region in the vicinity of the metal-semiconductor interface. Due to the resulting band bending, a potential barrier ϕ_{B0} is formed at the interface. This barrier is known as the Schottky barrier and is

given, ideally, by [107]

$$\phi_{B0} = \phi_m - \chi. \tag{5.1}$$

This implies that the potential barrier is basically independent of doping or any applied external voltages. However, on the semiconductor side, the potential barrier is referred to as the built-in potential V_{bi} which is given by

$$V_{bi} = \phi_{B0} - \phi_n. \tag{5.2}$$

Note that V_{bi} is slightly dependent on the semiconductor doping through ϕ_n. The rectifying barrier can be adjusted by either reinforcing or reducing the built-in potential barrier V_{bi} by applying a bias voltage to the metal-semiconductor junction. If a negative voltage is applied to the Schottky contact (with respect to the semiconductor), the semiconductor-to-metal barrier height increases, while ϕ_{B0} remains constant in this idealized case. This bias condition is referred to as reverse bias. In contrast, when a positive voltage is applied to the Schottky contact, V_{bi} is reduced while ϕ_{B0} remains essentially constant. In this forward bias situation, electrons can flow more easily from the semiconductor into the metal.

Table 5.2: Work function ϕ_m and Schottky barrier height ϕ_{B0} for various pure metals commonly used as Schottky contacts on ZnO. An electron affinity of $\chi = 4.2$ eV is assumed for ZnO.

Metal	$q\phi_m$	$q\phi_{B0}$
Ag	4.26	0.06 eV
Ir	5.27	1.07 eV
Ru	4.71	0.51 eV
Pt	5.65	1.45 eV
Au	5.10	0.90 eV

The first report on Schottky contacts on ZnO was published by *C. A. Mead* in 1965 [191]. More recently, significant progress was achieved by *M. W. Allen et al.* in fabricating high quality Schottky contacts based on oxidized Ag, Ir, Pt and Pd

contacts [192, 193, 195]. The devices fabricated within this work build primarily on the oxidized noble metal Schottky contact technology developed by *M. W. Allen et al.*. Table 5.2 lists the work functions and the theoretically calculated Schottky barrier heights of various metals on ZnO reported in the literature. The electron affinity values for ZnO in the literature vary from 4.1 - 4.4 eV [200, 201]. In Table 5.2, an average value of 4.2 eV was assumed. However, in practice simple expressions for the barrier heights as given by Eq. 5.1 are never realized experimentally, with ϕ_{B0} being rather independent of nominal ϕ_m values. The deviation of experimental barrier heights from the ideal case is mainly attributed to the unavoidable interface layer and the presence of interface states and defects [196]. Furthermore, the effective barrier height of all Schottky junctions is slightly reduced due to the 'image force lowering' effect. This is caused by the small attractive force, exerted on an electron approaching the barrier, by the positive 'image' charge in the metal [197]. The effective barrier heights in this work are extracted from current-voltage (I-V) measurements based on relationships derived in the next section.

Current-voltage (I-V) relationship

The current transport across a rectifying contact with an n-type semiconductor is determined by the flow of electrons over the potential barrier, which can be described by the thermionic emission theory developed by Bethe [198, 107]. Thermionic-emission theory is based on the assumption that (1) $q\phi_{B0} \gg kT$ (k is Boltzmann constant), (2) thermal equilibrium is established in the system, and (3) thermal equilibrium is not affected by the process of current flow across the junction. The current density from the semiconductor to the metal J_F is given by the concentration of electrons with energies sufficient to overcome the potential barrier towards the metal:

$$J_F = \int_{E_F+q\phi_n}^{\infty} q\upsilon_x dn, \tag{5.3}$$

where $E_F + q\phi_n$ is the minimum energy required for thermionic emission into the metal, and υ_x is the carrier velocity in the direction of transport and n is the electron

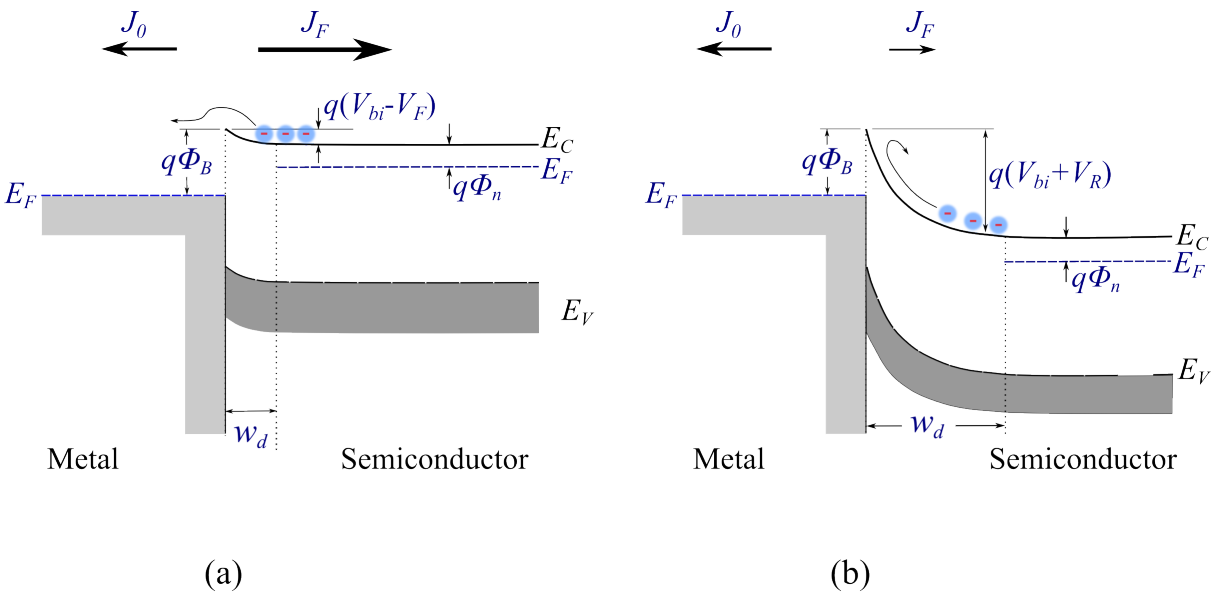

Figure 5.3: (a) Energy band diagram of a Schottky metal to a n-type semiconductor (a) under forward bias and (b) under reverse bias conditions. Ideally, the reverse current J_0 is independent of bias conditions.

density. Assuming that the Maxwell-Boltzmann approximation applies for the carrier population in the semiconductor and that all the electron energy above E_C *and* consists of kinetic energy (*1/2* m^* υ^2 = E - E_C, where m^* is the effective mass of the electron and υ the electron velocity), the current flow from the metal to the semiconductor can be expressed as [107]

$$J_F = A^* T^2 exp\left(-\frac{q\phi_B}{kT}\right) exp\left(\frac{qV_F}{kT}\right), \tag{5.4}$$

where V_F is the forward bias voltage (positive) applied to the Schottky contact and A* is the effective Richardson constant for thermionic emission

$$A^* = \frac{4\pi q m^* k^2}{h^3}. \tag{5.5}$$

The barrier height for electrons moving from the metal into the semiconductor remains constant under bias. Thus, the reverse current is also constant and equal to the current flowing from the semiconductor under thermal equilibrium and zero bias, which can be

derived from Eq. 5.4 for $V_F = 0$

$$J_0 = A^* T^2 exp\left(-\frac{q\phi_B}{kT}\right). \tag{5.6}$$

Consequently, the total current density across a Schottky contact is given by the sum of the forward and reverse currents

$$J = J_F - J_0 = J_0\left[exp\left(\frac{qV_F}{kT}\right) - 1\right]. \tag{5.7}$$

For an applied forward voltage $V_F \gg kT/q$, the second term in Eq. 5.7 can be neglected and the current density is exponentially proportional to V_F. When the Schottky contact is reverse biased (Fig. 5.3(b)), the potential barrier increases to (qϕ_B + V_R). As a result, $J_F \ll J_0$ and the net current density is equal to the saturation current density J_0 which is independent of V_F. Eq. 5.7 represents the ideal case of thermionic emission over a homogeneous and defect free Schottky barrier, without considering image force lowering and the effect of interface states. To account for these non-ideal behaviours, an ideality factor term η is introduced in Eq. 5.7 giving,

$$J = J_0\left[exp\left(\frac{qV_F}{\eta kT}\right) - 1\right]. \tag{5.8}$$

If the voltage dependence of the barrier height is only due to image force lowering, the ideality factor should be close to unity. However, due mainly to other nonidealities such as the spatial inhomogeneity of the barrier, real values of η are usually higher [199].

Depletion region

The key to realizing a field effect transistor is the ability to modulate the carrier density in a semiconductor channel. In MESFETs, this is accomplished by a Schottky contact which is used to deplete the channel by applying a reverse bias voltage. The width of the depleted region under the Schottky contact can be derived by solving Poisson's equation (dE/dx=ρ(x)/ϵ_0 ϵ_S) and applying appropriate boundary conditions which

yields [107],

$$w_d = \sqrt{\frac{2\epsilon_0\epsilon_S(V_{bi} + V_R)}{qN_D}}, \tag{5.9}$$

where the space charge volume density, ρ(x), is assumed to be constant and equal to the doping concentration N_D. ϵ_0 and ϵ_S are the vacuum and semiconductor permittivities respectively, and V_R is the magnitude of the applied reverse-bias voltage.

5.2.2 Metal-semiconductor ohmic contacts

Current flow across a metal-semiconductor contact occurs via several carrier transport mechanisms [201]: (1) thermionic emission (TE) of carriers over the top of the barrier; (2) field emission (FE) of carriers tunnelling through the entire barrier; (3) thermionic field emission (TFE), i.e., carriers tunnel through just the top of the barrier. Formation of non-rectifying ohmic contacts to ZnO can be achieved by reducing the barrier height to increase thermionic emission according to Eq. 5.4 and/or increasing the ZnO surface doping density such that the barrier width becomes thin enough for carriers to tunnel through via field emission. The characteristic electrical property for quantifying ohmic contacts is the contact resistivity, which is defined by

$$\rho_C = \lim_{A_C \to 0} R_C A_C, \tag{5.10}$$

where R_C is the total contact resistance and A_C is the contact area. Depending on the dominant conduction mechanism, the contact resistivity can be proportional to the following factors:

$$\rho_C \propto exp\left(\frac{\phi_B}{kT}\right) \quad for \quad TE, \tag{5.11}$$

$$\rho_C \propto exp\left(\frac{\phi_B}{E_{00}}\right) \quad for \quad FE, \tag{5.12}$$

$$\rho_C \propto exp\left[\frac{\phi_B}{E_{00}coth(E_{00}/kT)}\right] \quad for \quad TFE, \tag{5.13}$$

where ϕ_B is the barrier height and E_{00} is the tunnelling energy parameter defined by

$$E_{00} = \frac{qh}{4\pi}\sqrt{\frac{N}{m^*\epsilon_0\epsilon_S}}, \tag{5.14}$$

where N is the doping concentration of the semiconductor and m^* is the effective electron mass. E_{00} is proportional to $\sqrt{N}/T$, and consequently ohmic conduction by FE emission is only dominant at low temperatures or very high doping concentrations. In order to form an ohmic contact to n-type ZnO, the work function of the contact metal should be less than that of the electron affinity of ZnO ($\sim$ 4.2-4.35 eV). Therefore, Ti (4.33 eV) and Al (4.28 eV) have commonly been used for ohmic contacts to n-ZnO [201, 202, 203, 204].

In this work, all opaque ohmic contacts were made of non-alloyed, electron beam evaporated Ti with either a Au or Pt capping layer to prevent contact oxidation. If Ti is brought into intimate contact with ZnO, a very small barrier height ϕ_B of -0.02 eV ($\phi_B = \phi_{Ti}$ - χ_{Zn}) is expected. Moreover, Ti is reactive towards ZnO and has a higher affinity for oxygen than Zn. Ti therefore reacts with oxygen in ZnO to form an interfacial layer [202] . As a result, oxygen atoms move into the Ti metal, creating oxygen vacancies at the ZnO surface. Since oxygen vacancies act as donors in ZnO, this reaction increases the n-type carrier concentration of the ZnO subsurface layer, and consequently further reduces the barrier width [201]. Temperature-dependent measurements conducted by *H. S. Yang et al.* and *C-L. Tsai et al.* [205, 206] on Ti/Au ohmic contacts, made on bulk ZnO with similar carrier concentration ($\sim 10^{17}$ cm^{-3}) as in this work, concluded that the dominant current conduction mechanism is field emission. For the realization of transparent devices in this thesis, nonalloyed RF sputtered indium tin oxide (ITO) was routinely used to form ohmic contacts to ZnO. ITO is highly transparent, highly conductive and is known to make good ohmic contacts to n-type [207]. However, little is known about the dominant conduction mechanism across ITO/n-ZnO contacts.

5.2.3 MESFET device structure and operation

The MESFET has three metal-semiconductor contacts, a Schottky contact for the gate electrode (G) and two ohmic contacts for the source (S) and drain (D) electrodes, as shown in Fig. 5.4(a). The basic device parameters include L, the gate length, W, the gate width (perpendicular to the page), and t the thickness of the semiconductor film (channel). In most MESFETs, regardless of semiconductor type, the channel is made of n-type material, since electrons usually have a significantly higher mobility than holes.

Source and drain contacts, essentially identical, are differentiated only by the applied voltage bias. The source is grounded (electron source), and the gate and drain voltages are measured with respect to the source. In order to prevent excessive leakage current across the gate, the Schottky-gate voltage is varied in a range lower than the contact's built-in voltage (V_{bi}), while the drain contact is usually zero or forward biased; that is, $V_{GS} \leq V_{bi}$ and $V_{DS} \geq 0$. Under the bias conditions $V_{GS} = 0$ and $V_{DS} = 0$, no current flows between any of the electrodes. By increasing V_{DS} and at a sufficiently low V_{GS} (channel not fully depleted), a drain-source current (I_{DS}) flows due to the electric field between drain and source. For low V_{DS}, the channel resistance is constant and I_{DS} is linearly dependent on V_{DS}. With increasing V_{DS}, the increasing potential difference between the drain and gate electrodes leads to an expansion of the depletion region at the drain side of the channel. At a certain voltage, known as the pinch-off voltage (V_P), the depletion region extends to the substrate and the channel is said to be pinched off (Fig. 5.6(b)). As V_{DS} is increased further, the depletion region expands further and the pinch-off point moves toward the source. However, the potential at the pinch-off point remains the same, and so is the electron flow from the source to that point. Therefore, for $V_{DS} > V_P$, the current remains essentially constant and independent of V_{DS}. The width of the depletion region under the Schottky gate can be extended in accordance with Eq. 5.9. With decreasing V_{GS} and constant V_{DS}, the channel resistance increases due to the reduced channel cross-section. This causes the channel to pinch off at smaller V_{DS} values. A further decrease of V_{GS} extends the

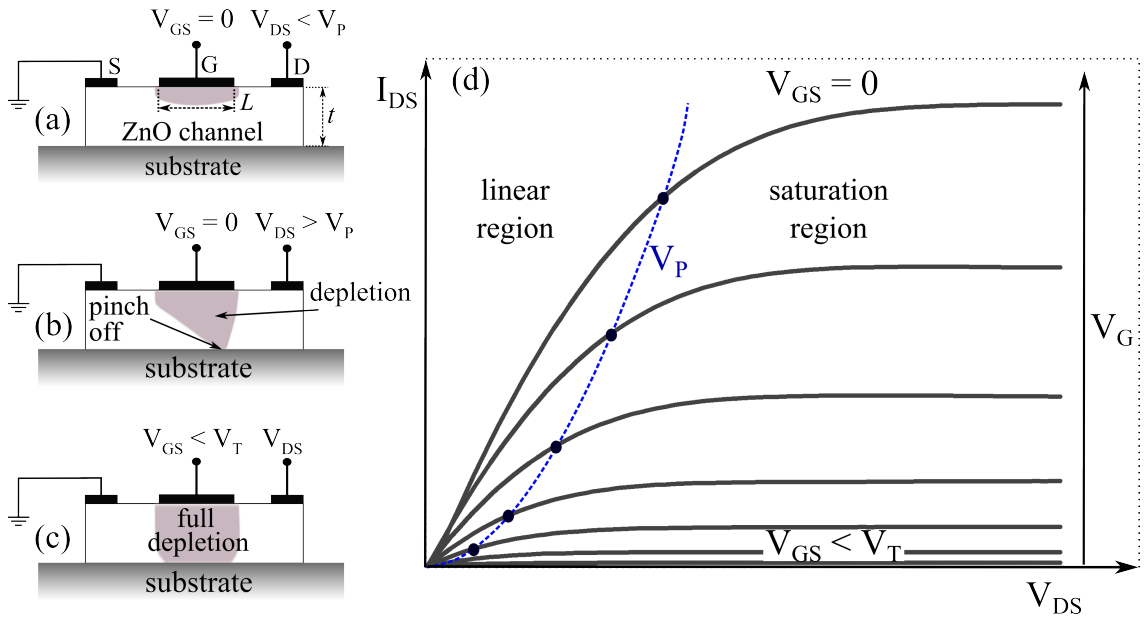

Figure 5.4: Schematics illustrating the operating principle of a MESFET. (a) MESFET in linear region. (b) MESFET in saturation region. (c) MESFET in off-state. (d) Typical output characteristics of a MESFET.

depletion region to the substrate and the channel becomes insulating such that I_{DS}=0, regardless of the applied V_{DS} (Fig. 5.4(c)). The gate voltage at which the channel is completely depleted is usually referred to as the threshold voltage V_T.

Current-voltage characteristics

The *I-V* characteristics of MESFETs are derived using the following assumptions: (1) uniform channel doping, (2) the vertical electric field is much higher than the lateral electric field in the channel $E_y \gg E_x$ (gradual channel approximation), (3) an abrupt depletion layer, (4) constant carrier mobility and (5) negligible gate current [107]. Given these assumptions, the drift current density along the channel is given by,

$$J(x) = Qv(x) = -qN_D\mu E_X = qN_D\mu\frac{\partial V}{\partial x}. \tag{5.15}$$

Considering that the effective cross-section area of the channel is $A = W\ (t - w_d)$, where w_d is the depletion layer width given by Eq. 5.9, the channel current is then

$$I_{DS}(x) = J(x)A = qN_D\mu\frac{dV}{dx}(t - w_d(x))W. \tag{5.16}$$

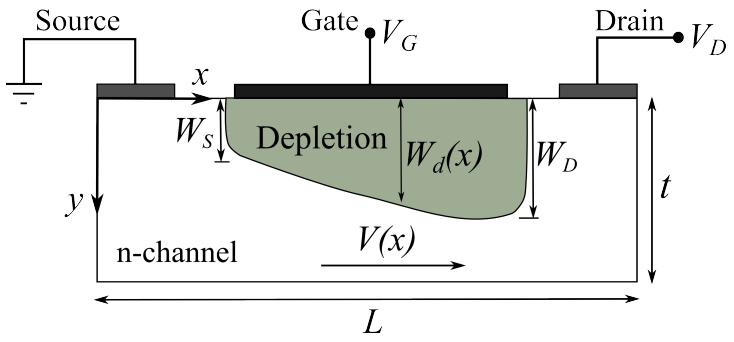

Figure 5.5: An illustration of the derivation MESFET I-V characteristics.

Since I_{DS} is constant along the channel (assuming negligible gate current)

$$\int_0^L I_{DS}(x)dx = LI_{DS} = qN_D\mu W \int_0^L \frac{dV}{dx}(t - w_d(x))dx. \tag{5.17}$$

By substituting V_R with $V_G + V(x)$ in Eq. 5.9, where V_G is the gate potential and $V(x)$ the channel potential, I_{DS} can be expressed as,

$$I_{DS} = \frac{qN_D\mu W}{L} \int_0^{V_{DS}} \left(t - \sqrt{\frac{2\epsilon_0\epsilon_S}{qN_D}(V_{bi} - V_G + V)} \right) dV, \tag{5.18a}$$

$$= g_i \left(V_{DS} - \frac{2}{3\sqrt{V_P}} \left[(V_{bi} + V_{DS} - V_G)^{3/2} - (V_{bi} - V_G)^{3/2} \right] \right), \tag{5.18b}$$

where

$$g_i = \frac{q\mu N_D t W}{L}, \tag{5.19}$$

is the full channel conductance (maximum $\partial I_{DS}/\partial V_{DS}$) achieved for a completely open channel ($w_d = 0$) and

$$V_P = \frac{qN_D t^2}{2\epsilon_0\epsilon_S}, \tag{5.20}$$

is the pinch-off voltage when $w_d = t$. Eq. 5.18(b) is only valid for the linear region, that is when the depletion region width is smaller than the film thickness $w_d < t$ which corresponds to drain-source voltages of $V_{DS} \leq V_G$ - V_T, where $V_T = V_{bi}$ - V_P is the threshold voltage of the MESFET. For very low drain voltages, $V_{DS} \ll V_{GS}$ and V_{DS}

$\ll V_{bi}$, Eq. 5.18(b) can be reduced to

$$I_{DS} = g_i \left(1 - \sqrt{\frac{(V_{bi} - V_{GS})}{V_P}}\right) V_{DS}, \tag{5.21}$$

where linear behaviour is observed. Using a Taylor's expansion around $V_G = V_T$, the previous equation can be further simplified to

$$I_{DS} \approx \frac{g_i}{2V_P}(V_{GS} - V_T)V_{DS}. \tag{5.22}$$

With increasing drain bias, the current saturates and becomes dependent only on V_{GS}. This condition is reached when the drain-source voltage $V_{DS} = V_{DS,sat} = V_P$ - V_{bi}. Accordingly, the current in the saturation region can be found by substituting $V_{DS,sat}$ in Eq. 5.18(b):

$$I_{DS,sat} = g_i \left[\frac{V_P}{3} - (V_{bi} - V_G)\left(1 - \frac{2}{3}\sqrt{\frac{V_{bi} - V_G}{V_P}}\right)\right], \tag{5.23}$$

from which the transconductance $dI_{D,sat}/dV_G$ is derived as

$$g_m = g_i \left[1 - \sqrt{\frac{V_{bi} - V_G}{V_P}}\right]. \tag{5.24}$$

In a similar fashion, a simplified expression can be derived for $I_{DS,sat}$ using a Taylor's expansion around $V_G = V_T$:

$$I_{DS,sat} \approx \frac{g_i}{4V_P}(V_G - V_T)^2 \tag{5.25}$$

and

$$g_m = \frac{dI_{DS,sat}}{dV_G} \approx \frac{g_i}{2V_P}(V_G - V_T) \tag{5.26}$$

where g_m is the transconductance of the MESFET.

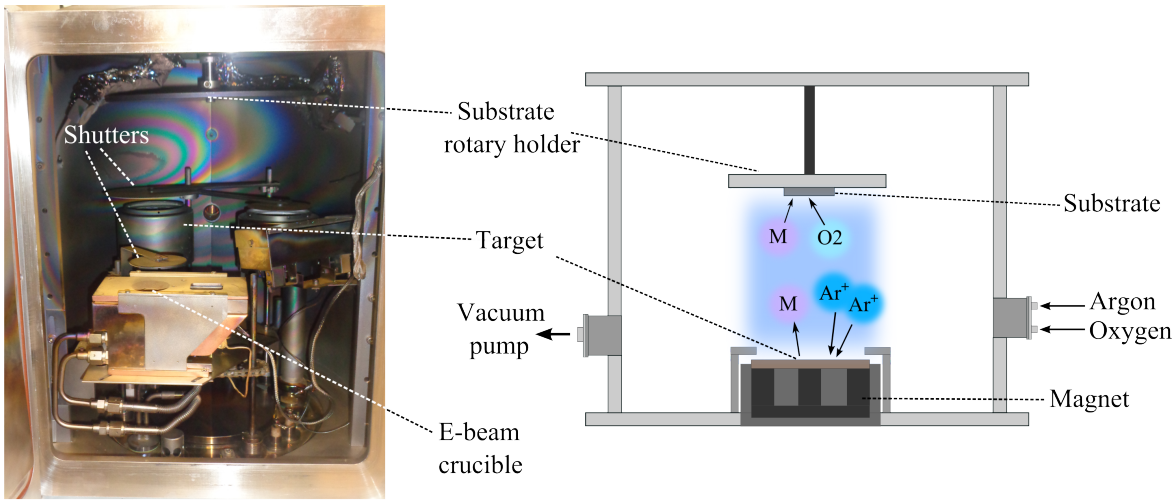

Figure 5.6: (a) A photograph of the deposition chamber of the combined electron beam evaporation and sputtering system. (b) Schematic setup of the sputter chamber and principle of non-reactive and reactive sputtering. M: Sputtered metal atoms, Ar^+: Argon ions, O_2: Oxygen atoms.

5.3 MESFET fabrication

5.3.1 RF magnetron sputtering

Sputtering is one of the primary deposition techniques in microelectronic fabrication, that has been used routinely in this thesis to deposit both Schottky and ohmic contacts. A photograph of the deposition chamber and a schematic of the system used in this work, a BOC Edwards Auto 500, are shown in Fig. 5.6(a) and (b), respectively. For sputtering, a plasma chamber is arranged such that high energy ions strike a target containing the material to be deposited. A high radio frequency voltage is applied between the cathode (target) and anode (substrate), where the plasma is formed by means of impact ionization between the two electrodes. The positively charged plasma gas ions are accelerated by an electric field towards the target where they eject atoms from the target material. To intercept as many of these ejected atoms as possible, the target and anode substrate are closely spaced, usually less than 10 cm. An inert gas, Ar in this work, is used to generate the plasma. To ensure a mean free path of the order of hundreds of micrometers for the ions, the gas pressure in the chamber is held

Table 5.3: Standard deposition parameters of reactively sputtered Schottky contacts and transparent ITO capping used in this thesis. Before RF sputtering or E-beam evaporation, the chamber is pumped down to a base pressure of 1×10^{-5} mbar.

Parameter	**AgOx**	**IrOx**	**RuOx**	**ITO**
Power (W)	50 W	50 W	50 W	175 W
Target	Ag	Ir	Ru	ITO
sputter time (min)	15	15	15	45
Ar/O_2 flux (sccm)	10/1.5	10/3.1	10/3.1	10/-
process pressure (mbar)	3.4×10^{-3}	3.6×10^{-3}	3.6×10^{-3}	3.2×10^{-3}

at a level less than 0.1 millibar [211].

All functional Schottky contact layers in this thesis were reactively sputtered using the Ar/O_2 flux ratios as given in Table 5.3. The oxygen partially oxidises the sputter-target material such that metal as well as metal oxide particles are deposited on the substrate. Oxidized metal contacts were found to have a higher work function and consequently increased Schottky barrier heights [193, 194]. Furthermore, the negatively charged oxygen ions bombard the substrate's surface during the initial phase of the deposition process. Thus, an in-situ plasma surface cleaning is achieved, which probably leads to the removal of a hydroxide-induced, highly conductive surface layer that reduces the Schottky barrier height.

After sputtering, the Schottky contacts were capped with either RF sputtered ITO layers, or electron beam evaporated (E-Beam) Au or Pt using the same vacuum chamber [211]. Each capping layer is 50-100 nm thick. Similar layers ITO were also used for the ohmic source and drain contacts. Opaque Ti/Au and Ti/Pt ohmic contacts were exclusively E-beam evaporated.

5.3.2 Pusled laser deposition

Pulsed laser deposition (PLD) finds wide spread use today as a flexible exploratory research tool for high-quality thin film deposition. This technique was first demonstrated in 1965 by Smith and Turner who used a ruby laser to ablate a variety of optically smooth thin films [212]. However, PLD owes its widespread use as a versatile growth

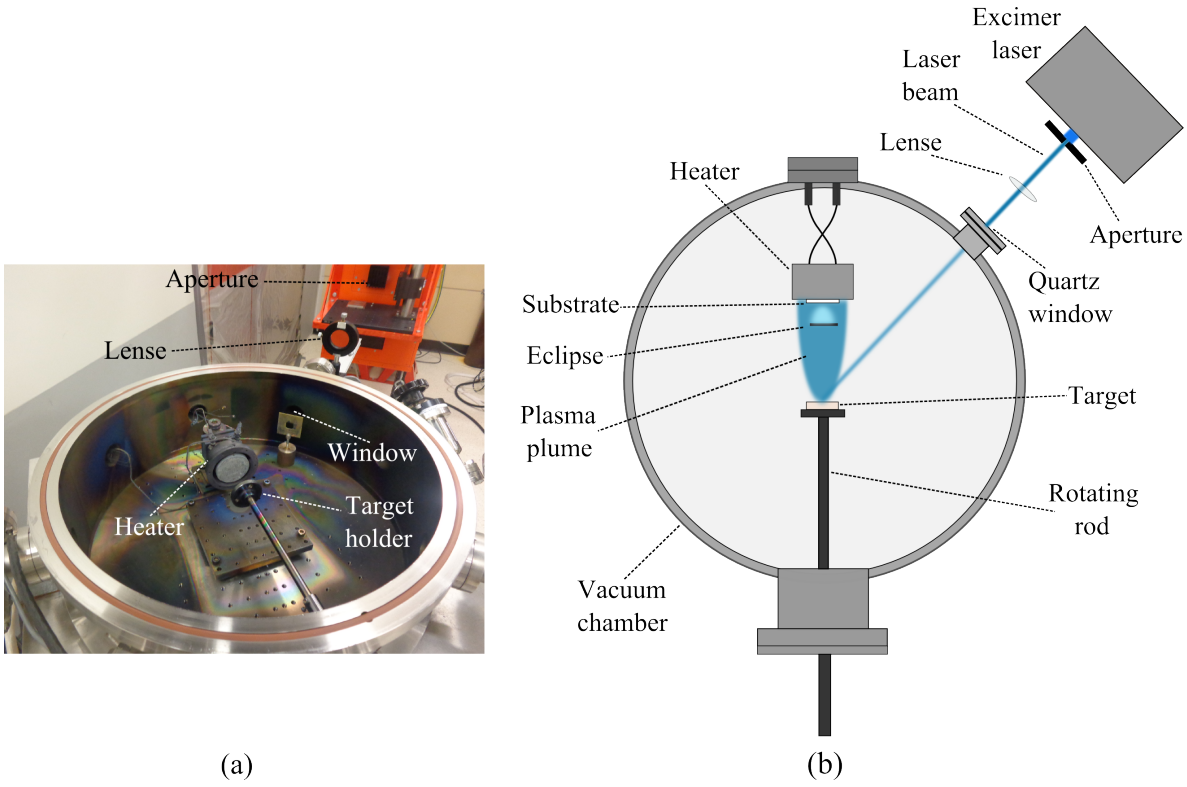

Figure 5.7: (a) A picture of the deposition chamber of the pulsed laser deposition system. (b) Schematic of the PLD deposition setup.

method to the development of high-power lasers in the late 1980s which enabled the efficient evaporation of all types of materials [22]. In PLD, high-power laser pulses with an energy density of more than 10^8 W cm^{-2} are used to melt, evaporate, and ionize material from a single target. The ablated atoms, ions and particles are transported in the plasma plume to the surface of a heated substrate, where they condensate and form an oxide thin film.

The main drawback of PLD is the incorporation of large particulates that are ejected from the target and deposited as droplets on the substrate. These droplets can seriously disrupt the crystal growth and compromise the film quality. For realization of electronic devices such as Schottky contacts, smooth droplet-free films are required. These large particulates can be blocked by placing a shadow mask (or eclipse plate) directly between the target and substrate. While large particulates are being blocked, lighter particles, such as atoms and atomic clusters, are scattered around the shadow mask by multiple collisions with the ambient background gas. Such an arrangement is referred to as

eclipse pulsed laser deposition (EPLD) and was first used by *Kinoshita et al.* [213] to prepare smooth superconducting YBCO films. However, the use of shadow masks to block the plume, comes at the cost of growth rate. Deposition rates are typically cut by factors of 5 when an eclipse mask is used [213]. The other significant downside is the limited scalability of the method, since the area of the eclipse mask can not be arbitrary large.

Within this thesis, EPLD has been primarily used to deposit IrO_X Schottky contacts on FCVA grown ZnO films. A photograph of the high vacuum PLD deposition chamber and a schematic of the PLD setup are shown in Fig. 5.10(a) and (b). Before deposition, the chamber is usually pumped down to approximately 5×10^{-5} Torr. The laser used was a Lambda Physik COMPex pulsed KrF excimer which lases at 248 nm (4.96 eV). A 750 mm focal length fused-quartz lens with an antireflective coating was used to focus the laser beam through a quartz window and onto the target. A rotating high purity Ir target was reactively ablated in an oxygen ambient at a pressure of 100 mTorr. The plasma plume was eclipsed using a 10×10 mm^2 shadow mask which was placed directly between the target and substrate. Growth was carried out at room temperature (RT) for 1 h, using a laser fluence of 15 J cm^{-2}. These conditions yielded IrO_X films with a thickness of 50-70 nm. The PLD system and growth conditions were selected to reproduce the IrO_X Schottky contacts published by *M. Allen et al.* [195].

5.3.3 Photolithography

Standard UV photoresist lithography was used throughout this work to fabricate all electronic devices. In photolithography, a pattern is projected onto a film surface, which is coated with a thin layer of photosensitive material known as photoresist. Photolithography can therefore be divided into two parts. The first is the design and fabrication of a mask that contains the patterns to be projected on the surface of the film. The second part is the actual photolithographic operation which involves the UV exposure and development (uncovering) of the selected areas of the photoresist. The masks were written using a Heidelberg μPG101 mask writer which uses a UV

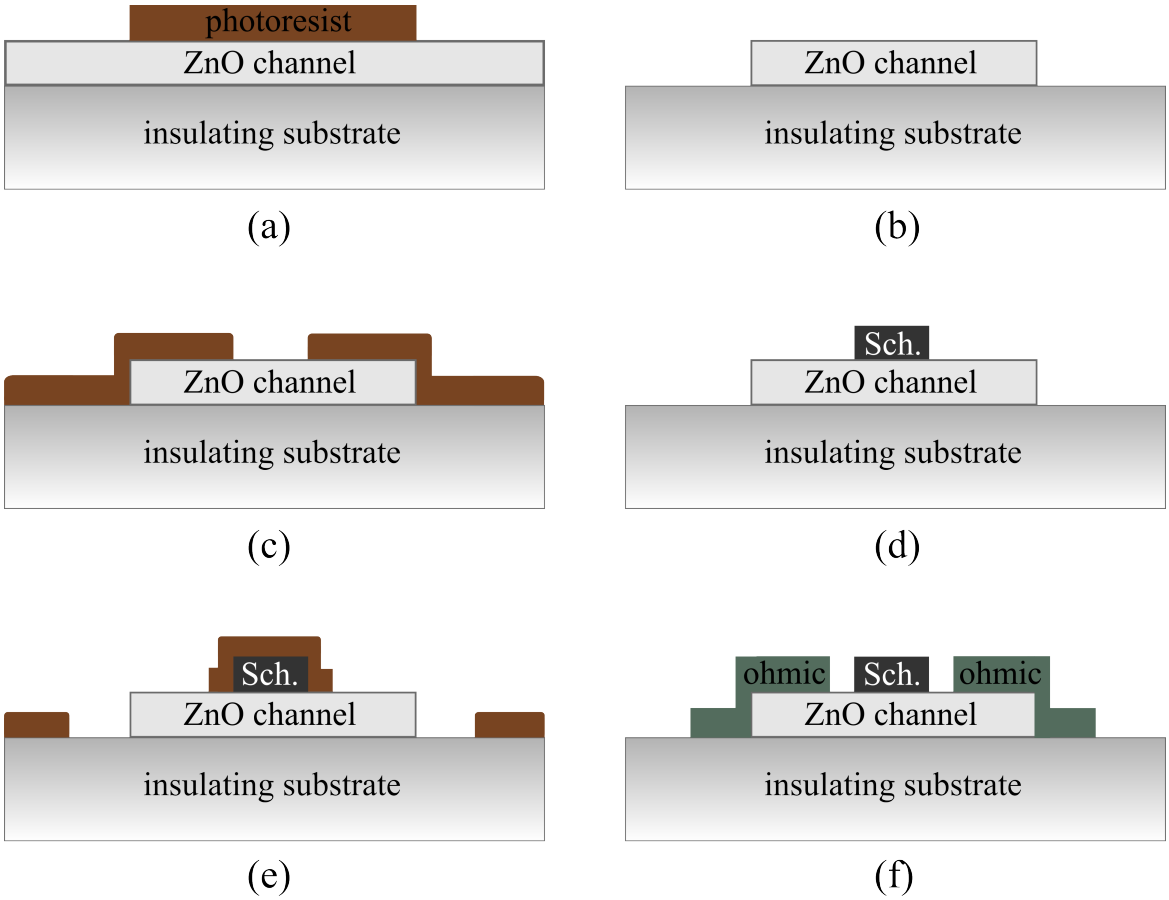

Figure 5.8: MESFET fabrication process:(a) ZnO film with photoresist covering the channel layer. (b) ZnO channel area after etching. (c) Patterned photoresist for Schottky contact deposition. (d) Schottky contact after lift-off. (e) Patterned photoresist for ohmic contact evaporation. (f) Complete MESFET after lift-off.

photodiode to write design patterns onto a chrome and photoresist covered mask plate. For the patterning of the ZnO samples, a Süss MA6 mask-aligner with a UV light source was used in combination with a positive (AZ1518) photoresist. Using these techniques, arrays of MESFETs with gate lengths (L) varying from 5 to 50 μm and gate widths (W) from 10 to 110 μm were fabricated.

A schematic describing the work flow of the fabrication process is shown in Fig. 5.8. For the complete process, three masking levels were required. Typically, 5 $\times$ 5 mm^2 ZnO film samples having a thickness of 30-60 nm were used for device fabrication. Such a small thickness is desirable for realizing MESFETs with low operational voltages. Otherwise, according to Eq. 5.20, the high voltage required to pinch off the channel will result in unreasonably high gate leakage. Prior to processing, the samples were

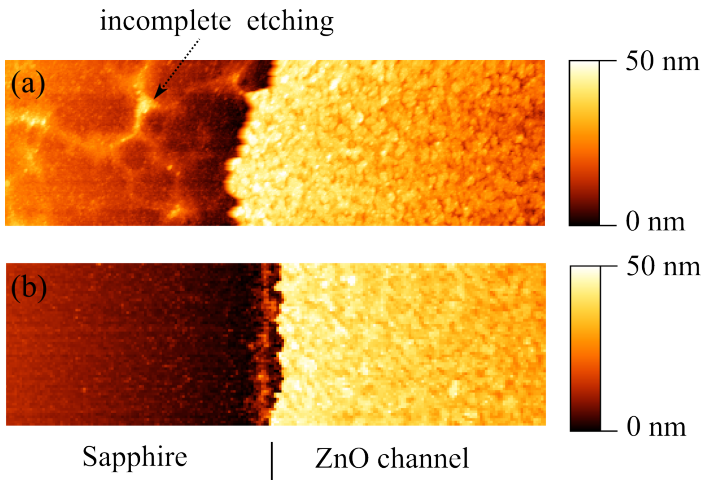

Figure 5.9: (a) Etching of the ZnO channel without plasma ashing. Traces of ZnO can still bee seen on sapphire. (b) Etching of ZnO channel after plasma ashing.

cleaned in an ultrasonic bath using acetone, methanol and isopropyl alcohol (IPA). The same solvents (without the ultrasonic bath) were also used to dissolve the unwanted photoresist. Before every lithographic step, the sample is spin-coated (4000 rpm for 60s) with a positive photoresist (AZ1518) and subsequently dried in open air at 100 °C for 1 min. The first process involves patterning the photoresist, using UV exposure for 10 s, to define the ZnO channel connecting the source and drain regions (i.e. mesa structure) (Fig. 5.8(b)). The ZnO was wet-chemically etched for 60 seconds using ammonium chloride NH_3Cl (5% dissolved in H_2O). This etchant is known to produce a controlled and reproducible etch rate in ZnO films [217]. However, since this etchant is relatively weak, debris and photoresist residuals could inhibit etching and lead to uneven surfaces. To clean the surface and enhance the etching process, the samples were first exposed to an 100 W oxygen plasma (plasma ashing) for 30 seconds. Fig. 5.9 shows the effect of oxygen plasma ashing on the etching of two similar ZnO channels. Poorly etched areas could easily provide parallel conduction paths through the channel and cause unwanted leakage currents between the electrodes. After mesa etching, the Schottky gate contact was deposited on the ZnO channel using patterned photoresist followed by a lift-off process. The length of Schottky contact along the channel defines the gate length. Finally, the ohmic source and drain contacts were fabricated using electron beam evaporation (E-Beam) and a subsequent photoresist lift-off. The order

of ohmic and Schottky contact fabrication are interchangeable. However, in this work the Schottky gate contacts were always deposited first, as they are most sensitive to processing induced surface contamination. However, if a post-deposition annealing process for the ohmic contacts is to be introduced, it would necessary to deposit the ohmic contacts first to avoid damaging the Schottky contact

5.4 Electrical characterisation techniques

5.4.1 Schottky diode characterization

Current voltage (*I-V*) measurements

Provided that the contact area of the Schottky diode is known and $V \gg kT/q$, η can be obtained from the forward bias I-V characteristics by plotting $ln(J)$ versus V and determining the slope of the linear region,

$$\eta = \frac{q}{kT} ln \left(\frac{dlnJ}{dV} \right)^{-1} . \tag{5.27}$$

The effective barrier height ϕ_B can be obtained by extrapolating the same linear region to $V = 0$ V to find the saturation current density J_0 and then using

$$\phi_B = -\frac{kT}{q} ln \left(\frac{J_0}{A^* T^2} \right) . \tag{5.28}$$

The most widely used method to determine the barrier height of a Schottky contact is from its I-V characteristics. As a result of the spatial contact inhomogeneity, this method usually underestimates the average barrier height [199]. The barrier heights of all Schottky contacts fabricated in this thesis were consistently determined using I-V characteristics. Fig. 5.10(a) shows a typical I-V plot of a PLD grown IrO_X Schottky diode on a FCVA ZnO film. The determination of J_0 for an AgO_X and an IrO_X Schottky contact is illustrated in Fig. 5.10(b). In general, AgO_X contacts were found to have lower saturation current densities and higher barrier heights.

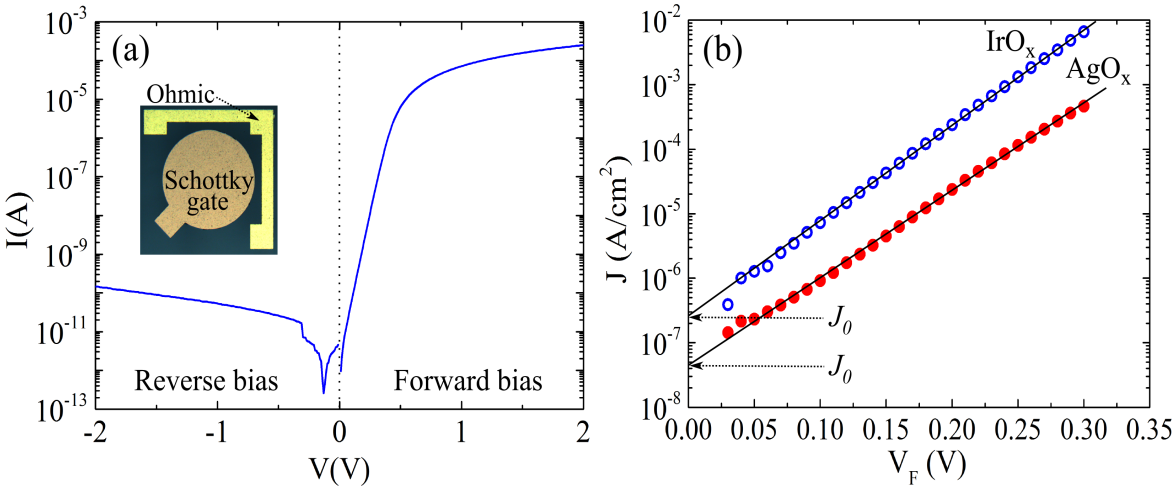

Figure 5.10: Characterization of a Schottky diode. (a) I-V characteristics of a PLD grown IrO_X Schottky contact on an FCVA ZnO film. The inset shows an image of the characterized Schottky contact with a gold capping layer. (b) Forward-bias current density J versus voltage V_F for AgO_x and IrO_x Schottky contacts. The ideality factor η is determined from the slope of the lines while the effective barrier heights are determined from the extrapolated current density J_0 at $V_F = 0$.

Capacitance voltage (C-V) measurements

Alternatively, the barrier height can be obtained from the capacitance voltage characteristics (C-V) of the Schottky contact. The depletion region underneath a Schottky contact is a natural dielectric. Sandwiched between the metal and the undepleted region of the semiconductor, the depletion region forms a parallel plate capacitor. Using Eq. 5.9, the capacitance per unit area of the Schottky contact can be given as a function of the reverse bias voltage V_R,

$$C = qN_D \frac{dw_d}{dV_R} = \sqrt{\frac{q\epsilon_0\epsilon_S N_D}{2(V_{bi} + V_R)}}. \tag{5.29}$$

The reciprocal of the previous equation gives a linear relationship between $1/C^2$ and V_R,

$$\left(\frac{1}{C}\right)^2 = \frac{2(V_{bi} + V_R)}{qN_D\epsilon_0\epsilon_S}. \tag{5.30}$$

$1/C^2$ is measured as a function of the applied bias voltage by applying a small a.c. signal, typically 10 kHz - 1 MHz. From the $1/C^2$ vs V_R plot, the effective donor

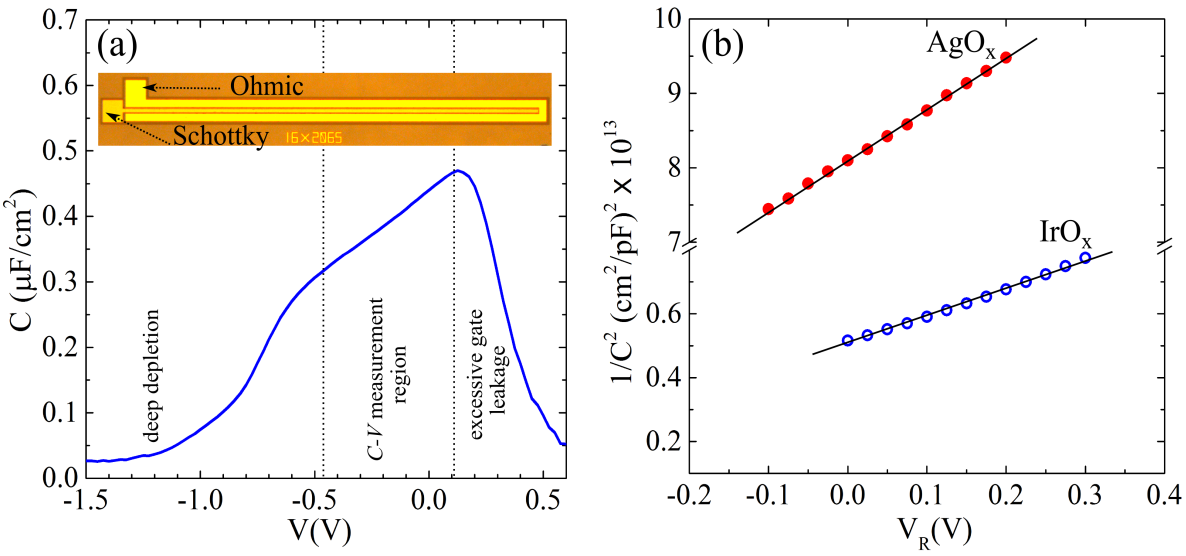

Figure 5.11: (a) C-V characteristics of a AgO_x Schottky contact on an FCVA ZnO film. The inset shows an image of a typical C-V test structure. (b) $1/C^2$ versus V_R for AgO_x and IrO_x on FCVA ZnO Schottky contacts fabricated in this thesis. The effective carrier concentration is determined from the slope and built-in potential is determined from the intercept with the V_R-axis.

concentration can be directly obtained from the slope,

$$N_D = \frac{2}{q\epsilon_0\epsilon_S}\left[\frac{d(1/C)^2}{dV_R}\right], \tag{5.31}$$

where V_{bi} is obtained from the intercept of the plot with the V_R axis. The barrier height can be subsequently determined using $\phi_B = V_{bi} + \phi_n$, where $\phi_n = (kT/q)ln(N_C/N_D)$ and N_C is the conduction band effective density of states ($N_C = 2.94 \times 10^{18}$ cm^{-3} for ZnO). In this thesis C-V measurements were mainly used to determine N_D in MESFET devices. An example of such a C-V measurement is shown in Fig. 5.11. Usually, a large area Schottky contact test structure (shown in inset) is used for this purpose.

5.4.2 Contact resistance

The most convenient parameter used to compare different ohmic contact technologies is the contact resistivity ρ_C. In practice, the contact resistivity is given by

$$\rho_C = R_C A_{ceff}, \tag{5.32}$$

where A_{ceff} is the effective contact area, that is, the effective current injection area. For lateral contacts, as illustrated in the inset of Fig. 5.12(b), only a proportion of the geometrical area of the contact is effectively used for current conduction. Therefore, a factor referred to as the transfer length L_T must be introduced, which represents the section where most of the current flows from the contact into the semiconductor underneath. It is defined as the length from which the voltage drops to e^{-1} of its value at the beginning of the contact and is given by

$$L_T = \sqrt{\frac{\rho_C}{\rho_{SC}}}, \tag{5.33}$$

where ρ_{SC} is the sheet resistivity of the semiconductor below the contact. One of the most common techniques to directly determine ohmic contact characteristics is the transmission line model (TLM) structure [209]. The structure consists of a metal grid pattern of unequal spacing L_i between the contacts. This leads to a scaled planar resistor structure. Each resistor changes only by its distance L_i between two adjacent contacts, as shown in Fig. 5.12(a). The total resistance between any two contacts is expressed by

$$R_i = \frac{\rho_S L_i}{W} + 2R_C. \tag{5.34}$$

Using Eq. 5.34, the semiconductor layer sheet resistivity ρ_S and the contact resistance R_C are determined by plotting the measured resistances as a function of the contact spacing L_i, where ρ_S is determined from the slope and $2R_C$ corresponds to the intercept at $L_i = 0$, as shown in Fig. 5.13(b). The contact resistivity is then determined from Eq. 5.32 by substituting the effective contact area,

$$\rho_C = R_C A_{ceff} = \rho_C = R_C W L_T. \tag{5.35}$$

Assuming a sheet resistance under the contacts, ρ_{SC}, that is equal to the sheet resistance of the semiconductor, ρ_S, Eq. 5.33 can be substituted in Eq. 5.35 to yield a new

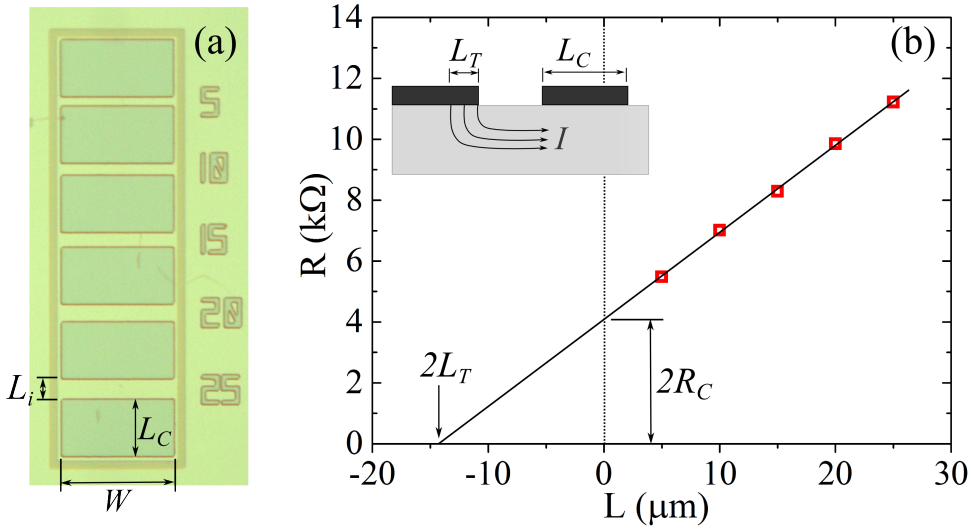

Figure 5.12: (a) A micrograph of a TLM structure of semi-transparent ITO ohmic contacts fabricated on a FCVA ZnO film. (b) The corresponding TLM measurement for extracting the contact and material resistivity. The resistivity of the material (ρ) is determined from the slope of the line.

form of Eq. 5.34

$$R_i = \frac{\rho_S L_i}{W} + \frac{\rho_S}{W} 2L_T. \tag{5.36}$$

Now, an extrapolation to $R_i = 0$ allows for the value of L_i to be determined ($|L_i(\text{intercept})| = 2L_T$), which in turn is used to determine the contact resistivity using Eq. 5.35. The main advantage of the TLM method is its ability to give two main electrical parameters, ρ_S and ρ_C. However, this is based on the assumption that the sheet resistance under the contact is equal to the semiconductor sheet resistivity. Nevertheless, TLM is the most widely quoted technique for determining the contact resistivity of ohmic contacts to ZnO. To obtain meaningful comparisons with ρ_C values reported in the literature, TLM was routinely used in this work. Contact resistivity values of 3×10^{-2} and 2×10^{-3} Ωcm were achieved for ITO and Ti/Au ohmic contacts, respectively. The corresponding ZnO films had carrier concentrations of 5×10^{-17} - 1×10^{-18} cm^{-3}. Since the process conditions for ohmic contact deposition were not optimized and no post deposition thermal treatment was used, these values are considerably higher than those of similar ohmic contacts reported in the literature [201].

5.4.3 MESFET performance metrics

Channel mobility

One of the most important figures of merit for a MESFET is the channel mobility, μ_{ch}. Channel mobility affects device behaviour in two ways. Firstly, carrier velocity and channel transit time are proportional to carrier mobility at low electric fields. Secondly, the channel current is linearly proportional to the carrier mobility. In electronic circuits, such as pixel driving circuits in display panels, a higher current speeds up the rate at which storage capacitors charge up, hence resulting in higher frequency switching response. The MESFET channel mobility can be either determined from the output characteristics for $V_{DS} \rightarrow 0$ using the drain transconductance $g_D = \partial I_{DS} / \partial V_{DS}$ or from the transfer characteristics in the saturation region using the saturation transconductance g_m. From Eq. 5.21 and Eq. 5.24, the relation between both transconductances is

$$g_D = \left.\frac{\partial I_{DS}}{\partial V_{DS}}\right|_{V_{DS}\rightarrow 0} = g_i \left[1 - \sqrt{\frac{V_{bi} + V_G}{V_P}}\right] = \frac{\partial I_{DS,sat}}{\partial V_G} = g_m. \tag{5.37}$$

From this, the full channel conductance g_i can be calculated and the channel mobility is then derived from Eq. 5.19,

$$\mu_{ch} = \frac{g_i L}{q N_D t W}. \tag{5.38}$$

Channel mobilities determined using this approach are very sensitive to the value of the doping concentration N_D, and hence require an accurate N_D value. However, an accurate C-V measurement is not allways possible when the doping concentration is low and film thickness is very small (30-60 nm), since the MESFET channel depletes rapidly over a very short voltage range. Alternatively, the channel mobility can be determined using Eq. 5.22 (linear region) or Eq. 5.26 (saturation region). In the latter case, the channel mobility is given by

$$\mu_{ch} = \frac{g_{max} t L}{\epsilon_0 \epsilon_S (V_{GS} - V_T) W}, \tag{5.39}$$

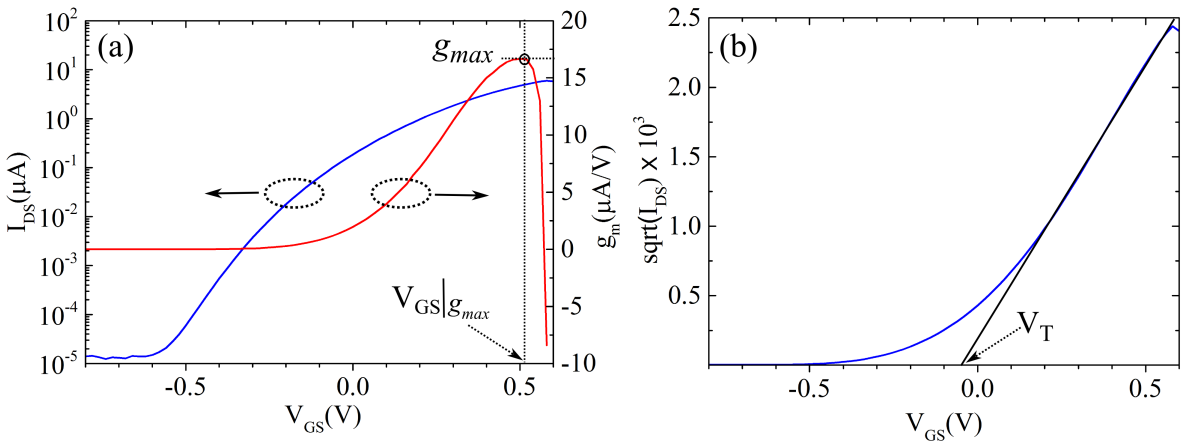

Figure 5.13: Transfer characteristics of a ZnO MESFET with AgO_X gate illustrating the derivation of the channel mobility. (a) The transfer characteristics I_{DS} vs V_{GS} and g_m vs V_{GS} measured at $V_{DS} = 1$ V. (b) the corresponding $\sqrt{I_{DS}}$ vs V_{GS} plot for determining the threshold voltage.

where g_{max} is the maximum transconductance determined from the transfer characteristics (I_{DS} vs V_{GS}) of the MESFET, as shown in Fig. 5.13(a). The threshold voltage is determined by extrapolating $\sqrt{I_{DS}}$ to V_{GS} as shown in Fig. 5.13(b). Given an accurate N_D value, both approaches (Eq. 5.39 and Eq. 5.40) yield similar results. However, in this work, the channel mobility was mainly determined using Eq. 5.39.

Subthreshold swing

In field effect transistors, the subthreshold characteristics have a significant impact on the switching behaviour of the transistor in terms of switching speed and the driving voltage swing. This is described by the so called subthreshold swing, that is the gate voltage swing required to increase/lower the subthreshold current of the transistor by one decade:

$$SS = \frac{\partial V_G}{\partial log I_{DS}}. \tag{5.40}$$

A smaller value of the subthreshold swing is desired as it represents the effectiveness of gate voltage control on the device switching between the *on* and *off* states. A theoretical treatment conducted by *C. L. Liang et al.* [214] set the theoretical minimum

value of SS to:

$$SS = ln(10)\frac{kT}{q}, \tag{5.41}$$

which is $\approx$ 60 mV/dec at room temperature. In a MESFET, the subthreshold current is mainly due to electron diffusion across the depletion region [214]. This electron injection between source and drain is controlled by the height of the potential barrier created by the gate voltage, which leads to an exponential dependence of the subthreshold current on the gate voltage, expressed approximately by [214]:

$$I_{DS} \approx I^0_{DS}\, exp\left[\frac{q}{kT}(V_{GS} - V_T)\right] \quad for \quad V_{DS} \gg \frac{kT}{q}, \tag{5.42}$$

where $I^0{}_{DS}$ is a factor that can be determined experimentally. However, in reality, an SS value of 60 mV/dec is impossible to achieve. In MESFETs, the current leakage across the Schottky gate (I_{SG}) reduces the effective subthreshold current I_{DS} for a given gate voltage according to Eq. 5.42. As a result, the subthreshold swing is inversely related to the Schottky barrier height (ϕ_B) of the gate, since a higher ϕ_B leads to a lower gate leakage current (Eq. 5.6). A slight decrease in barrier height of just 0.13 eV as shown Fig. 5.14 doubles the subthreshold swing. This is substantially different from MISFET based thin film transistors where SS is strongly dependent on the gate oxide capacitance and the density of charge trapping defects at the semiconductor-insulator interface [215].

5.5 Discussion of MESFET characteristics

All the MESFETs discussed in this thesis were based on FCVA ZnO films deposited on a-plane sapphire at 200 °C. These films were found to be c-axis oriented with an XRD FWHM of 0.2-0.3 (°) and RMS roughness of 2-3 nm. As shown in Chapter 4, films deposited on a-plain sapphire produced the highest carrier mobility and lowest resistivity. For MESFET fabrication, films with a thickness of 30-60 nm were used.

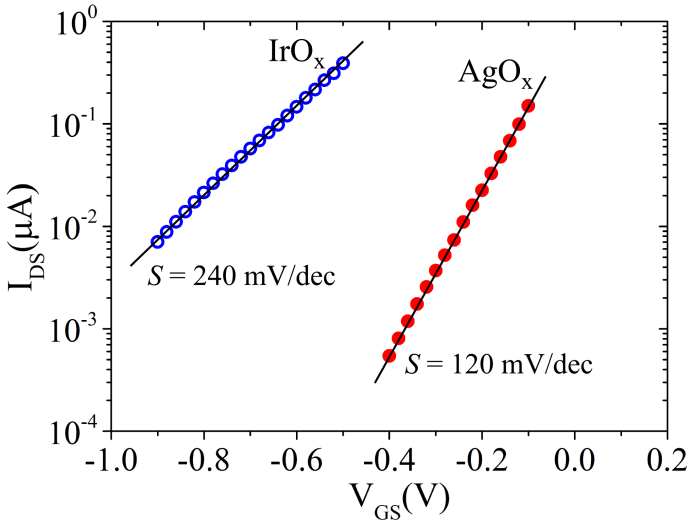

Figure 5.14: Subthreshold drain-source current of equally sized AgO_X and IrO_X gated MESFETs fabricated on the same ZnO film. The effective barrier heights (ϕ_B) of the AgO_X and IrO_X Schottky gates are 0.82 eV and 0.69 eV respectively.

5.5.1 MESFET characteristics

Effect of FCVA ZnO film annealing on MESFET performance

Fig. 5.15 shows typical *I-V* characteristics of Schottky gate contacts of equally sized MESFETS (W = 50 μm/L = 10 μm) fabricated on as-grown and annealed FCVA ZnO films. The ideality factors (η) and zero-bias effective barrier heights (ϕ_B) of these gate contacts were determined using standard thermionic theory and are given in Table 5.4 for devices fabricated on 800 °C films. The Schottky gates on the as-grown film had high leakage currents and a non-uniform forward bias region indicating an inhomogeneous, poorly formed contact, making the extraction of η and ϕ_B uncertain. The Schottky gates on the 650 °C annealed film showed improved rectifying behaviour but with a high ideality factor ($\eta > 1.5$) and a large series resistance, the latter due to the film's high resistivity. Schottky contacts on the 800 °C annealed film showed well-behaved Schottky contact characteristics with low leakage currents (<100 pA at -2 V), low ideality factors (1.1-1.3), and a high rectifying ratio $> 10^6$ at ±2V.

The relative performance of the Schottky gates was reflected in the switching performance of the corresponding MESFETs. The devices on the as-grown film showed incomplete channel pinch-off, high gate leakage and were not considered further. How-

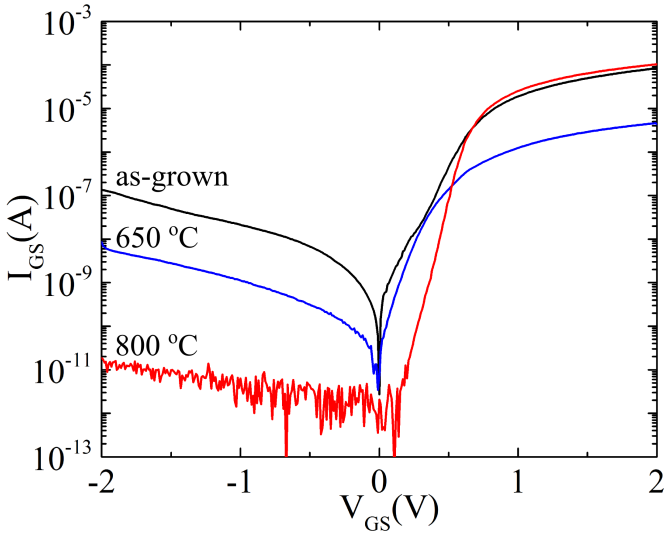

Figure 5.15: *I-V* characteristics of AgO_X Schottky contacts on MESFETs (W = 50 μm/L = 10 μm) fabricated on as-grown, 650 °C O_2 annealed, and 800 °C O_2 annealed FCVA ZnO films.

ever, the MESFETs fabricated on the annealed films showed efficient channel pinch-off with I_{on}/I_{off} ratios from 10^2 to 10^6 and well-behaved output characteristics. The output characteristics of typical MESFETs (W = 50 μm/L = 10 μm) on the films annealed at 650 °C and 800 °C are shown in Fig. 5.16 with the associated figures of merit summarized in Table 5.5 (for films annealed at 800 °C). The channel mobilities of the MESFETS fabricated on the 650 °C films were 1-2 cm^2/Vs, while channel mobilities of the 800 °C MESFETs were 8-31 cm^2/Vs, depending on the channel length. The increase in the channel mobility observed in the 800 °C annealed film is attributed to the lowering of the potential barrier height (E_B) at the grain boundaries of the film. As discussed in Chapter 4, the reduction of E_B is most likely a consequence of the increased doping concentration (Eq. 4.3) due to Al diffusion from the substrate.

Effect of device scaling on channel mobility

The channel mobilities reported here compare favourably with the best reported ZnO MESFETs in the literature. *Frenzel et al.* [26, 43] reported a channel mobility of 10-27 cm^2/Vs for similar MESFETs fabricated on PLD grown ZnO films on a-plane sapphire at a substrate temperature of 630 °C and a channel mobility of 10 cm^2/Vs

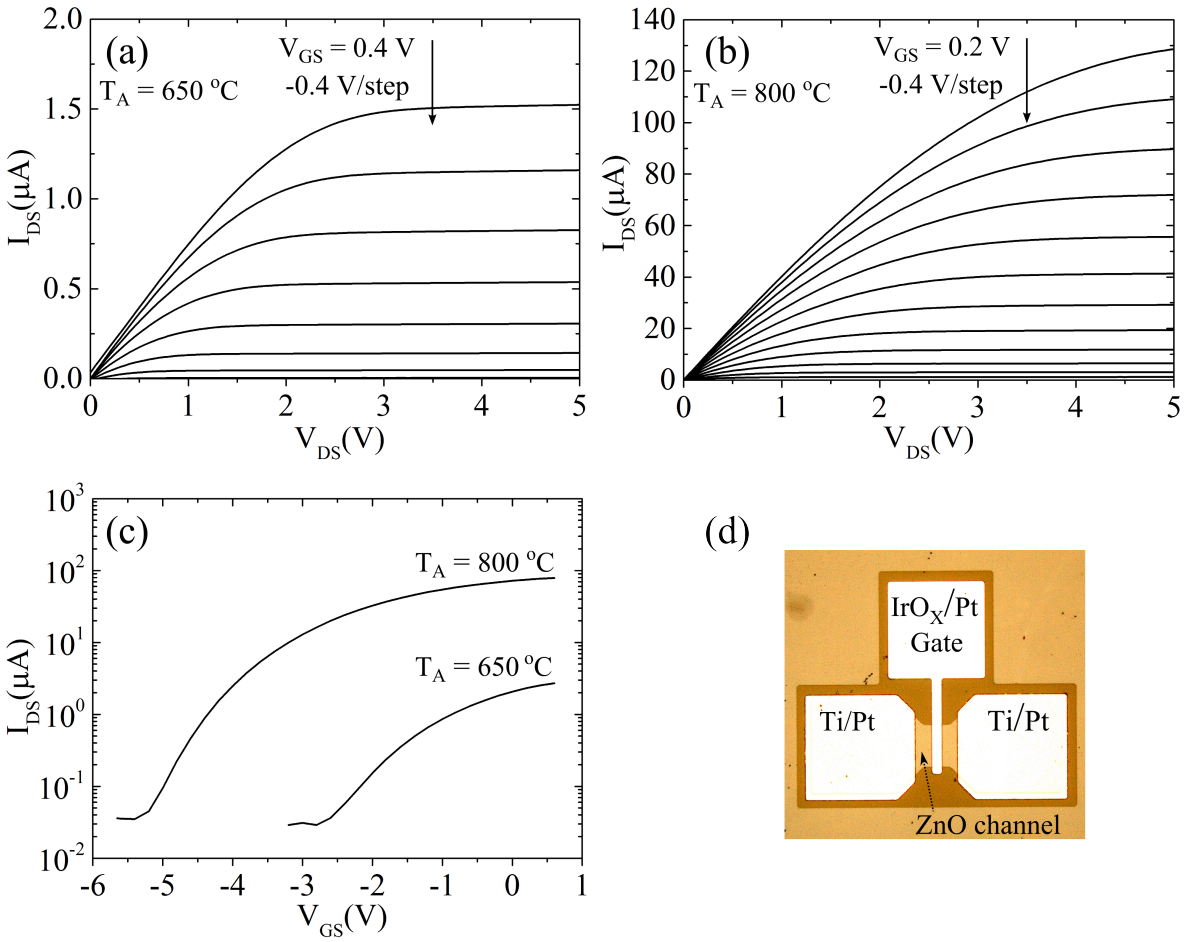

Figure 5.16: Output characteristics of PLD IrO_X Schottky gate MESFETs of the same dimensions (W = 50 μm/L = 10 μm) fabricated on (a) 650 °C and (b) 800 °C O_2 annealed 55nm thick FCVA ZnO films, and (c) the corresponding transfer characteristics of the MESFETs in (a) and (b). A micrograph of a MESFET with identical dimensions is shown in (d).

for MESFETs using ZnMgO channels with an Mg fraction of 0.3%.

Fig. 5.17 shows the effect of channel length scaling on the *apparent* channel mobility of the MESFETs in this work. The *apparent* channel mobility of the devices on the 800 °C annealed film (Fig. 5.16(b)) increases with increasing gate length reaching a maximum of $\sim$ 31 cm^2/Vs. This effect is due to the contact resistance in the drain and source regions which reduces the *apparent* channel mobility. To account for this, the parasitic voltage drop due to the source and drain contacts was de-embedded from the mobility calculation [216]. The resulting *intrinsic* channel mobility proved to be only weakly dependent on the channel length and was approximately constant at 50 cm^2/Vs.

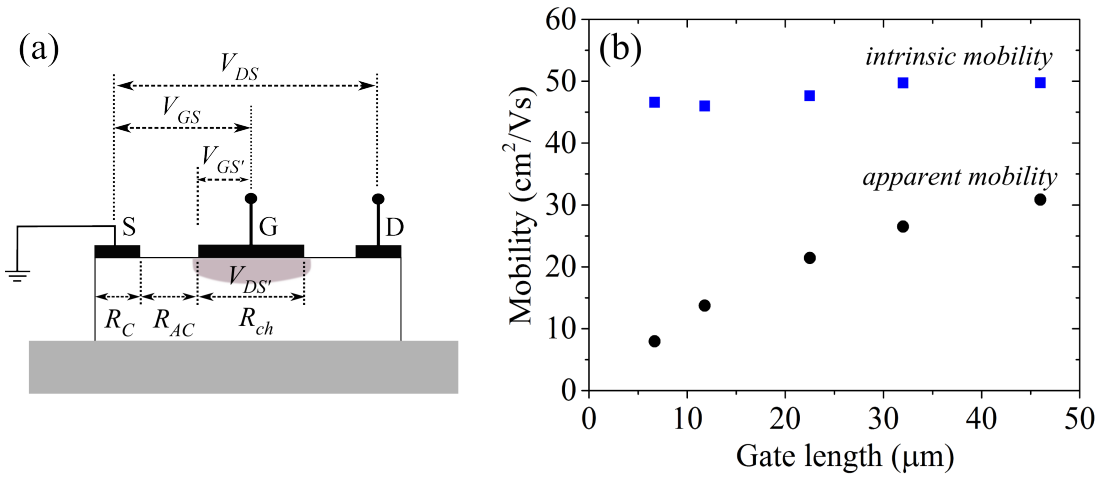

Figure 5.17: (a) A schematic illustrating the parasitic resistances. The intrinsic mobility is derived by using the real voltage values across the channel, $V_{DS'}$ and $V_{GS'}$. (b) *Apparent* and *intrinsic* channel mobility versus gate length (L) for IrO_X Schottky gate MESFETs fabricated on FCVA ZnO films annealed in O_2 at 800 °C. The MESFETs were fabricated on 55 nm thick FCVA ZnO films. No dependence on channel width (W) was observed.

Effect of gate material

A high quality Schottky contact is the main prerequisite for realizing a high performance MESFET transistor. Therefore, a systematic comparison of the influence of Schottky gate types on the different characteristics of ZnO MESFETs is important. For this purpose, MESFETs with reactively sputtered AgO_X, IrO_X, RuO_X and PLD grown IrO_X Schottky gates were fabricated and characterized. Table 5.4 lists the characteristics "best results" of the different Schottky contacts. The figures of merit were extracted from *I-V* measurements on MESFET devices, using standard thermionic emission theory described in section 5.4.1. Reactively sputtered Ag and oxidized Ir grown by PLD yielded the best results (Fig. 5.10(a) and Fig. 5.15). The achieved barrier heights (> 0.80 eV) and ideality factors (~ 1.12) of these two Schottky types are in good agreement with values of similar contacts deposited on bulk ZnO reported by *M. Allen et al.* [193, 195], indicative of nearly ideal contacts and excellent lateral homogeneity. However, the reactively sputtered Ir Schottky contacts showed substantially lower barrier heights (0.69 eV) and a higher ideality factor (1.4). Although the work function of Ru is larger than that of Ag (Table 5.1), reactively sputtered Ru yielded

Table 5.4: Characteristics of Schottky gate contacts made of reactively RF sputtered AgO_X, Ir_X, Ru_X and PLD grown IrO_X on FCVA ZnO MESFETs. The ZnO films were deposited on a-plane sapphire at 200 °C and annealed in O_2 at 800 °C for 1 hour. The listed values represent the best achieved results extracted from *I-V* characteristics using standard thermionic emission theory.

Dep. technique	**Gate type**	η	Φ_B **(V)**	**Rect. ratio at at ± 2V**	$\mathbf{R_S}$ **(kΩ)**
RF sputtering	AgO_X	1.14	0.82	3×10^7	19
	IrO_X	1.40	0.69	1×10^5	6
	RuO_X	1.93	0.56	3×10^3	141
PLD	IrO_X	1.13	0.84	5×10^7	12

the lowest ϕ_B (0.56 eV), and consequently the smallest rectification ratio (3.3×10^3). *M. Allen et al.* investigated the *I-V* characteristics of a variety of Schottky contact types in terms of their compliance with existing Schottky barrier formation models [218]. It was found that the barrier heights were more stronger correlated with the electronegativity of the metal than with its work function. However, neither of the existing models was able to predict the barrier heights of Schottky contacts to ZnO. The lack of an accurate model in the literature makes it difficult to explain the differences between the gate types.

The effect of the different Schottky gate types on the performance of the MESFETs is shown Fig. 5.18(a) to (f). For a meaningful comparison, the MESFETs are equally sized (W= 100 μ and L = 5 μ) and were fabricated on 5 mm × 5 mm samples diced from the same ZnO film. The ZnO film used was grown at 200 °C and subsequently annealed in O_2 at 800 °C for 1 hour. The properties of the ZnO film and the "best" figures of merit for each Schottky gate type are listed in Table 5.4. To reduce the operating voltage, i.e. to set a low pinch-off voltage, a ZnO film with a thickness of 35 nm was used. A low operating voltage is desirable as it prevents the Schottky gate being strongly reverse biased, which can lead to high leakage currents.

All device types showed well behaved MESFET output characteristics, as shown in Fig. 1.18(c)-(f). In general, the IrO_X and RuO_X MESFETs had significantly higher channel mobilities and delivered higher drain currents. However, the AgO_X MESFETs

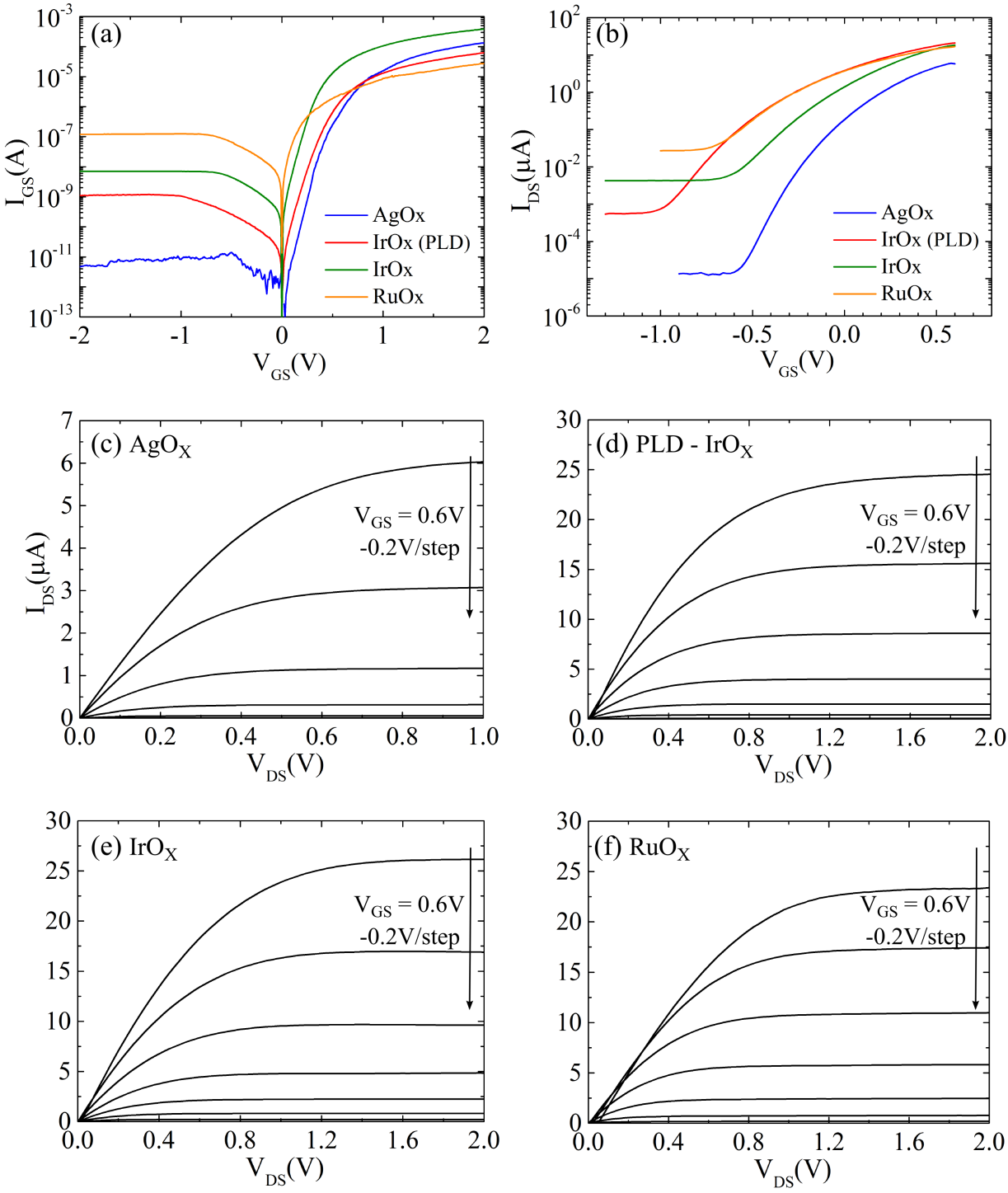

Figure 5.18: A comparison of the (a) Schottky gate characteristics and (b) the transfer characteristics of MESFETs with reactively sputtered AgO_X, PLD grown IrO_X, reactively sputtered IrO_X and reactively sputtered RuO_X. (c)-(d) The corresponding MESFET output characteristics for each of the different gate types.

Table 5.5: Electronic characteristics of equally sized (W=100μm/L=5μm) AgO_X, IrO_X and RuO_X MESFETs fabricated on an FCVA ZnO film. The ZnO film is 35 nm thick and was annealed at 800 °C prior to device fabrication. μ_{Hall} refers to the film electron mobility measured by the Hall effect and $\mu_{ch,intrinsic}$ refers to the intrinsic channel mobility after de-embedding the effect of the parasitic resistances in the MESFET channel.

n_{Hall} cm^{-3}	μ_{Hall} cm^2/Vs	Gate type	Gate dep. method	N_D-N_D cm^{-3}	$\mu_{ch,intrinsic}$ cm^2/V	I_{on}/I_{off}	SS mV/dec
1×10^{18}	30	Ag	RF sput.	3×10^{17}	16	1×10^6	140
1×10^{18}	30	Ir	RF sput.	2×10^{18}	42	8×10^4	240
1×10^{18}	30	Ru	RF sput.	-	31	4×10^3	340
1×10^{18}	30	Ir	PLD	1×10^{18}	33	1×10^5	210

showed a lower subthreshold swing (SS) and a higher I_{on}/I_{off} ratio. As discussed in section 5.4.3, the lower boundary of the subthreshold swing in MESFETs is mainly limited by the leakage current across the gate contact. Accordingly, the MESFETs with the lowest leakage current across the gate also showed the lowest SS and highest I_{on}/I_{off} ratio. Due to the high gate leakage current, the RuO_X MESFET shows the highest SS and lowest I_{on}/I_{off}. The higher leakage current is a direct consequence of the lower barrier height of the RuO_X Schottky gate, listed in Table 5.3. An accurate measurement of the net doping concentration (N_D) in the RuO_X MESFET was not possible, due to the lower quality of the contact.

Another noticeable difference between the AgO_X MESFETs and IrO_X MESFETs is the effect of the Schottky gate deposition on the channel carrier concentration. For the IrO_X MESFETs, the net donor density (N_D-N_A) extracted from capacitance–voltage measurements, given in Table 5.5, approximately matches the carrier concentration (n_{Hall}) obtained from standard Hall effect measurements. However, the deposition of the AgO_X Schottky gate appears to reduce the channel carrier concentration by almost one order of magnitude. Ag is known to act as an acceptor in ZnO, partly compensating the background electron concentration [102]. Ag diffusion into the channel during Schottky contact deposition has already been reported [219]. The lower drain current observed for the AgO_X MESFETs may be explained by the reduced carrier concentra-

tion of the channel caused by Ag diffusion, while the lower channel mobility may be a result of increased ionized impurity scattering and an increased grain boundary (GB) potential barrier height (E_B), due to the inversely proportional relationship between E_B and the carrier concentration, as given in Eq. 4.3. The effect of Ag diffusion on the ZnO channel was not reported by *H. Frenzel et al.* [43, 26, 160], for reactively DC sputtered AgO_X Schottky contacts on PLD grown ZnO channels. This suggests that Ag diffusion length may vary with gate deposition conditions and underlying ZnO film properties. In this thesis, AgO_X and IrO_X MESFETs fabricated on thicker films (55 nm) were found to have similar characteristics, probably due the relatively smaller Ag diffusion length compared to the overall channel thickness.

5.6 Summary

In this chapter, a process for the fabrication of MESFETs on ZnO thin films grown using a filtered cathodic vacuum arc (FCVA) was demonstrated. The key achievements, findings and challenges related to the fabrication process and device characteristics are:

- The devices were fabricated using standard photolithography in a simple 3-step process. When the PLD grown IrO_X Schottky contacts are excluded, the whole process is industrially scalable; using only wet etching, reactively sputtered Schottky gates and electron beam evaporated ohmic contacts.

- AgO_X, IrO_X and RuO_X gated MESFETs on ZnO thin films grown by FCVA were demonstrated. The MESFETs were fabricated on ZnO films deposited on a-plane sapphire and annealed in O_2 at 800 °C (before fabrication). These devices exhibited high quality Schottky contacts with η as low as 1.13, ϕ_B from 0.65-0.85 eV, and diode rectification over 10^6 (at $\pm$ 2 V). The MESFETs showed intrinsic channel mobilities $\sim$ 50 cm^2/Vs and I_{on}/I_{off} switching ratios from 10^3-10^6. The devices operated at low switching voltages, typically 1-5 V, and the subthreshold swing varied from 120 - 340 mV/dec, depending on the Schottky gate type. These results compare very well with some of the best TFTs, both MESFETs

and MISFETs, published in the literature using higher cost growth techniques, as shown in Table 5.1.

- As-grown FCVA ZnO films were not suitable for MESFET devices due to the low quality of the deposited Schottky contacts. Films annealed at 650 °C in O_2 yielded MESFETs with reasonable switching behaviour. However, the best results were consistently achieved on FCVA ZnO films annealed in O_2 at 800 °C. This is due to a higher carrier concentration as a result of Al diffusion from the sapphire substrate and increased channel mobility due to reduced grain boundary scattering.

- MESFET performance was dependent on both Schottky gate type and deposition technique. Reactively sputtered AgO_X and PLD grown IrO_X formed the best Schottky gates. However, Ag appears to diffuse into the MESFET channel, reducing the carrier concentration. As an alternative to PLD grown IrO_X, sputtered IrO_X MESFETs with well behaved field effect characteristics were demonstrated. In contrast, RuO_X gates had low rectification ratios (10^2-10^3) and produced the largest *SS*, due to a significantly lower Schottky barrier height.

- Parasitic source and drain resistances have significant impact on the scaling behaviour of the ZnO MESFETs. This is especially pronounced in short channel MESFETs where most of the drain-source voltage is dropped across the contact and access resistances. The non-optimized ohmic contacts of the MESFETs in this work prevent the full utilization of the high channel mobility, and potentially limit the operating frequency of the fabricated devices.

Chapter 6

The effect of gate type and channel quality on MESFET device stability

The stability of oxide based TFTs has always been a concern and a subject of research, especially for electronic display applications. The metal-insulator-semiconductor field effect transistor (MISFET) architecture usually implemented in pixel switching TFTs suffers from inherent drawbacks caused by charge trapping by defects and interface states at the gate insulator-semiconductor interface. These defects are believed to be partly responsible for bias instabilities [183, 184, 185]. In contrast, due to the presence of a depletion layer isolating the channel from the gate interface in a MESFET, charge trapping associated with insulator-semiconductor interfaces can potentially be avoided. This is expected to result in improved operational stability. However, the lack of an insulator between the gate and channel in a MESFET imposes some limitations in terms of leakage current and possible electromigration of gate material across the interface. While the stability of oxide MISFET based TFTs has been extensively studied [183, 184, 185], there are very few reports on the possible degradation mechanisms in thin film MESFETs [26, 160].

In this chapter, we investigate the effect of Schottky gate type and channel defects on the light, bias and temperature stability of ZnO thin film MESFETs. Due to their superior dc characteristics, only AgO_X and IrO_X MESFETs were chosen for

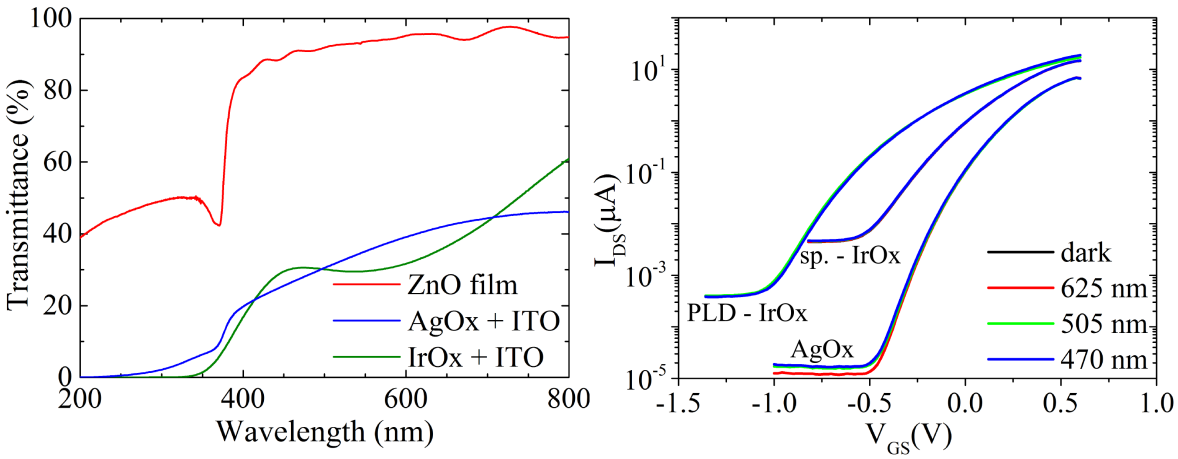

Figure 6.1: (a) Optical transmission measured through the ZnO film and Schottky gate stack. (b) Transfer characteristics of AgO_X and IrO_X MESFETs (W = 100 μm/L = 5 μm) in dark and under illumination of 1 mW.cm^{-2} blue, green and red light.

further investigation. These devices were subjected to standard positive bias (PBS) and negative bias (NBS) stress tests. Temperature dependent measurements were made from 20 to 190 °C.

6.1 Light and UV sensitivity

6.1.1 Effect of visible light

The photostability of the MESFET devices was tested using red, green and blue LEDs at a power intensity (on sample) of 1 mW.cm^{-2} which meets the testing requirements of flat panel displays [185]. Fig. 6.1 shows the optical properties of the FCVA ZnO film and the electrical characteristics of the fabricated AgO_X and IrO_X MESFETs. The ZnO film used for the channel had an optical transparency of more than 90% in the visible range (Fig. 6.1(a)). However, the gate-channel stack had a corresponding transparency of 30%–60%, although this has subsequently been shown to be easily improved by reducing the thickness of the respective Schottky layers [220]. The transfer characteristics of the AgO_X and IrO_X MESFETs, in dark conditions and under light illumination of 1 mWcm^{-2} at different visible wavelengths, are shown in Fig. 6.1(b). The lack of any significant changes upon sub-band gap illumination indicates a low concentration of deep level defects in the ZnO channel and ZnO/Schottky gate interface.

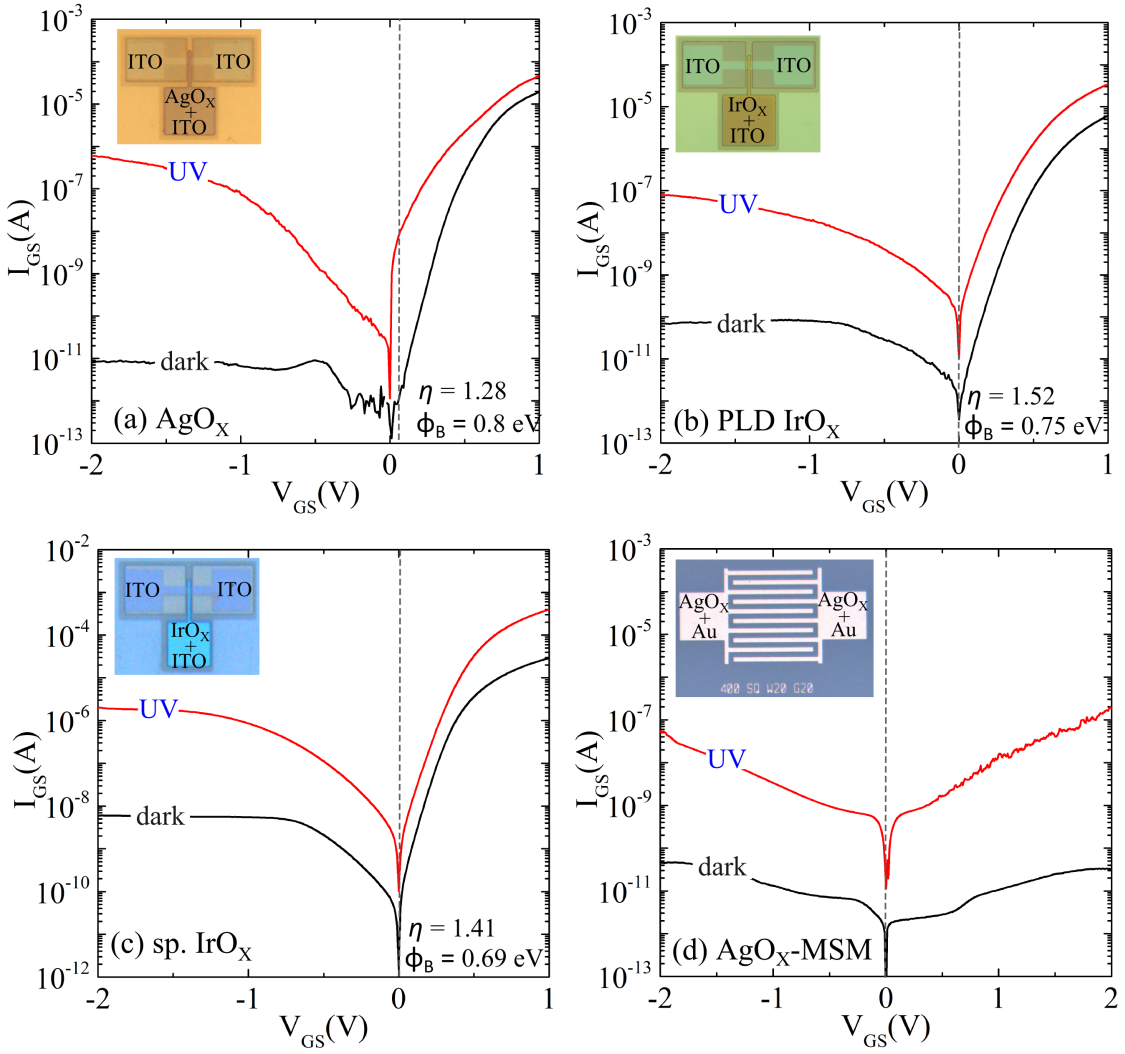

Figure 6.2: *I–V* characteristics in dark and under illumination of a fluorescent 365 nm UV light source with (P_{max} = 1.3 W.cm^{-2} at λ = 365 nm). (a) RF sputtered AgO_X, (b) PLD grown IrO_X and (c) RF sputtered IrO_X Schottky gate contacts on ZnO MESFETs (W = 25 μm / L = 10μm). (d) AgO_X MSM structure. All devices were fabricated on FCVA ZnO grown at a substrate temperature of 200 °C and post-annealed at 800 °C.

6.1.2 UV responsiveness

Fig. 6.2 shows typical *I-V* characteristics of semi-transparent RF sputtered AgO_X, PLD grown IrO_X and RF sputtered IrO_X with ITO capping layers (shown in Fig. 6.1), in dark and under illumination of a fluorescent UV source (P_{max} = 1.3 W.cm^{-2} at λ = 365 nm). Upon UV irradiation, the reverse current of the AgO_X Schottky contact increased by approximately 5 orders of magnitude at -2 V, indicating excellent UV responsiveness. Due to the higher reverse leakage current, the UV sensitivity is lower in the IrO_X Schottky contacts. For the sake of comparison, a AgO_X UV sensor based

on the metal-semiconductor-metal (MSM) structure was fabricated on a similar film. Overall, UV/visible spectral rejection ratios (at -2 V) of up to 5 orders of magnitude for AgO_X devices and 3 orders of magnitude for IrO_X devices were achieved. These results compare favourably with other ZnO UV based sensors reported in the literature [225, 226, 227]. Considering the small thickness ($\sim$ 40 nm) of the ZnO films used here, which allows up to 40% of the UV irradiation to pass through (Fig. 4.18), a significant improvement is expected for thicker ZnO films with larger irradiation areas.

6.2 Stability under bias stress

To test the MESFET devices for long-term stability under high power conditions, as required for displays such as AM-OLEDs, the MESFETs were subjected to positive bias stress (PBS) at V_{DS} = 1 V and V_{GS} = 0.6 V (open channel). This was followed by a negative bias stress (NBS) at V_{DS} = 1 V and V_{GS} = -1 V (fully depleted channel) to examine the effect of gate polarity on degradation mechanisms. Due to the small operating voltage of the MESFETs, and hence the very small observed voltage shifts, the stress tests were performed many times on different devices to ensure accuracy and reproducibility.

6.2.1 Positive bias stress (PBS)

Fig. 6.3(a)-(d) show the effect of a PBS test, at V_{DS} = 1 V and V_{GS} = 0.6 V, on the transfer and Schottky diode characteristics of FCVA ZnO MESFETs with RF sputtered AgO_X and IrO_X gate contacts. The evolution of the transfer curves under PBS is shown in Fig. 6.3(a). The MESFET figures of merit, extracted from the transfer characteristics, reveal a negligible drift in threshold voltage ($\leq$ 10 mV) but a substantial decrease in drain current (over 20% in 3 h) in the AgO_X MESFET compared to the IrO_X gated version. The current decrease in the AgO_X MESFETs was accompanied by a degradation of the Schottky gate barrier height, ideality factor and reverse leakage current, as shown in Fig. 6.3(c) and (d). The AgO_X Schottky gate degradation

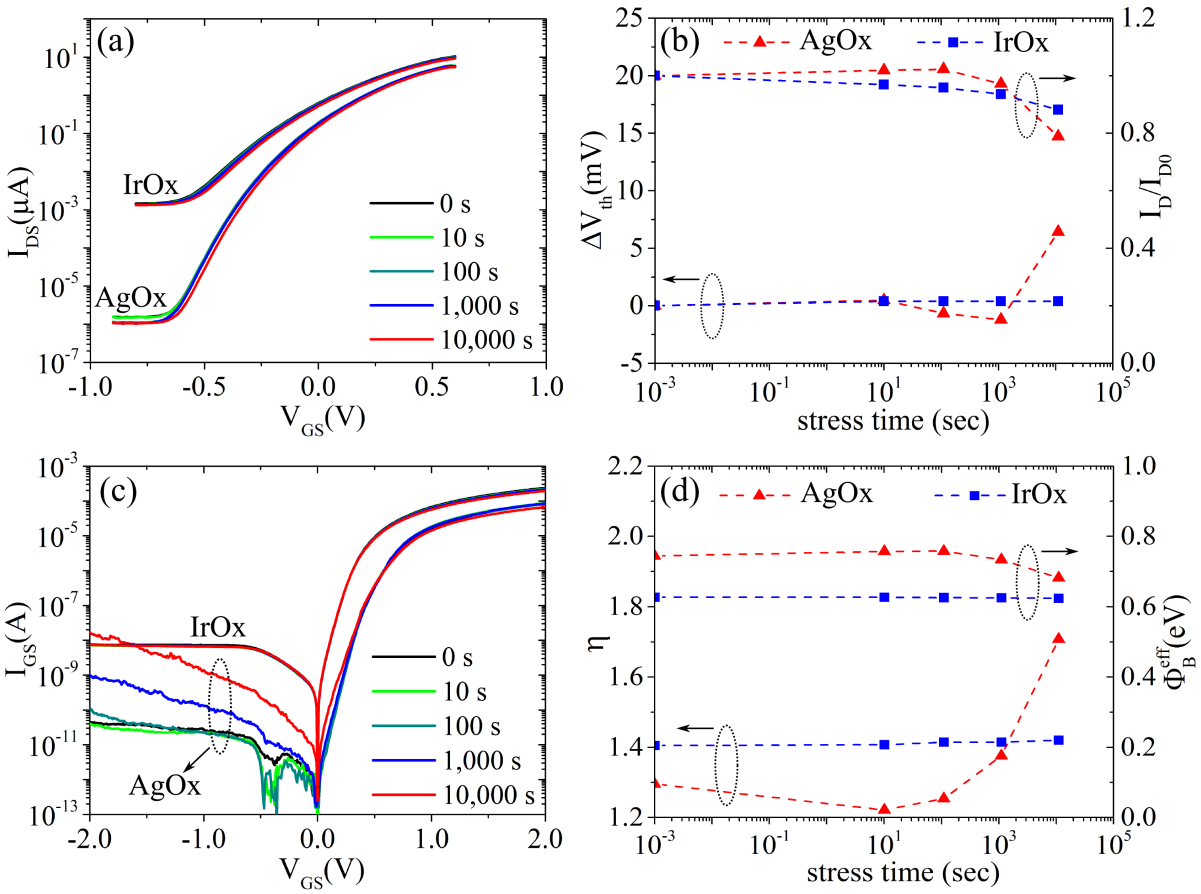

Figure 6.3: Effect of positive bias stress at $V_{GS} = 0.6$ V and $V_{DS} = 1$ V on the transfer characteristics (a)-(b) and Schottky diode characteristics (c)-(d) of AgO_X and IrO_X gated MESFETs. Both gate types were RF sputtered. The MESFETs were fabricated on FCVA ZnO film samples ($\sim$ 35 nm) diced from the same film.

was permanent with only a slight post-stress recovery. In contrast, the drain current decrease in the IrO_X MESFET recovered completely within a few hours after PBS, indicating that a different mechanism, such as charge trapping, was responsible for the current decrease.

6.2.2 Negative bias stress (NBS)

The effect of the NBS at $V_{DS} = 1$ V and $V_{GS} = -1$ V is shown in Fig. 6.4(a)-(d). During this NBS test, the characteristics of the IrO_X MESFET evolved in a similar way as for the PBS test. The IrO_X Schottky gate characteristics shown in Fig. 6.4(c) and (d) were largely uneffected while the corresponding transfer characteristics showed a recoverable drain current decrease of 20% over the stress period of 3 h. Interestingly, the

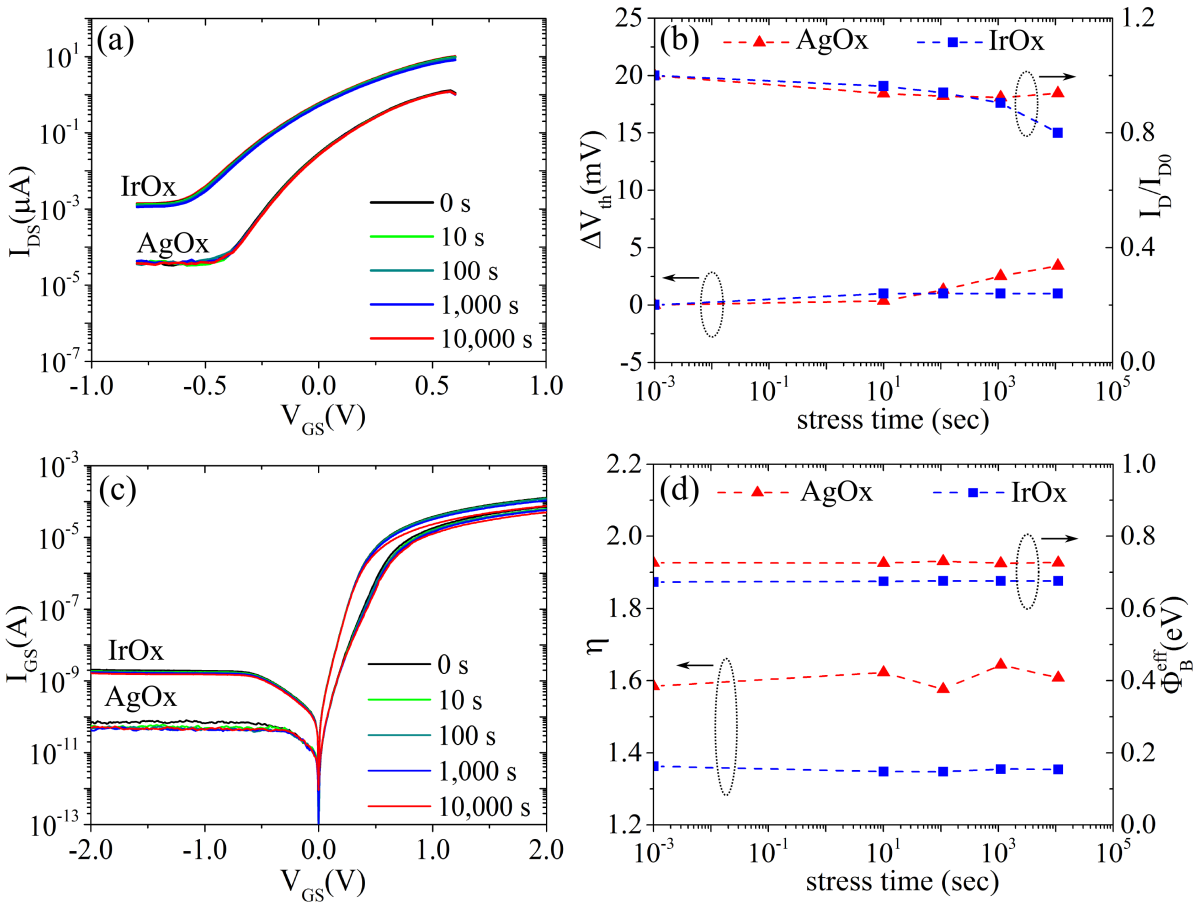

Figure 6.4: Effect of negative bias stress at V_{GS} = -1 V and V_{DS} = 1 V on the transfer characteristics (a)-(b) and Schottky diode characteristics (c)-(d) of AgO_X and IrO_X gated MESFETs. Both gate types were RF sputtered. The MESFETs were fabricated on FCVA ZnO film samples (∼ 35 nm) diced from the same film.

AgO_X MESFET characteristics showed a much higher stability than that previously observed in the PBS test, with negligible threshold voltage shift of ∼ 4 mV and a drain current decrease of only 5% after 3 h (Fig. 6.4(b)). All changes were completely recoverable post-stress with time. Electromigration of Ag in an electric field is a well known problem in electronics [221] and Ag is known to be readily soluble in ZnO [102]. Due to this high solubility, positive Ag ions may readily diffuse into the channel during PBS testing, causing irreversible damage. However, if the gate is negatively biased, no Ag diffusion will take place, resulting in the observed stable AgO_X gate characteristics shown in Fig. 6.4(b). Conducting the same PBS and NBS test under illumination of 1 mW cm^{-2} using a blue LED with a wavelength of 470 nm had a negligible effect and resulted in instability trends identical to the results shown in Fig. 6.3 and Fig. 6.4.

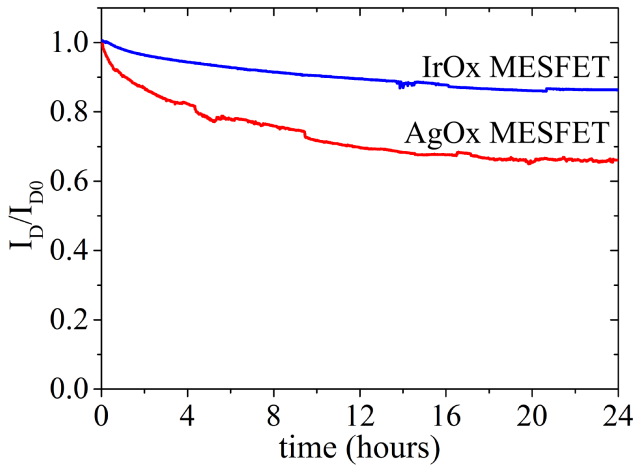

Figure 6.5: Normalized channel current plotted over 24 hours of AgO_X and IrO_X gated MESFETs fabricated on the same ZnO film and biased in the saturation region at V_{GS} = 0.6 V and V_{DS} = 1 V (PBS).

Fig.6.5 shows the normalized drain current over 24 h of PBS for two identical AgO_X and IrO_X gated MESFETs biased at V_{GS} = 0.6 V and V_{DS} = 1 V (open channel). As expected, the long PBS stress period resulted in permanent damage to the AgO_X Schottky gate, leading to significant irreversible drain current degradation. In contrast, the IrO_X Schottky gate was robust, although a recoverable 14% channel current decrease was observed. Over this stress period, the threshold voltage shift was negligible ($\Delta V_{th} < 20$ mV) and the full drain current was recoverable after post-stress resting. This full drain current recovery indicates that, during stress, charge carriers are temporarily trapped in the channel. After the bias stress is lifted, these carriers are then slowly released from the trap states, resulting in a recovery of the initial device characteristics. Considering that a Schottky depletion layer isolates the channel from the gate and that the gate characteristics remained uneffected during stress testing, it is reasonable to assume that this charge trapping occurs mainly in the channel.

In polycrystalline semiconductors, it is widely accepted that the overall performance of electronic devices is dominated by the density of defect states within the grain boundaries (GB)[222]. As discussed in section 4.1.3, the widely used GB mobility model suggests that the defect states at GBs are capable of trapping carriers, thereby immobilizing them. As a result, the GB defect states become charged, creating a

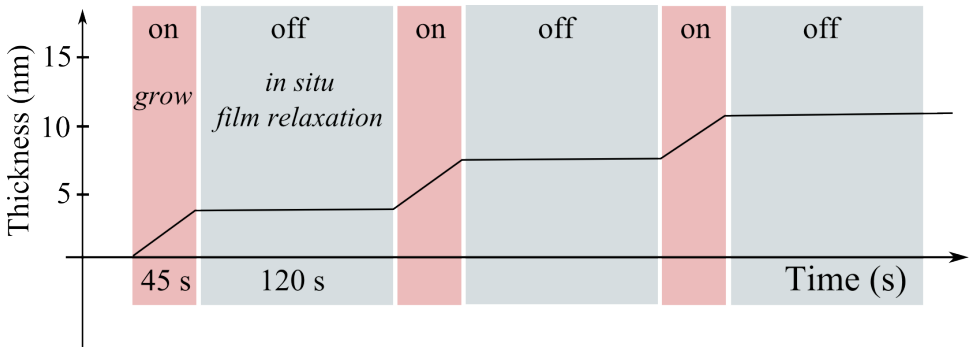

Figure 6.6: Schematic illustration of the interval growth method. The growth is interrupted every 45 s to allow film relaxation for 2 minutes under the same growth conditions.

potential energy barrier (E_B) which impedes the motion of carriers from one grain to another [106], with the total effective mobility is given by Eq. 4.6. When the current transport is predominantly limited by GB defects such that the mobility inside the grain is much larger than the mobility in the GB region, $\mu_G \gg \mu_{GB}$.exp(-E_B/kT), the drain-source current in a MESFET can be approximated as (Eq. 5.25):

$$I_{DS,sat} \approx \frac{W\epsilon_S}{2Lt}(V_{GS} - V_T)^2 \cdot \mu_{GB}\, exp\left(\frac{-E_B}{kT}\right). \tag{6.1}$$

Since all these parameters apart from the GB potential barrier (E_B) can be considered as constant during the stress testing of the IrO_X MESFET in Fig. 6.5, the exponential decay of the channel current during PBS can be linked to a gradually increasing E_B which in turn is caused by the trapping of carriers at GB defects. Although the exact nature of GB defects in ZnO is not fully understood, correlations of GB defects with oxygen vacancies as well as film morphology have been previously reported [19, 223].

6.3 The role of GB defects

To verify the effect of GB defects on MESFET stability, a second FCVA ZnO film was grown under identical growth conditions, except this second film was deposited in intervals (referred to as interval growth (IG)) where after every 45 sec (corresponding to a 4 nm layer) the growth was interrupted for 2 minutes while maintaining the same

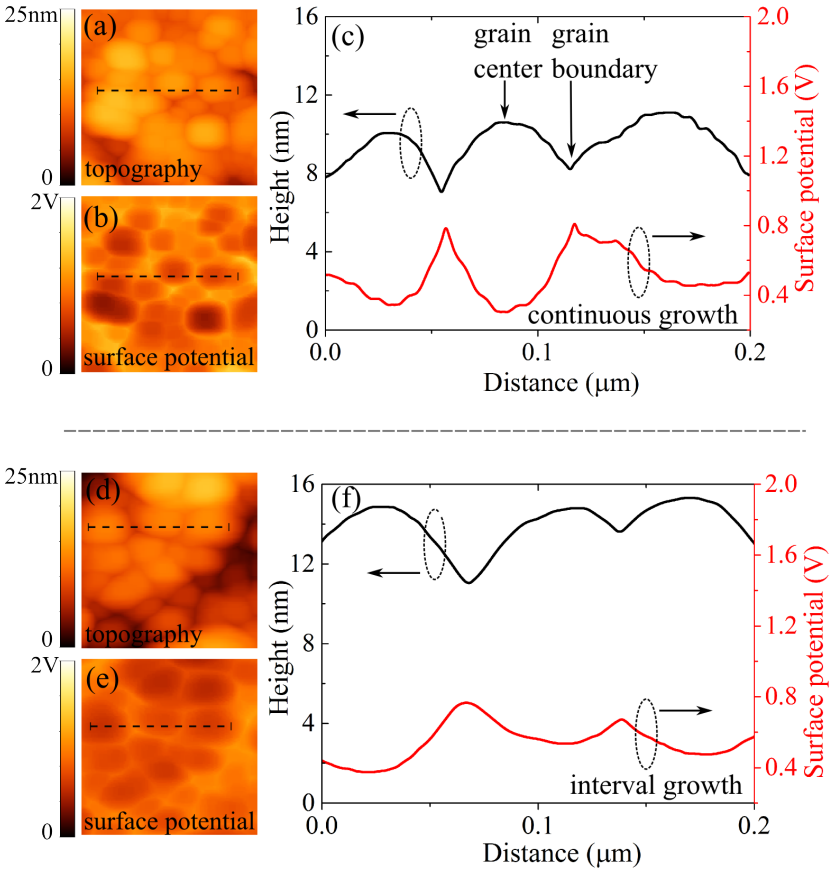

Figure 6.7: (a) and (d) 0.25 × 0.25 μm^2 AFM images of 35 nm thick CG and IG films, respectively. (b) and (e) the corresponding surface potential images. (c) and (f) profiles of arbitrary cross-sections of AFM and KPFM images.

chamber pressure and substrate temperature. A schematic showing the principle of IG growth is shown in Fig. 6.6. The aim of this IG was to improve film morphology and alter the oxygen content, while replicating the same film thickness for a meaningful comparison with the originally continuously grown (CG) film. This approach has been found to improve the quality of other metal oxide thin films and devices [224].

Fig. 6.7(a) and (d) show AFM images of the original CG ZnO film (used for devices in Fig. 6.3 and 6.4) and the IG ZnO film, respectively, in both cases after annealing at 800 °C in flowing oxygen. Using the same AFM and a conducting cantilever, KPFM was used to simultaneously scan the surface potential of each film [113, 114]. The resulting surface potential images and profiles of selected cross-sections are shown in Fig. 6.7(b) and (c) for the CG and Fig. 6.7(e) and (f) for the IG ZnO films. The higher potential of the grain boundaries compared to the grain centres is clearly visible in

Table 6.1: RMS roughness, grain size and potential barrier height E_B of 35 nm thick CG and IG ZnO films, measured using the AFM and KPFM, after annealing at 800 °C in oxygen gas. The carrier mobility μ_{model} and defect density at the GB (N_t) were calculated using the GB model (Eq.4.3 and Eq.4.6). μ_{Hall} is the carrier mobility resulting from Hall effect measurements.

Growth mode	**RMS roughness** (nm)	**Grain size** (nm)	**GB E_B** (mV)	μ_{model} (cm^2/Vs)	μ_{Hall} (cm^2/Vs)	N_t (cm^{-2})
Continuous	2.7	56	60	43	30	1.45×10^{12}
Interval	4.1	65	43	72	50	1.23×10^{12}

both films. The morphology and surface potential properties of both films averaged over larger 3 × 3 μm^2 scans are summarized in Table 6.1.

On average, the GB barrier heights of the IG film were 17 mV lower compared to the CG film, confirming a lower GB defect density. At the same time, the measured Hall effect mobility of the IG film increased by more than 60% compared to that of the CG film. Applying Eq. 4.6 to calculate the mobility using the measured GB potential barriers (E_B), from KPFM, gives values of 43 cm^2/Vs and 72 cm^2/Vs for the CG and IG ZnO films, respectively. For the calculated electron mobility (μ_{model}), an in-grain mobility (μ_G) of 180 cm^2/Vs was assumed, based on Hall effect measurements performed on a-plane ZnO crystals with a similar carrier concentration.

To investigate the effect of IG on MESFET stability, MESFETs with IrO_X Schottky gates were fabricated on the IG ZnO film, using the same deposition conditions as before. As expected, the MESFETs showed higher channel mobility (Table 6.2) and consequently higher drain currents. Notably, the extracted intrinsic mobilities of the IrO_X MESFETs on the CG and IG films, 42 cm^2/Vs (Table 5.5) and 70 cm^2/Vs (Table 6.2), respectively, are in excellent agreement with the carrier mobilities calculated using the GB-model and the measured KPFM E_B values. The results of the same PBS and NBS tests, as used earlier, on these devices are shown in Fig. 6.8(a)-(e). The Schottky gate characteristics (not shown here) were unchanged during both stress tests. As shown in Fig. 6.8(b) and (d), the drain current decrease is significantly lower compared to the previous IrO_x MESFET in Fig. 6.3 and 6.4. Over the 24 hours PBS test period

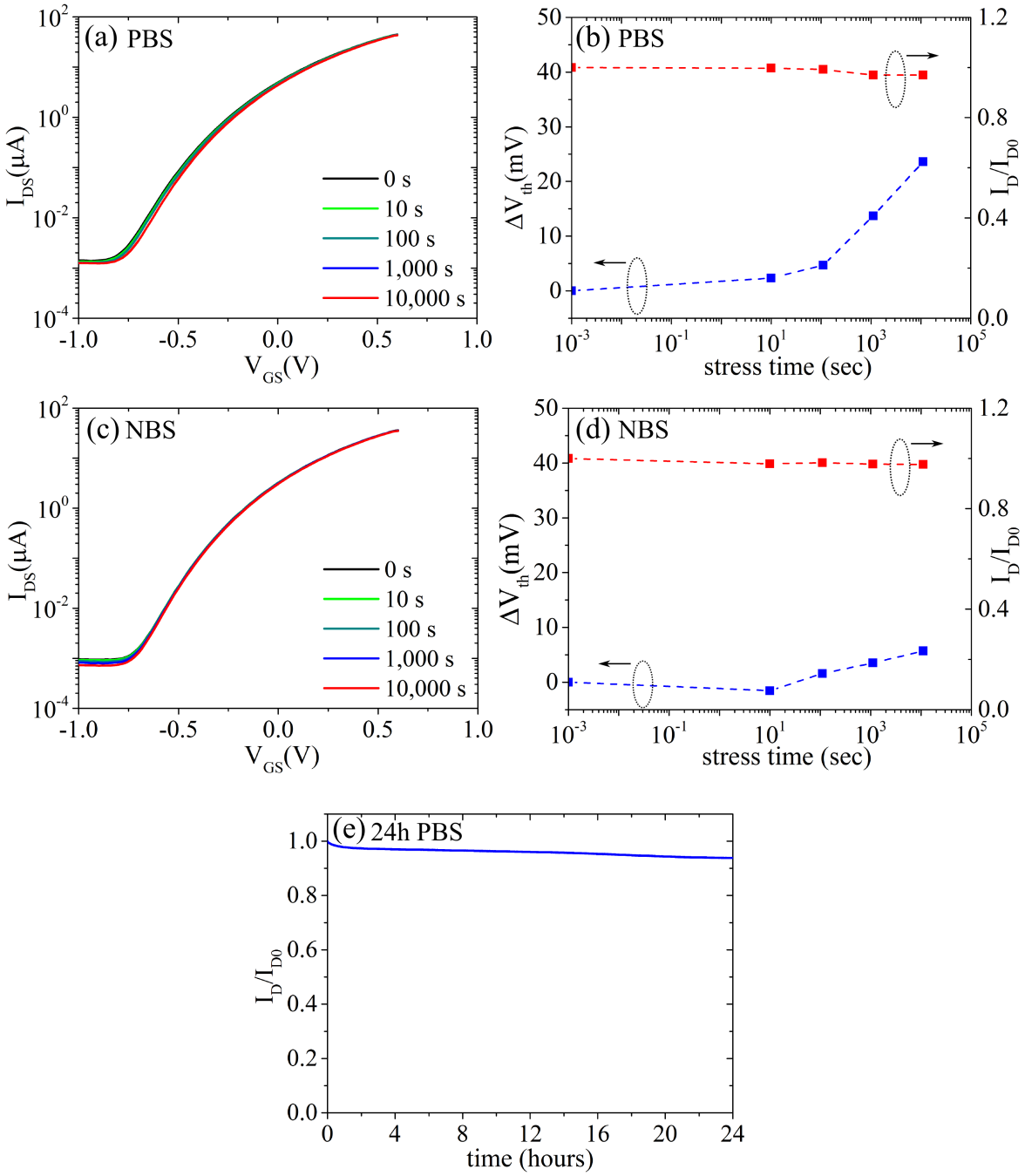

Figure 6.8: Effect of PBS and NBS on an IrO_X MESFET (W = 100 μm / L = 5 μm) fabricated on an interval growth ZnO film; (a) and (b) show the effect of PBS at V_{GS} = 0.6 V and V_{DS} = 1 V on the transfer characteristics; (c) and (d) show the effect of NBS at V_{GS} = -1 V and V_{DS} = 1 V; (e) shows the evolution of channel current during a PBS over 24 h. The Schottky gate characteristics were unaffected during all stress modes.

Table 6.2: Schottky gate characteristics ϕ_B and η, and performance metrics $\mu_{apparent}$, $\mu_{intrinsic}$, I_{on}/I_{off} and SS of an IrO_X MESFET (W = 100μm, L = 5μm) fabricated on the IG ZnO film. The underlying film has a carrier concentration n = 8.1×10^{17} cm^{-3}, a film resistivity ρ = 0.39 Ω.cm and a Hall mobility μ_{Hall} = 50 cm^{-3}/Vs.

ϕ_B (eV)	η	$\mu_{apparent}$ (cm^2/Vs)	$\mu_{intrinsic}$ (cm^2/Vs)	$\boldsymbol{I_{on}/I_{off}}$	$\boldsymbol{SS}$ mV/dec
0.72	1.4	34	70	10^4-10^5	210

the drain current decay was less than 7% and the threshold voltage shift was less than 35 mV, both fully recoverable post-stress. As the nature of GB defects in ZnO is largely unknown, it is difficult to draw definitive conclusions about how the IG technique improved the ZnO film quality. The larger grain size resulting from the IG reduces the overall defect density, but cannot account for the lowering of the GB potential barriers, as shown by KPFM. A possible explanation for this improvement is an *in situ* film relaxation between the growth intervals. Using the GB mobility model (Eq. 4.3) to calculate the GB defect density (N_t) yields defect densities of 1.45×10^{12} cm^{-2} and 1.23×10^{12} cm^{-2} at the GB's of the CG and IG ZnO films, respectively. As such, N_t at the GB decreases by $\sim$ 15% for the IG films. However, due to the exponential relationship between μ and N_t, this has a significant impact on both mobility and current stability. Interestingly, the N_t values derived here from KPFM measurements are very close to values previously reported by *P. Carcia et al.* [19] for RF sputtered ZnO films, that were used in one of the earliest demonstrated ZnO TFTs. In that report, N_t was found to increase with oxygen partial pressure, leading them to speculate that GB trapped oxygen was responsible for the charge trapping defects.

6.4 Temporary breakdown of PLD grown Schottky gates

Electromigration and charge trapping are not the only degradation mechanisms possible in ZnO MESFETs. Fig. 6.9 shows the effect of PBS and NBS on the bias stability

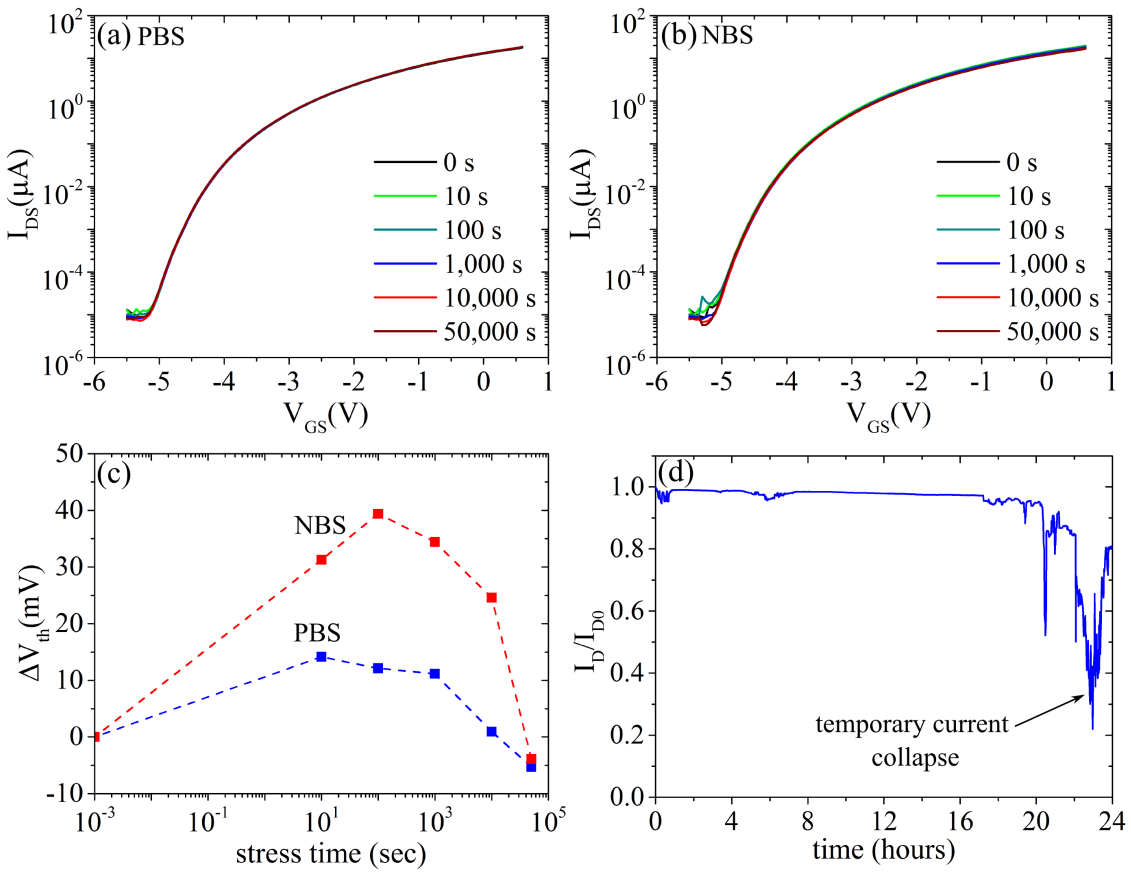

Figure 6.9: (a) Effect of positive bias stress at V_{GS} = 1 V and V_{DS} = 3 V, and (b) effect of negative bias stress at V_{GS} = -4.5 V and V_{DS} = 3 V on the transfer characteristics of a FCVA ZnO MESFET with PLD grown IrO_X Schottky gate (W/L = 25μm/20mum). (c) Effect of PBS and NBS on the threshold voltage shift. (d) The evolution of channel current during a PBS over 24 h. The MESFETs were fabricated on 55 nm thick FCVA ZnO films deposited on 200 °C and subsequently annealed 800 °C in O_2 gas.

of FCVA ZnO MESFETs with PLD grown IrO_X Schottky gates. These MESFETs showed a bias stability similar to that of MESFETs with RF sputtered IrO_X Schottky gates when stressed over 3 hours periods. The channel current decay and the threshold voltage shifts were very small, as shown in Fig. 6.9(a)-(c). However, long-term 24 h PBS stress resulted in a severe 'sudden' drain current collapse as shown in Fig. 6.9(d). This current collapse was found to result from temporary excessive gate leakage and did not result in permanent damage to the gate. The same phenomena was also observed in PLD-IrO_X MESFETs fabricated on thinner FCVA ZnO films. In all cases, the initial device characteristics were recovered post-stress test.

Similar Schottky gate degradation has been reported in many publications and has

been associated with a number of mechanisms, including electrochemical degradation, metal-semiconductor interdiffusion and defect assisted tunnelling through time dependent pathways [228, 229, 230]. However, the recovery of MESFET characteristics post-stress and the absence of this behaviour in all MESFETs with RF sputtered IrO_X Schottky contacts suggest that time-dependent trap formation at the metal-semiconductor interface and conductive percolative paths formation, which are dynamically activated and deactivated, are more likely to be the cause. These phenomena are known to vary with the materials involved and also the fabrication process [230].

6.5 Device characteristics at elevated temperatures

Fig. 6.10 (a,c,e) shows the *I-V* characteristics of AgO_X and IrO_X Schottky contacts measured over a temperature range of 298 K - 468 K (25 °C -195 °C) in 15 K steps. The measurements were performed in ambient conditions using an HP 4155A semiconductor parameter analyser and a microchamber prober station equipped with a Temptronic TP03000 temperature controller. The ideality factor (η) and the effective barrier height (ϕ_B) were determined for each temperature and the results are shown in Fig. 6.10 (b,d,f). The AgO_X devices were only measured up to a temperature of 438 K (165 °C), as it was not possible to accurately extract the Schottky contact parameters beyond this temperature, due to device degradation.

For all Schottky gate types, the forward current showed exponentially increasing behaviour, indicating the dominance of thermionic emission (Eq. 5.4). However, η and ϕ_B evolved differently with temperature depending on the Schottky contact type. In general, both η and ϕ_B decreased with temperature for AgO_X contacts. For PLD grown and sputtered IrO_X Schottky contacts, η increased with temperature while ϕ_B decreased. Whereas IrO_X gated devices were found to be temperature-resilient up to 468 K (195 °C) and recovered their room-temperature characteristics after cooling, AgO_X devices were irreversibly damaged after being subjected to temperatures beyond 390 K (100 °C).

Fig. 6.11(a)-(d) shows the change in transfer characteristics, channel mobilities and

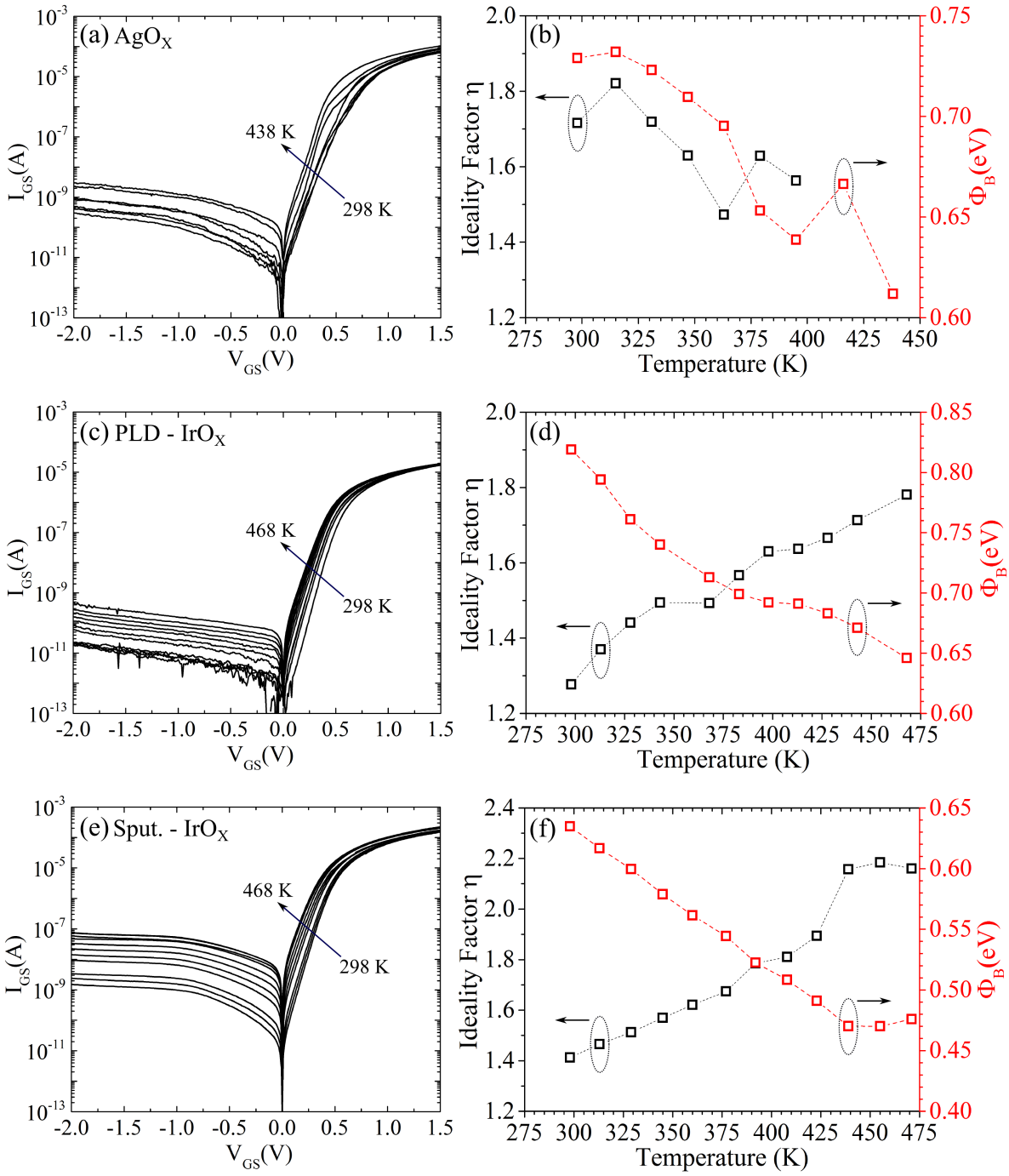

Figure 6.10: The effect of temperature variation on the *I-V* characteristics, ideality factor η and effective barrier height ϕ_B of (a) RF sputtered AgO_X, (b) PLD grown IrO_X and (c) RF sputtered IrO_X Schottky gate contacts with Au capping layers. The characteristics were measured on MESFETs with 35-60 nm thick ZnO channels.

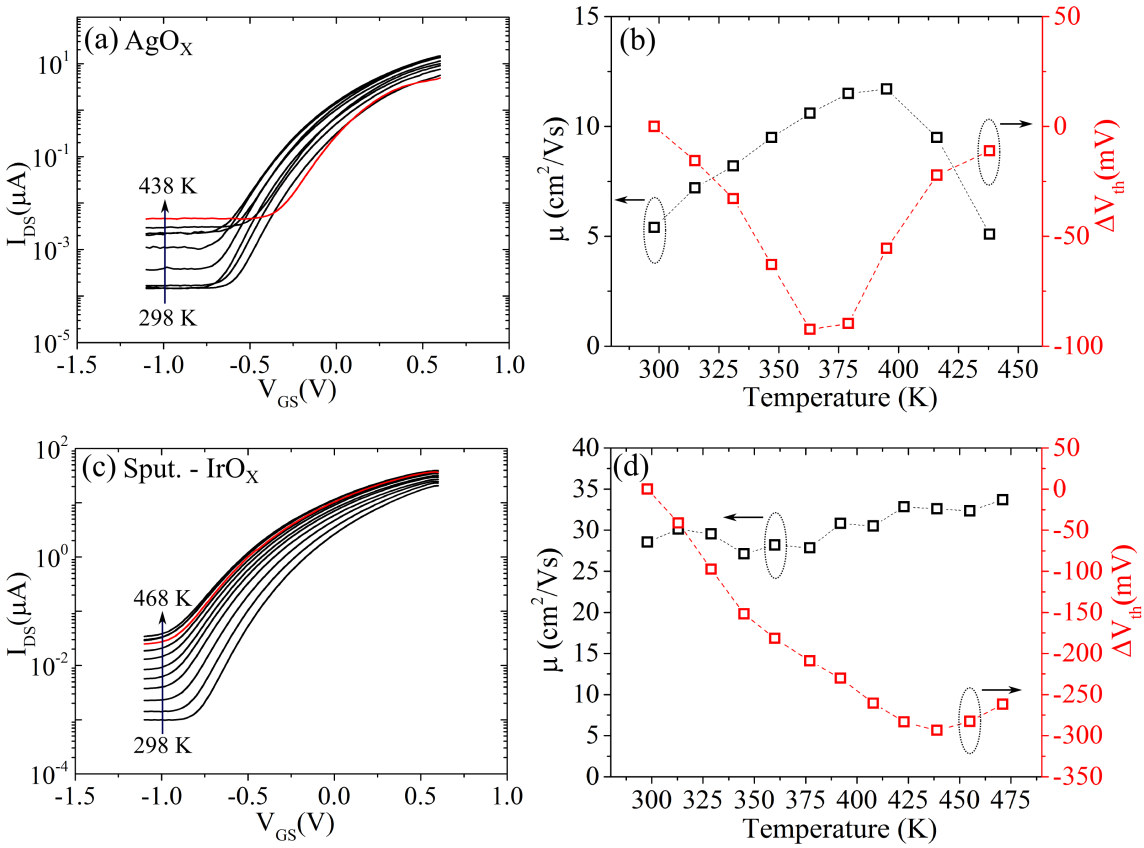

Figure 6.11: The effect of temperature on the transfer characteristics of two MESFETs with sputtered AgO_X and IrO_X gates fabricated on similar 40 nm thick FCVA ZnO films. (a) Transfer characteristics of the AgO_X MESFET over a temperature range of 298 K - 438 K. (b) The channel mobility and threshold voltage shift. (c) Transfer characteristics, and (d) the channel mobility and threshold voltage shift of the IrO_X MESFET over a temperature range of 298 K - 468 K. The red colored transfer curves represent the measurements taken at the highest temperature.

threshold voltage of two FCVA ZnO MESFETs gated with RF sputtered AgO_X and IrO_X Schottky contacts, respectively. For a meaningful comparison, both devices were fabricated on the same 35 nm thick film. Due to the increasing gate leakage with temperature, the off-current of both types of MESFETs increased monotonically. For AgO_X MESFETs, both current and channel mobility increase up to a temperature of 378 K (105 °C). Beyond this temperature, the drain current and channel mobility decrease again to a minimum at 438 K (165 °C). After cooling to room temperature, the initial I_{on}/I_{off} ratio was not recovered.

In contrast, the IrO_X MESFETs showed a substantially higher temperature resilience. As expected, due to thermal generation of carriers, the drain current increased

with increasing temperature. However, this current increase stopped at temperatures 440 - 468 K (167 - 195 °C), as indicated by the red-colored transfer curve measured at 468 K (195 °C). Over the temperature range from 298 K - 468 K (25 °C - 195 °C), only a slight increase in channel mobility was observed. At the same time, the threshold voltage shifted towards more negative voltages. The latter effect can be attributed to the decreasing barrier height, and corresponding decrease in depletion region width as depicted in Fig. 6.10(f). The IrO_X MESFET characteristics were recoverable after cooling to room temperature. However, repeated measurements up to 468 K (195 °C) were found to decrease the channel current slightly. The temperature robustness of the IrO_X MESFET presented here, exceeds that of comparable ZnO based MESFETs with Ag, Pt, Pd and Au Schottky gates reported in the literature [44].

6.6 Summary

In this chapter, thin film FCVA ZnO MESFET devices with AgO_x and IrO_x Schottky gates were characterised in terms of sensitivity to illumination, bias stress and temperature. The results of the tests and the key findings are summarized as follows:

- 1 mW/cm^2 sub-band gap illumination, using 470 nm (blue), 505 nm (green) and 625 nm (red) LED sources, had negligible effect on the transfer characteristics of AgO_X and IrO_X MESFETs, indicating a low concentration of deep level defects in the ZnO channel and the ZnO/Schottky interface.

- Both AgO_X and IrO_X Schottky diodes on FCVA ZnO with semi-transparent ITO capping layers were very responsive to above bandgap (365 nm) UV radiation. For AgO_X devices, a UV reverse current responsivity of 10^5 at a reverse voltage of 2 V was achieved.

- Regardless of bias polarity and gate type, stress related threshold voltage shifts were negligible ($\leq$ 35 mV).

- AgO_X MESFETs showed a bias-polarity dependent degradation. The irreversible

performance degradation during positive bias stress is likely to be due to the electromigration of Ag into the MESFET channel.

- ZnO MESFETs fabricated with IrO_x Schottky gates proved to be resilient under both positive and negative bias stress, suffering only from modest, recoverable channel current decay. The recovery of the MESFET characteristics indicates that temporary charge trapping in the channel is likely to be responsible for this current instability. Mapping of the surface potential of the ZnO channel material with Kelvin probe force microscopy suggested a strong relationship between the defect density at grain boundaries and both channel mobility and current stability. Interval growth techniques were found to reduce the density of defects at grain boundaries and lead to MESFETs with higher current stability.

- IrO_X MESFET were resilient over a temperature range from 25 °C - 195 °C, showing only a slight change in channel mobility and recoverable changes in Schottky gate characteristics. However, AgO_X MESFETs subjected to temperatures from 25 °C - 165 °C showed considerable, irreversible degradation at temperatures higher than 100 °C.

Chapter 7

Conclusions and outlook

In this thesis, the potential of the filtered cathodic vacuum arc (FCVA) technique to deliver device grade ZnO films was explored. The first chapters addressed the electronic and optical properties of FCVA ZnO films deposited on sapphire substrates. The last two chapters involved proving concepts, demonstrating working devices, and addressing device stability. In this chapter, we summarize the main findings and achievements in this work and propose fields of future work related to ZnO FCVA growth and device applications.

7.1 Conclusion

Microstructural properties

- Device grade ZnO thin films (30-60 nm) with an RMS roughness of 1-3 nm were deposited on sapphire substrates. In general, all depositions resulted in dense and macro-particle free polycrystalline films, confirming the efficient filtering capability of FCVA. In addition to polar c-axis oriented ZnO films deposited on a-plane and c-plane sapphire, non-polar a-plane and m-plane ZnO films on r-plane and m-plane sapphire, respectively, were realized. The evolution of ZnO film crystal quality with growth temperature (100 °C - 300 °C) was strongly dependent on the underlying substrate. Most probably due the lowest substrate:film lattice mismatch, c-plane ZnO on a-plane sapphire exhibited the highest crystal quality,

showing an XRD FWHM as low as 0.24° for thick films (∼ 300 nm) and 0.40° for thin films (∼ 40 nm), at an intermediate growth temperature of 200 °C.

- The crystallinity of c-plane and a-plane ZnO films deposited on a-plane and r-plane sapphire, respectively, improved after annealing in O_2, up to a temperature of 800 °C. The accompanying reduction in XRD FWHM and increase in grain size implies a relaxation of the existing strain and healing of lattice defects. However, films on c-plane and m-plane sapphire did not show significant improvement. The corresponding XRD and AFM data suggest that the density of lattice defects has increased, despite grain size improvement. Overall, the achieved crystal quality after annealing, ∼ 0.3° XRD FWHM for 40 nm thick c-plane and a-plane films, was comparable to the quality of ZnO films deposited by MBE and PLD at growth temperatures similar to the annealing temperatures used in this work.

Electronic and optical properties

- The as-deposited FCVA ZnO films showed an intrinsic n-type carrier concentration of 10^{17}-10^{19} cm^{-3}, which decreased with increasing growth temperature up to 300 °C. However, post growth annealing in atmosphere at just 200 °C resulted in a significant loss in native carrier concentration, leading to highly insulating ZnO films. This behaviour is consistent with reports suggesting hydrogen as the dominant donor in as-grown ZnO films. Raman spectra modes, previously associated with the existence of hydrogen by other researchers, were found to disappear upon annealing. However, after annealing at sufficiently high temperatures (> 650 °C), stable n-type doping is introduced via Al diffusion from the sapphire substrates.

- Kelvin probe force microscopy (KPFM) and electrical Hall effect measurements showed that the carrier mobility is predominantly limited by grain boundary potential barriers. Achieving a high mobility required a relatively high carrier concentration and sufficiently large grains. At a carrier concentration of ∼ 10^{18}, a carrier mobility of 30 - 110 cm^2/Vs was achieved for ZnO films on a-plane

sapphire, annealed at 800 °C in O_2 flow, which is comparable to the best reported mobilities for ZnO thin films.

- Annealing in O_2 leads to significant improvement in the electronic structure of FCVA ZnO films, as indicated by low temperature (4 K) PL measurements. The quality of the PL spectra is generally related to the density of structural defects induced by lattice mismatch during growth. ZnO films deposited on a-plane sapphire at 200 °C and 300 °C and annealed at 800 °C have well structured photoluminescence, with sharp NBE emission spectra and well defined Al donor-bound exciton (I_6), free exciton (F_X) and multiple phonon replica emission lines. However, the PL spectra obtained from a-plane ZnO films on r-plane sapphire, although well structured after annealing, exhibit pronounced emission lines characteristic of structural defects such as basal stacking faults [78, 145, 151, 153, 154]. The PL spectrum of as-deposited and annealed m-plane ZnO films showed only broad features, indicating low structural quality.

- All FCVA ZnO films deposited at 200 °C and 300 °C showed an optical transmittance of over 85%. The absorption edges were sharp, indicating low defect density and high UV/visible rejection ratios.

ZnO devices

- A simple scalable ZnO metal-semiconductor field-effect transistor (MESFET) fabrication process was demonstrated based on FCVA grown ZnO thin films. The fabricated devices showed high quality Schottky gate characteristics, with $\phi_B = 0.82$ eV and $\eta = 1.12$ for reactively sputtered AgO_X and PLD grown IrO_X Schottky contacts. The maximum achieved channel mobility of FCVA ZnO MESFETs was 70 cm^2/Vs, significantly larger than that for most reported ZnO TFTs deposited by other techniques. Semi-transparent MESFETs were found to be insensitive to visible light (1 mW/cm^2) and highly responsive to UV irradiation.

- The performance and stability of FCVA ZnO MESFETs is strongly dependent on both the Schottky gate type and Schottky layer deposition technique. In reactively sputtered AgO_X MESFETs, Ag seems to diffuse into the transistor channel, reducing the carrier concentration and mobility. Long-term positive bias stress of AgO_X MESFETs resulted in permanent damage, probably due to Ag electromigration from the Schottky contact into the channel. In contrast, IrO_X MESFETs were found to be resilient to continuous bias stress, suffering only from a small recoverable decrease in channel current. For all device types, the bias stress testes resulted in negligible threshold voltages shifts of ≤ 35 mV.

- Grain boundaries were a limiting factor, both for the channel mobility and the stability of MESFETs. KPFM measurements revealed a correlation between the density of defects at grain boundaries and the channel current stability of IrO_X MESFETs. It was shown that this defect density can be reduced by interval growth techniques, leading to an increase in channel mobility from 42 to 70 cm^2, and significant improvement in channel current stability.

- IrO_X MESFETs showed a high level of temperature resilience, preserving their field effect characteristics and channel mobility over a range from 25 °C - 195 °C. The initial MESFET characteristics were recoverable after cooling to room temperature. MESFETs with RF sputtered AgO_X gates showed a significantly reduced temperature robustness from 25 °C - 100 °C, with higher temperatures causing irreversible damage to the AgO_X gate contacts. At elevated temperatures, the threshold voltage shift was only 300 mV for IrO_X devices at 195 °C.

In conclusion, high quality FCVA ZnO films suitable for the fabrication of electronic devices were successfully and reproducibly deposited. Using ZnO films deposited by FCVA, high quality ZnO Schottky diodes with low ideality factors and high barrier heights were demonstrated. MESFETs, fabricated using simple scalable processes, showed excellent performance, with channel mobilities exceeding those of most ZnO TFTs fabricated via higher cost deposition techniques. Furthermore, these MESFETs

exhibited a high bias stability, high temperature resilience and insensitivity to visible light. The findings prove the significant potential of FCVA grown ZnO for a variety of applications and encourage further investigations into the electronic device applications of FCVA ZnO deposition.

7.2 Future work

7.2.1 Approaches for low temperature deposition

In this thesis, annealing was required to improve crystal quality and introduce thermally stable donor concentrations via Al diffusion from the sapphire substrate. However, in order to fabricate devices on low cost substrates such as quartz and glass, the processing temperature has to be reduced to temperatures lower than 500 °C. Preliminary work conducted in this thesis has shown that as-grown FCVA ZnO films can be improved using in-situ relaxation, i.e. interval growth techniques, where the growth is interrupted every few monolayers for in-situ relaxation/annealing. Fig. 7.1 (a) compares the crystal structure of FCVA ZnO films deposited using the interval growth (IG) method on sapphire and quartz substrates at 300 °C. Growth on quartz yielded c-axis oriented films with comparatively smaller grains. AgO_X Schottky contacts deposited on these as-grown films showed rectification ratios in the range of 10^4 - 10^5. However, the corresponding MESFETs showed insufficient pinch-off. These preliminary findings encourage further investigations and experimentation.

The first step towards a reduction in post-growth annealing temperature is using intentionally doped ZnO targets, such as Al:ZnO, to provide a thermally stable carrier concentration. This should allow the use of intermediate, 300 °C - 500 °C, temperatures for any post-growth treatment required to improve the crystallinity and the electronic quality of the films. Furthermore, reducing on-time (growth period during IG) to fewer monolayers and increasing the *in-situ* relaxation in conjunction with *in-situ* annealing using radiative heating and oxygen pressure modulation could further enhance the effect of interval growth.

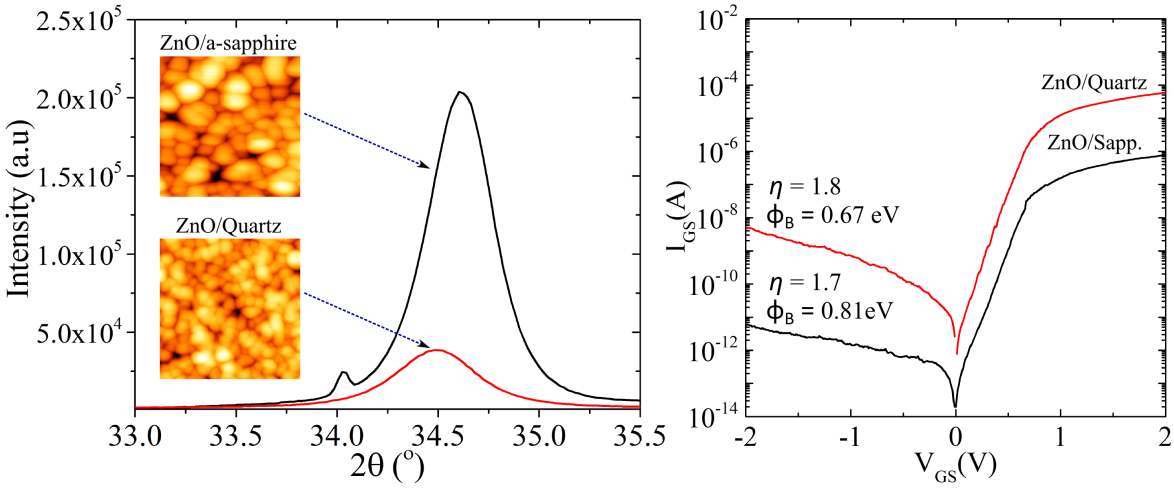

Figure 7.1: (a) XRD diffractogramms and AFM surface morphology (inset) of FCVA ZnO films deposited on a-plane sapphire and quartz substrates at 300 °C. (b) The corresponding *I-V* AgO_X Schottky diode characteristics on the FCVA ZnO films deposited on a-plane sapphire and quartz.

However, cathodic arc methods were far of being fully exploited in this thesis. A promising recent technique is to grow ZnO films using short cathode-substrate distances. Such a setup intensifies the deposited ion flux and enhances atomic scale heating. Al:ZnO films with a high electron mobility deposited at a very high growth rate for TCO applications have already been demonstrated using this technique [7, 231].

7.2.2 Devices and integrated circuits

Improving the AC response

The realization of transparent circuits for driving active matrix displays or reading-out image sensor pixels appears feasible using ZnO films deposited by FCVA, with ITO used as ohmic source/drain contacts and as capping layers for the Schottky gate contacts. Consequently, FCVA ZnO MESFETs can potentially be integrated with OLED technology, where the organic layers are deposited on top of the MESFETs to avoid being damaged by the energetic FCVA deposition [171].

However, in order to exploit the full potential of these MESFETs, contact and interconnection resistances have to be first optimized. Parasitic source/drain and interconnect resistances can have significant impact on the dynamic behaviour and switching

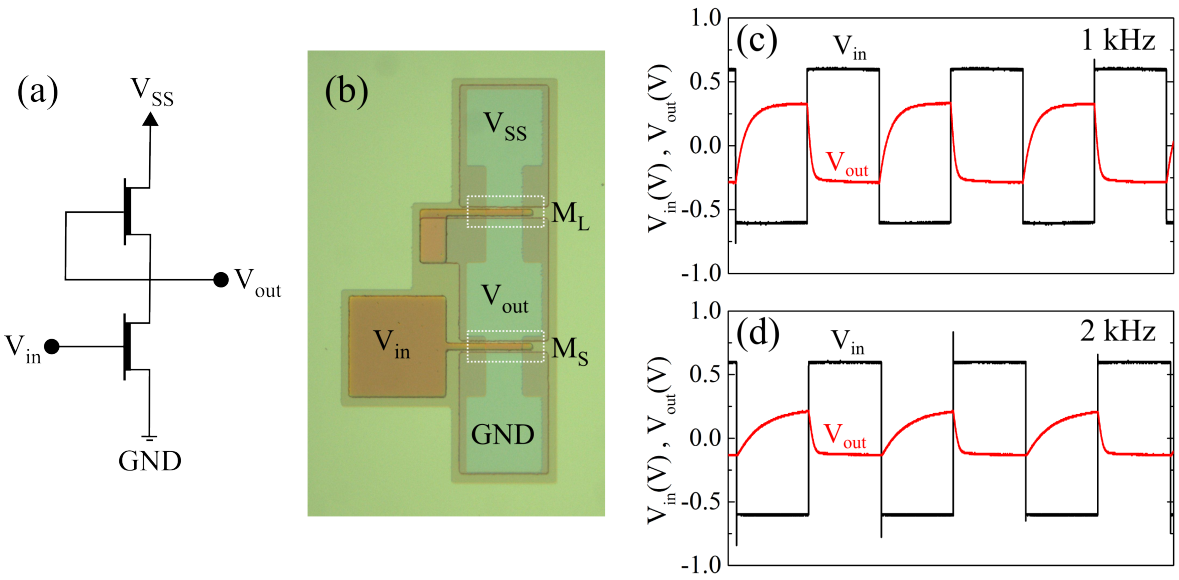

Figure 7.2: Effect of parasitic resistance and capacitance on the dynamic response of a simple MESFET inverter based on IrO_X MESFET with ITO ohmic contacts fabricated on a 800 °C annealed a-plane FCVA ZnO film. (a) A schematic and (b) a micrograph of the simple MESFET inverter. (c) and (d) show the AC response of the MESFET inverter at 1 kHz and 2 kHz, respectively.

speed of MESFETs. This was briefly investigated in this thesis, as illustrated in Fig. 7.2 using a simple MESFET inverter. Both MESFETs have equal width-to-length ratios of W/L=50μm/5μm. The ohmic contacts were made of 50 nm RF sputtered ITO with a specific contact resistance of $\rho_C = 3 \times 10^{-2}$ Ω-cm^2. The 50 nm thick IrO_X Schottky contacts were deposited by PLD and capped by a 50 nm layer of RF sputtered ITO. As can be seen in the figure, a substantial decrease in the output signal can already be observed at a signal frequency of 2 kHz.

The maximum achievable signal frequency (f_{max}) for such an inverter is limited by the rise and fall times of the output signal and is inversely related to the series pull-up (R_L) and pull-down (R_S) resistances and the output capacitance (C_{out}); i.e. $f_{max} \sim 1/(C_{out}\ R_S + C_{out}\ R_L)$. An f_{max} of 1 kHz is sufficient for typical refresh rates of display panels. However, considering that an LCD pixel is a capacitive load, further reduction of the contact resistance is required. For any future application circuits, annealing and/or ion implantation of device contacts will need be considered in the fabrication process. Many metallization schemes with specific contact resistances in the range of

10^{-6} - 10^{-7} Ω-cm^2 on n-type ZnO, far lower than the ones fabricated in this thesis, have been reported in the literature [201, 208].

Integration of passive circuit elements

The demonstration of integrated circuits requires the availability of passive circuit elements. Resistors and capacitors should be relatively easy to develop. ZnO, ITO or metallic layers can be used as resistor elements. However, the reproducibility of the different resistor types needs to be investigated. Metal-insulator-metal (MIM) capacitors can be fabricated using many of the insulators that have been already used in ZnO TFTs, such as SiO_2, SiN_X or HfO_2.

MISFETs

Once a high quality dielectric has been fabricated on FCVA ZnO, it would be interesting to fabricate FCVA MISFETs and directly compare their performance to MESFETs. While MESFETs are inherently capable of higher frequencies [232], they have relatively low gate breakdown voltages. Hence, ZnO MISFETs are more suitable for high voltage applications. These devices could find some useful applications in power electronics, e.g. providing integrated power inversion in solar cells [233].

UV sensing

Monitoring UV radiation levels is one application for which ZnO is well qualified. However, persistent photo-conductivity (PPC) is still a major problem. PPC is a defect related issue that was also found to depend on the presence of oxygen molecules on the ZnO surface. The photocurrent can persist for hours/days after UV illumination, which seriously degrades the response time and the frame rate of sensor arrays. This problem has usually been solved using passivation layers such as SiO_2 and Si_3N_4. Preliminary experiments conducted in this thesis has shown that PPC effects can be removed by applying a high gate voltage pulse (1 V) or a very low negative voltage pulse (channel pinch-off at -1 V). However, this was only possible using opaque MESFETS with PLD

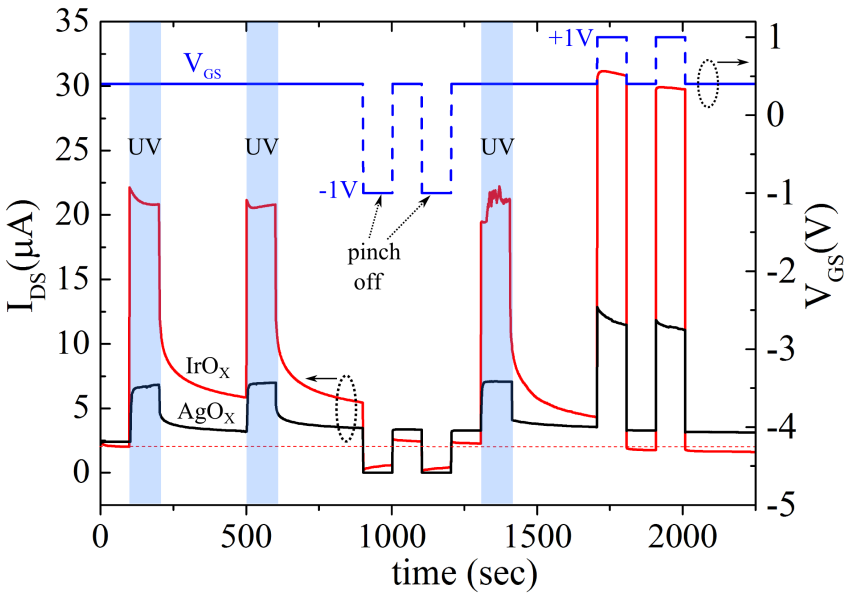

Figure 7.3: The effect of UV illumination on the drain current in an IrO_X (red line) and an AgO_X (black line) MESFET. The persistent photoconductivity (PPC) was erased in the IrO_X MESFET by applying a high positive or very low negative voltage pulse on the gate (blue line).

grown IrO_X gates with a Pt capping layer, as shown in Fig. 7.3. Using a MESFET as a photo-transistor for UV detection might be a more viable approach to overcome PPC issues. However, more investigations are needed to study the effect of gate type and gate-voltage pulse length on PPC. A similar approach has been successfully implemented in a photo sensor array using IGZO TFTs [234].

Schottky barrier batteries

One interesting application would be investigating the use of the FCVA ZnO Schottky diodes for micro-power generation. Micro batteries that directly convert the decay energy from beta (betavoltaics) and alpha (alphavoltaics) particles released by radioactive materials into electrical energy are very attractive for many long-life low power applications, such as implantable medical devices, space electronics and sensor networks. These devices were already used in early pacemakers before being replaced by the cheaper lithium batteries. However, the subject is still actively researched [235]. One of the drawbacks of previous betavoltaic devices was the rapid degradation due to radiation damage. However, radiation experiments on ZnO reveal a very high re-

silience against radiation [236], allowing the use of more energetic radioactive sources. Considering the very high half-life time of radioactive materials and the diminishing power requirements of modern electronic devices and micro electro-mechanical systems (MEMS), Schottky barrier batteries could potentially offer nano to micro Watt power levels for very long times periods.

Bibliography

[1] Ü. Özgür, D. Hofstetter, and H. Morkoç, *"ZnO devices and applications: A review of current status and future prospects,"* Proc. IEEE 98, 1255 (2010).

[2] D.C. Look, C. Coskun, B. Claflin, G.C. Farlow, *"Electrical and optical properties of defects and impurities in ZnO"* Physica B 340-342, 32 (2003).

[3] V. Avrutin, D.J. Silversmith, H. Markoc, *"Doping Asymmetry Problem in ZnO: Current Status and Outlook"* Proc. IEEE 98, 1269 (2010).

[4] A.J. Snell, K.D. Mackenzie, W.E. Spear, and P.G. LeComber, *"Application of amorphous silicon field effect transistors in addressable liquid crystal Display Panels"*, Appl. Phys. 24, 357 (1980).

[5] S.J. Pearton, D.P Norton, K. Ip, Y.W. Heo, and T. Steiner, *"Recent progress in processing and properties of ZnO"*, Prog. Mater. Sci. 50, 293 (2005).

[6] R. Triboulet and J. Perriere , *"Epitaxial growth of ZnO films"*, Prog. Cryst. Growth Charact. Mater. 47, 65 (2003).

[7] R. J. Mendelsberg, S. H. N. Lim, Y. K. Zhu, J .Wallig, D. J. Milliron, and A. Anders, *"Achieving high mobility ZnO:Al at very high growth rates by dc filtered cathodic arc deposition"*, J. Phys. D: Appl. Phys. 44, 232003 (2011).

[8] Ü. Özgür, Y.I. Alivov, C. Liu, A. Teke, M. A. Reshchikov, S. Dogan, V. Avrutin, S. J. Cho, and H. Morkoç, *"A comprehensive review of ZnO materials and devices"*, J. Appl. Phys. 98, 041301 (2005).

[9] J. D. Albrecht, P. P. Ruden, S. limpijumnong, W. R. L. Lambrecht, K. F. Brennan, *"High field electron transport properties of bulk ZnO"*, J. Appl. Phys. 86, 12 (1999).

[10] A. Janotti and C. G. Van de Walle, *"Native point defects in ZnO"*, Phys. Rev. B: Condens. Matter. 76, 165202 (2007).

[11] C. Klingshirn, *"ZnO: From basics towards applications"*, Phyisca Status Solidi B 244, No. 9, 3027 (2007).

[12] A. Anders, Cathodic Arcs: From fractal spots to energetic condensation, Springer-Verlag, pp 33-34, 2008.

[13] T. Yao, S. Hong, Oxide and Nitride Semiconductors, Springer-Verlag, Berlin-Heidelberg, 2009.

[14] R. Quay, Gallium Nitride Electronics, Springer-Verlag, Berlin-Heidelberg 2009.

[15] C. W. Litton, D. C. Reynolds, and T. C. Collins, Zinc Oxide Materials for Electronic and Optoelectronic Device Application, John Wiley and Sons Ltd, 2011.

[16] T. Minami, H. Nanto, and S. Takata, *"Highly Conductive and Transparent Aluminum Doped Zinc Oxide Thin Films Prepared by RF Magnetron Sputtering"*, Jpn. J. Appl. Phys. 23, 5, L280 (1984).

[17] O. Yamazaki, T. Mitsuyu, and K. Wasa, *ZnO Thin-Film SAW Devices*, EEE Trans. Sonics Ultrason. SU-27, No. 6 November (1980).

[18] Y.Q. Fu, J.K. Luo, X.Y. Du, A.J. Flewitt, Y. Li, G.H. Marks, A.J. Walton, and W.I. Milne, *Recent developments on ZnO films for acoustic wave based bio-sensing and microfluidic application: a review*, Sensor Actuat B-Chem 143, 606 (2010).

[19] P. F. Carcia, R. S. McLean, M. H. Reilly, and G. Nunes, Jr., *"Transparent ZnO thin-film transistor fabricated by rf magnetron sputtering"*, Appl. Phys. Lett. 82, 1117 (2003).

[20] Elvira M. C. Fortunato,a) Pedro M. C. Barquinha, Ana C. M. B. G. Pimentel, Alexandra M. F. Gonçalves, António J. S. Marques, Rodrigo F. P. Martins, and Luis M.N. Pereira, *"Wide-bandgap high-mobility ZnO thin-film transistors produced at room temperature"*, Appl. Phys. Lett. 85, 2541 (2004).

[21] A. Ohtomo and A Tsukazaki, *Pulsed laser deposition of thin films and superlattices based on ZnO*, Semicond. Sci. Tech. 20, S1 (2005).

[22] M. Lorenz, *Pulsed Laser Deposition of ZnO-Based Thin Films*, Springer series in materials science 104, 303 (2008).

[23] E. M. Kaidashev, M. Lorenz, H. von Wenckstern, A. Rahm, H.-C. Semmelhack, K.-H. Han, G. Benndorf, C. Bundesmann, H. Hochmuth, and M. Grundmann, *High electron mobility of epitaxial ZnO thin films on c -plane sapphire grown by multistep pulsed-laser deposition*, Appl. Phys. Lett. 82, 3901 (2003).

[24] K. Masuko, A. Ashida, T. Yoshimura, and N. Fujimura, *Electron transport properties of Zn0.88Mn0.12O / ZnO modulation-doped heterostructures*, J. Vac. Sci. Technol. B 27 (3), 1760 (2009).

[25] B. Bayraktaroglu, K. Leedy, and Robert Neidhard, *High-Frequency ZnO Thin-Film Transistors on Si Substrates*, IEEE IEEE Electron Device Lett. 30, NO. 9, 946 (2009).

[26] H. Frenzel, A. Lajn, H. von Wenckstern, M. Lorenz, F. Schein, Z. Zhang, and Marius Grundmann, *Recent Progress on ZnO-Based Metal-Semiconductor Field-Effect Transistors and Their Application in Transparent Integrated Circuits*, Adv. Mater. 22, 5332 (2010).

[27] J. R. Arthur, *"Molecular beam epitaxy"*, Surf. Sci. 500, 189 (2002).

[28] M. A. L. Johnson, S. Fujita, W. H. Rowland, JR., W. C. Hughes, J. W. Cook, JR., and J. F. Schetzina, *MBE growht and Properties of ZnO on Sapphire and SiC Substrates*, J. Electron. Mater. 25, 5 (1996).

[29] Y. Chen, D. M. Bagnall, H-J. Koh, J-T. Park, K. Hiraga, Z. Zhu, and T. Yao, *Plasma assisted molecular beam epitaxy of ZnO on c-plane sapphire: Growth and characterization*, J. Appl. Phys. 84, 7 (1998).

[30] D. M. Bagnall, Y. Chen, M. Y. Shen, Z. Zhu, T. Goto and T. Yao, *Room temperature excitonic stimulated emission from zinc oxide epilayers grown by plasma-assisted MBE*, J. Crys. Growth 184/185, 605 (1998).

[31] A. El-Shaer, A. Che Mofor, A. Bakin, M. Kreye, amd A. Waag, *High-quality ZnO layers grown by MBE on sapphire*, Superlattices Microstruct. 38, 265 (2005).

[32] S. Sasa, T. Maitani, Y. Furuya, T. Amano, K. Koike, M. Yano, and M. Inoue, *Microwave performance of ZnO/ZnMgO hetrostructure field effect transistors*, Phys. Status Solidi A 208, No. 2, 449 (2011).

[33] R.F.C Farrow, *Molecular Beam Epitaxy: Applications to key materials*, Noyes Publications (1995).

[34] B. Wessler, F.F. Lange, and W. Mader, *Textured ZnO thin films on (0001) sapphire produced by chemical solution deposition*, J. Mater. Res., Vol 17, No. 7, 1644 (2001).

[35] B.S. Ong, C. Li, Y. Li, Y. Wu, and R. Loutfy, *Satble, Solution-Processed, High-Mobility ZnO Thin-Film Transistors*, J. Am. Chem. Soc. 129, 2750 (2007).

[36] S.T. Meyer, J.T. Anderson, C.M. Hung, J. Thomson, J. F. Wager, and D.A. Keszler, *Aqueous Inorganic Inks for Low-Temperature Fabrication of ZnO TFTs*, J. Am. Chem. Soc. 130, 17603 (2008).

[37] Ł. Wachnicki, T. Krajewski, G. Łuka, B. Witkowski, B. Kowalski, K. Kopalko a, J.Z. Domagala, M. Guziewicz , M. Godlewski , E. Guziewicz, S. Ferrari, *Monocrystalline zinc oxide films grown by atomic layer deposition*, Thin Solid Films 518, 4556 (2010).

[38] D. H. Leva and S. F. Nelson, *Thin-film electronics by atomic layer deposition*, J. Vac. Sci. Technol. A 30(1), 018501 (2012).

[39] D. Zhao and D. A. Mourey, *Fast Flexible Plastic Substrate ZnO Circuits*, Electron Device Lett. 31, NO. 4, 323 (2010).

[40] S-H. K. Park, C-S. Hwang, M. Ryu, S. Yang, C. Byun, J. Shin, J-I. Lee, K. Lee, M. S. Oh, and S. Im, *Transparent and Photo-stable ZnO Thin-film Transistors to Drive an Active Matrix Organic-Light-Emitting-Diode Display Panel*, Adv. Mater. 21, 678 (2009).

[41] S.J. Lim, S. Kwon, and H. Kim, *ZnO thin films prepared by atomic layer deposition and rf sputtering as an active layer for thin film transistor*, Thin Solid Films 516, 1523 (2008).

[42] Th. Gruber, C. Kirchner, K. Thonke, R. Sauer, and A. Waag, *MOCVD Growth of ZnO for Optoelectronic Applications*, Phys. stat. sol. (a) 192, No. 1, 166 (2002).

[43] H. Frenzel, A. Lajn, M. Brandt, H. von Wenckstern, G. Biehne, H. Hochmuth, M. Lorenz, and M. Grundmann, *ZnO metal-semiconductor field-effect transistors with Ag-Schottky gates*, Appl. Phys. Lett. 92, 192108 (2008).

[44] H. Frenzel, A. Lajn, H. von Wenckstern, G. Biehne, H. Hochmuth, M. Grundmann, *ZnO-based metal-semiconductor field-effect transistors with Ag-, Pt-, Pd-, and Au-Schottky gates*, Thin Solid Films 518, 1119 (2009).

[45] D. Redinger and V. Subramanian, *High-Performance Chemical-Bath-Deposited Zinc Oxide Thin-Film Transistors*, IEEE Trans. Electron Devices, Vol. 54, No. 6, 1301 (2007).

[46] V. Musat, B. Teixeira, E. Fortunato, R.C.C. Monteiro, and P. Vilarinho, *Al-doped ZnO thin films by sol-gel method*, Surf. Coat. Technol. 180-181, 659 (2004).

[47] P.Fons, K.Iwata, A. Yamada,K.Matsubara,K. Nakahara, S.Niki, T. Tanabe, and H.Takasu, *Unixial locked epitaxy of ZnO on the a face of sapphire*, Appl. Phys. Lett. 77, 1801 (2000).

[48] S. Chu, M. Morshed, L. Li, J. Huang, J. Liu, *Smooth surface, low electron concentration, and high mobility ZnO films on c-plane sapphire*, Journal of Crystal Growth 325, 36-40 (2011).

[49] N. A. Jayah, H. Yahaya, M. R. Mahmood, T. Terasako, K. Yasui, and A. M. Hashim, *High electron mobility and low carrier concentration of hydrothermally grown ZnO thin films on seeded a-plane sapphire at low temperature*, Nanoscale Research Lettters, 10:7 (2015).

[50] A. Anders, *Energetic deposition using filtered cathodic arc plasmas*, Vacuum 67, 673 (2002).

[51] A. Anders, *Atomic scale heating in cathodic arc plasma deposition*, Appl. Phys. Lett. 80, 1100 (2002).

[52] M. M. M. Bilek, A. Anders, and I. G. Brown, *Magnetic system for producing uniform coatings using a filtered cathodic arc*, Plasma Sources Sci. Technol. 10, 606 (2001).

[53] X.L. Xu, S.P. Lau, J.S. Chen, G.Y. Chen, and B.K. Tay, *Polycrystalline ZnO thin films on Si (1 0 0) deposited by filtered cathodic vacuum arc*, J. Crys. Growth 223, 201 (2001).

[54] C. Yuen, S. F. Yu, S. P. Lau, Rusli, and T. P. Chen, *Fabrication of n-ZnO:Al/p-SiC(4H) heterojunction light-emitting diodes by filtered cathodic vacuum arc technique*, Appl. Phys. Lett. 86, 241111 (2005).

[55] A. Anders, S. H. N. Lim, K. M. Yu, J. Andersson, J. Rosén, M. McFarland, and J. Brown, *High quality ZnO:Al transparent conducting oxide films synthesized by pulsed filtered cathodic arc deposition*, Thin Solid Films 518, 3313 (2010).

[56] B.K. Tay, Z.W. Zhao, and D.H.C. Chua, *Review of metal oxide films deposited by filtered cathodic vacuum arc technique*, Mater. Sci. Eng. R 52, 1 (2006).

[57] P.J. Martin and A. Bendavid, *Review of the filtered vacuum arc process and materials deposition*, Thin Solid Films 394, 1 (2001).

[58] D. K. Schroder, Semiconductor Material and Device Characterization, 3rd Edition, John Wiley and Sons, Inc., 2008.

[59] Y. Leng, Materials Characterization: Introduction to Microscopic and Spectroscopic Methods, John Wiley and Sons Pte Ltd, 2008.

[60] E. Lifshin, X-ray Characterization of Materials, Wiley-VCH, 1999.

[61] H. Liu, S. Gao, F. Zeng, C. Song, and F. Pan, *Growth of epitaxial c-plane ZnO film on a-plane sapphire by radio frequency reactive magnetron sputtering*, Phys. Status Solidi RRL 7, 587-589 (2013).

[62] H. E. Swanson and R. K. Fuyat, *Standard X-ray Diffraction Powder Patterns*, National Bureau of Standards Circular 539, Volume 2, 1953.

[63] A. Chakraborty, H. Xing, M. D. Craven, S. Keller, T. Mates, J. S. Speck, S. P. DenBaars, and U. K. Mishra, *Nonpolar a-plane p-type GaN and p-n Junction Diodes*, J. Appl. Phys. 96, 4495 (2004).

[64] T. Mitsuyu, S. Ono, and K. Wasa, *Structures and SAW properties of rf-sputtered single-crystal films of ZnO on sapphire*, J. Appl. Phys. 51, 2464-2470 (1980).

[65] C. Munuera, J. Zùñiga-Pérez, J.F. Rommeluere, V. Sallet, R. Triboulet, F. Soria, V. Muñoz-Sanjose, C. Ocal, *Morphology of ZnO grown by MOCVD on sapphire substrates*, J. Crys. Growth 264, 70 (2004).

[66] S.K. Han, S.K. Hong, J.W. Lee, J.Y. Lee, J.H. Song, Y.S. Nam, S.K. Chang, T. Minegishi, and T. Yao , *Structural and optical properties of non-polar A-plane ZnO films grown on R-plane sapphire substrates by plasma-assisted molecular-beam epitaxy*, J. Crys. Growth 309, 121 (2007).

[67] Y. Chen, H.-J. Ko, S.-K. Hong, and T. Yao, *Morphology evolution of ZnO (000$\bar{1}$) surface during plasma-assisted molecular-beam epitaxy*, Appl. Phys. Lett. 80, 8, 1358 (2002).

[68] T. Hamada, A. Ito, E. Fujii, D. Chu, K. Kato, and Y. Masuda, *Preparation of single-crystalline ZnO films on ZnO-buffered a-plane sapphire by chemical bath deposition*, J. Crys. Growth 311, 3687 (2009).

[69] C-Y. Peng, J-S. Tian, W-L. Wang, Y-T. Ho, L. Chang, *Morphology evolution of a-plane ZnO films on r-plane sapphire with growth by pulsed laser deposition*, Appl. Surf. Sci. 265, 553 (2013).

[70] L. Gerward and J. S. Olsen, *The High-Pressure Phase of Zincite*, J. Synchrotron Rad. 2, 233 (1995).

[71] C-Y. Peng, J-S. Tian, W-L. Wang, Y-T. Ho, S-C. Chuang, Y-H. Chu, and L. Chang, *Effect of growth temperature on a-plane ZnO formation on r-plane sapphire*, J. Vac. Sci. Technol. A 29, 03A110 (2011).

[72] T. Moriyama and S. Fujita, *Epitaxial growth of nonploar ZnO by MOVPE*, Phys. stat. sol. (c) 3, 726 (2006).

[73] Y. Kashiwaba, T. Abe, A. Nakagawa, H. Endo, I. Niikura, and Y. Kashiwaba, *Homoepitaxial growth of high-quality nonpolar ZnO films by MOCVD and evaluation of the homoepitaxial ZnO films by XRD measurements for asymmetric planes*, Phys. Status Solidi A 206, 944 (2009).

[74] J. M. Pierce, B. T. Adekore, R. F. Davis, and F. A. Stevie, *Homoepitaxial growth of dense ZnO(0001) and ZnO(11$\bar{1}$0) films via MOVPE on selected ZnO susbtrates*, J. Cryst. Growth 283, 147 (2005).

[75] Y. Li, Y. Zhang, H. He, Z. Ye, J. Jiang, J. Lu, and J. Huang, *Epitaxial growth of non-polar m-plane ZnO thin films by pulsed laser deposition*, Mater. Res. Bull. 47, 2235 (2012).

[76] J-H. Kim, S-K. Han, S-I. Hong, S-K. Hong, J-W. Lee and J-Y. Lee, J-H. Song, J. S. Park, and T. Yao *Growth and structural properties of ZnO films on (10-10) m-plane sapphire substrates by plasma-assisted molecular beam epitaxy*, J. Vac. Sci. Technol. B 27, 1625 (2009).

[77] H. C. Ong, A. X. E. Zhu, and G. T. Du, *Dependence of the excitonic transition energies and mosaicity on residual strain in ZnO thin films*, Appl. Phys. Lett. 80, 941 (2002).

[78] J.M. Chauveau, P. Vennéuguès, M. Laügt, C. Deparis, J. Zuniga-Perez, and C. Morhain, *Interface structure and anisotropic strain relaxation of nonpolar wurtzite* (11$\bar{2}$0) *and* (10$\bar{1}$0) *orientations: ZnO epilayers grown on sapphire*, J. Appl. Phys. 104, 073535 (2008).

[79] S. Mridha and D. Basak, *Effect of thickness on the structural, electrical and optical properties of ZnO films*, Mater. Res. Bull. 42, 875 (2007).

[80] V. Gupta and A. Mansingh, *Influence of postdeposition annealing on the structural and optical properties of sputtered zinc oxide film*, J. Appl. Phys. 80, 1063 (1996).

[81] R. D. Vispute, V. Talyansky, Z. Trajanovic, S. Choopun, M. Downes, R. P. Sharma, T. Venkatesan, M. C. Woods, R. T. Lareau, K. A. Jones, and A. A. Iliadis, *High quality crystalline ZnO buffer layers on sapphire (001) by pulsed laser deposition for III-V nitrides*, Appl. Phys. Lett. 70, 2735 (1997).

[82] S. Elzwawi, H-S. Kim, M. Lynam, E. L. H. Mayes, D. G. McCulloch, M. W. Allen, and J. G. Partridge, *Stable n-channel metal-semiconductor field effect transistors on ZnO films deposited using a filtered cathodic vacuum arc*, Appl. Phys. Lett. 101, 243508 (2012).

[83] T. Ungár, *Microstructural parameters from X-ray diffraction peak broadening*, Scripta Mater. 51, 777 (2004).

[84] P. Pant, J.D. Budai, and J. Narayan, *Nonpolar ZnO film growth and mechanism for anisotropic in-plane strain relaxation*, Acta Mater. 58, 1097 (2010).

[85] S. Adachi, Properties of Semicoductor Alloys: Group-iV, III-V and II-VI Semiconductors, John Wiley & Sons , 2009.

[86] D.C. Look, D.C. Reynolds, J.R. Sizelove, R.L. Jones, C.W. Litton, G. Cantwell, and W.C. Harsch, *Electrical properties of bulk ZnO*, Solid State Commun. 105, 399 (1998).

[87] B.K. Meyer, H. Alves, D.M. Hofmann, W. Kriefseis, D. Forster, E. Bertram, J. Christen, A. Hoffmann, M. Straßburg, M. Dworzak, U. Haboeck, and A.V. Rodina, *Bound exciton and donor-acceptor pair recombinations in ZnO*, Phys. Stat. Sol. (b) 241, 231 (2004).

[88] M.D. McCluskey and S.J. Jokela, *Defects in ZnO*, J. Appl. Phys. 106, 071101 (2009).

[89] A. Janotti and C. Van de Walle, *New insights into the role of native point defects in ZnO*, J. Crys. Growth 287, 58 (2006).

[90] A.A. Sokol, S.A. French, S.T. Bromley, C.R.A. Catlow, H.J.J. van Dam, and P. Sherwood, *Point defects in ZnO*, Faraday Discuss., 267, 267 (2007).

[91] S. B. Zhang, S.-H. Wei, and A. Zunger, *Intrinsic n-type versus p-type doping asymmetry and the defect physics of ZnO*, Phys. Rev. B. 63, 075205 (2001).

[92] F.A. Selim, M.H. Weber, D. Solodovnikov, and K.G. Lynn, *Nature of Native Defects in ZnO*, Phys. Rev. Lett. 99, 085502 (2007).

[93] D.C. Look, G.C. Farlow, P. Reunchan, S. Limpijumnong, S.B. Zhang, and K. Nordland, *Evidence for Native-Defect Donors in n-Type ZnO*, Phys. Rev. Lett. 95, 225502 (2005).

[94] A.F. Kohan, G. Ceder, D. Morgan, and C.G. Van de Walle *First-principles study of native point defects in ZnO*, Phys. Rev. B 61, 15019 (2001).

[95] F. Tuomisto, K. Saarinen, D.C. Look, and G.C. Farlow, emphIntroduction and recovery of point defects in electron-ittadiated ZnO, Phys. Rev. B 72, 085206 (2005).

[96] C.G. Van de Walle, *Hydrogen as a Cause of Doping in Zinc Oxide*, Phys. Rev. Lett 85, 1012 (2000).

[97] A. Janotti and C.G. Van de Walle, *Hydrogen multicentre bonds*, nature materials 6, 44 (2006).

[98] D.M. Hofmann, A. Hofstaetter, F. Leiter, H. Zhou, F. Henecker, B. Meyer, S.B. Orlinskii, J. Schmidt, and P.G. Baranov, *Hydrogen: A relevant Shallow Donor in Zinc Oxide*, Phys. Rev. Lett 88, 045501 (2002).

[99] A. Behrends, A. Wagner, M.A.M. Al-Suleiman, H-J. Lugauer, M. Strassburg, R. Walter, A. Weimar, A. Waag, and A. Bakin, *Transparent conductive Ga-doped ZnO films fabricated by MOCVD*, Phys. Status. Solidi A 209, 708 (2012).

[100] Y. Yan, M.M. Al-Jassim, and S-H. Wei, *Doping of ZnO by group-IB elements*, Appl. Phys. Lett. 89, 181912 (2006).

[101] M.A. Myers, J.H. Lee, and H. Wang, *Highly stable non-polar Ag-doped ZnO thin films grown on r-cut sapphire*, Mater. Lett. 100, 78 (2013).

[102] J. Chai, R.J. Mendelsberg, R.J. Reeves, J. Kennedy, H. Von Wenckstern, M. Schmidt, M. Grundmann, K. Doyle, T.H. Myers, and S.M. Durbin, *Identification of deep acceptor level in ZnO due to silver doping*, J. Electron. Mater. 39, 577 (2010).

[103] C. G. Van de Walle, *Hydrogen as a Cause of Doping in Zinc Oxide*, Phys. Rev. Lett. 85, 1012 (2000).

[104] J. W. Y. Seto, *The electrical properties of polycrystalline silicon films*, J. Appl. Phys. 46, 12 (1975).

[105] G. Baccarani, B. Riccò, and G. Spadini, *Transport properties of polycrystalline silicon films*, J. Appl. Phys. 49, 5565 (1978).

[106] J. Levinson, F. R. Shepherd, P. J. Scanlon, W. D. Westwood, G. Este, and M. Rider, *Conductivity in polycrystalline semiconductor thin film transistors*, J. Appl. Phys. 53, 1193 (1982).

[107] S.M. Sze and K.K. Ng, *Physics of Semiconductor Devices*, John Wiley and Sons Inc., (2007)

[108] M.W. Allen, C.H. Swartz, T.H. Myers, T.D. Veal, C.F. McConville, and S.M. Durbin, *Bulk transport measurements in ZnO: The effect of surface electron layers*, Phys. Rev. B 81, 075211 (2010).

[109] D.H. Zhang, *Adsorption and photodesorption of oxygen on the surface and crystallite interfaces of sputtered ZnO films*, Mater. Chem. Phys. 45, 248 (1996).

[110] L. Li, C.X. Shan, S.P. Wang, B.H. Li, J.Y. Zhang, B. Yao, D.Z. Shen, X.W. Fan, and Y.M. Lu, *Degenerate layer at the ZnO/sapphire interface*, J. Phys. D: Appl. Phys. 42, 195403 (2009).

[111] X.L. Xu, C.D. Beling, S. Fung, Y.W. Zhao, N.F. Sun, T.N. Sun, Q.L. Zhang, H.H. Zhan, B.Q. Sun, J.N. Wang, W.K. Ge, and P.C. Wong, *Formation mechanism of degenerate thin layer at the interface of GaN/sapphire system*, Appl. Phys. Lett. 76, 152 (2000).

[112] D.C. Look and R.J. Molnar, *Degenerate layer at GaN/sapphire interface: Influence on Hall-effect measurements*, Appl. Phys. Lett. 70, 3377 (1997).

[113] M. Nonnenmacher, M.P. O;Boyle, and H.K. Wickramasinghe, *Kelvin probe force microscopy*, Appl. Phys. Lett. 58, 2921 (1991).

[114] H. Huang, H. Wang, J. Zhang, and D. Yan, *Surface potential images of polycrystalline organic semiconductors obtained by Kelvin probe force microscopy*, Appl. Phys. A 95, 125 (2009).

[115] C. F. Klingshirn. Semiconductor optics. Springer Berlin / Heidelberg, (2005).

[116] C. V. Raman, *The molecular scattering of light*, Nobel Lecture, December 11, 1930.

[117] J.K. Dangbegnon, K.T. Roro, and J.R. Botha, *Towards p-type ZnO using post-growth annealing*, Phys. Stat. Sol. (a) 205, 155 (2008).

[118] K. Ogata, K. Sakurai, Sz. Fujita, Sg. Fujita, and K. Matsushige, emphEffects of thermal annealing of ZnO layers grown by MBE, J. Cryst. Growth. 214/215, 312 (2000).

[119] W. Mtangi, F.D. Auret, W.E. Meyer, M.J. Legodi, P.J. Janse van Rensburg, S.M.M. Coelho, M. Diale, and J.M. Nel, *Effects of hydrogen, oxygen, and argon annealing on the electrical properties of ZnO and ZnO devices studied by current-voltage, deep level transient spectroscopy, and Laplace DLTS*, J. Appl. Phys. 111, 094504 (2012).

[120] W.C.T.Lee, M. Henseler, P. Miller, C.H. Swartz, T.H. Myers, R.J. Reeves, and S.M. Durbin., *Effect of annealing on the morphology and optoelectrical characteristics of ZnO thin films grown by plasma-assisted molecular beam epitaxy*, J. Electron. Mater. 35, 1316 (2006).

[121] P.T. Hsieh, Y.C. Chen, M.S. Lee, K.S. Kao, M.C. Kao, and M.P. Houng, *The effect of oxygen concentration on ultraviolet luminescence of ZnO films by sol-gel technology and annealing*, J Sol-Gel Sci Technol 47, 1 (2008).

[122] K. Iwata, H. Tampo, A. Yamada, P. Fons, K. Matsubara, K. Sakurai, S. Ishizuka, and S. Niki. *Growth of ZnO and device applications*, Appl. Surf. Sci. 244, 504 (2005).

[123] H.S. Kang, J.S. Kang, J.W. Kim, and S.Y. Lee, *Annealing effect on the property of ultraviolet and green emissions of ZnO thin films*, J. Appl. Phys. 95, 1246 (2004).

[124] J-H. Lee, B-W. Yeo, B-O. Park, *Effects of the annealing treatment on electrical and optical properties of ZnO transparent conduction films by ultrasonic spraying pyrolysis*, Thin Solid Films 457, 333 (2004).

[125] M.G. Wardle, J.P. Goss, and P.R. Briddon, *First-principles study of the diffusion of hydrogen in ZnO*, Phys. Rev. Lett. 96, 205504 (2006).

[126] G.A. Shi, M. Stavola, S.J. Pearton, M. Thieme, E.V. Lavrov, and J. Weber, *Hydrogen local modes and shallow donors in ZnO*, Phys. Rev. B 72, 195211 (2005).

[127] N. Ashkenov, B.N. Mbenkum, C. Bundesmann, V. Riede, M. Lorenz, D. Spemann, E.M. Kaidashev, A. Kasic, M. Schubert, and M. Grundmann, *Infrared dielectric functions and phonon modes of high-quality ZnO films*, J. Appl. Phys. 93, 126 (2003).

[128] G.J. Exarhos and S.K. Sharma, *Influence of processing variables on the structure and properties of ZnO films*, Thin Solid Films 270, 27 (1995).

[129] I. Lorite, P. Díaz-Carrasco, M. Gabás, J.F. Fernández, and J.L. Costa-Kämer, *Correlation between intrinsic defects and carrier transport in ZnO thin films by confocal Raman spectroscopy*, Mater. Lett. 109, 167 (2013).

[130] F. Rubio-Marcos, C.V. Manzano, J.J. Reinosa, I. Lorite, J.J. Romero, J.F. Fernández, and M.S. Martín-González, *Modification of optical properties in ZnO particles by surface deposition and anchoring of NiO nanoparticles*, J. Alloys Compd. 509, 2891 (2011).

[131] C.F. Windisch, G.J. Exarhos, C. Yao, and L-Q. Wang, *Raman study of the influence of hydrogen on defects in ZnO*, J. Appl. Phys. 101, 123711 (2007).

[132] C. Bundesmann, N. Ashkenov, M. Schubert, D. Spemann, T. Butz, E.M. Kaidashev, M. Lorenz, and M. Grundmann, *Raman scattering in ZnO thin films with Fe, Sb, Al, Ga, and Li*, Appl. Phys. Lett. 83, 1974 (2003).

[133] A. Schildknecht, R. Sauer, K. Thonke, *Donor-related defect states in ZnO substrate material*, Physica B 340-342, 205 (2003).

[134] D.C. Look, D.C. Reynolds, C.W. Litton, R.L. Jones, D.B. Eason, and G. Cantwell, *Characterization of homoepitaxial p-type ZnO grown by molecular beam epitaxy*, Appl. Phys. Lett. 81, 1830 (2002).

[135] I.C. Robin, P. Marotel, A.H. El-Shaer, V. Petukhov, A. Bakin, A. Waag, M. Lafossas, J. Garcia, M. Rosina, A. Ribeaud, S. Brochen, P. Ferret, and G. Feuillet, *Compared optical properties of ZnO heteroepitaxial, homoepitaxial 2D layers and nanowires*, Journal of Crystal Growth 311, 2172 (2009).

[136] M.R. Wagner, G. Callsen, J.S. Reparaz, J.-H. Schulze, R. Kirste, M. Cobet, I.A. Ostapenko, S. Rodt, C. Nenstiel, M. Kaiser, A. Hoffman, A.V. Rodina, M.R. Philips, S. Lautenschläger, S. Eisermann, and B.K. Meyer, *Bound excitons in ZnO: Structural defect complexes versus shallow impurity centers*, Phys. Rev. B 84, 035313 (2011).

[137] H. Alves, D. Pfisterer, A. Zeuner, T. Riemann, J. Christen, D.M. Hofmann, and B.K. Meyer, *Optical investigations on excitons bound to impurities and dislocations in ZnO*, Optical Materials 23, 33 (2003).

[138] D.C. Reynolds, D.C. Look, B. Jogai, and H. Markoc, *Similarities in the band-edge and deep-centre photoluminescence mechanisms of ZnO and GaN*, Solid State Commun. 101, 643 (1997).

[139] Y.W. Heo, D.P. Norton, and S.J. Pearton, *Origin of green luminescence in ZnO thin films grown by molecular-beam epitaxy*, J. Appl. Phys. 98, 073502 (2005).

[140] N.Y. Garces, L. Wang, L. Bai, N.C. Giles, L.E. Halliburton, and G. Cantwell, *Role of copper in the green luminescence from ZnO crystals*, Appl. Phys. Lett. 81, 622 (2002).

[141] M.A. Reshikov, V. Avrutin, N. Izyumskaya, R. Shimada, H. Markoc, and S.W. Novak, *About the Cu-related green luminescence band in ZnO*, J. Vac. Sci. Technol. B 27(3), 1749 (2009).

[142] R. Dingle, *Luminescent transitions associated with divalent copper impurities and the green emission from semiconducting zinc oxide*, Phys. Rev. Lett. 23, 579 (1969).

[143] A. El-Shaer, A.C. Mofor, A. Bakin, M. Kreye, A. Waag, *High-quality ZnO layers grown by MBE on sapphire*, Superlattice Microst. 38, 265 (2005).

[144] X.L. Xu, S.P. Lau, and B.K. Tay, *Structural and optical properties of ZnO thin films produced by filtered cathodic vacuum arc*, Thin Sold Films 398-399, 244 (2001).

[145] J.-M. Chauveau, C. Morhain, B. Lo, B. Vinter, P. Vennégueès, M. Lauügt, D. Buell, M. Tesseire-Doninelli, and G. Neu, *Growth and characterization of A-plane ZnO and ZnCoO based heterostructures*, Appl. Phys. A 88, 65 (2007).

[146] Y.S. Nam, S.W. Lee, K.S. Baek, S.K. Chang, J-H. Song, J-H. Song, S.K. Han, S-K. Hong, and T. Yao, *Anisotropic optical properties of free and bound excitons in highly strained A-plane ZnO investigated with polarized photoreflectance and photoluminescence spectroscopy*, Appl. Phys. Lett. 92, 201907 (2008).

[147] M. Schirra, R. Schneider, A. Reiser, G.M. Prinz, M. Feneberg, J. Biskupek, U. Kaiser, C.E. Krill, R. Sauer, and K. Thonke, *Acceptor-related luminescence at 3.314 eV in zinc oxide confined to crystallographic line defects*, Physica B 401, 362 (2007).

[148] M.S. Kim, G. Nam, S. Kim, D.Y. Kim, D-Y. Lee, J.S. Kim, S-O. Kim, J.S. Kim, J.S. Son, and J-Y. Leem, *Photoluminescence studies of ZnO thin films on R-plane sapphire substrates grown by sol-gel method*, JOL 132, 2581 (2012).

[149] J. Elanchezhiyan , K.R. Bae, W.J. Lee, B.C. Shin, and S.C. Kim, *Growth and characterization of non-polar ZnO thin films by pulsed laser deposition*, Materials Letters 64, 1190 (2010).

[150] S. Lautenschlaeger, S. Eisermann, M.N. Hofmann, U. Roemer, M. Pinnisch, A. Laufer, B.K. Meyer, H. von Wenckstern, A. Lajn, F. Schmidt, M. Grundmann, J. Blaesing, and A. Krost, *Morphological , structural and electrical investigations on non-polar a-plane ZnO epilayers*, J. of Crys. Growth 312, 2078 (2010).

[151] P. Vennégueès, J.-M. Chauveau, M. Korytov, C. Deparis, J. Zuniga-Perez, and C. Morhain, *Interfacial structure and defect analysis of nonpolar ZnO films grown on R-plane sapphire by molecular beam epitaxy*, J. Appl. Phys. 103, 083525 (2008).

[152] J. W. Lee, S. K. Han, S.-K. Hong, J. Y. Lee, T. Yao, *Characterization of microstructure and defects in epitaxial ZnO* $(11\bar{2}0)$ *films on* Al_2O_3 $(1\bar{1}02)$ *substrates by transmission electron microscopy*, Journal of Crystal Growth 310, 4102 (2008).

[153] P. Corfdir, P. Lefebvre, J. Levrat, A. Dussaigne, J.-D. Ganiere, D. Martin, J. Ristic, T. Zhu, N. Grandjean, and B. Deveaud-Pledran, *Exciton localization on basal stacking faults in a-plane epitaxial lateral overgrown GaN grown by hybride vapor phase epitaxy*, J. Appl. Phys. 105, 043102 (2009).

[154] P. Vennégueès, J.-M. Chauveau, Z. Bougrioua, T. Zhu, D. Martin, and Grandjean, *On the origin of basal stacking faults in nonpolar wurtzite films epitaxially grown on sapphire substrates*, J. Appl. Phys. 112, 113518 (2012).

[155] D. Hull, *Introduction to Dislocations*, 2nd Ed, Pergamon Press, 1975.

[156] G. Tang, H. Liu, and W. Zhang, *The Variation of Optical Band Gap for ZnO:In Films Prepared by Sol-Gel Technique*, Advances in Materials Science and Engineering 2013, ID:348601 (2013).

[157] V. Srikant and D. R. Clarke, *Optical absorption edge of ZnO thin films: The effect of substrate*, J. Appl. Phys. 81, 6357 (1997).

[158] K. H. Kim, K. C. Park, and D. Y. Ma, *Structural, electrical and optical properties of aluminum doped zinc oxide films prepared by radio frequency magnetron sputtering*, J. Appl. Phys. 81, 7764 (1997).

[159] Y. G. Wang, S. P. Lau, H. W. Lee, S. F. Yu, B. K. Tay, X. H. Zhang, K. Y. Tsee, and H. H. Hng, *Comprehensive study of ZnO films prepared by filtered cathodic vacuum arc at room temperature*, J. Appl. Phys. 94, 1597 (2003).

[160] H. Frenzel, A. Lajn, and Marius Grundmann, *One decade of fully transparent oxide thin-film transistors: fabrication, performance and stability*, Phys. Status Solidi PRL 7, 605 (2013).

[161] P. Barquinha, R. Martins, L. Pereira, and E. Fortunato, *Transparent Oxide Electronics: From Materials to Devices*, John Wiley & Sons Ltd, (2012).

[162] P.K. Weimer, H. Borkan, G. Sadasiv, L. Meray-Horvath, and F.V. Shallcross, *Integrated circuits incorporating thin-film active and passive elements*, Proc. IEEE, 1479 (1964).

[163] T.P. Brody, J.A. Asars, and G.D. Dixon, *A 6×6 Inch 20 Lines-per-Inch Liquid-Crystal Display Panel*, IEEE Trans. Electron Devices 20, 995 (1973).

[164] J. Kanicki, F.R. Libish, J. Griffith, and R. Polastre, *Performance of thin hydrogenated amorphous silicon thin-film transistors*, J. Appl. Phys. 69, 2339 (1991).

[165] S. Masuda, K. Kitamura, Y. Okumura, S. Miyatake, H. Tabata, and T. Kawai. *Transparent thin film transistors using ZnO as an active channel layer and their electrical properties*, J. Appl. Phys. 93, 1625 (2003).

[166] B.J. Norris, J. Anderson, J.F. Wager, and D.A. Keszlar, *Spin-coated zinc oxide transparent transistors*, J. Phys. D: Appl. Phys. 36, L105 (2003).

[167] K. Nomura, H. Ohta, A. Takagi, T. Kamiya, M. Hirano, and H. Hosono, *Room-temperature fabrication of transparent flexible thin-film transistors using amorphous oxide semiconductors*, Nature 432, 488 (2004).

[168] R. L. Hoffman, *ZnO-channel thin-film transistors:Channel mobility*, J. Appl. Phys. 95, 5815 (2004).

[169] H.Q Chiange, J.F. Wager, R.L. Hoffman, J. Jeong, and D.A. Keszler, *High mobility transparent thin-film transistors with amorphous zinc tin oxide channel layer*, Appl. Phys. Lett. 86, 013503 (2005).

[170] S. Sasa, M. Ozaki, K. Koike, M. Yano, and M. Inoue, *High-performance ZnO/ZnMgO field-effect transistors using a hetero-metal-insulator-semiconductor structure* Appl. Phys. Lett. 89, 053502 (2006).

[171] P. Görrn, M. Sander, J. Meyer, M. Kröger, E. Becker, H-H. Johannes, W. Kowalsky, and T. Riedl, *Towards See-Through Displays: Fully Transparent Thin-Film Transistors Driving Transparent Organic Light-Emitting Diodes*, Adv. Mater. 18, 738 (2006)

[172] E. Fortunato, P. Barquinha, A. Pimentel, L. Pereira, G. Gon, and R. Martins, *Amorphous IZO TTFTs with saturation mobilities exceeding 100 cm^2/Vs*, phys. stat. sol. (RRL) 1, R34 (2007).

[173] J. Jiang, Q. Wan, J. Sun, and A. Lu, *Ultralow-voltage transparent electric-double-layer thin-film transistors processed at room-temperature*, Appl. Phys. Lett. 95, 152114 (2009).

[174] M-J. Lee, S. I. Kim, C. B. Lee, H. Yin, S-E. Ahn, B. S. Kang, K. H. Kim, J. C. Park, C. J. Kim, I. Song, S. W. Kim, G. Stefanovich, J. H. Lee, S. J. Chung, Y. H. Kim, and Y. Park, *Low-Temperature-Grown Transition Metal Oxide Based Storage Materials and Oxide Transistors for High-Density Non-volatile Memory*, Adv. Funct. Mater. 19, 1587 (2009).

[175] H. Koide, Y. Nagao, K. Koumoto, Y. Takasaki, T. Umemura, T. Kato, Y. Ikuhara, and H. Ohta, *Electric field modulation of thermopower for transparent amorphous oxide thin film transistors* Appl. Phys. Lett. 97, 182105 (2010).

[176] H. Z. Zhang, L. Y. Liang, A. H. Chen, Z. M. Liu, Z. Yu, H. T. Cao, and Q. Wan, *High-performance transparent thin-film transistor based on Y_2O_3/In_2O_3 with low interface traps*, Appl. Phys. Lett. 97, 122108 (2010).

[177] S. M. Yoon, S. Yang, C. Byun, S. H. K. Park, D. H. Cho, S. W. Jung, O. S. Kwon, and C. S. Hwang, *Fully Transparent Non-volatile Memory Thin-Film Transistors Using an Organic Ferroelectric and Oxide Semiconductor Below 200 $^\circ C$*, Adv. Funct. Mater. 20(6), 921 (2010).

[178] J. Y. Bak, S. Yang, and S. M. Yoon, *Transparent Al–In–Zn–O Oxide semiconducting films with various in composition for thin-film transistor applications*, Ceram. Int. 39, 2561 (2013).

[179] B. K. Sharma, B. Jang, J. E. Lee, S-H. Bae, T. W. Kim, H-J. Lee, J.-H. Kim, and J-H. Ahn, *Load-controlled roll transfer of oxide transistors for stretchable electronics*, Adv. Funct. Mater. 23, 2024 (2013).

[180] H. Zhang, Q. Wan, C. Wan, G. Wu, and L. Zhu, *Tungsten oxide proton conducting films for low-voltage transparent oxide-based thin-film transistors*, Appl. Phys. Lett. 102, 052905 (2013).

[181] E. Fortunato, P. Barquinha, and R. Martins, *Oxide Semiconductor Thin-Film Transistors: A Review of Recent Advances*, Adv. Mater. 24, 2945 (2012).

[182] M. Grundmann, H. Frenzel, A. Lajn, M. Lorenz, F. Schein, and H. von Wenckstern, *Transparent semiconducting oxides: materials and devices*, Phys. Status Solidi A 207, 1437 (2010).

[183] J. F. Conley, *Instabilities in Amorphous Oxide Semiconductor Thin-Film Transistors*, IEEE Trans. On Device and Mater. Rel. 10, 460 (2010).

[184] R. B. M. Cross and M. M. De Souza, *Investigating the stability of zinc oxide thin film transistors*, Appl. Phys. Lett. 89, 263513 (2006).

[185] J. K. Jeong, *Photo-bias instability of metal oxide thin film transistors for advanced active matrix displays*, J. Mater. Res. 28, 2071 (2013).

[186] C. Brox-Nilsen, J. Jin, Y. Luo, P. Bao, and A. M. Song, *Sputtered ZnO Thin-Film Transistors With Carrier Mobility Over 50 cm^2/Vs*, IEEE Trans. Electron Devices 60, 3424 (2013).

[187] J.F. Wager, *Transparent Electronics*, Science 300, 1245 (2003).

[188] F. Braun, *Ueber die Stromleitung durch Schwefelmetalle*, Annalen der Physik 229, 556 (1875).

[189] W. Schottky, *Zur Halbleitertheorie der Sperrschicht- und Spitzengleichrichter*, Zeitschrift für Physik A Hadrons and Nuclei 113 (5-6), 367 (1939).

[190] N. F. Mott, *The Theory of Crystal Rectifiers*, Proc. R. Soc. Lond. A 171, 27 (1939).

[191] C. A. Mead, *Surface barriers on ZnSe and ZnO*, Physics Letters 18, 218 (1965).

[192] M. W. Allen, M. M. Alkaisi, and S. M. Durbin, *Metal Schottky diodes on Zn-polar and O-polar bulk ZnO*, Appl. Phys. Lett. 89, 103520 (2006).

[193] M. W. Allen, S. M. Durbin, and J. B. Metson, *Silver oxide Schottky contacts on n-type ZnO*, Appl. Phys. Lett. 91, 053512 (2007).

[194] A. Lajn, H. von Wenckstern, Z. Zhang, C. Czekalla, G. Biehne, J. Lenzner, H. Hochmuth, M. Lorenz, M. Grundmann, S. Wickert, C. Vogt and R. Deneke, *Properties of reactively sputtered Ag, Au, Pd, and Pt Schottky contacts on n-type ZnO*, J. Vac. Sci. Technol. B 27 (3), 1769 (2009).

[195] M. W. Allen, R. J. Mendelsberg, R. J. Reeves, and S. M. Durbin, *Oxidized noble metal Schottky contacts to n-type ZnO*, Appl. Phys. Lett. 94, 103508 (2009).

[196] J. Bardeen, *Surface States and Rectification at a Metal Semi-Conductor Contact*, Physical Review 71, 717 (1947).

[197] W. Mönch. *Barrier heights of real Schottky contacts explained by metal-induced gap states and lateral inhomogeneities*, J. Vac. Sci. Technol. B 17, 1867 (1999).

[198] H. A. Bethe, "Theory of the boundary layer of crystal rectifiers", MIT Radiation Laboratory Report, (1942).

[199] J. H. Werner and H. H. Gü, *Barrier inhomogeneities at Schottky contacts*, J. Appl. Phys. 69, 1522 (1991).

[200] M. W. Allen, *Schottky Contact Formation to Bulk Zinc Oxide*, PhD Dissertation, University of Canterbury, June 2008.

[201] L. J. Brillson and Y. Lu, *ZnO Schottky barriers and Ohmic contacts*, J. Appl. Phys. 109, 121301 (2011).

[202] H-K. Kim, S-W. Kim, B. Yang, S-H. Kim, K. H. Lee, S. H. Ji, and Y. S. Yoon, *Electrical and Interfacial Properties of Nonalloyed Ti/Au Ohmic and Pt Schottky Contacts on Zn-Terminated ZnO*, Jpn. J. Appl. Phys. 45, 1560 (2006).

[203] H-K. Kim, K-K. Kim, S-J. Park, T-Y. Seong, and I. Adesida, *Formation of low resistance nonalloyed Al/Pt ohmic contacts on n-type ZnO epitaxial layer*, J. Appl. Phys. 94, 4225 (2003).

[204] S. Y. Kim, H. W. Jang, J. K. Kim, C. M. Jeon, W. I. Park, G-C. Yi, and J-L. Lee, *Low-Resistance Ti/Al Ohmic Contact on Undoped ZnO*, J. Electron. Mater. 31, 868 (2002).

[205] H. S. Yang, D. P. Norton, S. J. Pearton, and F. Ren, *Ti/Au n-type Ohmic contacts to bulk ZnO substrates*, Appl. Phys. Lett. 87, 212106 (2005).

[206] C-L. Tsai, Y-J. Lin, Y-M. Chin, W-R. Liu, W. F. Hsieh, C-H. Hsu, and J-A. Chu, *Low-resistance nonalloyed ohmic contacts on undoped ZnO films grown by pulsed-laser deposition*, J. Phys. D: Appl. Phys. 42, 095108 (2009).

[207] Y-Z. Chiou and K-W. Lin, *Annealing Effect of Transparent Ohmic Contacts to n-ZnO Epitaxial Films*, J. Electrochem. Soc. 153, G141 (2006).

[208] S-H. Kim, K-K. Kim, S-J. Park, and T-Y. Seong, *Thermally Stable and Low Resistance Re/Ti/Au Ohmic Contacts to n-ZnO*, J. Electrochem. Soc. 152 (3), G169 (2005).

[209] M. J. Deen and F. Pascal, *Electrical characterization of semiconductor materials and devices–review*, J Mater Sci: Mater Electron 17, 549 (2006).

[210] C. A. Mead, *Schottky Barrier Gate Field Effect Transistor*, Proceedings of the IEEE, 307 (1966).

[211] S. A. Campbell, *Fabrication Engineering at the Micro- and Nanoscale*, Oxford University Press, 2008.

[212] H.M. Smith and A.F. Turner , *Vacuum deposited thin films using a ruby laser*, Appl. Opt. 4, 147 (1965).

[213] K. Kinoshita, H. Ishibashi, and T. Kobayashi, *Improved surface smoothness of $YBa_2Cu_3O_y$ films and related multilayers by ArF excimer laser deposition with shadow mask 'eclipse method'*, Jpn J. Appl. Phys. Part 2: Lett. 33, 417 (1994)

[214] C. L. Liang, N. W. Cheung, R. N. Sato, and N. A. Doudoumopoulos, *A Diffusion Model of Subthreshold Current for GaAs MESFETs*, Solid-State Electron. 34, 131 (1991).

[215] L-Y. Su, H-Y. Lin, H-K. Lin, S-L. Wang, L-H. Peng, and J. J. Huang, *Characterization of Amorphous IGZO Thin-Film Transistors With Low Subthreshold Swing*, IEEE Electron Device Lett. 32, 1245 (2011).

[216] Y. Li, J. Xiang, F. Qian, S. Gradečak, Y. Wu, H. Wu, H. Yan, D. A. Blom, and C. M. Lieber, *Dopant-Free GaN/AlN/AlGaN Radial Nanowire Heterostructures as High Electron Mobility Transistors*, Nano Lett. 6, 1468 (2006).

[217] S-C. Chang, D. Hicks, and R. Laugal, *Patterning of zinc oxide thin films*, Solid-State Sensor and Actuator Workshop, 5th Technical Digest., IEEE, 41 (1992).

[218] M. W. Allen and S. M. Durbin, *Role of a universal branch-point energy at ZnO interfaces*, Phys. Rev. B 82, 165310 (2010).

[219] H. von Wenckstern, A. Lajn, A. Laufer, B. K. Meyer, H. Hochmuth, M. Lorenz, and M. Grundmann, *Ag related defect state in ZnO thin films*, AIP Conference Proceedings 1199, 122 (2010).

[220] H. Frenzel, A. Lajn, H. von Wenckstern, and M. Grundmann, *Ultrathin gate-contacts for Metal-semiconductor field-effect transistor devices: An alternative approach in transparent electronics*, J. Appl. Phys. 107, 114515 (2010).

[221] S. J. Krumbein, *Metallic Electromigration Phenomena*, IEEE Trans. Compon. Packag. Manuf. Technol., Vol. 11 No. 1, March (1988).

[222] D. H. Redinger, *Lifetime Modeling of ZnO Thin-Film Transistors*, IEEE Trans. Electron Devices 57, 3460 (2010).

[223] J. D. Ye, S. L. Gu, F. Qin, S. M. Zhu, S. M. Liu, X. Zhou, W. Liu, L. Q. Hu, R. Zhang, Y. Shi, and Y. D. Zheng, *Correlation between green luminescence and morphology evolution of ZnO*, Appl. Phys. A 81, 759 (2005).

[224] M. Katayama, S. Ikesaka, J. Kuwano, H. Koinuma, and Y. Matsumoto, *High quality anatase TiO_O film: Field-effect transistor based on anatase TiO_O*, Appl. Phys. Lett. 92, 132107 (2008).

[225] S. J. Young, L. W. Ji, S. J. Chang, and Y. K. Su, *ZnO metal-semiconductor-metal ultraviolet sensors with various contact electrodes*, J. of Crys. Growth 293, 43 (2006).

[226] N. N. Jandow, F. K. Yam, S. M. Thahab, H. Abu Hassan, K. Ibrahim, *Characteristics of ZnO MSM UV photodetector with Ni contact electrodes on poly propylene carbonate (PPC) plastic substrate*, Curr. Appl. Phys. 10, 1452 (2010).

[227] A. Vasudevan, S. Jung, and T. Ji, *On the Responsivity of UV Detectors Based on Selectively Grown ZnO Nanorods*, IEEE Sensors J. 12, 1317 (2012).

[228] D. Shvydka, V. Parikh, V. G. Karpov and A. D. Compaan, *Spatial and Temporal Variations in Electronic transport Through a CdTe-Based Schottky barrier*, Mater. Res. Soc. Symp. Proc. 865, 361 (2005).

[229] P. Marko, M. Meneghini, S. Bychikhin, D. Marcon, G. Meneghesso, E. Zanoni, D. Pogany, *IV, noise and electroluminescence analysis of stress-induced percolation paths in AlGaN/GaN high electron mobility transistors*, Microelectron. Rel. 52, 2194 (2012).

[230] E. Zanoni, M. Meneghini, A. Chini, D. Marcon, and G. Meneghesso, *AlGaN/GaN-Based HEMTs Failure Physics and Reliability: Mechanisms affecting Gate Edge and Schottky Junction*, IEEE Trans. Electron Devices 60, 3119 (2013).

[231] Y. Zhu, R. J. Mendelsberg, S. H. N. Lim, J. Zhu, J. Han, and A. Anders, *Improved structural and electrical properties of thin ZnO:Al films by dc filtered cathodic arc deposition*, J. Mater. Res. 27, 857(2012).

[232] F. J. Klüpfel, F-L. Schein, M. Lorenz, H. Frenzel, H. von Wenckstern, and M. Grundmann, *Comparison of ZnO-Based JFET, MESFET, and MISFET*, IEEE Trans. Electron Devices 60, 1828 (2013).

[233] L. Huang, W. Rieutort-Louis, Y. Hu, J. Sanz-Robinson, S. Wagner, J. C. Sturm, N. Verma, *Integrated All-silicon Thin-film Power Electronics on Flexible Sheets For Ubiquitous Wireless Charging Stations based on Solar-energy Harvesting*, IEEE Symposium on VLSI Circuits, Digest of Technical Papers (2012).

[234] S. Jeon, S. Ahn, I. Song, C-J. Kim, U-I. Chung, E. Lee, I. Yoo, A. Nathan, S. Lee, J. Robertson, and K. Kim, *Gated three-terminal device architecture to eliminate persistent photoconductivity in oxide semiconductor photosensor arrays*, Nat. Mater. 11, 301 (2012).

[235] D-Y. Qiao, X-J. Chen, Y. Ren, and W-Z. Yuan, *A Micro Nuclear Battery Based on SiC Schottky Barrier Diode*, J. Microelectromech. Syst. 20, 685 (2011).

[236] K. Koike, T. Aoki, R. Fujimoto, S. Sasa, M. Yano, S. Gonda, R. Ishigami, and K. Kume, *Radiation hardness of single-crystalline zinc oxide films*, Phys. Status Solidi C 9, 1577 (2012).

List of Abbreviations

Abbreviations

2DEG	Two Dimensional Electron Gas
ALD	Atomic Layer Deposition
AFM	Atomic Force Microscopy
AM-OLED	Active Matrix Organic Light Emitting Diodes
a-Si	Amorphous Silicon
AZO	Aluminium doped Zinc Oxide
B2B	Band to Band Transition
CdS	Cadmium Sulphide
CdSe	Cadmium Selenide
CMOS	Complementary Metal Oxide Semiconductor
CMOS	Complementary Metal Oxide Semiconductor
eA^0	Free Electron to Neutral Acceptor Transition
D^0h	Free Hole to Neutral Donor Transition
DAP	Donor Acceptor Pair Transition
DB	Defect Band
DX	Neutral Donor Bound Exciton
FCVA	Filtered Cathodic Vacuum Arc
FDP	Flat Panel Displays
FWHM	Full Width Half Maximum
FX	Free Exciton
GaAs	Gallium Arsenide
GaN	Gallium Nitride
GB	Grain Boundary
GIZO	Gallium Indium Zinc Oxide
HFET	Heterostructure Field Effect Transistor
ITO	Indium Tin Oxide
IGZO	Indium Gallium Zinc Oxide

KPFM	Kelvin Probe Force Microscopy
MBE	Molecular Beam Epitaxy
MESFET	Metal Semiconductor Field Effect Transistor
MgO	Magnesium Oxide
MISFET	Metal Insulator Field Effect Transistor
MOCVD	Metal Organic Chemical Vapour Deposition
MOVPE	Metal Organic Vapour Phase Epitaxy
NBE	Near Band Edge
NBS	Negative Bias Stress
LO	Longitudinal Phonon
O_i	Oxygen Interstitial
O_{Zn}	Oxygen Antisite
PBS	Positive Bias Stress
PECVD	Plasma Enhance Chemical Vapour Deposition
PLD	Pulsed Laser Deposition
PL	Photoluminescence
RMS	Root Mean Square
SAW	Surface Acoustic Wave
SEM	Scanning Electron Microscopy
Si	Silicon
SiC	Silicon Carbide
TCO	Transparent Conductive Oxide
TES	Two Electron Satellite
TFT	Thin Film Transistor
TLM	Transmission Line Model
ToF-SIMS	Time-of-Flight Secondary Ion Mass Spectroscopy
UHV	Ultra High Vacuum
UV	Ultra Violet
V_O	Oxygen Vacancy

V_{Zn}	Zinc Vacancy
XRD	X-Ray Diffraction
Zn_i	Zinc Interstitial
Zn_O	Zinc Antisite
ZnO	Zinc Oxide
ZnMgO	Zinc Magnesium Oxide
ZTO	Zinc Tin Oxide

Constants and variables

k_B	Boltzmann Constant (8.61733 eV/K)
h	Planck Constant ($4.135667516 \times 10^{-15}$ eV.s)
q	Elementary Charge ($1.60217657 \times 10^{-19}$ As)
ϵ_0	Vacuum Permittivity (8.854187×10^{-12} F/m)
A^*	Effective Richardson Constant (1.20173×10^6 $Am^{-2}K^{-2}$)
λ	Wave Length
σ	Conductivity
ρ	Resistivity
ρ_C	Contact Resistivity
ϵ_S	Semiconductor Permittivity
χ	Electron Affinity
ν	frequency
α	Absorption Coefficient
μ	Charge Carrier Mobility
μ_{ch}	Channel Mobility
μ_G	Mobility inside the Grain
μ_{GB}	Mobility in the Grain Boundary
η	Ideality Factor
ϕ_B	Schottky Potential Barrier
ϕ_m	Metal Work Function

ϕ_S	Semiconductor Work Function
χ	Electron Affinity
E_G	Bandgap
E_C	Conduction Band Minimum
E_V	Valence Band Maximum
E_F	Fermi Energy
E_B	Potential Barrier Height at the Grain Boundary
f	frequency
g_i	Channel Conductance
g_m	Transconductance
J	Current Density
L	MESFET Gate-Channel Length
L_G	Grain Size
L_T	Transfer Length
m^*	Effective Electron Mass
$N,\ n$	Carrier Concentration
N_t	Defect Density at the Grain Boundary
T	Temperature
υ_c	Thermal Collection Velocity
V_{bi}	Built-in Voltage
V_F	Forward Voltage
V_H	Hall Voltage
V_R	Reverse Voltage
W	MESFET Gate-Channel Width